UNIVERSITY OF CAPE TOWN
IYUNIVESITHI YASEKAPA • UNIVERSITEIT VAN KAAPSTAD

Characterisation of Glass Fibre Polypropylene and GFPP based Fibre Metal Laminates at high strain rates

Reuben Ashley Govender

Thesis presented for the Degree of
Doctor of Philosophy
in the Department of Mechanical Engineering
Faculty of Engineering and the Built Environment
University of Cape Town

December 2011

Blast Impact and Survivability Research Unit

Declaration

I, Reuben Ashley Govender, hereby:

(a) grant the University of Cape Town free license to reproduce the above thesis in whole or in part, for the purpose of research;

(b) declare that:

(i) the above thesis is my own unaided work, both in concept and execution, and that apart from the normal guidance from my supervisor, I have received no assistance apart from that explicity stated in the Acknowledgements.

(ii) neither the substance nor any part of the above thesis has been submitted in the past, or is being, or is to be submitted for a degree at this University or at any other university.

I am now presenting the thesis for examination for the degree of PhD in Mechanical Engineering.

Reuben Ashley Govender

30 August 2011

Abstract

Fibre reinforced polymers (FRP) are finding increasing use in structures subjected to high rate loading such as blast or impact. Proper design of such structures requires thorough characterisation of the material behaviour over a range of loading rates from quasi-static to impact. This thesis investigated the quasi-static and impact response of Glass Fibre Polypropylene (GFPP) in compression, bending and delamination. The bending and delamination response of Fibre Metal Laminates (FMLs) based on GFPP and aluminium was also investigated at quasi-static and impact rates.

High strain rate ($5 \times 10^2 - 10^3/s$) compression tests were conducted on GFPP using a compressive Split Hopkinson Pressure Bar (SHPB) and a Direct Impact Hopkinson Pressure Bar (DIHPB), in the through-thickness and in-plane directions. In both loading directions, the peak stress of GFPP increased linearly with the logarithm of strain rate. For in-plane loading, the failure modes were dominated by localised fibre buckling and kink bands, leading to delamination. The through thickness loading produced macroscopic shear and spreading failure modes. However, both of these failure modes are linked to in-ply fibre failures, due to through thickness compression causing transverse tensile strain. Previous studies of similar materials have not explicitly stated the link between through thickness compression and fibre failure associated with transverse tensile strain.

A novel test rig was developed for Three Point bend testing at impact rates. The specimen was supported at the outer points on a rigid impacter and accelerated towards a single output Hopkinson Pressure Bar (HPB), which impacted the specimen at its midspan. Previous impact bend test rigs based on HPBs were limited to testing specimens with deflections to failure up to approximately 1 mm, whereas the rig implemented herein measured deflections up to approximately 10 mm. This configuration permits the output HPB to be chosen purely on the magnitude of the expected impact force, which resulted in superior force resolution to configurations used in other studies. The HPB Impact Bend rig was used to test GFPP and aluminium-GFPP FML specimens, at impact velocities ranging from 5 to 12 m/s. The flexural strength of GFPP increased with strain rate, while the flexural response of the FML specimens was relatively insensitive to strain rate.

Several candidate delamination test geometries were investigated at quasi-static displacement rates (1 mm/min), and the Single Leg Bend (SLB) test was identified as suitable for adaptation to higher rate testing. Single Leg Bend delamination tests of both GFPP and FML specimens were performed using the HPB Impact Bend rig, at impact velocities of 6 to 8 m/s. The shape of the force displacement response for the high rate testswas markedly different from the quasi-static tests, for both the GFPP and FML specimens. Finite element (FE) simulation of the quasi-static and impact rate SLB tests on GFPP indicated that the difference was probably due to the interaction of flexural vibrations and stress waves in the specimen and the impacter cross member. The experimental results and FE analysis suggest that the delamination fracture toughness of GFPP decreases slightly as strain rate increases. High rate delamination tests on FML specimens resulted in unstable crack growth.

Acknowledgements

Of the many people who deserve thanks, some are particularly prominent:

Prof. Gerald Nurick, my supervisor, who has guided and provided opportunities, while allowing me remarkable freedom to explore.

My co-supervisor Assoc. Prof. Genevieve Langdon, who has been a source of guidance and support in many aspects of my life.

Mr Trevor Cloete, for the many and varied conversations, which have been an invaluable part of my learning experience.

Mintek and the NRF, who provided financial support to the author from 2006 to 2008. ARMSCOR, for their general funding of BISRU, which helped support the author from 2009 to 2011.

The staff and students of the Blast Impact and Survivability Research Unit - I have never experienced a more collegial atmosphere.

Glen Newins and the Mechanical Engineering Workshop staff, who were always patient when I arrived with yet another revision to my designs.

My friends both at UCT and further afield, for their encouragement and support.

My siblings for their support and understanding of the sacrifices this endeavour has entailed.

My parents, my first and most influential teachers: you laid my foundations then freed me to build on them as I wished. I can never express my love and gratitude often enough.

Contents

List of Figures

List of Tables

Nomenclature

Greek Lower Case Symbols

δ	Displacement or deflection
κ_{Cal}	Calibration factor
$\dot{\varepsilon}$	Strain rate
σ_{ij}	Stress component, with planar normal *i* and direction *j*
ε_i	Incident strain wave
ε_r	Reflected strain wave
ε_t	Transmitted strain wave

Greek Upper Case Symbols

Λ	Wavelength

Roman Lower Case Symbols

a	Crack length
d	Diameter
f	Frequency
$l(t)$	Instantaneous length
r	Radius
t	Thickness
v	Velocity

w Width

Roman Upper Case Symbols

$A(t)$ Instantaneous area

A_o Original area

C Compliance

C_o Fundamental wave velocity

C_p Phase velocity

E Elastic modulus

G Strain energy release rate

L_o Original length

P Force

Abbreviations

COV **C**oefficient **o**f **V**ariation

CZM **C**ohesive **Z**one **M**odel

DCB **D**ouble **C**antilever **B**eam

ELS **E**nd **L**oaded **S**plit

ENF **E**nd **N**otch **F**lexure

FML **F**ibre **M**etal **L**aminate

FRP **F**ibre **R**einforced **P**olymer

GFPP **G**lass **F**ibre **P**oly**P**ropylene

HPB **H**opkinson **P**ressure **B**ar

LEFM **L**inear **E**lastic **F**racture **M**echanics

NLFM **N**on-**L**inear **F**racture **M**echanics

ONF **O**ver **N**otched **F**lexure

PTFE	Poly Tetra Flouro Ethylene -Teflon ™
SBS	**S**hort **B**eam **S**hear
SCB	**S**ingle **C**antilever **B**eam
SHPB	**S**plit **H**opkinson **P**ressure **B**ar
SLB	**S**ingle **L**eg **B**end
VCCT	**V**irtual **C**rack **C**losure **T**echnique
WIF	**W**edge **I**nsert **F**racture

Direction and Naming Convention

This thesis uses numerical indices to indicate direction for certain scalar, vector and tensor quantities. The indices 1, 2 and 3 replace x, y and z directly. Vector quantities such as velocity $\boldsymbol{v}$ have individual components v_i, where i refers to the direction of the component. Tensor quantities such as stress $\boldsymbol{\sigma}$ have individual components σ_{ij}. The first index i refers to the direction of the unit normal of the surface on which the stress component acts, and the second index j refers to the direction in which the component acts. With reference to the graphic below, σ_{11} is the stress component where the normal is in the 1 direction, and the stress also acts in the 1 direction. Hence σ_{11} is a direct stress, where a positive value indicates tension and a negative value compression. The components σ_{12} and σ_{13} are shear stresses.

In the context of fibre reinforced composite materials, the 1 and 2 direction lie in the plane of the fibres, corresponding to the warp and weft directions respectively. The 3 direction is perpendicular to the fibre plane, which is often referred to as the "through thickness" direction.

A subscript o, for example A_o, denotes an initial quantity. Subscripts in Roman numerals, for example G_I or G_{II}, refer specifically to fracture modes.

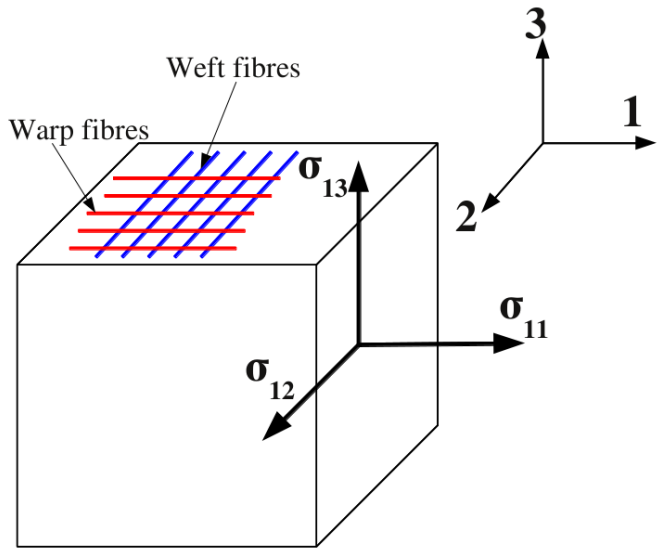

Chapter 1

Introduction

1.1 Background

Fibre reinforced polymers (FRP) exhibit a high strength to mass ratio, making them an attractive choice for applications where mass reduction is important. However, typical examples of FRP usage such as aerospace and high performance vehicles also require structures which are damage tolerant, particularly under impact loading. Delamination of FRP structures is a common problem, often linked to impact damage where very little surface damage is visible.

Designing any structure for impact loading requires knowledge of the material properties, and how these properties change with the rate of loading. The anisotropic nature of FRP requires that the material properties be determined in different directions of loading, as well as at different rates. Delamination testing is a developing field and even at quasi-static rates only a handful of test methods have been standardised. The investigation of delamination at higher rates of loading is a growing field of research.

The FRP investigated in this thesis is Twintex®, which is glass fibre reinforced polypropylene (GFPP). In addition to GFPP, a fibre metal laminate (FML) based on GFPP and aluminium, will be investigated. FMLs are a hybrid composite, consisting of FRP layers bonded between metallic sheets. A well known example of a FML is GLARE (GLAss REinforced), which consists of alternating layers of aluminium and glass fibre reinforced epoxy [1, 2].

FMLs are an attempt to combine the toughness and impact resistance of metals, with the strength to mass ratio of FRP. FMLs such as GLARE have been considered for

use in modern passenger aircraft such as the A380, in structures such as the leading edges of the wings and tail. Langdon, Nurick and colleagues [3, 4, 5] at the Blast Impact and Survivability Research Unit (BISRU) at UCT have conducted extensive blast loading tests on FMLs based on aluminium and GFPP as a candidate material for blast resistant structures. Delamination and debonding were prominent failure modes observed during these experiments. However, the characterisation of both GFPP and FML specimens reported in these investigations was limited to quasi-static testing. Hence investigation of the in plane, interlaminar and interfacial properties of GFPP and GFPP based FMLs will assist in further analysis and modelling of the blast test results. The development of an impact delamination or debonding test protocol will aid the selection and design of FMLs and other sandwich panels that will be subjected to blast or impact loading.

The high strain rate testing will be conducted using the Split Hopkinson Pressure Bar (SHPB), which is a means of testing materials at strain rates of the order of 5×10^2 to $5 \times 10^3/s$. The SHPB was originally developed for compression testing [6] and has been successfully adapted for tensile loading, for example [7, 8]. While the SHPB has been used extensively to test other FRP (for example [9, 10, 11]), GFPP has not been tested with the SHPB. Different configurations of the SHPB for bend testing have been reported, for example [12, 13]. However, bend testing of relatively flexible specimens poses challenges to the SHPB bend test configurations described in the literature. Bend testing is of interest because many delamination test methods involve specimens loaded in bending.

1.2 Problem Definition

GFPP has not been well characterised at high strain rates. The delamination properties of GFPP, particularly as loading rates increase, is of particular interest. The delamination properties of FMLs based on GFPP and aluminium will also be investigated.

This thesis will investigate:

- The compressive properties of GFPP at quasi-static rates, and under impact loading at strain rates ranging from approximately 500 to 1500 $/s$.

- The flexural properties of GFPP and GFPP based FMLs at quasi-static rates and under impact loading.

- Delamination test methods and adaptation of an appropriate method to impact loading. This method will be applied to GFPP and GFPP based FMLs.

Tensile tests, both at quasi-static and higher rates, are outside of the scope of this thesis.

1.3 Hypothesis

The peak strength of GFPP increases as a function of strain rate. The delamination resistance of GFPP and GFPP based FMLs decreases as the rate of loading increases.

1.4 Thesis Outline

Chapter 2 reviews publications pertinent to this thesis. The topics reviewed are studies on Glass Fibre Polypropylene (GFPP), mechanical testing of fibre reinforced polymers (FRPs) for in-plane and delamination properties, Fibre Metal Laminates (FMLs), computational modelling of delamination and high strain rate testing of FRPs. The review highlights opportunities for novel research in the area of high strain rate testing of GFPP.

Chapter 3 details the manufacture of GFPP and FML panels and test specimens.

Chapter 4 describes the experimental methodology for compression testing of GFPP at quasi-static and high strain rates, using the Split Hopkinson Pressure Bar (SHPB). The results of these tests are presented and analysed for rate dependence.

Chapter 5 focusses on bend testing of GFPP and FMLs. The standardised test methodology for quasi-static tests is described and the results presented. The development of a novel apparatus for conducting bend tests at impact rates, using a HPB, is discussed. The results of HPB Impact Bend tests on GFPP and FMLs are presented.

Chapter 6 investigates several delamination test methods, to choose the most suitable candidate for delamination testing at high rates. The adaptation of the chosen test method to high rate testing using the HPB Impact Bend apparatus is described. Results for delamination tests at quasi-static and impact rates for GFPP and FML specimens are presented.

Chapter 7 analyses and discusses notable features of the experimental results presented in Chapters 4, 5 and 6. Computational models are used to confirm assumptions

made in analysing the experimental data or to elucidate details of the experimental results.

Chapter 8 summarises the findings of this thesis and recommends future development of this field of research.

Chapter 2

Literature Review

Each of the major aspects of this thesis have their own history and a review would be incomplete without a discussion of the relevant history. As the different technologies investigated and applied in this thesis have developed independently, each topic is reviewed separately. This chapter is split into the following sections:

- Fibre Reinforced Polymer (FRP) Materials
- Mechanical testing of FRP
- Delamination testing of FRP
- Properties of Glass Fibre Polypropylene (GFPP)
- Computational modelling of delamination of FRP
- Fibre Metal Laminates (FMLs)
- High Strain Testing, focussing on the Split Hopkinson Pressure Bar (SHPB)

2.1 Fibre Reinforced Polymers

Fibre reinforced materials are a sub-set of composite materials. Fibre reinforced materials are not a recent development. Composite bows, where the wooden stave was stiffened and strengthened by bonding it to animal bone, horn and sinew, were used in the Ancient Greek era [14]. However, materials based on man-made fibres such as glass, carbon or aramid, to reinforce a polymer matrix (thermosets such as epoxy and polyester, and thermoplastics such as polypropylene and poly-ether-ether-ketone PEEK) have only become widely used as engineering materials post World War II. FRPs exhibit higher specific stiffness (elastic modulus to density ratio) and higher specific strength (failure strength to density ratio) than most engineering metals [15]. FRPs are more expensive (per unit of raw material) than metals, and require specialised manufacturing techniques. This restricted the early use of FRP to applications where cost and ease of manufacture are superceded by mass reduction and high strength, such as aerospace, racing vehicles and high performance sporting equipment. Within the aerospace industry, the percentage of components manufactured from FRP has increased [16] with the forthcoming Boeing 787 Dreamliner utilising composite materials for as much as 50% of its primary structure [17]. As the FRP industry has matured, FRPs have become more ubiquitous, with surfboards and canoes makinge extensive use of glass FRP. Low maintenance window frames are being manufactured from thermoplastic glass FRP [18].

The FRP investigated in this thesis consists of commingled E-glass and polypropylene, which is sold under the brand name Twintex® . It is currently manufactured by Owens Corning ®[19]. This thesis utilised Twintex® in a balanced 2 x 2 twill weave fabric, which contains 60% glass fibres by mass (35 % by volume) [19]. Manufacturing of components from Twintex® require heating the raw material (either in the form of fabric or pre-consolidated panels) to above the melting temperature (180 to 230 $^{\circ}C$) while applying pressure via a mould with the desired final shape. Specific details on the manufacture of Twintex® panels and specimens in this study are discussed in Chapter 3. Any reference in this thesis to glass fibre polypropylene (GFPP) from Chapter 3 onwards implies a laminate manufactured from Twintex® . A summary of published studies on the mechanical properties of GFPP is presented in §2.4, after the different methods of mechanical testing of FRPs are introduced.

2.2 Mechanical Testing of FRPs

A goal of this thesis is characterisation of the mechanical properties of GFPP at strain rates ranging from approximately 10^{-4} to $10^{3}/s$. Quasi-static testing of FRPs is standardised for quasi-static strain rates ($\dot{\varepsilon} \approx 10^{-4}$ to $10^{-2}/s$) and is discussed for compression in §2.2.1 and bending in §2.2.2. Adams [20] presents a thorough review of quasi-static FRP testing for tension, compression, bending and shear. Delamination testing, which has been standardised to some extent but has research areas still open to discussion, is reviewed in §2.3. High strain rate testing with the Split Hopkinson Pressure Bar (SHPB), which is not standardised, has a substantial body of literature from which good testing practice may be drawn. The application of the SHPB to testing of FRPs is reviewed in §2.7.3 to §2.7.5 for compression, bending and delamination respectively.

2.2.1 Compression Testing

Compression testing of FRPs is discussed in three ASTM standards, which use different methods of applying the load to the specimen, shown in Figure 2.1:

- ASTM D 695 [21] uses pure end loads to compress a prismatic specimen, of circular or rectangular cross section. The preferred specimen dimensions indicate a length of 25.4 mm and width or diameter of 12.7 mm, with a recommendation to use a longer specimen for elastic modulus tests. This method, which was originally specified for rigid plastics, is suitable for testing FRP specimens obtained from relatively thick laminates. A special support is needed to test specimens from thin laminates, which may only be tested in the in-plane direction. The requirements for the test fixtures described in [21] are to ensure pure axial loading via hardened parallel faces. A ball joint, shown in Figure 2.1(a), is suggested to prevent transmission of any moments to the specimen. End loading may result in crushing failures of the loaded specimen ends, rather than failures in the middle of the specimen.
- ASTM D 3410 [22], shown in Figure 2.1(b) applies shear loading of the gripped lateral surfaces of the specimen, to produce compressive loading in the unsupported gauge section. This method uses pure shear loading to avoid premature crushing failures of the specimen ends associated with end loading. This method is only suitable for in-plane compression, as the recommended specimen length is 140 to 155 mm to provide sufficient length for gripping. The fixture described in

[22] is fairly bulky, as it must contain the tapered wedge grips and the alignment rods.

- ASTM D 6641 [23] uses combined shear of the gripped lateral surfaces and direct compression of the end faces of the specimen, to produces compressive loading the the unsupported gauge section. As with ASTM D 3410, this means of loading is intended to reduce the occurrence of crushing failures caused by pure end loading. Specimens of similar dimensions to ASTM D 3410 are specified.

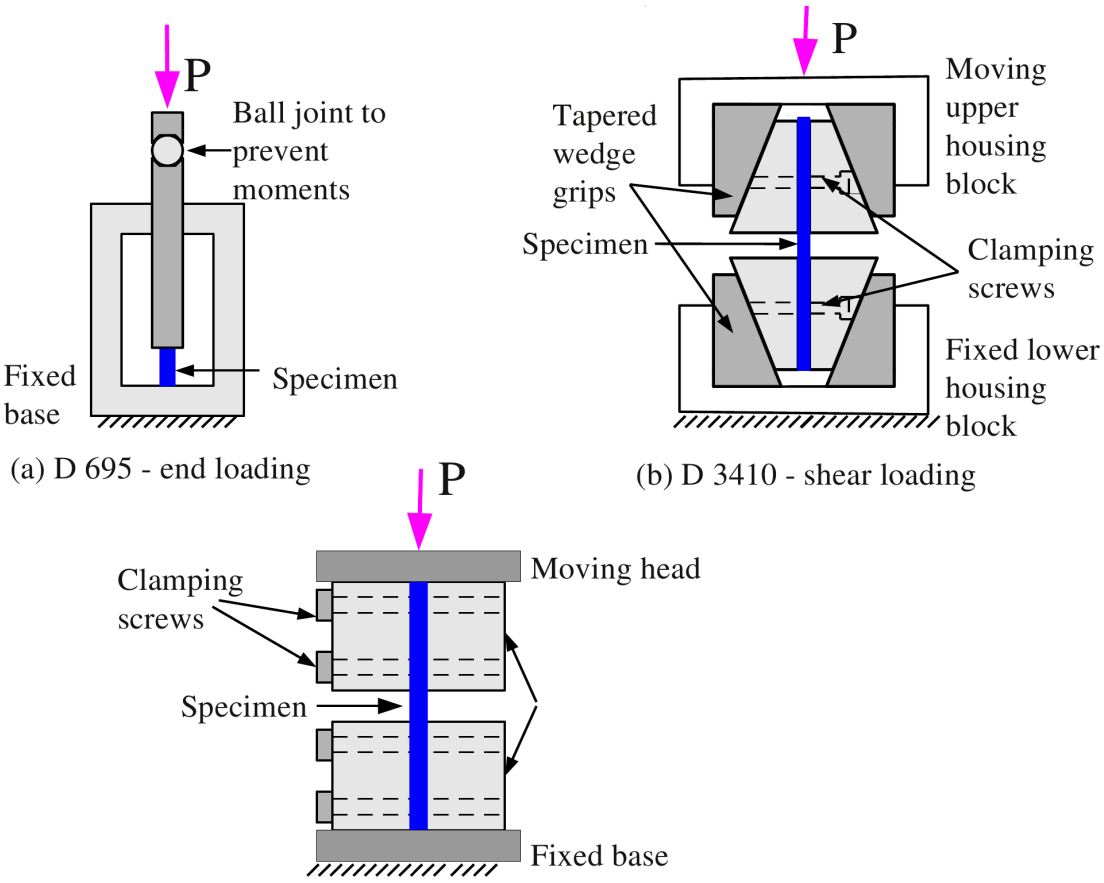

Figure 2.1: Schematics of ASTM compression fixtures (Figures adapted from [21, 22, 23])

Adams [20] discusses the need to avoid buckling failures in compression testing of unidirectional FRPs, in order to obtain the "true" laminate strength. In compression loading of woven FRP, buckling failures at the scale of the weave are highly likely due to the fibres not being straight. Hence for compression of woven FRP testing, it is necessary to avoid global or Euler buckling of the specimen, but not fibre buckling at the weave scale.

Obtaining material properties at high strain rates requires test specimens and fixtures with low mass, to facilitate acceleration to the higher testing speeds and to minimise the contribution of inertial force to the measured forces. The regular fixture for ASTM D 3410 has a mass of 45 kg and even a smaller version has a mass of 10.5 kg [20]. The mass of the fixture for ASTM D 6641, estimated from the dimensions specified in [23], is approximately 5 kg. Fixture masses of this order of magnitude are not suitable for testing at higher rates, where the displacement rates are of the order of m/s rather than quasi-static displacement rates of mm/min. While ASTM 695 shows recommended fixtures, the requirement of the standard is that the specimen is loaded axially between parallel faces that cannot transmit moments to the specimen. This requirement is met by compression SHPB testing without the need for any additional test fixtures. The application of the SHPB to high rate material characterisation is discussed in detail in §2.7.2.

2.2.2 Bend Testing

The popularity of bend testing of FRPs is due to its simplicity: rectangular specimens without the need for tabs; test fixtures which may be used for a variety of specimen dimensions and materials; data reduction based on elementary beam theory familiar to engineering undergraduates. Standardised bend testing of FRPs using either three or four point bend fixtures, shown in Figure 2.2, is described in ASTM D790 [24] and D7264 [25] and for four point bending in ASTM D 6272 [26]. For FRPs, the recommended span S to thickness t ratio is 16:1, which may be increased to ensure that failure is at the outer fibres due to flexure. Three point bending must be conducted with the load applied at mid-span [24, 25], while four point bending may apply the load symmetrically at either $\frac{1}{3}$ or $\frac{1}{4}$ of the span inwards from the outer supports [26]. Four point bending has the advantage of exerting a constant moment between the loading rollers, but requires a more complicated hinged loader, to ensure that the loads are equal.

Bend testing at higher rates may be performed using drop weight testers, instrumented with load cells at the central impacter. These testers may be custom designed but are commercially available [27, 28]. The impact velocity of such testers is limited by the available drop height, unless equipped with spring or pneumatic systems. Any impact testing system using a load cell will suffer from "ringing" due to stress waves generated by the impact, discussed further in §2.7. Impact bend tests have been developed using the Hopkinson Pressure Bar (HPB), which is discussed in detail in §2.7.4.

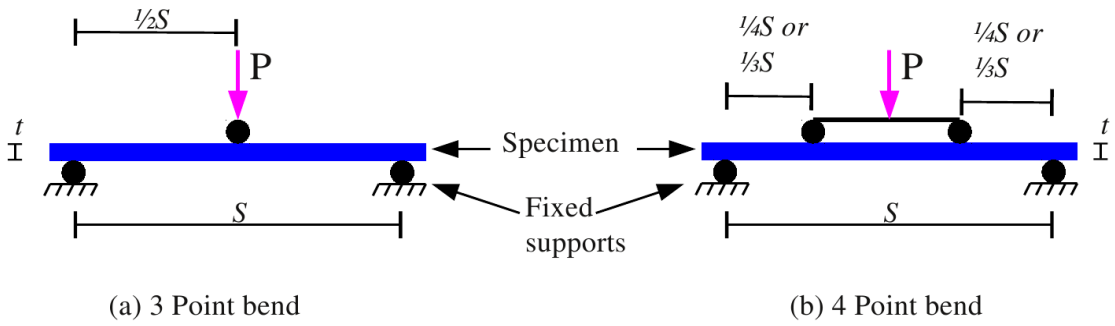

(a) 3 Point bend (b) 4 Point bend

Figure 2.2: Schematics of three and four point bend tests

2.3 Delamination Testing of Fibre Reinforced Polymers

Quasi-static test methods for the through thickness and delamination properties of FRPs have been standardised by organisations such as ASTM. Some of these standards are explicitly defined for unidirectional FRPs. However, guidelines for testing woven (fabric or textile) FRPs are given in ASTM D 6856. The relevant quasi-static standardised tests are reviewed in order to select candidate test methods for adaptation to high rate tests. FMLs have not (to date) been been used in sufficient volumes to warrant standardisation of testing. The application of FRP delamination tests to debonding of FMLs has been published, and is discussed where relevant.

The ASTM standards pertaining to delamination properties of FRP are summarised in Table 2.1, followed by detailed reviews of the individual test methods. Test methods providing through thickness strength data are described in §2.3.1, and those related to delamination fracture toughness data are discussed in §2.3.2.

Table 2.1: Standardised tests for delamination properties of FRP

Description	**ASTM Standard**	**Properties obtained**
Through Thickness Tension	D 7291 [29]	Through thickness tensile strength σ_{33} and modulus E_{33}
Lap Shear (also Double Notch Shear)	D 3846 [30]	Nominal interlaminar shear strength σ_{31}
Short Beam Shear (SBS)	D 2344 [31]	Apparent interlaminar shear strength σ_{31}
Iosepescu (V-Notch Shear)	D 5379 [32]	Shear strength-strain (dependent on specimen laminate orientation)
Double Cantilever Beam (DCB)	D 5528 [33]	Mode I interlaminar fracture toughness strain energy release rate G_I
Mixed Mode Flexure	D 6671 [34]	Mixed mode I-II interlaminar fracture toughness / strain energy release rate G_{I-II}

2.3.1 Through Thickness Failure Strength Testing

2.3.1.1 Tension

ASTM D 7291 [29] describes the test method for measuring the through-thickness modulus E_{33} and strength σ_{33} of FRPs. A cylindrical specimen is glued between metal end tabs and direct tension applied via the end tabs, shown in Figure 2.3. Waisted (or spool) specimens are required for measuring the through-thickness tensile strength, while straight sided cylinders (not shown) are used to determine the modulus. Test data using this method is reported in a handful of publications [35, 36, 37]. This test is very sensitive to the alignment of the FRP section and metal end tabs [29], so proper preparation of the specimens can be time consuming. As any failure in the adhesive layer between FRP and metal end tab will invalidate the test, selection of an appropriate adhesive is also non-trivial. Lifshitz and Leber [11] used a similar specimen in conjunction with a SHPB to obtain high strain rate data for both glass and carbon fibre reinforced epoxy, which is discussed in §2.7.5.1.

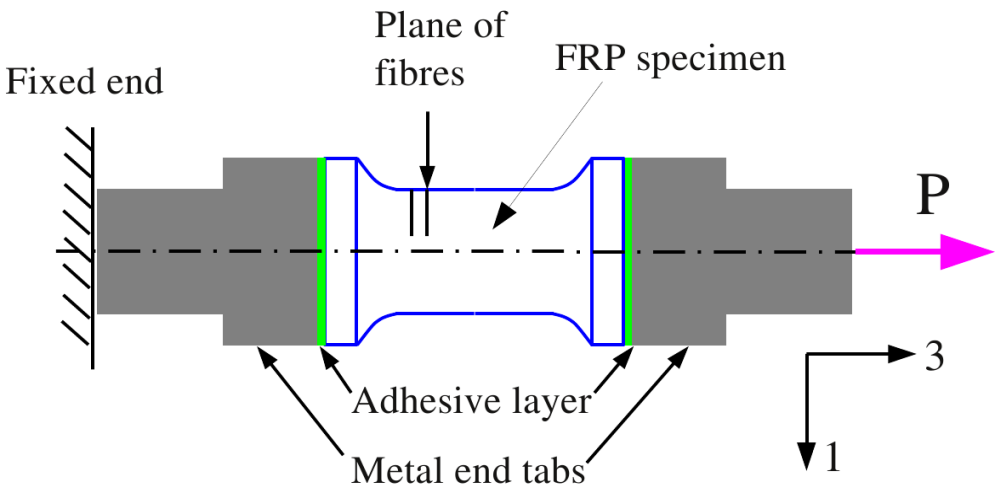

Figure 2.3: Schematic of specimen for through-thickness tensile tests (Figure adapted from [29])

2.3.1.2 Lap Shear

Lap shear testing requires a specimen with geometry such that applied axial tension or compression is carried by interlaminar shear in the gauge section, as shown in Figure 2.4. Lap shear testing for FRPs is standardised in ASTM D 3846 [30]. This standard requires a supporting jig to prevent buckling of the specimen, as the recommended

specimen thickness is relatively small (2.5 to 6.6 mm). The specimen geometry shown in Figure 2.4 is also referred to as "Double Notch Shear". The standard specifies that the shear strength is calculated from the maximum force and the cross sectional area subjected to the shear load [30], without any application of stress concentration factors. However, various computational studies [38, 39, 40] have shown that a considerable stress concentration is present at the corner of the notch, and that the shear stress across the gauge section is nonuniform. Dong and Harding [40] suggested a revised specimen geometry, shown in Figure 2.5, to minimise the variation of shear stress in the gauge section. The revised specimen geometry with a characteristic Z-profile was applied to quasi-static and SHPB tests [40, 41, 42], which are discussed in §2.7.5.2.

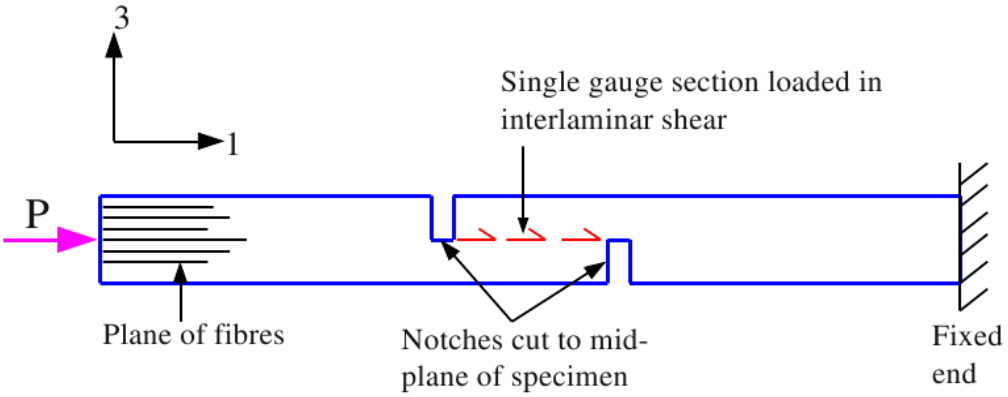

Figure 2.4: Schematic of lap shear specimen and loading (Figure adapted from[30])

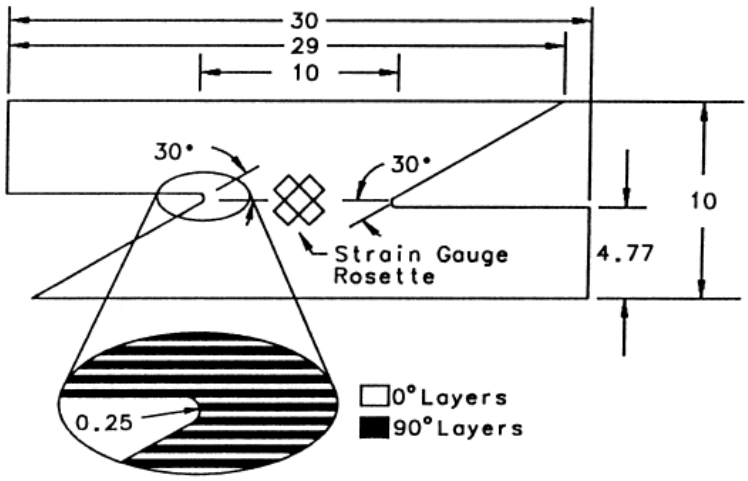

Figure 2.5: Lap shear specimen geometry to minimise variation of stresses in gauge section [42]

The specimen geometry shown in Figure 2.4 is most correctly referred to as single lap shear, as a single gauge section is subjected to shear stresses. Double lap shear

involves a specimen which is symmetric about the mid-plane, to give two gauge sections subjected to interlaminar shear as shown in Figure 2.6. Specimen geometries for double lap shear have been reported in [43, 44]. The asymmetry of the single lap shear specimen gives rise to moments within the specimen, which cause the specimen to deform perpendicular to the applied load. This requires the test fixture to provide some lateral support to prevent the specimen from shifting. The symmetry of the double lap shear specimen causes the internal moments in the specimen to cancel, so lateral support is not needed prior to failure. However failure in the two gauge sections is not likely to be simultaneous, and the specimen will tend to shift toward the side that fails first. Double lap shear also suffers from the same stress concentrations and nonuniform stress as single lap shear. Hence double lap shear has not been a widely adopted test method.

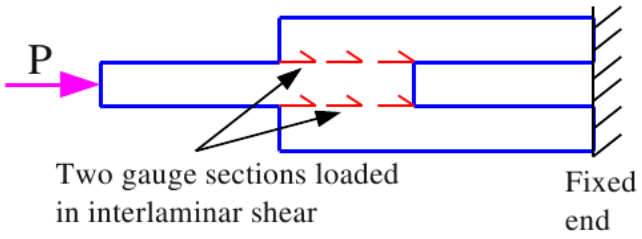

Figure 2.6: Schematic of double lap shear specimen and loading

2.3.1.3 Short Beam Shear

The Short Beam Shear (SBS) test is a three or four point bend test, where the unsupported span is sufficiently small so that the shear stresses dominate the bending stresses. SBS testing of FRPs is standardised in ASTM D 2344 [31]. A schematic of SBS testing using 3 Point bending is shown in Figure 2.7.

Using classical beam theory, the maximum bending stress will be proportional to the support span S and occurs at the upper and lower surfaces. The transverse shear stress σ_{13} is independent of S. σ_{13} causes a complementary interlaminar shear stress σ_{31}, which has a parabolic distribution across the thickness and is maximum on the mid-plane of the specimen and zero at the upper and lower surfaces (Figure 2.8). Thus reducing S reduces the bending stress σ_{11} without reducing σ_{31} and the likelihood of interlaminar shear failure is increased. Due to the parabolic distribution, the maximum interlaminar shear stress σ_{31}, for a rectangular cross section of width w and thickness t,

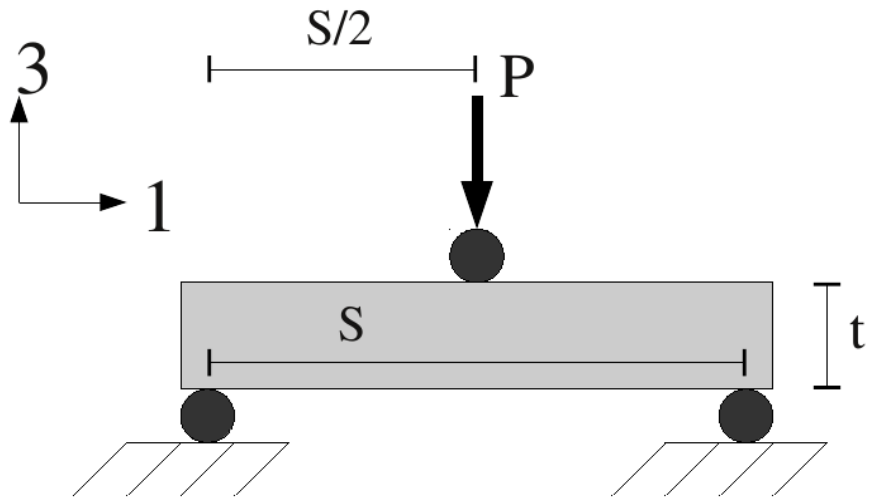

Figure 2.7: Schematic of Short Beam Shear layout

is related to transverse load P by :

$$\sigma_{31} = \frac{3P}{4wt} \tag{2.1}$$

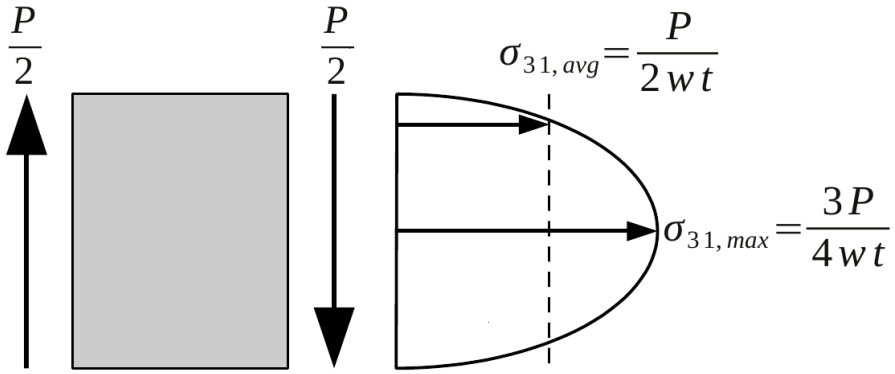

Figure 2.8: Plot of parabolic shear stress distribution in rectangular beam

The standard span to thickness ratio is 4, and the width to thickness ratio is 2. The apparent interlaminar shear strength (ILSS) is generally calculated from the peak load during the SBS test. ASTM D 2344 states that "because of the complexity of the internal stresses and the variety of failure modes that can occur in this specimen, it is not generally possible to relate the short beam shear strength to any one material property" [31]. Classical beam theory does not account for the contact stresses under the rollers used for support and loading. This results in the parabolic shear distribution only being accurate mid way between the central load and the outside supports. Furthermore, FRPs tend to be weaker in compression than tension. As the peak in-plane

compressive stress occurs directly under the central load, with the additional contact stresses from the roller, failure often initiates under the central load as a combination of compression and shear, before propagating diagonally towards the midplane. For a standard SBS test to provide a valid interlaminar shear strength, failure must initiate midway between the central load and outside support, on the specimen midplane. Finite element analyses of the SBS test by Xie and Adams [45], Pahr *et al* [43] and Feraboli and Kedward [46] confirmed that the parabolic shear stress distribution is only accurate midway between the central load and outside support. Pahr *et al* showed a "*delamination risk parameter*", indicating the likelihood of ply failure due to shear and transverse stresses for the SBS test, shown in Figure 2.9. The dark band shows the high probability of failure due to interlaminar shear at the specimen mid-plane, which is the desired failure. However, there is also a high probability of failure near the loading and support rollers, which can result in an invalid test if failure initiates in these regions.

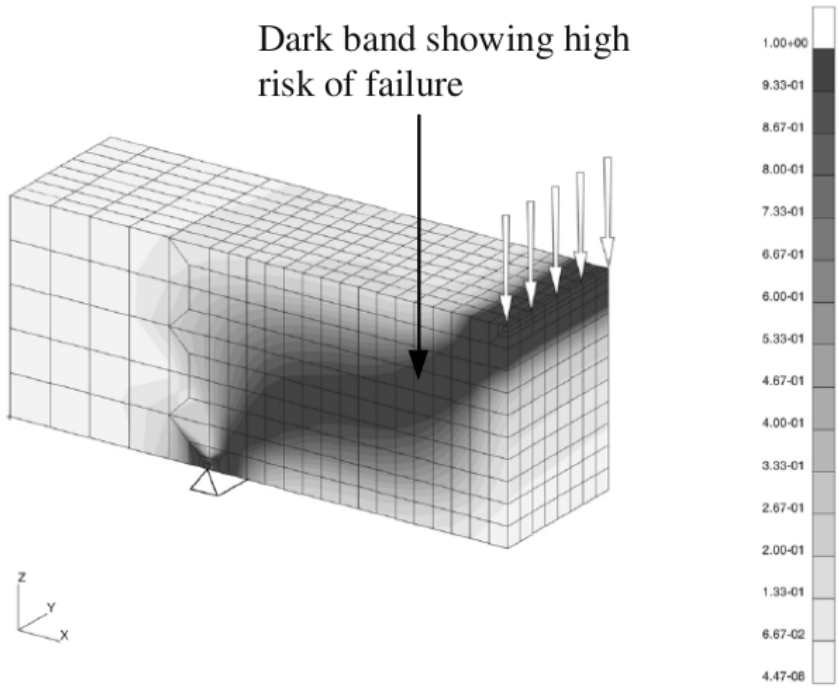

Figure 2.9: Contour plot from FEA showing delamination risk parameter for a SBS specimen [43]

Abali *et al* [47] suggested a modification to the SBS test. The modification replaced the central roller with a thin rubber pad, glued to an aluminium backing, shown in Figure 2.10. The central load then becomes a distributed, near uniform pressure as opposed to the concentrated line load when using cylindrical rollers. Abali *et al* [47] showed, both via beam theory and FE models, that this reduces the bending and contact loads sufficiently that interlaminar shear is the dominant failure mode. The mod-

ified SBS set up was applied to woven carbon fibre reinforced carbon matrix composites. This modification aided quasi-static SBS tests but would complicate high rate or impact tests considerably: the measured impact force would be due to the combined compliance of the specimen and the rubber insert, and hence not a true reflection of specimen stress.

A common theme amongst these studies [45, 43, 46, 47] is that some modification of the specimen geometry suggested by ASTM D 2344 is required to ensure that delamination failure initiates midway between the central load and outside supports. If failure initiates on the mid-plane, away from the loading and support rollers, then the SBS test provides reasonable bounds on the interlaminar shear stress. However, even if interlaminar shear is present, the presence of other failure modes such as local buckling can make the force-displacement response non-linear. Any non-linearity makes determining the force at which failure occurred problematic.

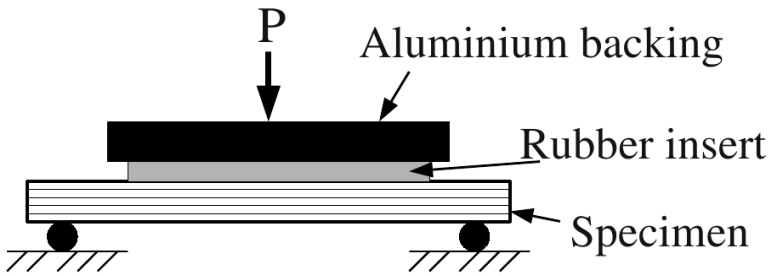

Figure 2.10: Schematic of modified Short Beam Shear test proposed by Abali *et al* (Figure adapted from [47])

2.3.1.4 Iosipescu or V-Notch Beam Shear Testing

The Iosipescu or V-Notch shear test, which is described in ASTM D 5379 [32], uses a special fixture (generally known as a Wyoming fixture) to apply shear loads to a notched specimen. A schematic of the fixture and specimen are shown in Figure 2.11.

The shear strain is normally determined experimentally from two strain gauges mounted in the gauge section, oriented at $\pm 45^{\circ}$ to the load direction. The apparent shear strength is taken to be the average shear stress in the section between the V-noches, without applying any factor for stress concentration. Given specimen width w and thickness t, the average shear stress σ_{31} is :

$$\sigma_{31} = \frac{P}{wt} \tag{2.2}$$

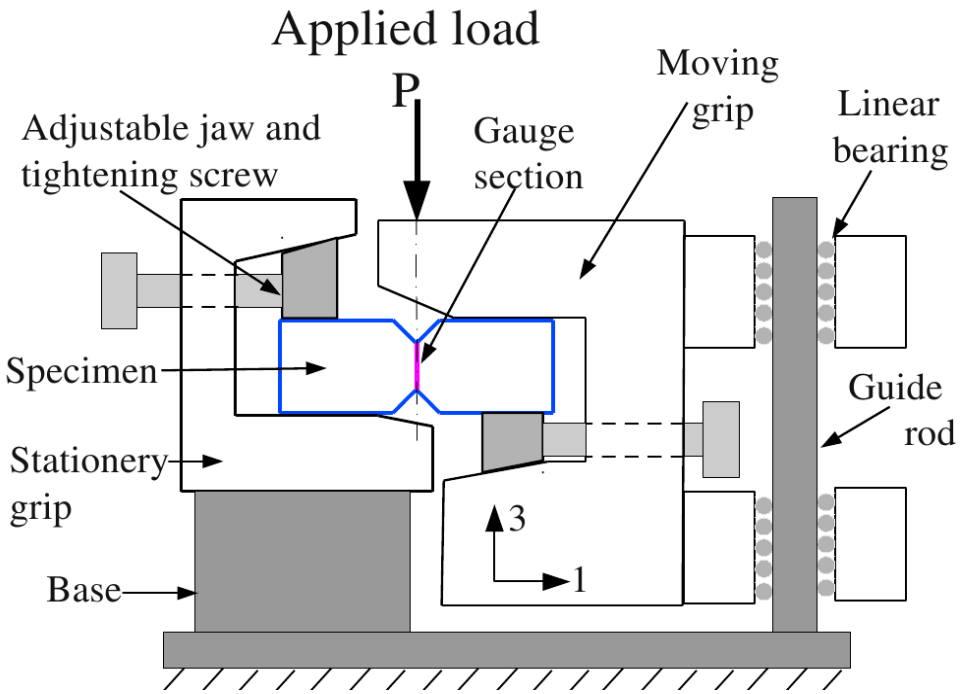

Figure 2.11: Schematic of the Iosipescu fixture and specimen, based on [32]

The Iosipescu test may be applied to any plane in a composite laminate by cutting the specimen and notches in the appropriate plane. The orientation of laminates within the specimen for in-plane shear (σ_{12}) and interlaminar shear (σ_{31}) are shown in Figure 2.12. The standard specimen dimensions for in-plane shear testing are easily obtained from laminates of 1.5 to 5 mm thickness. However, in order to obtain an interlaminar shear specimen with standard Iosipescu geometry, a laminate of at least 76 mm thickness is required. Manufacture of a laminate of this thickness is a non-trivial exercise. Hufenbach and colleagues [48] used a jig to produce laminates of uni-directional GFPP with the required dimensions and orientation. However, their results for interlaminar shear strength showed significant scatter at various strain rates.

The Iosipescu test requires careful control of several parameters to produce consistent results. The line of application of external load must be very closely aligned with the V-notches, as this is the only section where the specimen experiences pure shear. If there is a small misalignment, the gauge section between the V-notches experiences shear and bending stresses. The uniformity of the shear stress in the gauge section is affected by both the V-angle and tip radius. Hence the shear strength calculated from an Iosepescu test requires further analysis, typically via FEA, in order to determine a "true" shear strength for constitutive models.

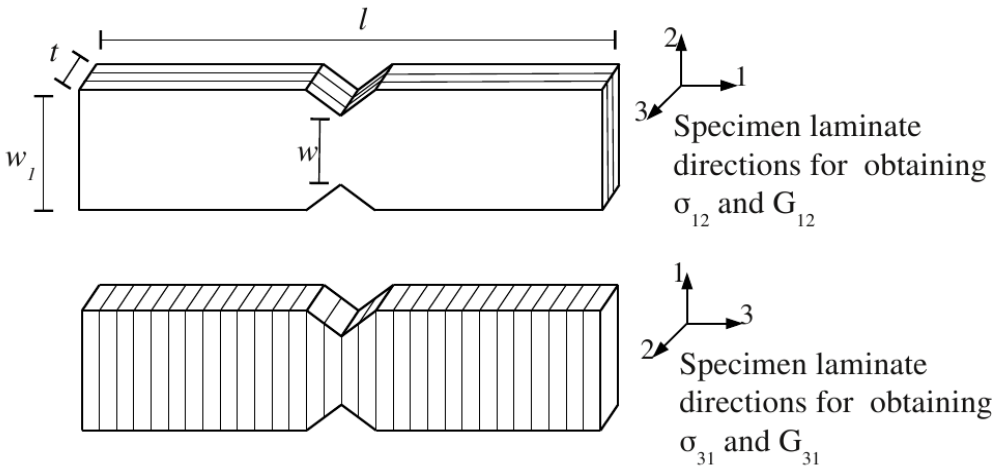

Figure 2.12: Schematic of orientation of laminate directions within Iosepescu specimen for obtaining different shear properties ([32])

The fixtures required for correct application of the load to an Iosepescu specimen are relatively heavy. Large fixture inertia complicates high rate testing, due to the requirement to accelerate the fixtures to the desired speeds and the separation of inertia and specimen forces from the measured forces. These attributes, along with the difficulty and expense involved in the specimen manufacture, make the Iosepescu test an unlikely candidate for high rate testing.

Figure 2.13: Photograph of interlaminar specimens and laminating jig for Iosipescu tests by Hufenbach *et al* [48]

2.3.2 Fracture Mechanics Based Tests for Delamination of FRP

Fracture mechanics is based on the dissipation of energy, supplied by external work or internal strain energy, by growth of existing cracks or flaws in materials. If the available strain energy release rate G (energy dissipated per unit area of crack growth) exceeds some critical value G_C, then an existing crack will grow. Fracture mechanics tests determine the value of G_C for various modes of fracture. The different modes of fracture are shown in Figure 2.14. A Roman numeral subscript is used to denote the specific mode; e.g. Mode I - G_{IC}.

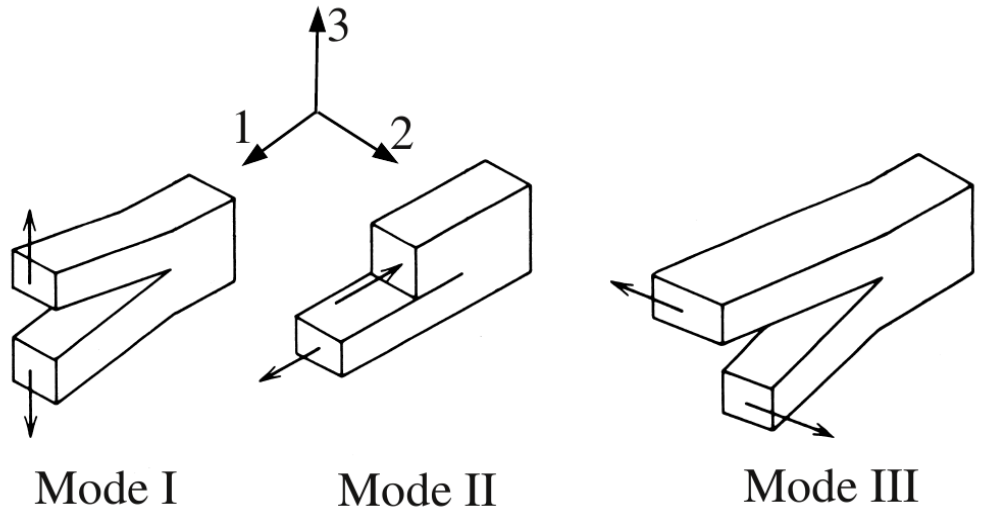

Figure 2.14: Schematic explaining different modes of fracture
(Figure adapted from Hertzberg[49])

Fracture mechanics can be divided into Linear Elastic Fracture Mechanics (LEFM) and Non-Linear Fracture Mechanics (NLFM). LEFM is applicable to situations where the energy considerations around the crack tip are limited to the elastic strain energy stored in the material. NLFM can be applied where other forms of energy dissipation, such as plastic deformation, become significant. While the majority of engineering materials will exhibit some plastic deformation in the region of a crack tip, if the plastic zone is small then LEFM is still valid. LEFM may be described in terms of stress intensity factors, which have the form $\sigma\sqrt{a}$, and critical fracture toughness K_{iC}. However, this approach requires knowledge of the stress field in the vicinity of the crack. For composites, the more popular approach has been to characterise fracture in terms of strain energy release rates, as these may be calculated from the global forces acting on

the specimen and the change in specimen compliance as a function of crack length.[1] G may be calculated from [50, 51]:

$$G = \frac{P^2}{2w}\frac{\partial C}{\partial a} \tag{2.3}$$

P is the force, w is the specimen width, C is the specimen compliance and a is the crack length.

The relationship between compliance and crack length must be determined, either from a closed form analytical solution for the specimen geometry, or calibration of empirical data ("compliance calibration method") [50]. During the test, the force and crack length must be recorded in order to calculate G. The relevant standards suggest visual tracking of the crack length, aided by a travelling microscope. If testing is conducted at displacement rates higher than the recommended 1 mm/min, visual tracking of the crack becomes more problematic as the rates increase and eventually become impossible. It is possible to determine crack propagation from photographs taken at regular intervals or video footage. Acoustic emission monitoring has been employed to determine crack initiation (for example [52, 53]) at microscopic scales, rather than employ visual crack monitoring which will only detect crack initiation on a macroscopic scale. Ultrasonic testing (for example [54]), has been explored for determining crack position during quasi-static tests.

Summaries of standardised tests for interlaminar fracture have been presented by O'Brien [55] and Brunner *et al* [56]. Various standards have been accepted for different interlaminar fracture toughness tests of unidirectional FRP. The standardised tests were initially designed for unidirectional layup FRP. Application to multidirectional layups often results in the interlaminar crack jumping between adjacent lamina [56]. This renders the test invalid, as G values obtained from tests where this occurs are a mix of inter- and intra-laminar toughness, rather than a pure interlaminar toughness. While the standards do not mention woven FRP, it is unlikely that a interlaminar crack in a woven FRP will change to an intralaminar crack. Woven FRP can exhibit "stick-slip" crack growth: short periods of rapid crack growth, interspersed with longer periods where the crack grows very slowly, if at all. "Stick-slip" crack growth may be due to changes in crack growth rate depending on whether the fibres are parallel or perpendicular to the crack growth, at the crack tip.

[1] For a linear elastic, isotropic material there is a simple relationship between the critical fracture toughness and strain energy release rate. However, for composites which are largely anisotropic this relationship no longer holds.

2.3.2.1 Mode I Testing

Mode I interlaminar fracture toughness testing via the Double Cantilever Beam (DCB) test is standardised by ASTM, ISO and the ESIS. A schematic showing DCB test geometry, from ASTM D 5528 [33], is shown in Figure 2.15. The DCB test requires the application of interlaminar tension, which is transmitted to the specimen either through piano or block hinges, which are bonded to the specimen above the existing flaw. Frames from a video of a DCB test are shown in Figure 2.16. The DCB test produces stable crack propagation for most unidirectional composite laminates, which allows one to determine both initiation and propagation values for G_{Ic}. Standardised DCB tests are restricted to a cross head speed (CHS) of 0.5 to 5 mm/min, keeping the tests in the quasi-static regime. ASTM D 5528 allows calculation of G_I from the compliance-crack length relationship derived from beam theory or compliance calibration. Modified beam theory results have been presented to allow for the rotation and shear displacement of the arms at the crack root. The bonded hinges prevent compliance calibration for different crack lengths before the actual test. If the crack growth is stable, the specimen may be unloaded after a small increment of crack growth and then reloaded. The slope of the unload-reload curve at each crack length is then used to determine the compliance.

Other means of Mode I interlaminar testing have been utilised, but are not standardised, such as the Wedge Insert Fracture (WIF) test [57, 58] and the Boeing Wedge test [58]. Both of these test methods involve forcing a wedge between lamina, as shown in Figure 2.17. The Boeing Wedge test involves driving the wedge between the laminates until a crack initiates and then holding the wedge position stationary while the crack grows over an extended period of time [58]. The Boeing Wedge test is intended as an adhesive joint durability test, which is easily conducted in an environment that leads to degradation of the joint, such as immersion in water [58]. As the wedge is held stationary, this method is not suitable for an investigation of loading rate. The WIF method, termed "Forced Wedge Test" by Adams [58], has the wedge driven at a constant velocity. Adams argued against the use of this method, as varying friction between the wedge and uneven fracture surfaces results in an unstable force response [58].

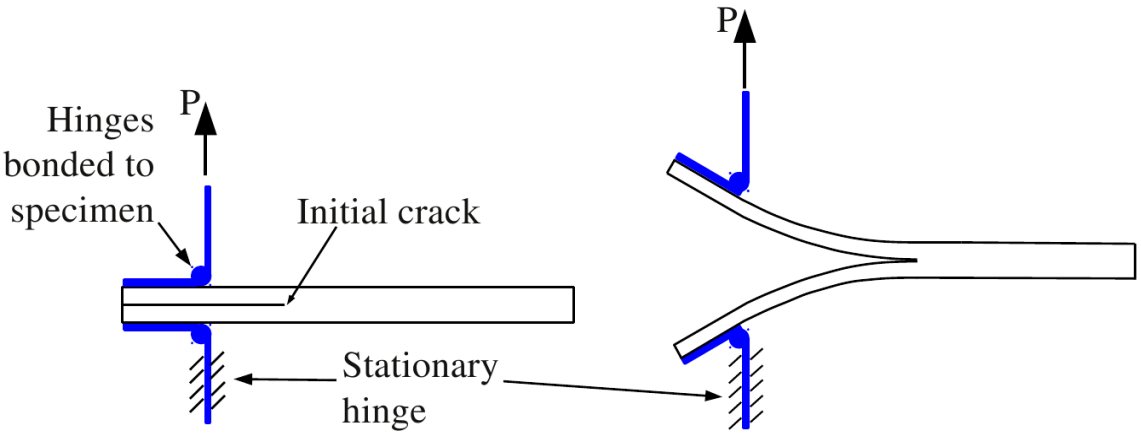

Figure 2.15: Schematic of Double Cantilever Beam test

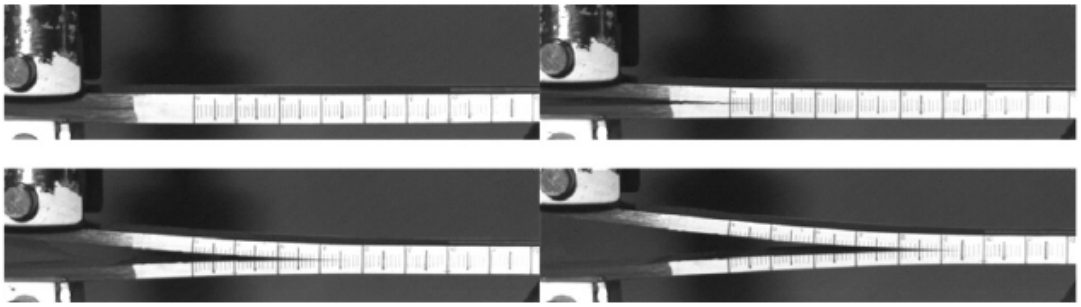

Figure 2.16: Frames from video of Double Cantilever Beam test (Brunner *et al* [56])

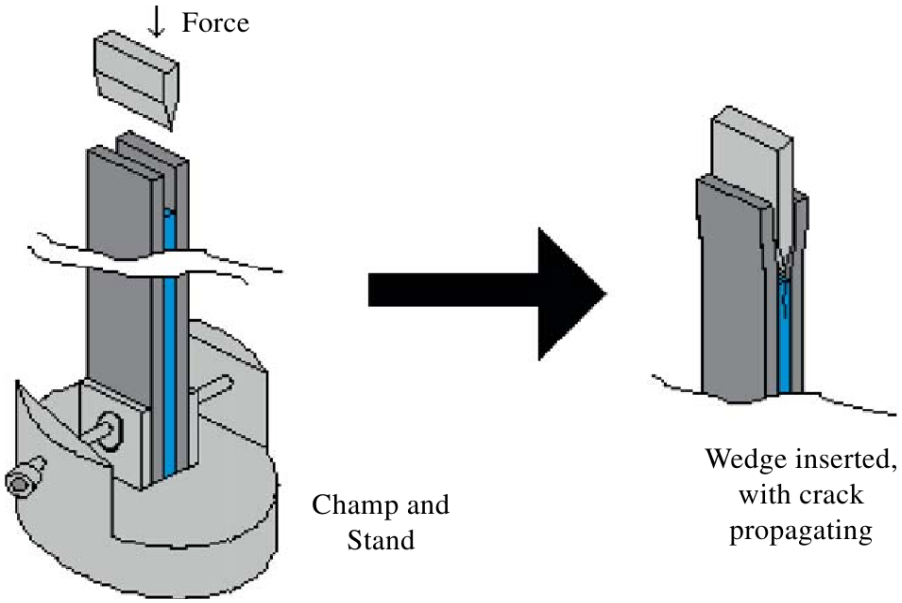

Figure 2.17: Schematic of Forced Wedge test [58]

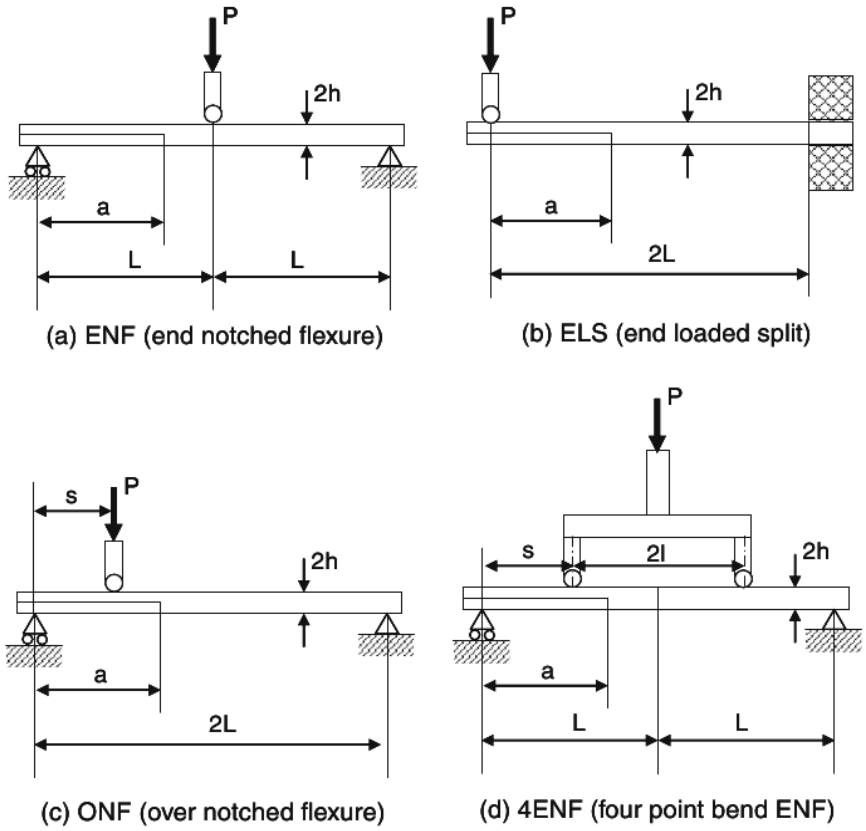

Figure 2.18: Schematics of test methods for Mode II (Wang *et al* [60])

2.3.2.2 Mode II Testing

Mode II interlaminar fracture has not been standardised by ASTM or ISO. ASTM has a work item for Mode II testing [59] based on the End Notch Flexure (ENF) geometry, but this has not been accepted as a standard at the time of writing. Despite the lack of standardisation for Mode II testing (or perhaps because of it), a variety of Mode II test methods are presented in the literature. Wang *et al* [60] presented four of the more popular Mode II test methods, shown in Figure 2.18.

The most popular Mode II test is the ENF test, shown in Figure 2.18(a). A specimen is subjected to bending via 3 point loading, which induces Mode II loading via complementary shear. The simplicity of the specimen and easy availability of 3 point bending apparatus are the likely reasons for the popularity of the ENF. However, the ENF is unlikely to produce stable crack propagation. As soon as cracking initiates, the crack front enters a more highly stressed region of the specimen. This promotes further propagation of the crack, leading to an abrupt failure shortly after crack initiation. Brunner *et al* [56] refer to the stabilised ENF test described by the Japanese standard

for Mode II testing [61]. Tanaka *et al* [62] described the stabilised ENF test, which uses crack shear displacement as a control feedback parameter for the testing machine. The cost and difficulty of implementing the necessary control hardware and software on conventional testing frames is the most likely reason for the stabilised ENF test not being adopted by more researchers. The compliance-crack length relationship for the ENF test is easily obtained experimentally: shifting the specimen laterally on the supports gives different effective crack lengths. The specimen is subjected to a load below that required for crack initiation, at each effective crack length, and the compliance measured from the load-deflection curve.

The 4 Point Bend End Notch Flexure (4ENF), shown in Figure 2.18(d), was examined in great detail by Davidson and colleagues [63, 64, 65, 66]. As the specimen between the inner supports has a uniform stress state, crack growth between the inner supports of the 4ENF test is stable. This allows one to determine initiation and propagation values for G_{II}. However, the inherent assymetry due to the crack necessitates multiple hinges in the 4ENF test fixture (Figure 2.19). This results in more fixture compliance than the 3 point ENF test, but this can be corrected for during compliance calibration. Sun and Davidson [65] studied the effect of friction and geometric nonlinearities on G_{II} measured from 3 and 4 point ENF tests via finite element simulation. Davidson *et al* [66] investigated these effects, as well as that of fixture compliance, and concluded that the 4ENF test is more susceptible to innaccuracies from friction and geometric effects than the 3 point ENF test. The 4ENF test is calibrated for compliance in the same manner as the ENF test.

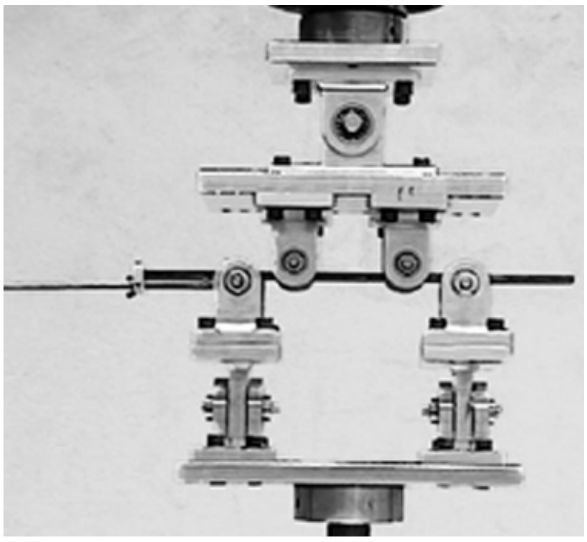

Figure 2.19: Fixture for 4ENF testing (Shuecker *et al* [63])

The End Loaded Split (ELS) test produces stable Mode II crack growth [56, 67], as the crack grows into a less stressed region of the specimen. The ELS consists of transverse loading of a cantilever clamped specimen (Figure 2.18(b) and 2.21), which requires a specimen identical to those for ENF or 4ENF (Four Point End Notch Flexure) tests. In [56, 68] the clamp was shown as a sliding fixture (Figure 2.20), while [67] showed a fully built in clamp (Figure 2.21).

Figure 2.20: Sliding fixture for End Loaded Split test (Blackman *et al* [68])

The Over Notched Flexure (ONF) test, shown in Figure 2.18(c), is essentially a ENF test with the load point shifted from mid-span, to between the crack tip and its closest support. As crack propagation will be into a less stressed region, the ONF can produce stable crack growth. Wang *et al* [60] stated that the ONF test produced increasing values of G_{II}, unlike ELS and 4ENF tests on the same carbon fibre reinforced epoxy specimens, which produced almost constant propagation values of G_{II}. This apparent increase was attributed to friction between the fracture surfaces. Szekrenyes and Uj [69] used the ONF test to measure G_{II} for glass fibre-polyester specimens.

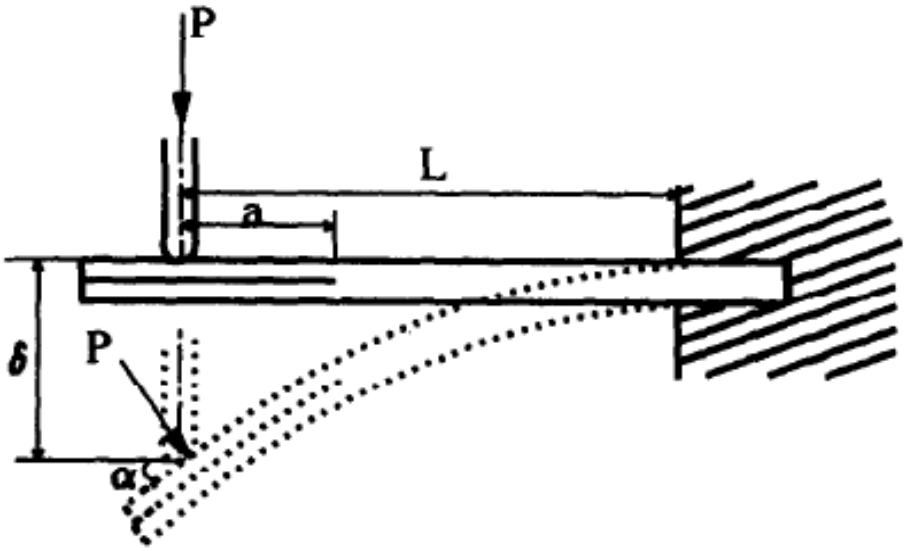

Figure 2.21: Clamped fixture for End Loaded Split testing (Wang *et al* [67])

Any method of Mode II testing, regardless of whether crack growth is stable, faces the problem of locating the crack tip accurately. The interlaminar crack tip is often preceded by matrix damage, which renders the crack tip "fuzzy" [68]. This results in considerable scatter in measured G_{II} values. O'Brien [70] reviewed a variety of results for Mode II interlaminar fracture. O'Brien [70] discussed some of the uncertainties around the micromechanisms in FRP that lead to a macroscopic interlaminar Mode II fracture. It was further noted that most structural interlaminar failures were mainly mixed Mode I-II, with the Mode I component being dominant. This suggests that characterising the mixed mode failure was more important than determining values for pure Mode II fracture with little scatter.

2.3.2.3 Mixed Mode I-II Testing

Mixed mode I-II testing is standardised for unidirectional FRP under ASTM D 6671 [34], using the mixed mode bending (MMB) apparatus, that was first presented by Crews and Reeder [71]. The MMB, shown schematically in Figure 2.22, is a combination of the DCB and ENF tests, into a single specimen, with a single load applied via a hinged lever. The MMB test allows for continuous variation in the Mode I / Mode II ratio by adjusting the length of the lever arm.

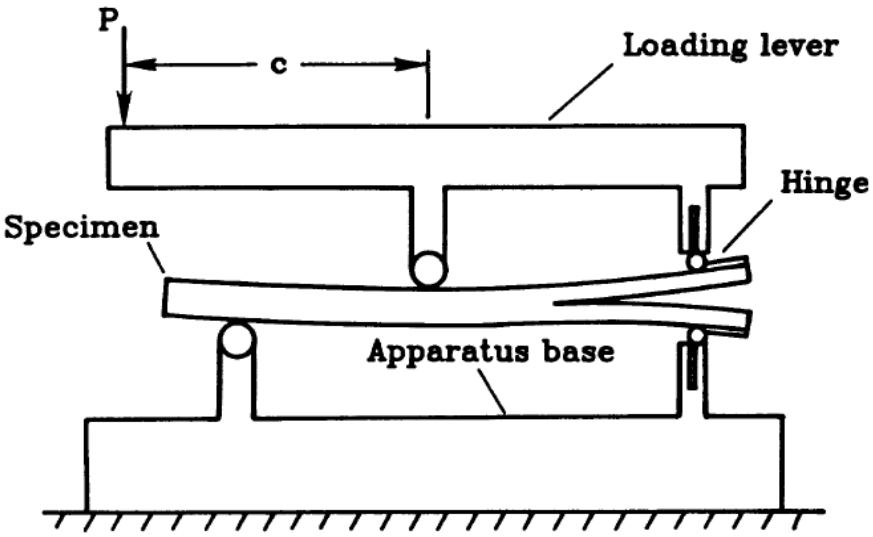

Figure 2.22: Schematic of Mixed Mode Bending test (Crews *et al* [71])

The initial loading mechanism, with the loading point above the plane of the specimen, resulted in significant nonlinearity. Further work by Crews and Reeder [72] redesigned the loading apparatus to minimise the nonlinearity by relocating the loading point to the specimen midplane. The specimens require hinges, similar to those for DCB tests, which are bonded on either side of the initial flaw. As with DCB tests, the bonded hinges interfere with pre-testing experimental compliance calibration. Unfortunately, the MMB test does not always result in stable crack growth, which can prevent compliance calibration using crack growth data obtained during the test. Reeder [73] suggested that the compliance be based on a bending modulus determined from the initial portion of the test, and corrected for the compliance of the MMB apparatus.

Some alternatives to the MMB, which are not standardised, are the Single Cantilever Beam (SCB), Double End Notch Flexure (DENF), Single Leg Bending (SLB), Crack Lap Shear (CLS), centre cracked Four Point Bend and Unsymmetric Double Cantilever Beam (UCSB). These typically require changes to the specimen geometry

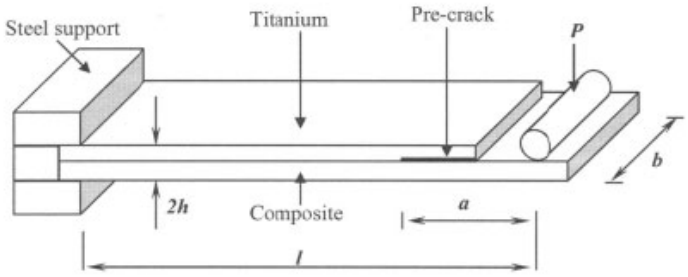

Figure 2.23: Schematic of Single Cantilever Beam test (Cortes *et al* [77])

to change the fracture mode ratio - in the MMB test the specimen is unchanged and the mode ratio is changed by altering the lever arm. However, MMB is an unlikely candidate for adaptation to high rate tests, due to the number of moving parts and relatively high intertia of the MMB test fixture.

Single Cantilever Beam

The SCB test has been employed by Cantwell and colleagues [74, 75, 76, 77] to investigate the mixed mode interfacial fracture toughness of FMLs and sandwich structures. The SCB test is similar to the ELS test, in that a cantilever clamped specimen is subjected to a perpendicular end load. However, in the SCB, the end load is only applied to the lower leg of the pre-cracked specimen as shown in Figure 2.23. Depending on the relative flexural stiffness of the upper and lower legs, a mix of Mode I and II will be present in the delamination. An example of an SCB test with a stiffened upper leg, and consequently higher Mode I component, is shown in Figure 2.24. Experimental compliance calibration for small cracks, prior to the actual fracture test, is easily achieved by sliding the specimen horizontally in the clamp, while maintaining a fixed cantilever length. As crack propagation during the SCB test is generally stable, the compliance-crack length relationship may also be determined from measurements made during the fracture test.

The SCB test has also been adapted to higher rate testing [74, 78] by using an instrumented drop weight tester to apply the end load. It was not possible to record the crack growth during the extremely short duration of these tests. Compliance of the specimen and the crack length was determined both before and after the fracture test, and an empirical crack-compliance relationship established. The empirical relationship was then differentiated, allowing calculation of G_C via Equation 2.3.

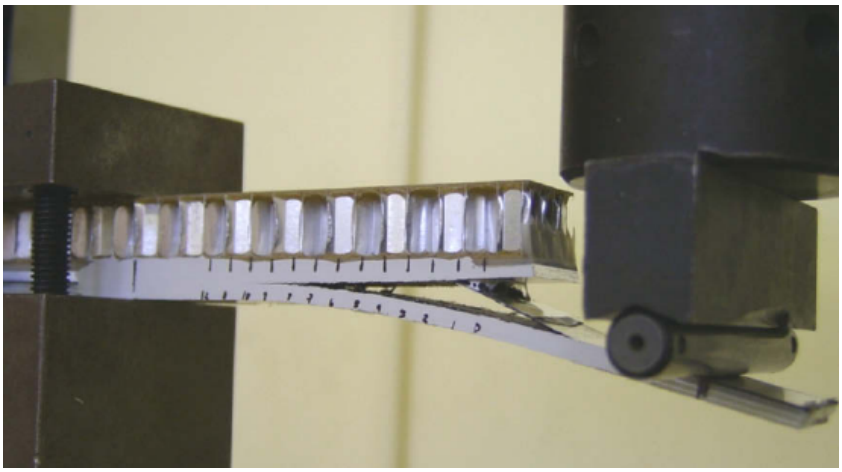

Figure 2.24: Single Cantilever Beam test in progress (Carillo *et al* [76])

Single Leg Bend

The Single Leg Bend (SLB) test is based on Three Point bend loading, with the portion of the leg below the crack plane removed as shown in Figure 2.25. The concept was proposed by Yoong and Hong [79], to provide a mixed Mode I-II loading. Due to the Mode I component, the crack opens visibly, which aids in identification of the crack tip, and avoids the difficulties associated with "fuzzy" crack tips in pure Mode II loading. The SLB test is also attractive from the perspective of only requiring a Three Point bend fixture, with one support raised by the thickness of the removed leg. Hence any impact rig adapted for Three Point bend tests is easily adapted for SLB tests. For a SLB specimen made of one material, with symmetric upper and lower legs, the fracture mode ratio $\frac{G_I}{G_{II}}$ approaches $\frac{4}{3}$. The fracture mode ratio of the SLB test may be altered by changing the relative stiffness of the upper and lower portions of the beam. This may be achieved by altering the thickness ratio of the upper and lower portions. Alternatively, a bimaterial specimen, such as a FML, will generally have a stiffness difference due to the different moduli of the component materials. Cantwell *et al* [80] used the SLB test geometry to investigate the interfacial fracture of sandwich panels, consisting of GFRP skins and balsa wood cores.

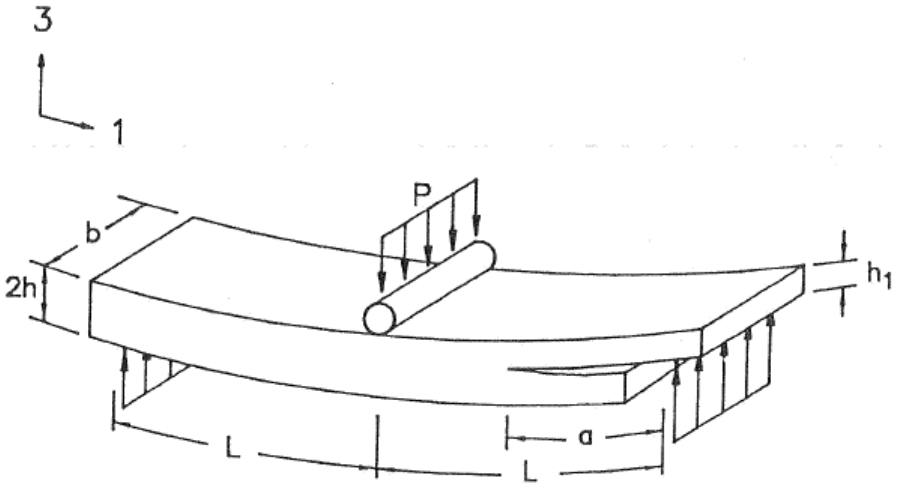

Figure 2.25: Single Leg Bend test configuration for mixed Mode I-II loading (Yoong and Hong [79])

2.4 Mechanical Properties of Glass Fibre Polypropylene

Published studies on the macroscopic mechanical properties of GFPP composites are summarised in Table 2.3, with the relevant abbreviations in Table 2.2. The review is limited to studies on the mechanical properties of consolidated GFPP, or the effect of processing methods on mechanical properties. Studies of GFPP with regard to manufacturing related issues, such as the properties of the unconsolidated fabric or modification of processing methods to accomodate complex part geometries, and microscopic mechanical properties, such as individual fibre tests, are outside the scope of this project and are not included in this review. From the publications listed in Table 2.3, the following items were of particular interest.

The in-plane tensile, compressive and shear properties of GFPP were studied by Brown and colleagues [81] at strain rates varying from quasi-static to approximately $10^2 s^{-1}$. The elevated rate tests were conducted using an instrumented falling weight tower. Schematics of the compression and tensile loading rigs are shown in Figure 2.26 and Figure 2.27 respectively. The shear tests were accomplished by tensile loading of specimens at $\pm 45^\circ$ to the fibre axes. The stress-strain responses published by Brown *et al* [81] contain oscillations - a typical example being the reported tensile stress-strain curve shown in Figure 2.28. These oscillations are not due to specimen response, but from stress waves propagating and reflecting within the loading fixtures, specimen and load cell. Even after signal filtering, the remaining oscillations are large enough to complicate identification of the peak stresses and can obscure any specimen nonlinearity.

Table 2.2: Abbreviations used in Table 2.3

DCB	Double Cantilever Beam	ENF	End Notch Flexure
G_x	Mode x Strain energy release rate	I-P	In-plane
Q-S	Quasi-static	SLB	Single Leg Bend
S-M	Swirl Mat	W-K	Warp Knitted

Table 2.3: Published studies on mechanical properties of GFPP

Author(s)	**Fibre geometry**	**Tests conducted**	**Parameters reported**
Bureau *et al* [82]	Woven	Three Pointt bend: Sub-zero and elevated temperature: Q-S and fatigue	Flexural modulus and strength, cycles to failure for given stress
Brown *et al* [81]	Woven	I-P compression, tension and shear: Q-S and drop weight	I-P strength in compression, tension and shear for $\dot{\varepsilon} = 10^{-2}$ to $10^{2}/s$
Wang *et al* [52]	Woven, W-K and S-M	Single edge notch tension: Q-S	Intralaminar fracture toughness
Lariviere *et al* [83, 84]	UD	Transverse tension and DCB: Q-S	Transverse tensile strength, Interlaminar G_I
Santulli *et al* [85, 86]	Woven	Short beam shear, 3 Pt bend, Q-S Instrumented falling weight, dart penetration, Charpy impact	Apparent interlaminar shear strength, Charpy impact absorption energy, Dart absorption energy
Reyes & Sharma [87]	Woven	I-P tension: Q-S and impact	I-P tensile strength for $\dot{\varepsilon} = 10^{-5}$ to $10^{2}/s$
Ding [88]	UD	DCB, ENF: Q-S	Interlaminar G_I and G_{II}
Perrin *et al* [89]	UD	DCB: Sub-zero and elevated temperature: Q-S	Interlaminar G_I at varying temperatures

Continued on following page ...

Table 2.3 – Continued

Author(s)	**Fibre geometry**	**Tests conducted**	**Parameters reported**
Pattofatto *et al* [90]	Woven	Perforation tests: Q-S and impact	Perforation force & energy
Reyes Villanueva [91]	UD	DCB, ENF, SLB: Varying rates	G_I, G_{II} & $G_{I/II}$
Hufenbach *et al* [48]	Woven	Iospescu (shear) : Q-S to intermediate	Shear stress-strain behaviour at varying rates
Guillén and Cantwell [75]	UD	Tensile (45 °), 3 Pt Bend, DCB, ENF (Q-S)	G_I, G_{II} & σ_{11}

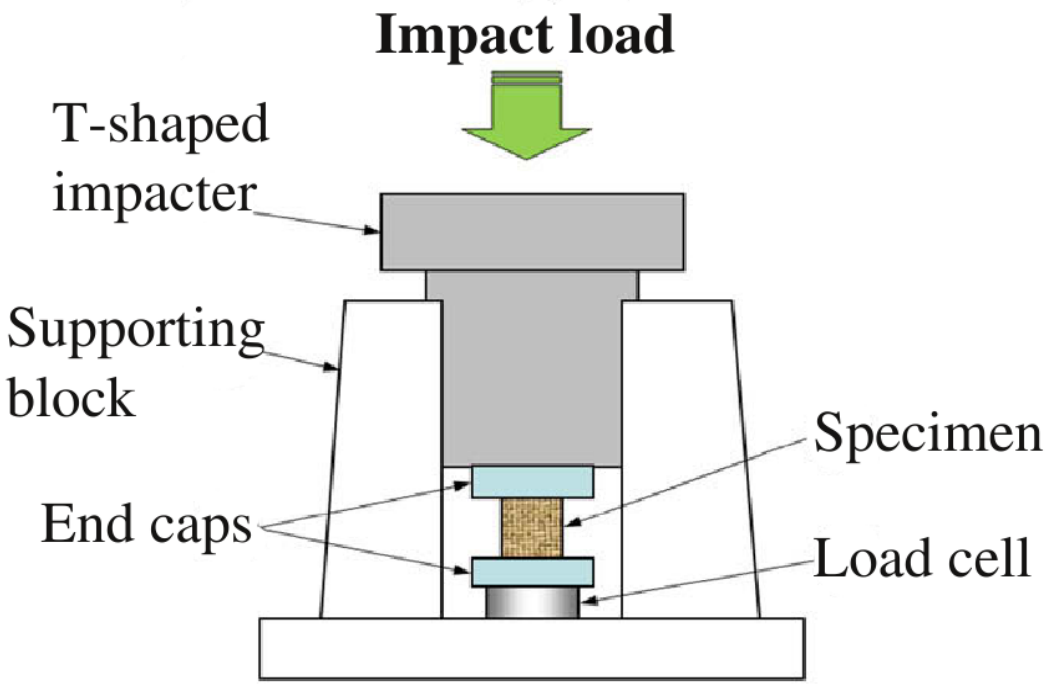

Figure 2.26: Schematic of impact compression rig employed by Brown (Figure adapted from [81])

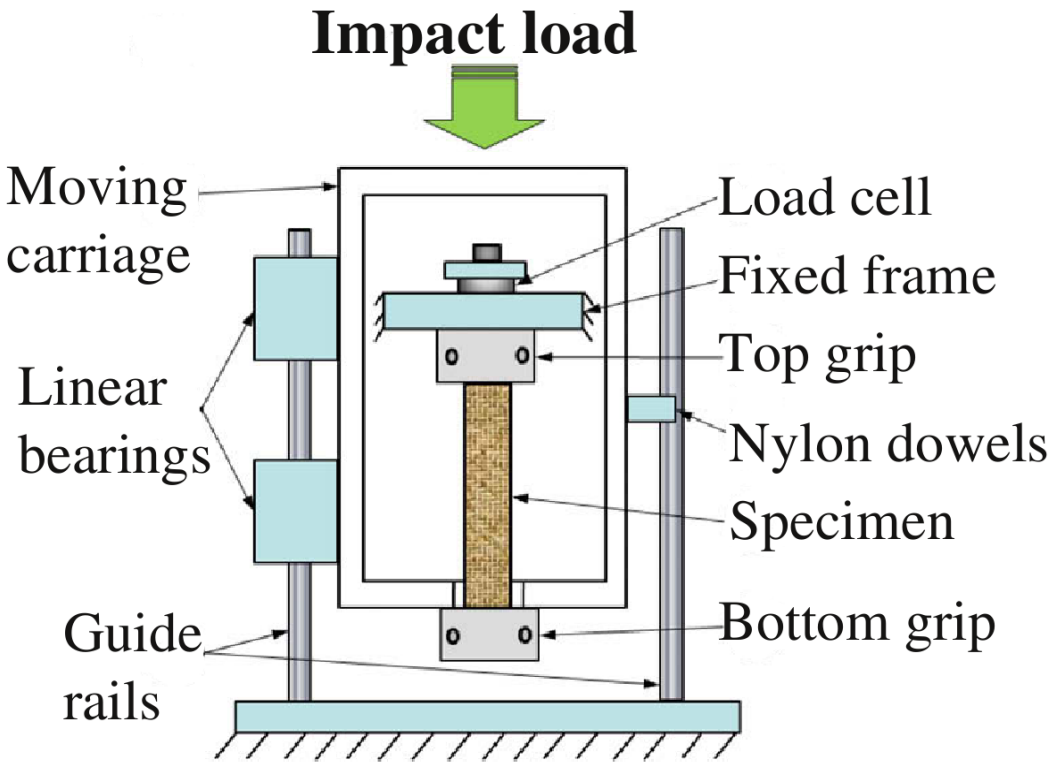

Figure 2.27: Schematic of impact tensile rig employed by Brown (Figure adapted from [81])

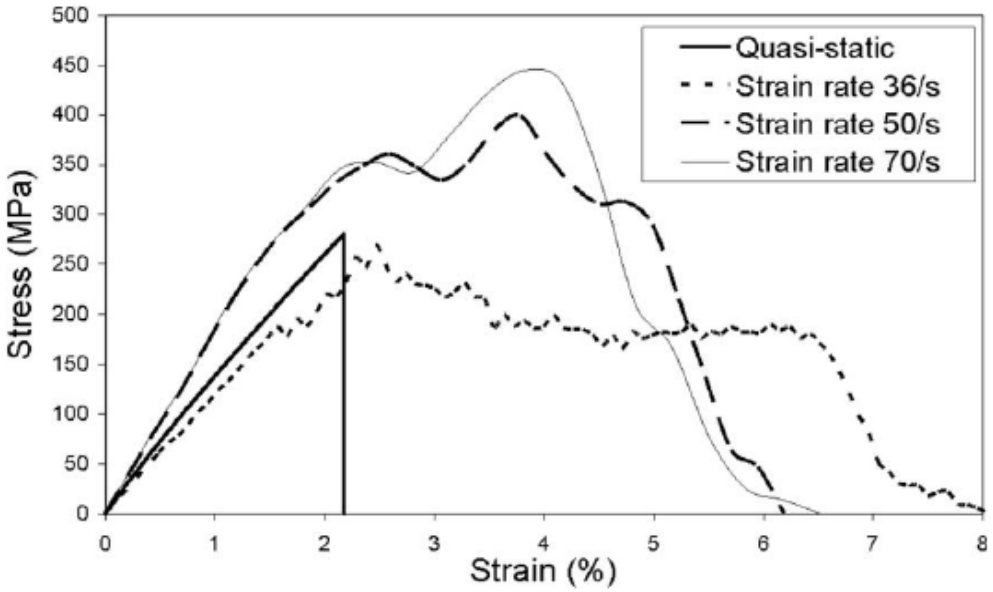

Figure 2.28: Graph of GFPP tensile stress-strain response reported by Brown [81]

Reyes and Sharma [87] used a pneumatically driven impact rig to investigate the tensile properties of GFPP up to strain rates of $10^2/s$, using a non-contact optical system to measure specimen strain. The stress data presented in [87] does not suffer from the oscillations noted in [81]. However, details of the force measurements and signal processing were not presented, which limits further evaluation of the data or the possibility of repeating the tests.

At the time of writing, the only publication utilising Hopkinson Pressure Bars (HPB) for investigation of GFPP was Pattofatto *et al* [90]. Pattofatto *et al* [90] used a HPB to perform a dynamic perforation test of GFPP panels, with a view to using inverse modelling to determine failure parameters. No publications were found that used a conventional compression or tension Split Hopkinson Pressure Bar (SHPB) to characterise GFPP at high rates. This was surprising as SHPB have been used extensively to characterise other FRPs at high rates.

Reyes Villanueva [91] studied the interlaminar fracture of unidirectional GFPP for Mode I, II and mixed Mode I/II loading. Mixed mode tests were conducted using the Single Leg Bend (referred to as the Mixed Mode Flexure) at displacement rates varying from 0.1 mm/min to 2 m/s. The details of the force measurement at the higher rates were not discussed. Only a single value of $G_{I/IIC}$ was reported at each rate - it is assumed that this is the propagation value determined for each rate.

The published quasi-static elastic moduli and failure strengths of GFPP, at room temperature, are collated in Table 2.4. The manufacturer's data sheet [19] provides separate data for parameters in the warp (1) and weft (2) directions. The other publications cited did not specify whether testing was in the warp or directions, in which case the properties are assumed to pertain to the warp direction. Data on the through-thickness properties (3 direction) is scarce. The data on interlaminar shear strength (σ_{13}) has a relatively large spread, where the maximum reported value is 2.3 times greater than the lowest reported value. The spread in the data is most likely due to the use of different test methods by the different sources - Iosepescu for [19, 48] and Short Beam Shear for [86].

Table 2.4: Published quasi-static mechanical properties of Glass Fibre Polypropylene

Property	**Symbol**	**Range of Values**	**Source(s)**
Elastic moduli	E_{11}	11.1 - 15.5 GPa	[19, 81, 82]
	E_{22}	12.2 - 13.6 GPa	[19]
	E_{33}	No data available	
Poisson's ratios	ν_{12}	0.10-0.12	[19]
	ν_{13}	No data available	
	ν_{23}	No data available	
Tensile strength	σ_{11}^t	252 - 320 MPa	[19, 82, 87]
	σ_{22}^t	230 - 320 MPa	[19, 87]
	σ_{33}^t	No data available	
Compressive strength	σ_{11}^c	138 - 197 MPa	[19, 81]
	σ_{22}^c	138 - 164 MPa	[19]
	σ_{33}^c	No data available	
Shear moduli	G_{12}	1.0 - 1.9 GPa	[19, 48]
	G_{13}	1.6 - 1.9 GPa	[19]
	G_{23}	1.6 - 1.8 GPa	[19]
Shear strength	σ_{12}	17.1 - 35 GPa	[19, 48, 92]
	σ_{13}	12.0 - 28 GPa	[19, 48, 86]
	σ_{23}	11.2 - 20 GPa	[19, 48]

The interlaminar strain energy release rates are summarised in Table 2.5. The propagation value for Mode I has a very large spread. Some of these studies were investigating the effect of different manufacturing parameters on the interlaminar fracture properties, which resulted in a large spread of data within the individual publications: Lariviere *et al* [84] investigated the effect of different sizing compounds; while Guillén and Cantwell [75] and Perrin *et al* [89] investigated different heating and moulding strategies. For Mode II testing with the ENF test, it is conventional to only report the initiation value, but there was a large discrepancy between the sources. The sources of Mode II data both used the ENF test, but with different data reduction approaches:

- Ding [88] reported values for G_{IIc} of 1.6 -2.0 kJ/m^2 based on the crack initiation point and and experimentally derived compliance calibration.
- Villanueva [91] reported G_{IIc} ranging from 3.5 to 4.0 kJ/m^2, based on the maximum force and direct beam theory. Guillén and Cantwell [75] reported G_{IIc} ranging from 3.0 to 3.7 kJ/m^2, without specifying the method of data reduction.

The mixed Mode I-II tests reported by Villanueva [91] were conducted using the Mixed Mode Flexure test (referred to as Single Leg Bend in this thesis), which has a ratio of $\frac{G_I}{G_{II}}$ of $\frac{4}{3}$.

Table 2.5: Published interlaminar fracture properties of Glass Fibre Polypropylene

Mode	**Strain Energy Release Rate** (kJ/m^2)		**Source**
	Initiation	Propagation	
I	0.2-1.3	0.8 - 2.7	[75, 84, 88, 89, 91]
II	1.6-4.0		[75, 88, 91]
III	No data available		
I-II	2.5	3.0 - 5.0	[91]

2.5 Fibre Metal Laminates

2.5.1 The Origins of Fibre Metal Laminates

Fibre Metal Laminates (FMLs) were developed during collaborative research between Fokker Aircraft and the Delft University of Technology (TU Delft). Due to the shortage of machining facilities in post-WW II Netherlands, Fokker had developed construction methods using thin sheets of aluminium bonded together, rather than a single monolithic sheet of equivalent thickness [1, 2]. In the early 1970s, Fokker and Delft investigated laminated aluminium structures that were stiffened by adding fibres to the adhesive layers. The hybrid composite formed from laminating aluminium and fibre reinforced adhesive came to be known as fibre metal laminates. The most well known example of a FML is GLARE (GLAss REinforced in [93]), based on aluminium and glass fibre reinforced epoxy, which is used in the structure of the Airbus A 380 [94].

FMLs, as with other laminated structures, exhibit superior fatigue peformance to monolithic plates of similar thickness [95]. If an FML develops a crack in the metallic layers, the crack propagates until the FRP-metal interface. At this interface the applied load is transferred to the FRP layers by shear stresses. The crack in the metal may cause minor delamination between the metal and FRP layers in the immediate vicinity of the crack. However, the FRP layer carries a substantial portion of the load, and its stiffness restricts the opening of the crack in the metal layer. This phenomenon is known as "crack-bridging". More detailed descriptions of fatigue in FMLs have been written by Alderliesten [96, 97]. A diagram showing the crack-bridging effect is shown in Figure 2.29.

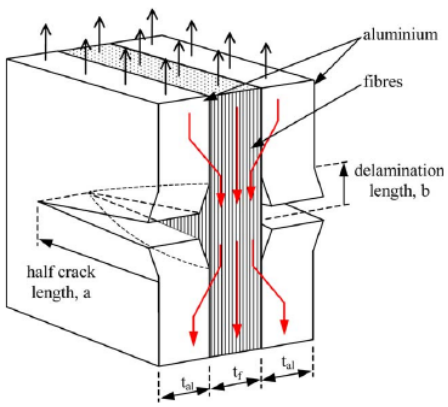

Figure 2.29: Crack-bridging in a cracked FML panel (Alderliesten *et al* [96])

2.5.2 Delamination in FMLs

The interaction between delamination and fatigue crack growth in FMLs has been reported by Alderliesten and colleagues[98, 99, 100], who have focused on specimens with cyclic in-plane loading. Static in-plane loading leading to delamination of GLARE has been reported by Hashagen and de Borst [101], de Vries *et al* [102] and Hinz *et al* [103], for either spliced or lap shear FML specimens. de Vries *et al* calculated different values for R, the delamination resistance, based on purely elastic behaviour, elasto-plastic behaviour and the influence of residual stresses.

These investigations are concerned with slow delamination growth from cracks in the metallic layers. This thesis is more concerned with the large scale delamination events associated with blast loading, reported by Langdon and colleagues [3, 104, 4] and impact events reported by Cantwell and colleagues [75, 105] and Hoo Fatt *et al* [106]. Blast and impact loads are generally perpendicular to the structure, producing flexure and shear loading that would not be present in the in-plane studies [98, 99, 100]. Villanueva, Cantwell and colleagues [91, 74, 75] have investigated thermoplastic based FMLs subjected to out of plane loading. Mixed-mode Single Cantilever Beam (SCB) test results were reported for FMLs based on unidirectional glass fibre-polypropylene and aluminium 2024-T3. The interfacial fracture properties of the thermoplastic based FML were shown to improve as the cooling rate was increased during manufacture of the panels [75]. Villanueva [91] reported SCB tests at different rates, including using a drop weight tester to achieve impact velocities of 2 m/s, on unidirectional GFPP based FMLs as well as unidirectional carbon fibre based FMLs. As crack growth was not monitored for the higher rate tests, the fracture toughness was estimated using the peak force and experimental compliance measured before and after the tests.

2.6 Computational Modelling of Delamination

As FRPs are frequently used in components with complicated geometry (e.g. aircraft leading edges), computational models are essential for structural analysis of these components. This study is limited to finite element (FE) models as these are the most commonly used computational method for the types of structures, loading and failure that FRPs experience. Delamination (or fracture of any type) poses difficult questions for modelling - fracture is by definition a discontinuity in the material, and material models are rooted in continuum mechanics, which assumes that any field in the material, may be described with smooth, continuous functions. As with fracture of other materials, delamination modelling has evolved from simple element deletion based on strength criteria, to techniques allowing progressive failure or damage. The focus of the computational work in this thesis is on delamination and its effects at a macroscopic to structural scale of modelling, to aid in engineering design using FRPs and FMLs. Modelling of fracture at a microscopic scale is outside the scope of this thesis.

The initiation of failure of any kind is typically achieved by a stress based failure criterion. Propagation of a crack can be modelled using fracture mechanics, such as the Virtual Crack Closure Technique (VCCT). However the computational models that captured crack initiation have not been able to capture the propagation and *vice versa*, until the advent of the cohesive zone model (CZM).

2.6.1 Stress Based Delamination Models for Continuum Elements

Many of the failure criteria for FRPs are written in terms of stress, rather than strain. Due to the relatively low strains and high stresses at which FRPs fail, there is less uncertainty in the stress measurement in comparison to the strain measurement. This review limits itself to the failure criteria related to delamination - a myriad of failure criteria for in-ply failure are also available.

Any stress based failure criterion has the general form:

$$f(\sigma_{ij}) \geq 1 \tag{2.4}$$

Hou *et al* [107] presented a FEM simulation based on Brewer and Lagace's delamination criteria [108] that couples interlaminar tension and shear according to :

$$\left(\frac{\sigma_{33}}{Z_R}\right)^2 + \left(\frac{\sigma_{13}}{S_{13}}\right)^2 + \left(\frac{\sigma_{23}}{S_{23}}\right)^2 \leq 1 \tag{2.5}$$

For $\sigma_{33} \geq 0$. Z_R is the interlaminar tensile strength, while S_{13} and S_{23} are the interlaminar shear strength, parallel and transverse to the fibre directions respectively.

For simple brittle failure models, when the function $f(\sigma_{ij})$ equals 1, the element is deemed to have failed and is deleted. Deletion of elements requires careful management of the newly created surfaces, which must not be permitted to penetrate one another. In addition, the deletion of an element poses problems for mass and energy conservation of the model. More advanced damage models do not delete the element at this point, but permit a progressive degradation of the allowable stress in the element as further strain accumulates.

If continuum elements are used to model delamination problems, the element and lamina thickness must be equal. This can result in a very large number of elements for thick laminates. A further complication is that a very small element thickness may reduce the critical time step for explicit FEA codes, which then results in a large number of steps for typical problems.

2.6.2 Virtual Crack Closure Technique

Krueger [109] presents a good summary of the Virtual Crack Closure Technique (VCCT) and its application to delamination of composites. The VCCT requires that the direction of crack propagation be known beforehand, which is the case for delamination. This technique assumes that the energy required to open a crack by an increment Δa is the same as the energy required to close the crack by the same increment. The forces and displacements required to calculate the energy are obtained from FE analyses. The two step crack closure technique, applied to a 2D problem, is illustrated in Figure 2.30:

Two FE analyses are performed, the first with the crack at the initial position shown in Figure 2.30(a) and the second with the crack extended by one element shown in Figure 2.30(b). The increment of energy ΔE required to extend the crack by one element Δa is approximated by:

$$\Delta E = \frac{1}{2}[P_1\delta_1 + P_2\delta_2] \tag{2.6}$$

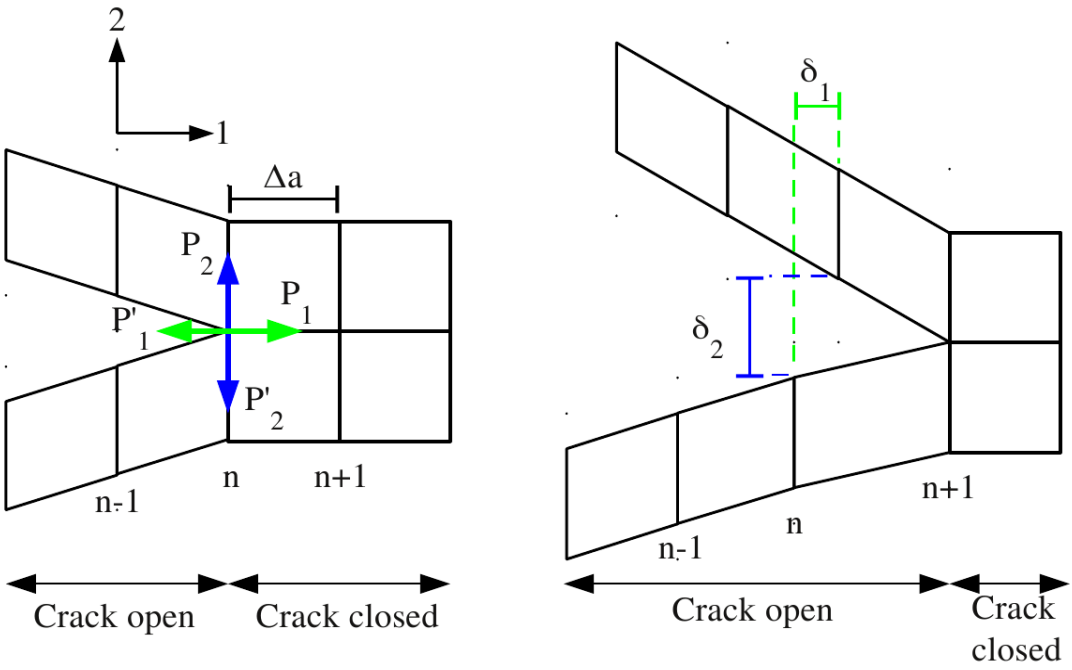

(a) First step – crack at Node n closed

(b) Second step – crack at Node n open

Figure 2.30: Two step Virtual Crack Closure Technique (Figure adapted from [51, 109])

P_1 and P_2 are the horizontal and vertical forces, obtained from the first step. The horizontal and vertical displacements δ_1 and δ_2 are obtained from the second step. This technique allows one to calculate the contributions of the different fracture modes simply by separating according to the components of force and displacement in the directions parallel and perpendicular to the crack propagation.

The Mode I and II strain energy release rates are obtained from :

$$G_I = \frac{1}{2w\Delta a}[P_2\delta_2] \tag{2.7}$$

$$G_{II} = \frac{1}{2w\Delta a}[P_1\delta_1] \tag{2.8}$$

Where w is the width of the structure being analysed and Δa is the increment of crack growth from step 1 to 2. For 3D analyses, the Mode III contribution may also be calculated according to:

$$G_{III} = \frac{1}{2w\Delta a}[P_2\delta_3] \tag{2.9}$$

Where P_3 and δ_3 are the nodal forces and displacements perpendicular to the plane shown in Figure 2.30.

The need to perform two analyses may be avoided if it is assumed that the forces in the vicinity of the crack tip do not change substantially for a small increment of crack growth. The energy release rates may then be calculated using the forces at the crack tip and one node in front, and the displacements from the two nodes trailing the crack tip. The equations and diagrams pertinent to the single step VCCT are presented in §7.3.4.

Sharp crack tips are associated with a discontinuity in the displacement field. This leads to a singularity in the stress and strain fields at the crack tip. In order to improve the accuracy with which this singularity is modelled, higher order elements with modified shape functions may be used [51]. In this case, Eqs. 2.7-2.9 are slightly modified with weighting functions to account for the singularity.

The VCCT is useful for determining strain energy release rates and the ratios of the fracture modes present where the specimen geometry does not lend itself to analytical solutions. The VCCT may also be applied as a fracture criterion between elements, from a predefined crack front. The potential strain energy release rate of the node(s) at the crack front are calculated using Equation 2.7 to 2.9. When the potential strain energy release rate at the crack front equals a predefined critical energy release rate, fracture is deemed to occur. The node at the crack tip is split into two nodes, allowing the crack to propagate one element at a time. This technique is limited by the need to define a crack tip or front, at the start of the analysis.

2.6.3 Cohesive Zone Models

Cohesive zone models (CZM) attempt to address the problem of a predefined crack tip by marrying a stress based damage or crack initiation criteria, with an energy release rate critera for modelling propagation once a crack has initiated [110, 111, 112, 113, 114]. In delamination problems, CZM are typically implemented between two surfaces of either continuum or shell elements. This allows the CZM to control the interlaminar response, while the intralaminar response is governed by the continuum or shell elements. Implementing a CZM as“zero-thickness“ Cohesive Zone elements avoids the need for elements with extremely small dimensions in the through-thickness direction, as would be needed for continuum elements. The initially bonded surfaces are meshed with Cohesive Zone elements. A predefined crack tip is not needed with CZM - whichever element reaches the critical stress first will determine where delamination

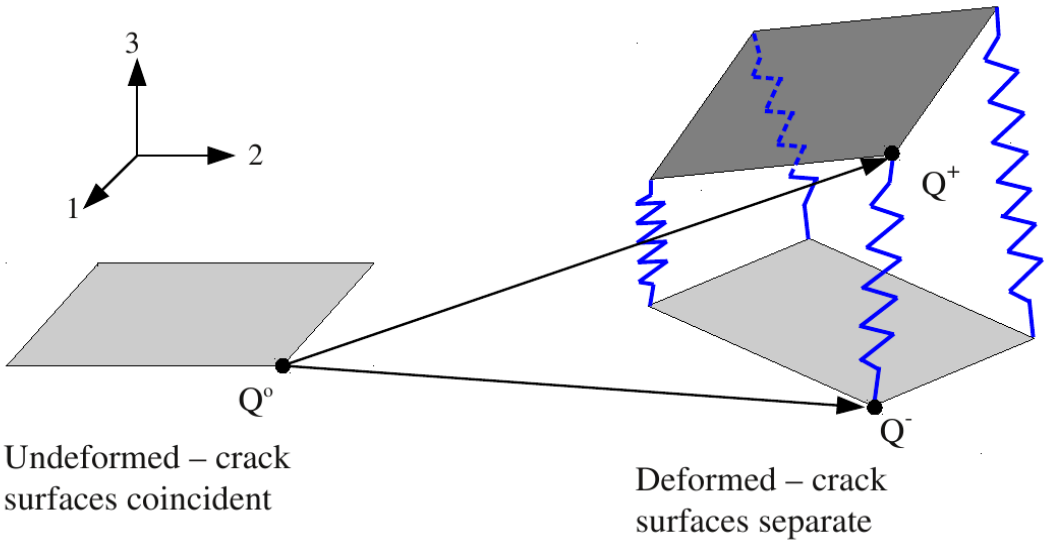

Figure 2.31: Interfacial surface deformation using a cohesive zone approach (Figure adapted from Goyal *et al* [111])

initiates in the model. The Cohesive Zone elements may be thought of as interfacial springs, joining the laminar surfaces (Figure 2.31).

The simplest constitutive model for the CZM is the bilinear model [110, 113], shown in Figure 2.32, based on the interfacial tractions σ and displacement jumps δ between the two surfaces. The initial response of the CZE is very stiff (K), to prevent separation of the adjacent layers. When the stress of the CZE reaches a critical value (σ_C), damage d starts to accumulate. The permissible stress of the element is decreased linearly with δ. The stiffness of the element is also decreased to $K(1-d)$. The reduced stiffness permits the nodes of the CZE to separate with greater ease, and the reduced stress capacity forces the adjacent nodes to carry more of the applied load. The total area under the stress-displacement is based on the permitted strain energy release rate, which defines the maximum interfacial displacement jump δ_{max}. More complicated models may use constitutive laws based on trapezoidal or exponential forms [111, 115]. The more complicated constitutive laws may mimic the experimentally observed cohesive behaviour more closely than the bilinear law, but also contain more parameters that require more experiments to characterise.

Interfacial failure will typically involve tensile opening and shear modes. Hence failure envelopes are used to adjust the critical stress and displacement jump of the cohesive zone constitutive model. The criterion for damage initiation is generally based on the critical stresses and has the form $f(\sigma_j) \leq 1$. A typical form of $f(\sigma_j)$ is the

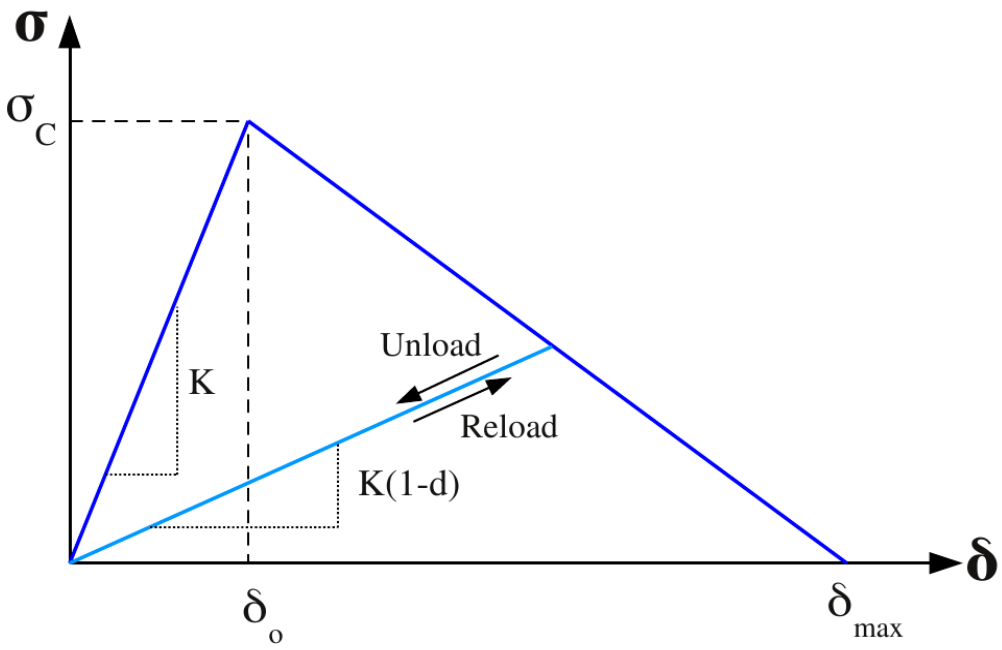

Figure 2.32: Bilinear constitutive model for CZM
(Figure adapted from Camanho *et al* [110])

quadratic law:

$$\left(\frac{\sigma_1}{\sigma_{1C}}\right)^2 + \left(\frac{\sigma_2}{\sigma_{2C}}\right)^2 + \left(\frac{\sigma_3}{\sigma_{3C}}\right)^2 \leq 1 \tag{2.10}$$

The propagation criteria is independent of the initiation criteria, and is typically based on comparing the potential energy release rate G_j to the critical energy release rate G_{jC}. Typical envelope functions are the power law [112, 113]:

$$\left(\frac{G_I}{G_{IC}}\right)^\alpha + \left(\frac{G_{II}}{G_{IIC}}\right)^\alpha + \left(\frac{G_{III}}{G_{IIIC}}\right)^\alpha \leq 1 \tag{2.11}$$

Estimates for σ_{1C} and σ_{2C} may be obtained from interlaminar tensile (§2.3.1.1) and shear (§2.3.1.2-2.3.1.4) tests respectively. The values of G_C are determined from delamination tests for a single fracture mode, such as discussed in §2.3.2. α may be determined from experimental data of failure envelopes, which requires mixed-mode delamination test data. Typically, α often lies between 1 (linear envelope) and 2 (elliptic envelope). Other failure envelopes based on energy release rates include the Benzeggagh-Kenane criteria [116]. The choice of failure envelope should be based on experimental data for critical energy release rates G_C at different fracture mode ratios.

CZM does not show a distinct crack tip, as the VCCT would, but rather indicates elements where damage has initiated after reaching the critical stress σ_C. CZ elements are only deleted once δ_{max} is reached. For a fixed σ_C, δ_{max} increases with maximum energy release rate G_C. Hence for a CZM model with a high G_C, damage initiation in an element will precede element deletion substantially. CZM may be thought of as smearing the crack front over several elements as a "damage process zone".

CZM has been applied to modelling of delamination in specimens, for example Blackman *et al* [117] (DCB specimens), Turon *et al* [114, 118] (DCB, 4ENF and MMB specimens), Balzani and Wagner [119] (DCB and MMB specimens) and Hallett *et al* [120] (matrix cracking and delamination interaction in tensile specimens). Examples of structural or component scale modelling involving CZM are presented by Ye and Chen [121] (7 Point bend of stiffened panel), Chen, Ravey *et al* [122] (T-stiffened panels under tension) and Overgaard *et al* [123] (wind turbine blades subjected to transverse moments and shear). Johnson *et al* [124] used CZM and in-plane damage models to simulate the failure of large GFRP panels subjected to low velocity impact.

An application of cohesive zone modelling applied to FMLs is described by Cid Alfaro *et al* [125]. Cid Alfaro *et al* discuss the differences between treating the metal layers of an FML as elastic-brittle or elastic-plastic, with the interfacial debonding captured by a cohesive zone model and the corresponding laminate failure behaviour. Karagiozova *et al* [126] used CZM to simulate debonding of the metal-FRP interface in FML panels subjected to blast loading.

2.7 High Strain Rate Testing Using The HPB

Force measurements in quasi-static experiments are typically made with load cells, based on strain gauges. A fundamental requirement for a valid load cell measurement is that the forces acting on either side of the load cell must be in equilibrium. During high rate testing, stress waves are likely to arise in the specimen, fixtures and the load cell itself. If impact loading is part of the experiment, the presence of large amplitude stress waves is guaranteed. The presence of stress waves makes force equilibrium of the load cell unlikely, and often manifests as oscillations in the force measurements. These oscillations can obscure specimen response sufficiently to invalidate the test. These oscillations may be reduced by filtering the raw load cell signal. An example of unfiltered and filtered force signals from an impact bend test [92] is shown in Figure 2.33. The filtered force has a peak of approximately 900 N, while the unfiltered force has a local peak of almost 1200 N at the same displacement and an overall peak of almost 1400 N. The reported peak will be a function of the filtering, and is hence a subjective measurement. This problem is exacerbated in commercial systems where the force history is filtered or conditioned, without details of the filtering being available to the end user. This makes it extremely difficult to determine whether the oscillations removed by filtering were part of the reponse of the specimen, fixtures or the load frame itself.

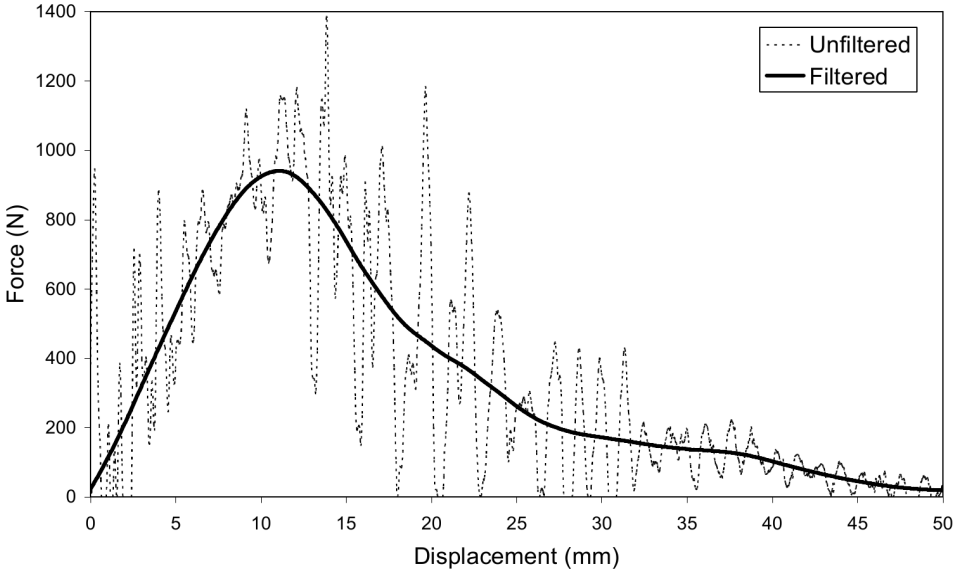

Figure 2.33: Unfiltered and filtered force signals from a conventional load cell during an impact bend test [92]

The Hopkinson Pressure Bar (HPB) provides a means of measuring transient impact forces. A HPB is simply a long bar of constant cross section, instrumented to measure strain at one or more axial locations. A properly designed HPB experiment does not have the equilibrium requirement of a conventional load cell. Instead, the HPB is made long enough that the duration of the force measurement is less than the time taken for a stress wave to travel to the bar end and return to the location of strain measurement. The force and velocity of the ends of the HPB may be calculated from wave theory (§4.3.1), provided that the incident and reflected waves do not overlap.

An alternative means of measuring impact forces is a piezoelectric force transducer. A piezoelectric material, such as quartz, produces an electric charge which is proportional to the applied force. However, piezoelectric force transducers are relatively expensive and are not manufactured locally. Damage due to overloading requires specialised repairs, necessitating return of the transducer to an overseas manufacturer, if the damage can be repaired at all.

In contrast, an individual HPB is relatively inexpensive and robust. Damage to the strain gauge station or the bar tip due to excessive loads is easily repaired locally. Hence HPB are the preferred means of measuring impact forces in this work.

Brief reviews of the origins of the HPB, and its application to general material characterisation, are presented below. The application of SHPB to FRP testing for axial, bending and delamination tests is reviewed in more detail.

2.7.1 The Origins Of The Hopkinson Pressure Bar

Hopkinson [127] measured the peak pressure and duration of impulsive loading with long cylindrical steel bars. The loading was achieved by firing a standard rifle bullet at the bar, or detonating a gun-cotton charge a short stand off distance from the end of the bar. The peak pressure and duration of the compressive wave generated by the impact were obtained by measuring the momentum transmitted to short end pieces weakly attached to the end of the long cylindrical bar. However, this method could not determine the shape of the wave (its pressure-time history). It was assumed that the wave propagation in the bars obeyed one dimensional wave theory, as the axial length of the bars was much greater than the diameter. Hence the shape of the pulse did not distort as it propagated axially along the bar. The axial stress and displacement were also assumed to remain constant across the radius.

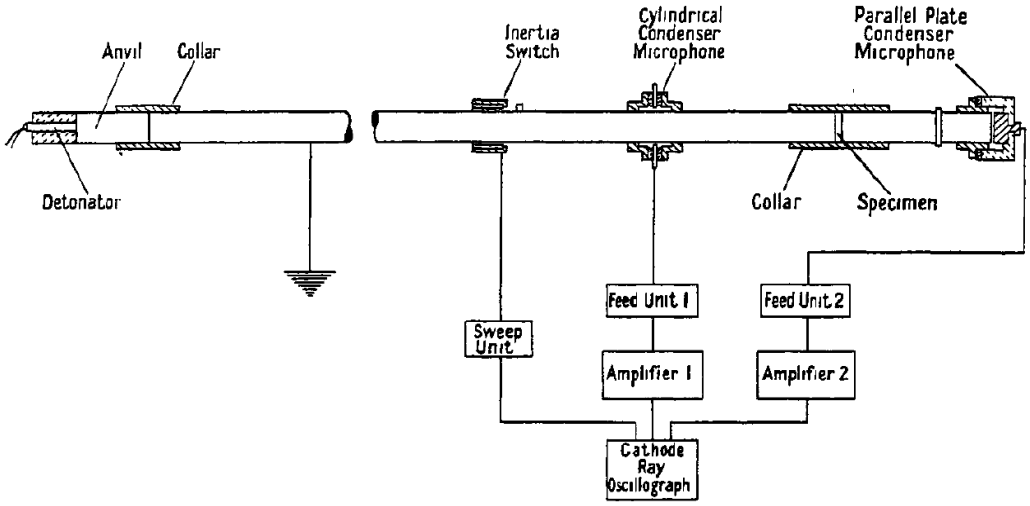

Figure 2.34: Schematic of Kolsky's SHPB [6]

Davies [128] used parallel plate and cylindrical condensors (capacitors) to electronically record the axial displacement history of the unloaded face and the radial displacement history of a cross section of the bar. The axial stress - time relationship could be determined from either of these, allowing Davies to determine the shape of the stress wave. Davies also noted that the pulse would change in shape and duration as it propagated axially.

2.7.2 The Application Of The Split Hopkinson Pressure Bar (Kolsky Bar) To Material Characterisation

Kolsky [6] adapted Davies' instrumented HPB [128] to material characterisation by sandwiching a thin cylindrical specimen between two HPB, shown in Figure 2.34. This device became known as a "Split Hopkinson Pressure Bar" (SHPB), or "Kolsky Bar".

Detonation of a small charge against the first (input or incident) bar created a compressive stress pulse which propagated axially towards the specimen. The pulse was partially transmitted into the specimen and reflected back into the input bar at the specimen-bar interface. In turn, the stress pulse in the specimen would be partially transmittted and reflected at the interface of the specimen and the second (output or transmission) bar. As the specimen length, and hence wave transit time, is comparatively short, the specimen would reach a uniform uni-axial stress state after a short time. The pulses in the long bars were recorded via condensor microphones (capacitative sensors) and displayed on an oscilloscope.

Current compressive SHPB apparatus have the following key differences from that described by Kolsky [6]:

- The compressive loading pulse is generated by firing a striker, typically from a gas gun, against the input bar. This has fewer safety issues than detonation of explosives, and produces a more repeatable and predictable loading pulse.
- The condensor microphones, measuring radial displacement, have been replaced by axial strain gauges. Two diametrically opposed, axially aligned strain gauges are typically used, which cancels out any bending wave travelling in the bars. The strain gauge signals are amplified and captured by digital oscilloscopes or data acquisition systems.

The equations for processing HPB data are presented and discussed in detail in §4.3.1.

Any experiment utilising HPB is subject to certain limitations:

- The relationships for calculating the stress and particle velocity at the ends of the HPB, from the strain measured at the gauge, assume elastic material behaviour. Hence the stress in the bars may not exceed the elastic limit, which determines the maximum force that the bars may accurately measure.
- The incident and reflected waves must not overlap - hence the duration of the incident wave is limited by the time it takes for a wave to travel from the gauge station to the bar end, reflect and return. The duration of the incident wave limits the duration of loading of the specimen. This limitation may be overcome with the use of multiple gauge stations.

The SHPB has been extended from its original compression configuration, to testing materials in tension (for example [7, 8, 129]) and shear (for example [130, 131]). The SHPB has been successfully applied to non-metallic specimens such as FRP (for example [9, 10, 132]. In the interests of brevity, this review of SHPB testing will be limited to the following key areas:

- Compression testing of FRPs
- Bend testing
- Delamination testing

2.7.3 The Split Hopkinson Pressure Bar Applied to High Rate Compressive Testing of Fibre Reinforced Polymers

This review of SHPB testing of FRPs will focus on compressive SHPB testing of glass FRPs. SHPB testing of FRP in compression was initially reported in the 1970s by Billington and Bressendon [133] and Griffiths and Martin [134]. The pioneering work of Harding and colleagues [135, 136, 137] on tensile SHPB testing of glass and carbon FRPs is noted, but will not be discussed in detail as tensile testing is outside the scope of this thesis. SHPB tests on FRP aimed at delamination failures are discussed in detail in §2.7.5. Examples of compressive SHPB testing of glass FRP have been reported by Song *et al* [9], Gillespie, Gama and colleagues [10, 138], Ravichandran and colleagues [132, 139], Ochola *et al* [140] and Akil *et al* [141]. The following key features of SHPB testing of FRP were noted:

- The equilibration of forces acting on the input and output faces of the specimen is improved by keeping the specimen length small. The largest value reported for this dimension was 17.8 mm [138], with most others falling in the range of 5 - 12.7 mm. It is essential to compare the force histories at the specimen input and output faces to confirm specimen equilibrium for every test.
- In order to conduct post-mortem fractographic studies, it is necessary to recover the specimen after a single loading event. As the stress waves propagating within the SHPB will persist after the initial loading, it is necessary to prevent repetitive loading of the specimen. The simplest means of preventing repetitive loading in a compressive SHPB is to make the output HPB shorter than the input HPB [139], which causes the output bar to separate from the specimen before the second loading wave in the incident bar returns to the specimen. Gama *et al* [10] prevented repetitive loading by arresting the input HPB by means of a momentum trap. The details of momentum trapping are presented by Nemat-Nasser [142].
- If no special steps are taken, the specimen strain rate will vary quite dramatically during a SHPB test. Gama *et al* [10] reported a typical test where the peak strain rate $\dot{\varepsilon}$ had a maximum of approximately 1900 $/s$, which fell to 900 $/s$ during the specimen loading, and is reported as an average of 1100 $/s$. It is desirable to maintain a constant strain rate during the loading of the specimen, which is achieved by pulse shaping of the incident wave [143]. Song *et al* [9] used sacrificial elements between the striker and input bar, which are described in detail

in [143, 144], to achieve a nearly constant strain rate. Pulse shaping can also be achieved by altering the profile of the striker [145, 146].

- Glass FRP displays an increase in failure strength with increasing strain rate. The differing matrix materials tested (epoxy in [9, 132, 140]; vinylester in [139, 147, 141]; polyester in [148]) suggest that the rate dependency of the failure strength is due to the glass fibres.

Li *et al* [149] reported SHPB tests on a glass fibre-polypropylene composite, based on a random fibre direction glass mat. Unfortunately no specimen details were included in [149], and the reported results do not discuss specimen equilibrium or failure modes. No other investigations on SHPB testing of GFPP have been published.

2.7.4 The HPB Applied to Bending Tests

The HPB has been adapted for dynamic bend tests, to study a variety of phenomena including metal fracture [12, 150] and composite failure [151, 152]. These studies can be divided into two subsets:

- A single HPB is used to centrally load a rigidly supported specimen - see Figure 2.35. This was initially investigated by Ruiz and Mines [12] as an alternative to instrumented pendulum Charpy tests. Examples of this arrangement have been presented by Bacon *et al* [153], Martins *et al* [154], Rittel *et al* [155], Rubio *et al* [150] and Luo *et al* [151]. The specimen central force and displacement histories are calculated from the superimposition of the incident and reflected waves at the bar-specimen interface.

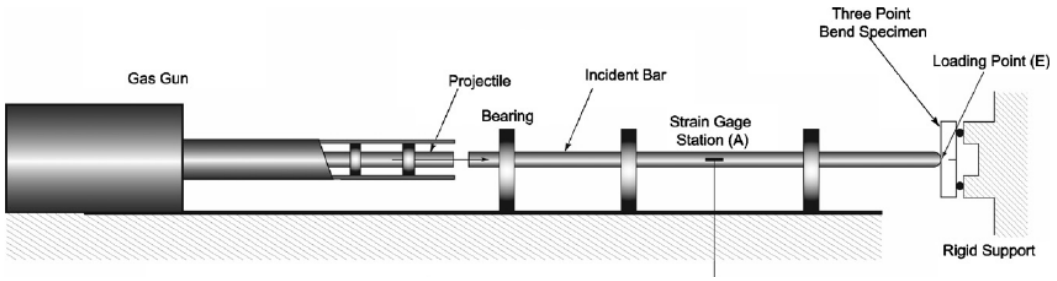

Figure 2.35: Three Point bending via a single HPB [154]

- A bending specimen is incorporated into a regular SHPB set up (input and output bars), which have appropriate end fixtures to accomodate the bending specimen - see Figure 2.36. A single output bar with a bending support (for example Jiang *et*

al [156] and Park *et al* [157]), or two output bars separated by the apropriate span (for example Ogawa *et al* [152] and Rubio-Gonzalez *et al* [13]), may be utilised. The incident, reflected and transmitted waves are all used to calculate the specimen force and deflection history, as the specimen outer supports move with the transmitted bar.

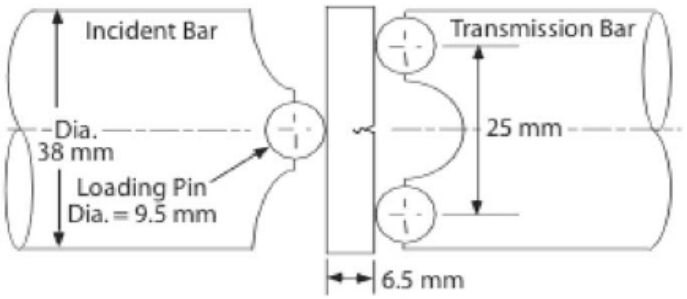

Figure 2.36: Three Point bend specimen with input(incident) and output(transmission) HPB [156]

Any system using an input HPB to apply the central load faces the issue of the large impedance mismatch between the input bar and the specimen loaded in bending. Unless the specimen is extremely rigid in bending, most of the compressive incident loading wave is reflected in tension. The force derived from the sum of the incident and reflected waves is relatively small in comparison to the force associated with the incident wave and hence has significant uncertainty. The magnitude of the incident wave must be less than the yield stress of the input bar material. Hence the input bar material and diameter imposes a limit on the maximum force that may be applied to the specimen.

Furthermore, the duration of the applied loading is limited by the length of the input bar if a single strain gauge station is used. This duration may be increased by using additional gauge stations and wave reconstruction techniques, which are often non-trivial in application.

As the force transmitted to a specimen in bending is relatively small, the use of a single output bar with the required fixture to provide the outer specimen supports (for example Jiang *et al* [156] or Nwosu *et al* [158, 159]) results in a very small measured transmitted stress wave. This situation is exacerbated by using an output bar of sufficient diameter to mount the outer supports without additional fixtures (see Figure 2.36). The uncertainty in this stress measurement may be reduced by using semiconductor strain gauges. Semiconductor strain gauges can detect much smaller strains

than foil strain gauges, but are substantially more expensive and have a much lower permissible strain, which can lead to gauge failure both during application of the gauge and due to higher than anticipated loads. However, the negative aspects of semiconductor strain gauges may be avoided if the HPB diameter and material are chosen such that the applied loading results in bar strains of a magnitude easily resolved by conventional foil strain gauges.

Better examples of a SHPB adapted for bending are presented by Rubio-Gonzalez *et al* [13] (shown in Figure 2.37), Ogawa *et al* [152], Yokoyama *et al* [160] and Delvare *et al* [161]. This system used HPB with rounded ends to load the specimen directly (rather than indirectly via fixtures) and used two independent output bars to support the specimen. The absence of large fixtures to support the specimen means that the forces measured in the bars are the loads applied to the specimen, without the complications of fixture inertia. Should any assymetry arise in the specimen and hence in the outer reaction forces, the independent output bars will measure the separate reactions. This provides useful information for validation of the test. Rubio-Gonzalez *et al* [13] analysed the entire experiment using FEA, which accounts for any stress wave propagation within the specimen.

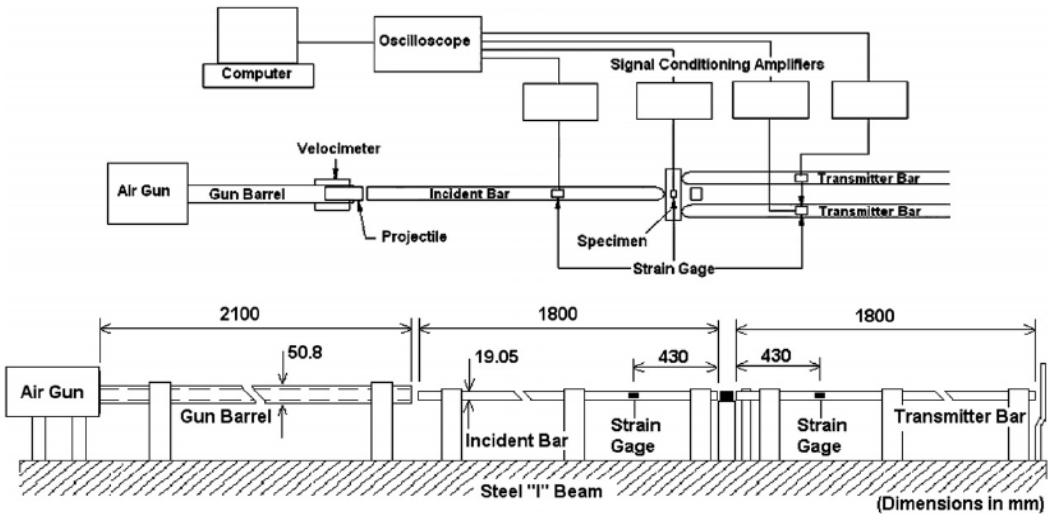

Figure 2.37: SHPB adapted for dynamic bending test by Rubio-Gonzalez *et al* [13]

Delvare *et al* reported that the stresses measured with the twin output bars were practically zero as seen in Figure 2.38. This could be attributed to:

- Delvare's SHPB set up used 40 mm diameter aluminium output bars. Aluminium bars of such large diameter are appropriate for measuring large forces (tens to

hundreds of kN). Hence the applied forces may have been less than the noise threshold for the bars and given strain gauge amplification system.

- The material being investigated was a quasi-brittle clay brick, with a relatively large support span (200 mm). The deflection to fail a brittle specimen is relatively low, and is likely to fail soon after the load is applied. In dynamic bending, there is a finite time difference between the load being applied at mid-span, and a reaction being exerted at the outer support. This time difference depends on the speed of bending waves in the specimen, and the support span. It is possible that the specimen failed before the bending wave reaching the outer support HPB and hence the force exerted by the specimen on the output bar was negligible.

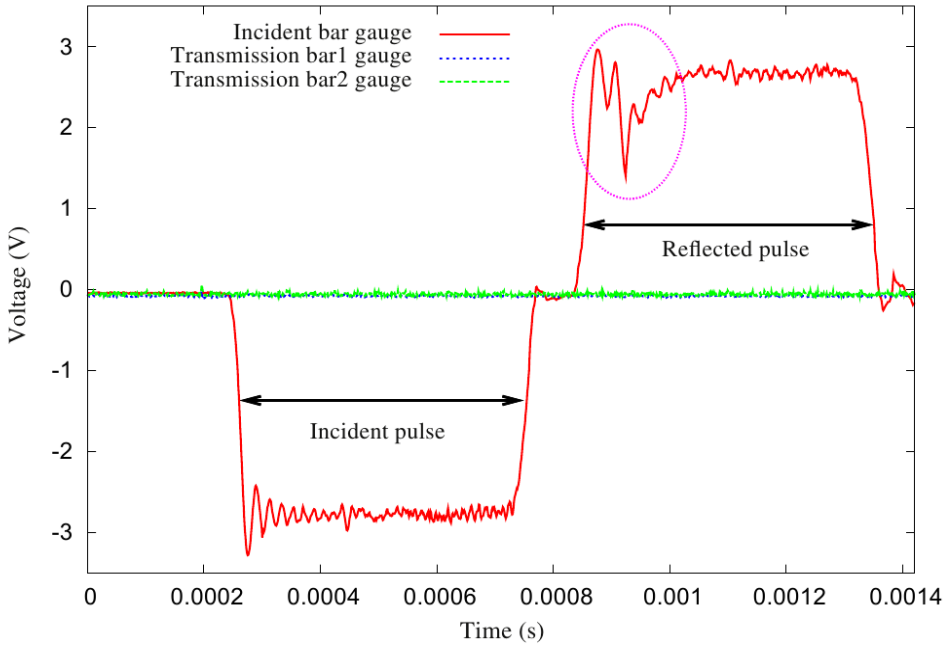

Figure 2.38: SHPB signals showing negligible output bar stresses [161]

The twin output HPB arrangement for bending is limited by practical considerations:

- The metallic fracture specimens tested in [13, 160] and ceramics in [152, 161] all failed at specimen deflections of less than 1 mm. The GFPP bending and delamination specimens to be tested in this thesis have anticipated deflections to failure of the order of 5 - 10 mm. In order to obtain specimen deflections of this magnitude using the arrangement shown in Figure 2.37, longer bars and strikers would be needed. The arrangement described in [13] is already 5.7 m long. As

the HPB bed available for this thesis is 9 m long, adapting the twin output HPB arrangement within these constraints is unlikely to provide sufficient specimen deflections.

- The support span of the specimen is determined by the separation of the twin output HPB. The details of the output bar supports are not described in any of [13, 152, 160, 161], but from the schematics and photographs the separation distance of the output bars is fixed. This is an understandable compromise, as supports that provided adjustable separation, while maintaining proper alignement for the twin output HPB would be fairly complicated. However, not being able to adjust the specimen support span would be very limiting for the experiments proposed for this thesis.

2.7.5 Application of the HPB to Delamination Testing

2.7.5.1 Interlaminar Tension or Mode I Loading

Lifshitz and Leber [11] used a tensile SHPB to test both glass fibre reinforced epoxy and carbon fibre reinforced epoxy specimens in combined interlaminar tension and shear, at strain rates of approximately 100 to 250 $/s$. The specimen geometry is shown in Figure 2.39. The specimens were glued to the HPB faces, which limited testing to one specimen per day. The test program was successful for the glass fibre reinforced epoxy specimen. However, it was noted that the machining of the specimens was extremely difficult, and the carbon fibre specimens often sustained damage during machining which lead to premature failure [11]. The machining difficulties (which would be compounded for a thermoplastic FRP or FML), and the time limitations imposed by gluing the specimen directly to the HPBs, make this an unfeasibly expensive test method.

Conventional DCB tests have not been adapted for use on a HPB arrangement, in the open literature. This is probably due to the relatively large displacements (tens of mm) and specimen gripping requirements of a DCB test. The large displacements would require unfeasibly long bars. The hinged grips required for a DCB test would add inertia to the ends of the bars, potentially obscuring the specimen response.

However, HPB systems have been adapted for Wedge Insert Fracture (WIF) tests, that create a Mode I interlaminar crack. Kusaka and colleagues [162] and Sun and Han [163] both modified HPB systems to drive a wedge into a suitably machined FRP specimen. The set up of Sun and Han [163] is shown in Figure 2.40. Kusaka *et al* [162] used a specimen similar to the conventional DCB specimen without bonded hinges,

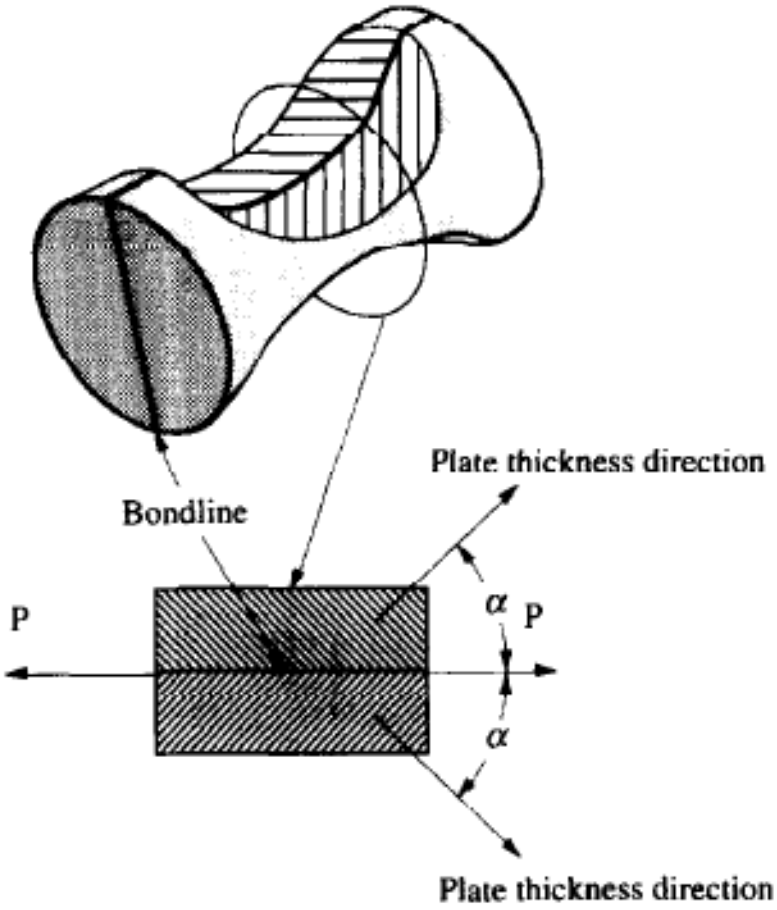

Figure 2.39: Interlaminar tension / shear specimen geometry utilised by Lifshitz and Leber [11]

rather than the V-notched specimen of Sun and Han [163]. The opening was by a wedge effect, achieved by a transverse cylinder driven by an input HPB.

Sun and Han [163] noted that the force exerted by the specimen on the transmitter bar was so small that semiconductor strain gauges (with a gauge factor 50 times that of conventional foil gauges) were necessary to measure transmitted stress wave. As noted in §2.7.4, semiconductor strain gauges are expensive and fragile. The use of semiconductor gauges may be avoided by selecting the output HPB material and diameter appropriate to the anticipated forces. The force exerted by the specimen on the transmitter bar, and the crack history as measured by the crack detection gauges shown in Figure 2.40, were used as boundary conditions in a finite element simulation in ABAQUS. FEA was subsequently used to calculate G_{Ic}. The glass fibre-epoxy and carbon fibre-epoxy specimens tested by Sun and Han [163] exhibited almost no rate sensitivity with regard to G_{Ic}.

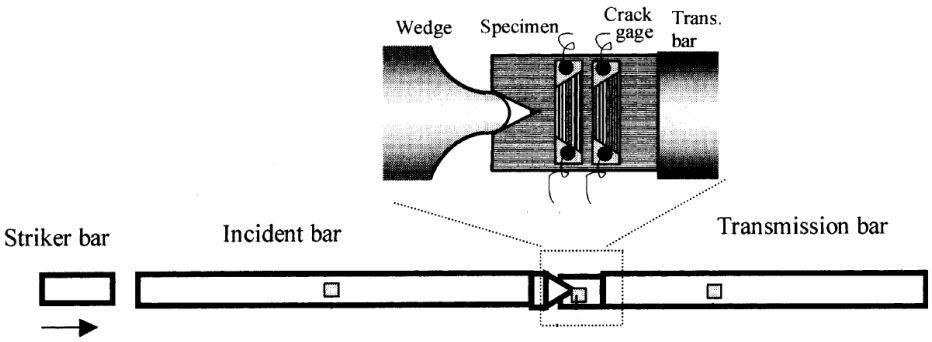

Figure 2.40: SHPB adapted for wedge insert fracture [163]

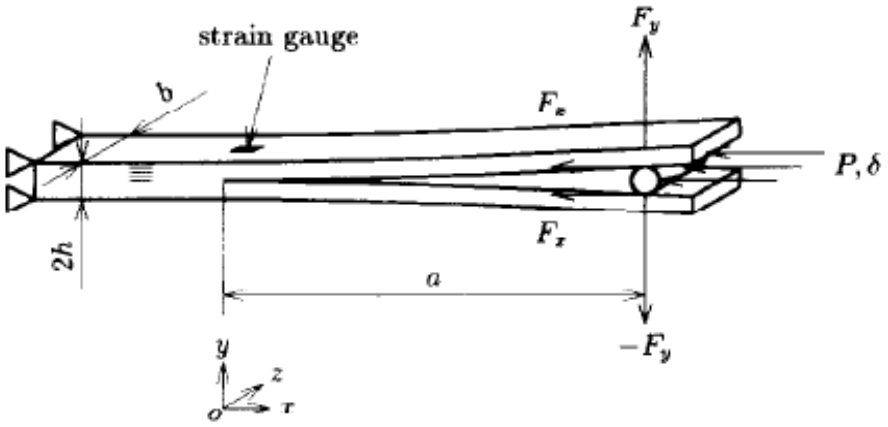

Figure 2.41: DCB specimen for wedge insert fracture, employed by Kusaka *et al* [162]

Kusaka *et al* [162] did not use the forces measured by the HPB in their system to determine the energy release rates - at no point are the input and output bar stress waves presented. The relationship between the surface strain on the outside of the specimen (see strain gauge on Figure 2.41) and the energy release rate was determined using beam theory and LEFM principles. The specimens were instrumented with strain gauges and the energy release rate was calculated purely from the measured specimen surface strain, without reference to the HPB forces or velocities. This raises the question as to why a SHPB set up was used at all, since the same boundary conditions can be easily created without using a HPB.

There is potential to improve on the SHPB arrangements described in [162] and [163] by addressing the issues around force measurement.

Both Kusaka *et al* [162] and Sun and Han [163] raise the issue of characterising loading rate. As a specimen undergoing fracture has a non-uniform, discontinuous strain

field, it is not possible to characterise the rate of the experiment using strain rate. Both expressed the rate of the experiment in terms of the time derivate of G_I. Kusaka *et al* [162] also noted the displacement rate of the arms of the DCB, and observed that for displacement rates ranging from $10^{-3}\,m.s^{-1}$ to $10\,m.s^{-1}$ the critical fracture toughness G_{Ic} was practically constant.

2.7.5.2 Interlaminar Shear or Mode II Loading

The HPB is readily adapted to a test where the faces of the specimen are loaded evenly in compression, and the specimen geometry causes a failure other than compression, such as a lap shear test. Harding and colleagues [41, 42, 40] have used lap shear specimens, loaded with a SHPB , to investigate the interlaminar shear strength of unidirectional carbon FRP.

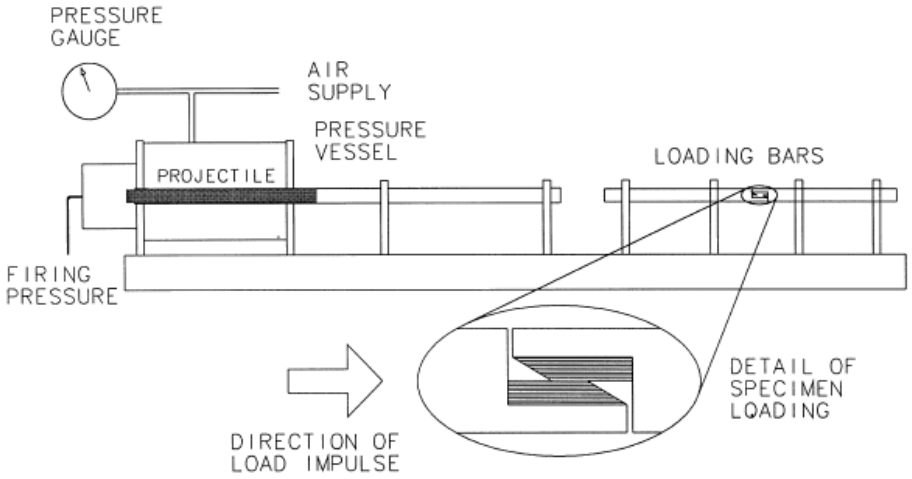

Figure 2.42: Schematic of SHPB adapted for lap shear specimen [42]

Harding and colleagues [41, 42, 40] adapted the lap shear specimen geometry over time to the form shown in Figure 2.42, in order to reduce the variation in interlaminar shear stress σ_{31} over the gauge section of the specimen. Hallett *et al* [42] showed that in order to match a macroscopic force-displacement response, the material model required a much higher values of σ_{31} than the average σ_{31} obtained from the experiments. This was attributed to the presence of stress concentrations and significant compressive normal stresses at the tip of the notch. Furthermore, there was considerable scatter in the data for tests performed at high strain rates (400 - 800 /s). While useful for estimating the value of σ_{31} at which damage initiates, a lap shear specimen is not suited for determining fracture toughness or strain energy release rates, due to the relatively short gauge length through which the failure propagates.

Nwosu *et al* [158, 159] presented a SHPB modified to test composite ENF and SLB specimens, with the bar end fixtures shown in Figure 2.43. This HPB arrangement has features which compromise the validity of the reported results. A requirement for valid SHPB results is that the forces required for specimen acceleration are small in comparison to the deformation forces. The composite specimens used would be sufficiently small in mass (on their own) but require a fixture to support the specimen, which is attached to the output bar. The mass of this fixture is not reported, but based on the specimen span of 52 mm, specimen width 25 mm and bar diameter of 25 mm, the fixture mass is at least one order of magnitude larger than the specimen. Hence there is uncertainty as to what fraction of the reported forces is attributable to acceleration forces. An example of the input and output bar stresses from a test conducted by Nwosu *et al* [158] is shown in Figure 2.44.

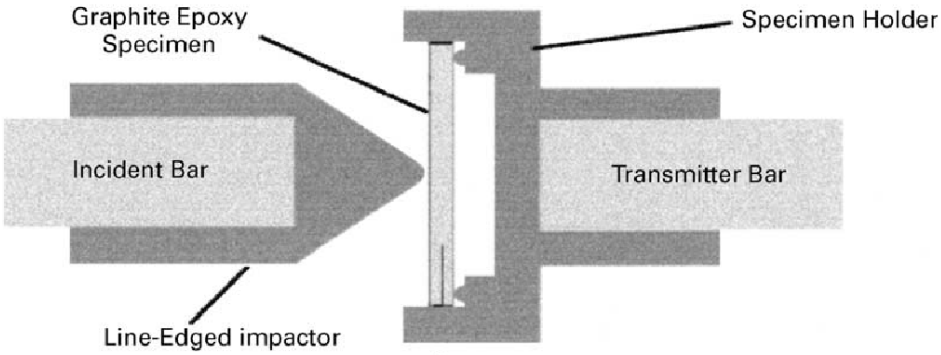

Figure 2.43: Schematic of fixtures for SHPB adapted for ENF test by Nwosu *et al* [158]

In the reported signals, the transmitted stress wave is less than 10% of the magnitude of the incident or reflected stress waves. This is due to the substantial impedance mismatch between the input bar and specimen loaded in bending. Hence there is significant uncertainty in measuring the force acting on the specimen and fixtures. Furthermore, the duration of the transmitted stress wave (approx. 1.2 ms) is more than double than that of the incident wave (approx. 0.5 ms). As the applied force only acts on the specimen for the duration of the incident wave, the persistence of the transmitted wave must be due to something other than the applied force. This could be attributed to the relatively large mass of the output bar fixture, which will exert an inertial reaction force on the output bar after it is initially accelerated by input bar. The significant inertial component makes it difficult to discern what portion of the force measured by the output bar is due to specimen deflection. As with the other HPB bending arrangements, the majority of the incident wave is reflected, so the force

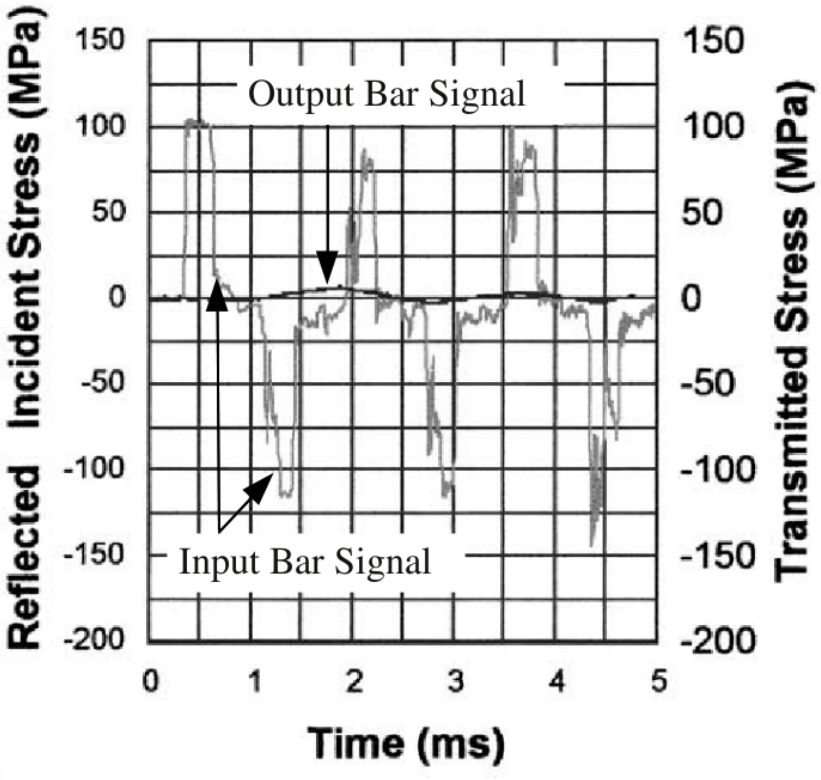

Figure 2.44: Graph of SHPB signals from Nwosu *et al* [158]

determined from the difference of the incident and reflected waves will have a high degree of uncertainty.

2.7.5.3 Comments on use of HPB for interlaminar fracture testing

A common factor in the above investigations is the use of analytical solutions to determine the interlaminar fracture toughness. These solutions are generally derived for quasistatic loading, where the stress state is not time dependent. However, if a HPB is used to apply loads then stress waves will be present, which makes the stress state of the specimen both spatially and temporally dependent. For specimens loaded in transverse bending, both through-thickness and flexural stress waves will be present. The material parameters obtained by application of quasi-static relationships to HPB fracture experiments should be viewed as initial estimates. These initial estimates of material properties can be applied in computational models, which can capture the stress wave behaviour.

2.8 Summary

A review of the literature pertinent to this thesis has highlighted the following opportunities for research:

- Reported compression and tensile testing of GFPP is generally at quasi-static strain rates, with a limited set of data at approximately $\dot{\varepsilon} = 100/s$, obtained from an impact test method which is not widely used. The SHPB is a generally accepted means of performing high strain rate testing and would provide strength data for $\dot{\varepsilon}$ ranging from 500 to 1500 $/s$.
- Bend tests utilising the HPB often have compromised force measurements, which are exacerbated as the specimen stiffness decreases. As the force data from a bend test are of prime interest, bending HPB arrangements should be examined and re-designed with the criteria of providing accurate, reliable force data.
- Delamination testing under impact loading is often performed using load cells for force measurement. Measuring impact forces using load cells can be problematic, due to stress waves excited by impact. The limited literature on delamination testing using HPB does not consider issues such as fixture inertia and the impedance matching between bars and specimen, that reduce the accuracy of the reported results. Existing delamination test methods should be evaluated and a suitable candidate adapted for high rate testing on a HPB based apparatus.

Chapter 3

Panel and Specimen Manufacture and Preparation

This chapter describes the manufacture of the FRP and FML panels, and the preparation of specimens from these panels. All panels were manufactured by the author in the BISRU laboratory.

3.1 GFPP Panel Manufacture

The Glass Fibre Polypropylene (GFPP) panels were manufactured from Twintex ®, which is a comingled E-glass fibre and polypropylene system, currently manufactured by Owens Corning®[19]. The form of Twintex® used was balanced 2x2 twill weave fabric, with a nominal areal density of 1500 g/m^2. A single ply of this fabric moulds to an approximate thickness of 0.5 mm. The fabric was cut into 300 x 300 mm sheets, which were laid up in a Teflon coated steel mould. This fabric is nominally isotropic in the warp and weft directions [19]. All lay-ups were based on the warp fibres being parallel. A single sheet of Xiro was placed between the outer plies of the lay-up and the mould. Xiro refers to a polypropylene based thermoplastic adhesive, manufactured by Collano as Collano Xiro 23.100. In this instance, the Xiro was a source of polypropylene to improve the surface finish of the panels. A thermocouple was inserted at the approximate mid plane of the laminate to monitor matrix temperature. The completed lay up and mould were placed in an oven and heated till the mid plane reached 190 °C. Once this temperature was reached, the oven temperature was maintained for 20 minutes to allow even heat distribution. The mould was then removed from the oven and placed centrally in a hydraulic press, which was at room temperature of approximately 25 $^{\circ}C$.

Centering was facilitated by a jig plate. The load on the press was increased until a laminate pressure of 1200 kPa was reached (typically 11 tons for a 300x300 mm panel). The panel was allowed to cool under pressure to room temperature before removal from the press and mould. Guillén and Cantwell [75] had showed that this heating and and rapid cooling cycle resulted in improved delamination resistance for GFPP.

The manufacture of relatively thick GFPP ($\geq 15mm$), was problematic due to difficulties in accurate stacking of a large number of Twintex sheets. As the Twintex sheets only became tacky at temperatures above 120 °C, it was possible for handling to disturb sheets from their original stack position. If the sheets were not accurately stacked, the mould top was likely to slide during the pressing process, which could result in uneven panel thickness. A single panel of 20 mm nominal thickness was produced by carefully laying up 44 plies and alignment of the mould, to ensure minimal disturbance during heating and pressing. As this process was very time consuming, no further panels of this thickness were manufactured. If panels of this thickness are required in future, it is recommended that constrained moulds, either of the picture frame or with alignment pins, be used to facilitate manufacture.

3.2 FML Panel Manufacture

The FML used in this thesis was based on Aluminium 1200 H4, and GFPP. The aluminium panels used were cut to the required size and subjected to a chromate conversion surface treatment (Alodine ™). This surface treatment was suggested by Reyes Villanueva [91] as producing the best bond between aluminium sheets and FRP layers with a polypropylene matrix. The Alodine surface treatment also minimised corrosion of the aluminium sheets. Before laying up the panel, all aluminium sheets were degreased with acetone.

The panels were laid up in a steel mould, which was coated with Teflon to allow easy removal. Pre-cut sheets of aluminium and GFPP fabric were laid in the mould according to the desired lay up. A typical lay up is shown in Fig. 3.1. A single sheet of Xiro was placed between any aluminium sheet and the adjactent Twintex layers to improve the bond. Xiro contains approximately 0.2% maleic anhydride (by mass) [164], which improves the bond between aluminium and polypropylene matrix FRPs [91]. The completed lay-up was subjected to the same heat and pressure cycle as the GFPP panels.

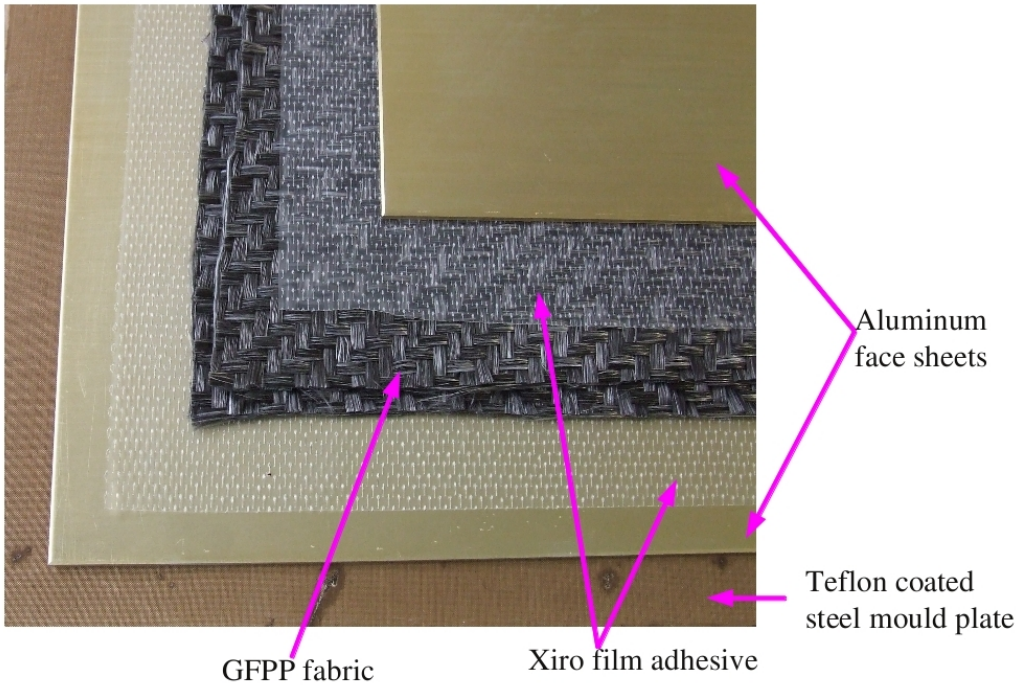

Figure 3.1: Typical lay up of aluminium, Xiro and GFPP fabric in mould, prior to heating and consolidation

3.3 Fracture Specimen Preparation

Specimens for fracture mechanics tests require the presence of a flaw, the location and size of which are both known. For delamination tests, this is easily achieved by inserting a thin film at the desired location of the laminate stack. The film must not bond to at least one of the adjacent lamina, as well as minimise flow of matrix material or adhesive into the flaw region. This was achieved by inserting a piece of folded aluminium foil, approximately 15 μm thick at the desired location. This is the same technique used by Villanueva and Cantwell for similar thermoplastic FMLs [91, 74]. The procedure recommended in ASTM D5528 [33] recommends using a Poly Tetra Flouro Ethylene (PTFE, commonly available as Teflon ®) film as the starter defect. Aluminium foil was preferred as the elevated processing temperatures required for the polypropylene based layers could have influenced the integrity of PTFE film. It was necessary to use a folded insert, as this quarantees an unbonded area at least as large as the insert. If a single layer insert was used, the matrix flow during pressing may reduce the unbonded area. The lay up including a starter defect was processed with the same heating cycle and cold pressing as used for the GFPP and FML panels.

It is noted that the folded aluminium insert is thicker than the polymer films normally used for starter defects, and that this may have an effect on the initiation value of fracture toughness. To reduce the effect of the insert, the initial flaw was advanced a short distance by cyclic loading. This was achieved by loading all specimens in Three Point Bending, to a maximum load of 100 N for 50 load / unload cycles.

3.4 Specimen Machining

The cutting of specimens from thermoplastic FRPs such as GFPP and FMLs based on GFPP is a non-trivial exercise. The following machining techniques were evaluated:

- GFPP panels were cut with non-serrated, diamond abrasive coated circular saws. As the available circular saw did not have coolant jets, both the blade and panel reached localised temperatures high enough to melt the polypropylene matrix in the region of the cut. This caused clogging of the blade within centimetres of starting the cut, and a poor surface finish with exposed fibres. This was not attempted with FML panels, as the diamond abrasive blade is unsuitable for cutting soft metals such as aluminium.

- Serrated, tungsten tipped circular saw blades were used to cut both GFPP and FML panels. The serrated blades were able to cut the width of a panel without overheating. However, the resulting surface finish and poor dimensional control required that the specimens be finished on a milling machine. The serrated blades may have caused local fibre pull-out, where the fibres ran perpendicular to the direction of cut.

- Abrasive water jet cutting was contracted to WaterJet Technologies, Bellville. This resulted in an acceptable surface finish, with good dimensional tolerances. To prevent possible delamination or debonding due to penetration of the high pressure water between laminae, the cut was always started at a location in the panel 20 to 30 mm away from the specimen. Flat surfaces of the specimen were finished on polishing tables, using 220 and 500 grit SiC polishing discs.

Water jet cutting was used to machine the test specimens, as it was the only technique that gave an acceptable surface finish and did not damage the composite layer.

Chapter 4

Compression Tests

This chapter describes the quasi-static and high strain rate compression testing of GFPP. All quasi-static tests were conducted on a Zwick^{TM}1484 Universal Testing Machine. High strain rate tests were conducted on a Split Hopkinson Pressure Bar (SHPB).

4.1 Quasi-Static Experimental Details

4.1.1 Failure Strength Determination

The compression tests were designed to enable direct comparison with the compression SHPB tests, rather than following published standards. The test and specimens described in ASTM D 3410 [22] requires shear loading of the lateral surfaces of the specimen (rather than end loading). The wedge grips required for shear loading make this unsuitable for SHPB testing, due to the high mass of the grips. ASTM D 695 [21] describes compression testing via end loading, but utilises specimens of a relatively long gauge length (25.4 mm). Testing long specimens in the SHPB results in poor equilibration of the forces on each specimen face, making the test data inadmissable.

Specimens were tested in both through-thickness, and in-plane compression. Specimens were water-jet cut from the required panel, and the specimen faces were polished using 220 and 500 grit SiC polishing paper. The through-thickness specimens were cylinders, of nominal diameter 11 mm and length 12 mm. The in-plane specimens were cuboid blocks, of nominal width and breadth 11 mm and thickness 12 mm. These specimen dimensions were chosen to be suitable for SHPB testing and are consistent with dimensions chosen in [9, 10, 138, 141]. It is noted that these specimen dimensions do not provide the four to five weave repeats that are normally used for

quasi-static testing. In order to meet the weave repeat requirement, the specimen dimensions would have to be increased to approximately 30 to 40 mm width or diameter. If the same specimen dimesions were used for the high rate SHPB tests, this would require HPB with diameters of 60 to 80 mm, with strikers of similar diameters, which are not practical given the available gas gun and support structure. It was deemed more important to have specimens of similar dimensions for the quasi-static and SHPB tests, than to meet the weave repeat requirement.

The specimens were compressed between hardened steel anvils, using a molybdenum based grease to lubricate the faces. Tests were conducted in displacement control at cross head speeds of 0.1, 1 and 10 mm/min. Five specimens were tested at each quasi-static rate.

True stress and strain were calculated using the standard relationships in Equations 4.1 and 4.2, using a constant volume assumption. If specimens fail by fracture, rather than plastic deformation, the constant volume assumption becomes inaccurate once fracture initiates. Hence true stress and true strain are typically only calculated up to fracture initiation.

The raw force $P(t)$-displacement $\delta(t)$ data was converted to true stress σ-true strain ε relationships by:

$$\sigma(t) = \frac{P(t)}{A(t)} \tag{4.1}$$

$$\varepsilon(t) = ln\big(\frac{L_o + \delta(t)}{L_o}\big) \tag{4.2}$$

The instantaneous specimen area $A(t)$ is calculated from the original area A_o and length L_o and instantaneous length $l(t)$, assuming constant volume :

$$A(t)l(T) = A_o L_o \tag{4.3}$$

$$A(t) = \frac{A_o L_o}{l(t)} \tag{4.4}$$

$$= \frac{A_o L_o}{L_o + \delta(t)} \tag{4.5}$$

4.2 Quasi-Static Results

4.2.1 Through-Thickness Direction

The force-displacement results for compression of GFPP at 0.1 mm/min in the through-thickness direction are shown in Figure 4.1. The results for tests conducted at 1 and 10 mm/min have no qualitative differences, and merely differ in the magnitudes of force and displacement to failure. The data for the tests at 1 and 10 mm/min is shown in Appendix A.1. The response is linear, until abrupt failure following peak load. No barrelling or other non-uniform deformation of the specimens was observed during the tests. Prior to failure, the deformation is uniform. As the constant volume and uniform deformation assumptions are reasonable for this case, true stress and strain may be calculated from the force-displacement results. The pertinent parameters for the tests conducted at different rates are summarised in Table 4.3, in §4.5.3. No values for the quasi-static or high rate through-thickness compressive strength of GFPP are reported by either the manufacturer [19] or in the literature (see Table 2.4) so there are no reference values to compare these results to.

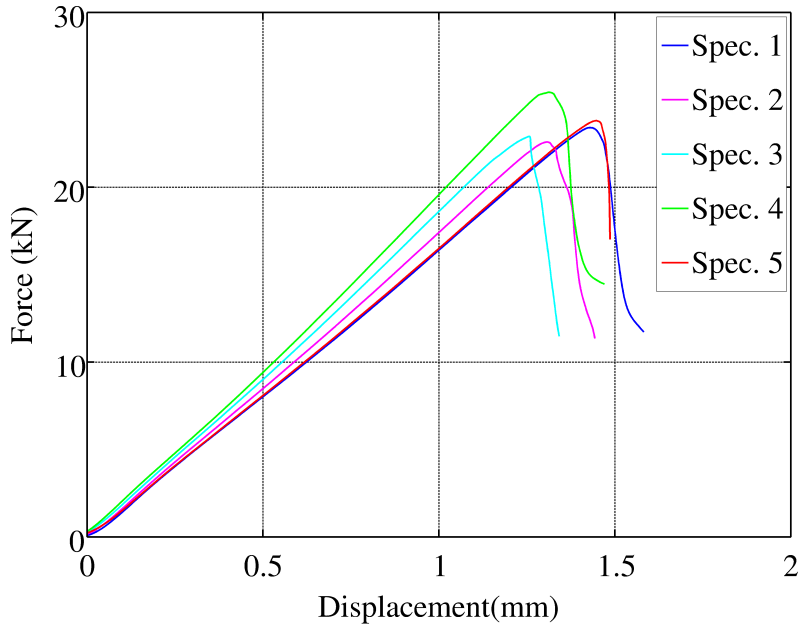

Figure 4.1: Plot of force displacment response for through thickness compression of GFPP at 0.1 mm/min

Failure manifested as fragmentation of the specimen. The fragments remained partially attached for all but four of the specimens. For these four, the smaller fragment

was ejected from the test fixture and was never recovered. The dominant failure modes observed were macroscopic shear, and spreading.

Macroscopic shear failure is shown in Figure 4.2. The band of shear is approximately 45 °to the direction of loading. However, at higher magnification of the failed region in Figure 4.3, the fragments have a "tongue and groove" appearance. This suggests that within each lamina, failure occurs due to tensile strain transverse to the direction of loading. Failures within individual lamina interact with each other via interlaminar failure and the gross appearance of failure appears as shear. Spreading failure is shown in Figure 4.4 and 4.5. Spreading failure is localised to one or both of the specimen ends in contact with the loading platens. As with the macroscopic shear failure, tensile strain transverse to the loading direction causes failure within a lamina. In spreading failure, the delamination grows from the failure location directly to the lateral surface of the specimen, rather than interacting with an adjacent lamina. This allows the entire fragment above the delamination to slide transverse to the loading direction, giving the specimen a spread appearance.

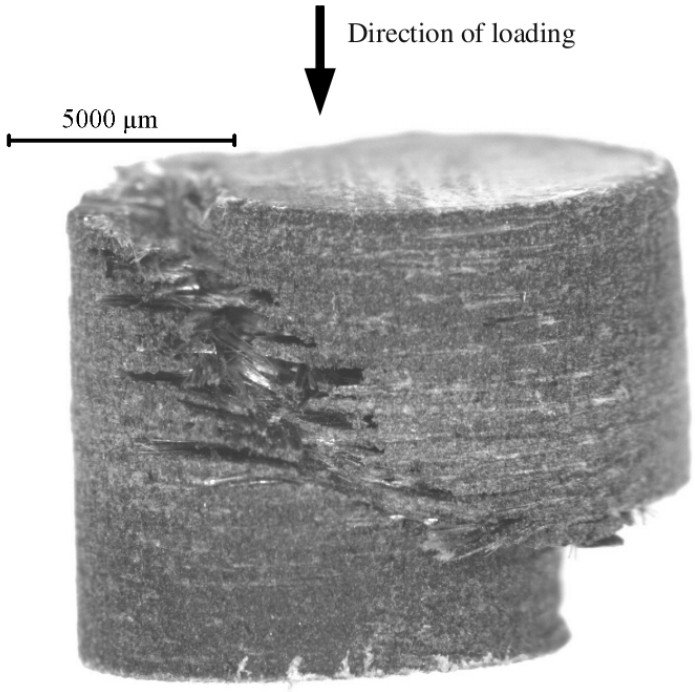

Figure 4.2: Photograph of failed GFPP specimen following through thickness compression, showing macroscopic shear

Hence failure in through thickness compression of GFPP appears to be initiated by ply failure due to transverse tensile strain. The gross specimen appearance is determined by whether the delamination growing from the ply failure reaches the specimen surface or another ply failure first.

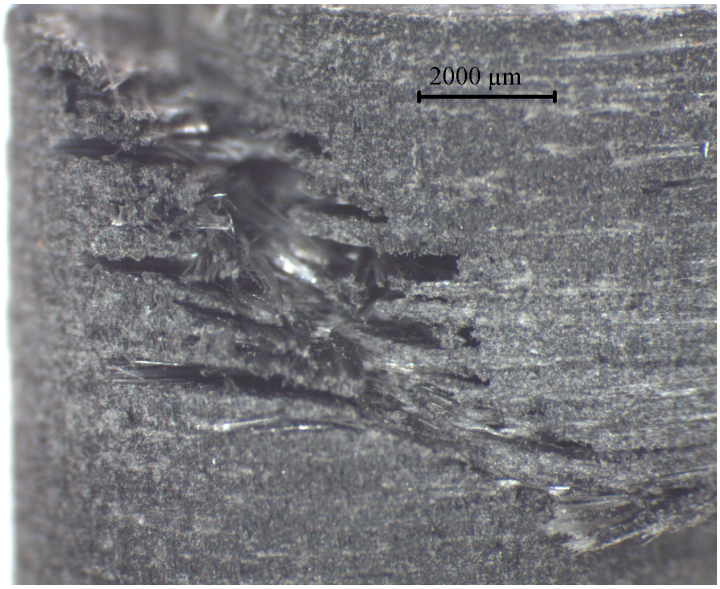

Figure 4.3: Magnified view of photographed failure region of specimen with macroscopic shear

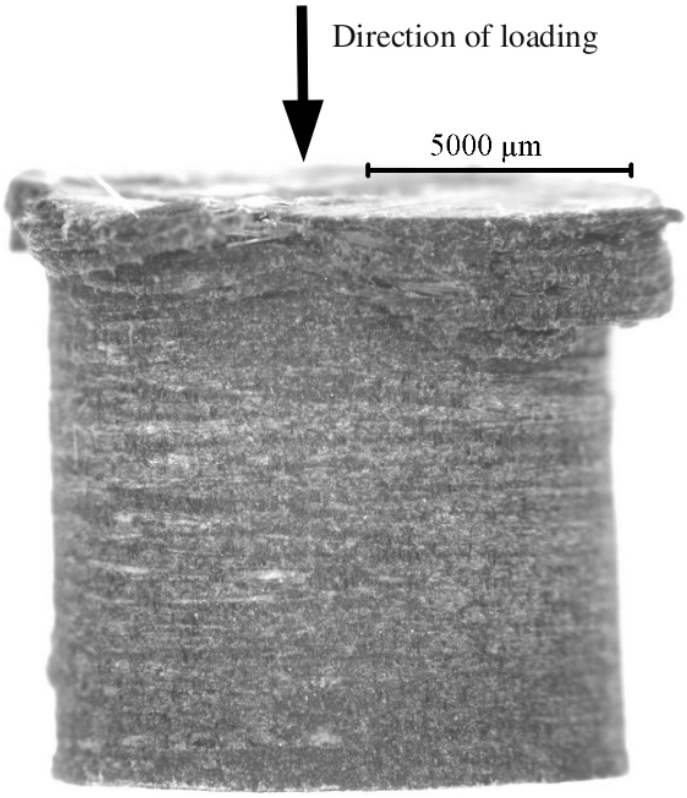

Figure 4.4: Photograph of failed GFPP specimen following through-thickness compression, showing spreading failure (side view)

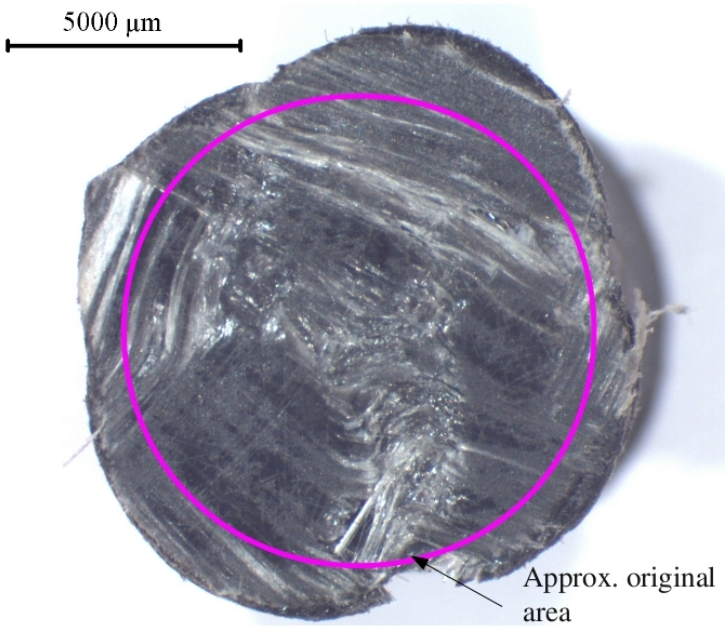

Figure 4.5: Photograph of GFPP specimen with spreading failure (top view)

4.2.2 In-Plane Direction

The force-displacement results for compression of GFPP in the in-plane direction, at cross head speeds of 0.1, 1 and 10 mm/min are shown in Figure 4.6 to 4.8 respectively. For all three rates, a significant "toe-in" region was apparent at the start of compression. The force-displacement curves presented have been been shifted such that a linear fit of the data will pass through the origin. Hence the actual force intercepts the y-axis at approximately 1 kN. A common feature of tests conducted at 0.1 and 1 mm/min is the presence of minor drops in force before the peak force, which is followed by an abrupt drop. The minor force drops occur at displacements of approximately 0.3 mm, with the local peak ranging from 48% to 74% of the overall peak force. The tests conducted at 10 mm/min do not have the same drop in force visible at the slower rates, but do show a definite non-linearity at displacements between 0.3 and 0.35 mm.

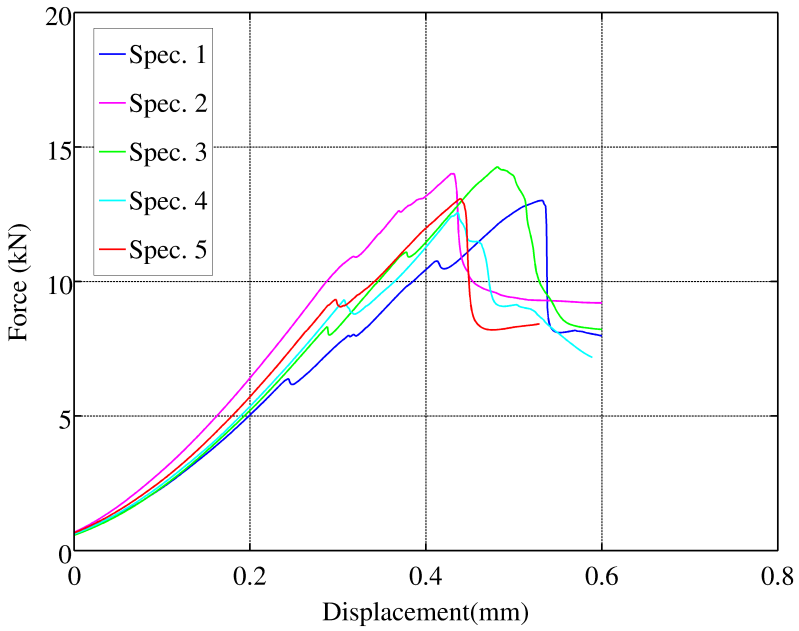

Figure 4.6: Plot of force-displacement response of in-plane compression of GFPP at 0.1 mm/min

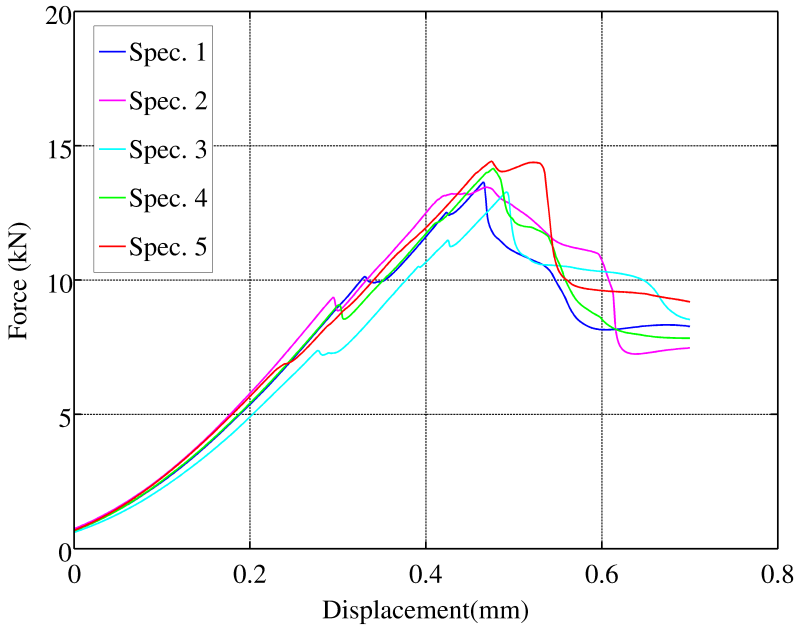

Figure 4.7: Plot of force-displacement response of in-plane compression of GFPP at 1 mm/min

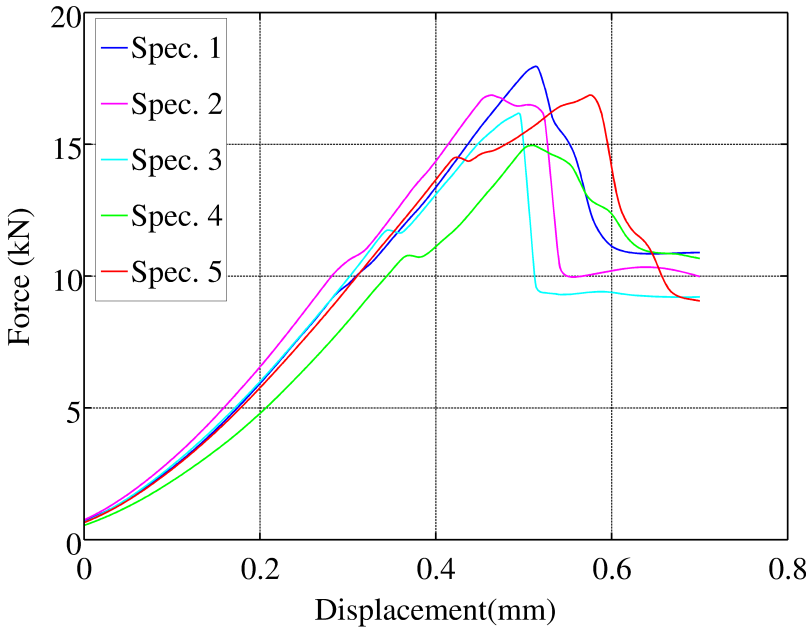

Figure 4.8: Plot of force-displacement response of in-plane compression of GFPP at 10 mm/min

At the slower rates, brooming of the loaded specimen surfaces was observed (Figure 4.9), which is the likely cause of the minor force drops. The abrupt failure following peak load was associated with relatively large delaminations becoming visible. Inspection of specimens after the tests revealed kink bands, shown in Figure 4.10. The tests conducted at 10 mm/min had durations slightly less than 4 seconds, rendering visual observation of failure modes during tests impractical. However, post-mortem inspection of specimens tested at 10 mm/min showed the presence of brooming, kink bands and delaminations.

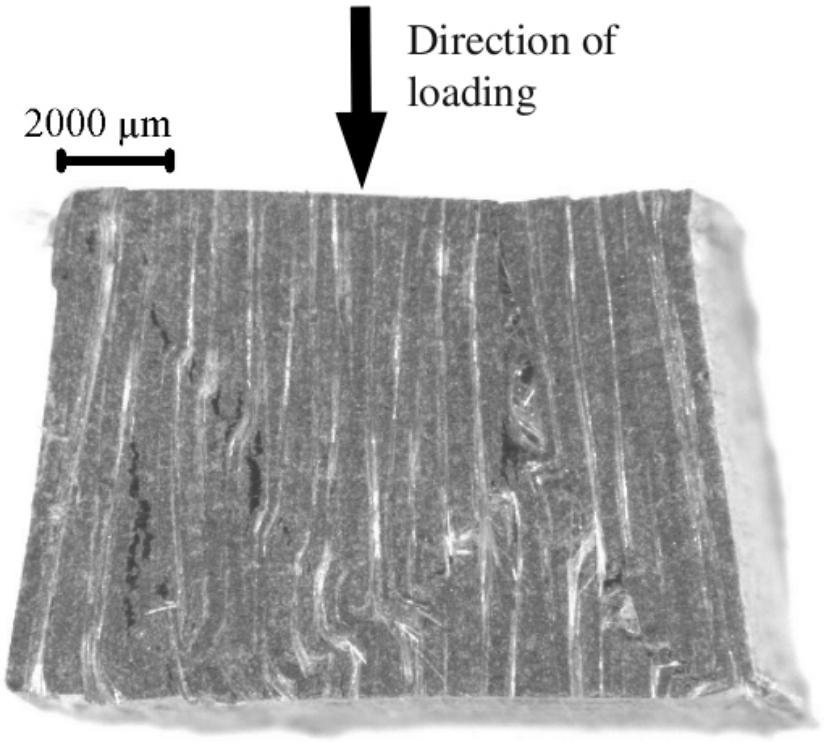

Figure 4.9: Photograph of typical GFPP specimen after in-plane compression

The failure modes noted during the in-plane compression tests are all very localised failures, and specimen deformation is not uniform across the length. In order to calculate true stresses and strains, one must either have instantaneous specimen area and gauge length from full field deformation measurements of the specimen, or be able to assume that the specimen deforms uniformly and maintains a constant volume. As full field measurements were not available and the specimen deformation became non-uniform prior to gross failure, the accuracy of true stress and strain calculations would be questionable. Hence for the in-plane compression tests, the strength data presented is in terms of engineering stress and strain, based on the original specimen dimensions.

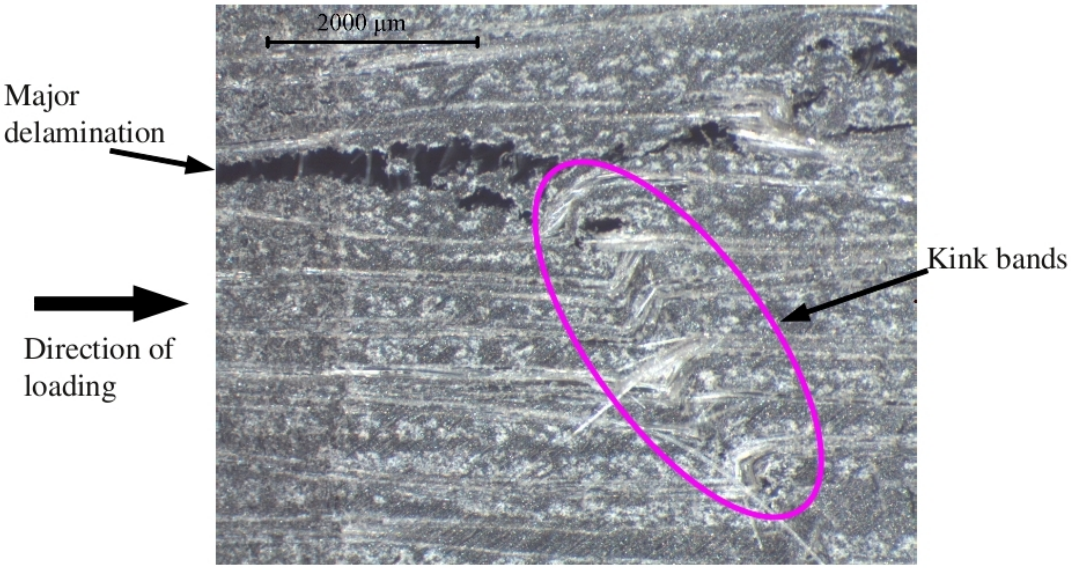

Figure 4.10: Magnified photograph showing kink bands and delamination of GFPP specimen after in-plane compression

4.3 High Strain Rate Compression Testing Using the Split Hopkinson Pressure Bar

4.3.1 Theory of the SHPB

A comprehensive description of SHPB testing, including the derivation of the data processing equations, is presented by Gray [165]. The equations presented in this section are a summary of the derivation presented by Gray [165].

A typical example of the strain gauge signals from a compressive test on cast iron is shown in Figure 4.11. The amplified voltages captured from the strain gauge bridges are converted to strains by multiplying by the appropriate calibration factor. The signal from the input bar is split into the incident strain wave $\varepsilon_i(t)$ and the reflected strain wave $\varepsilon_r(t)$. The transmitted strain wave $\varepsilon_t(t)$ is contained in the output bar signal.

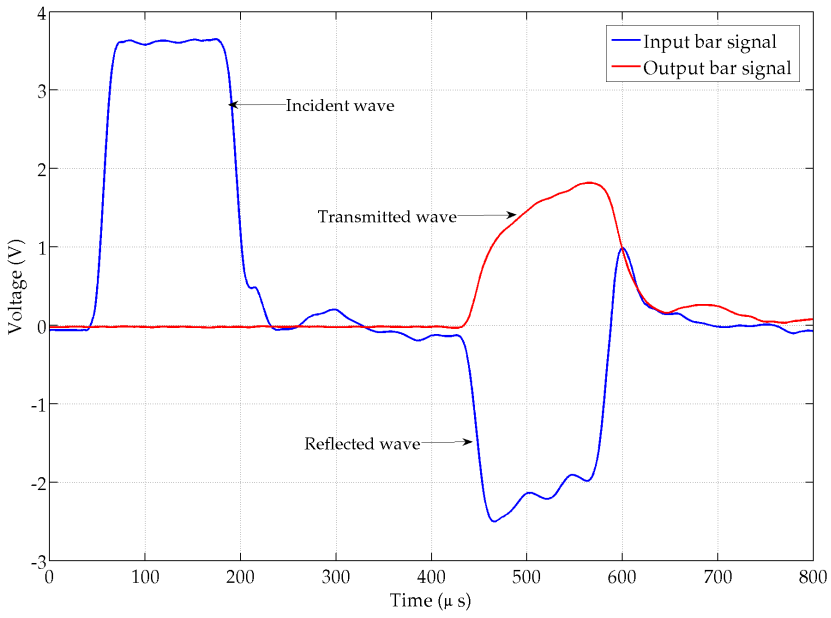

Figure 4.11: Typical strain gauge signals for a SHPB test (of cast iron)

The strain waves are then shifted from the location of the strain gauges, to the respective bar-specimen interfaces. If the radius of the HPB is small in comparison to the wavelength of the loading pulse, one dimensional wave propagation may be assumed. This means that the wave does not change shape as it propagates axially in the bar. Hence the axial shift from gauge to interface is achieved by a straight shift in time based on the propagation distance and the fundamental wave velocity C_o of the

bar material. C_o is given by:

$$C_o = \sqrt{\frac{E_{bar}}{\rho_{bar}}} \tag{4.6}$$

However, the assumption of one dimensional wave propagation is not completely true. Pochammer [166] and Chree [167] arrived independently at the solution for a sinusoidal disturbance travelling in a cylinder of finite radius. This predicted that the propagation velocity of a sinusoid (phase velocity C_p) depended on its wavelength Λ. A real pulse of the type excited in a SHPB test consists of many sinusoidal oscillations of differing wavelengths. As the wave propagates, the individual sinusoidal components will shift slightly relative to each other due to the different phase velocities, which is known as dispersion. This manifests in a change in shape of the wave. This behaviour of the waves in HPB was noted as early as 1948 by Davies [128] and confirmed by later researchers [168, 169]. A method to correct for dispersion was proposed independently by Gorham [170] and Follansbee and Frantz [171].

A wave is transferrred from the time domain to the frequency domain via the Fourier transform:

$$\boldsymbol{\varepsilon(\omega)} = \int_{\infty}^{\infty} \varepsilon(t) e^{-j\omega t} dt \tag{4.7}$$

Where $\varepsilon(t)$ is any function in the time domain, and $\boldsymbol{\varepsilon(\omega)}$ is a complex function in the frequency domain.

The propagation of the wave along the bar is modelled as a time shift of the function describing the wave at a known location $\varepsilon(t)$. Thus the wave at the interface $\varepsilon^i(t)$ is related to the wave at the strain gauge station $\varepsilon^g(t)$ by:

$$\varepsilon^i(t) = \varepsilon^g(t + \delta t) \tag{4.8}$$

A time shift $\varepsilon(t + \delta t)$ in the time domain is achieved by a phase shift in the frequency domain:

$$\varepsilon(t + \delta t) \leftrightarrow \boldsymbol{\varepsilon(\omega)} e^{i\omega\delta t} \tag{4.9}$$

For a wave propagating down a bar, the time shift δt depends on the propagation distance z and the phase velocity C_p. Hence the wave shifted from the gauge station ε^g by a known propagation distance z to the interface (ε^i) is given in the frequency domain by :

$$\boldsymbol{\varepsilon^i(\omega)} = \boldsymbol{\varepsilon^g(\omega)} e^{i\omega \frac{Z}{C_p(\omega)}} \tag{4.10}$$

The phase velocity C_p - angular frequency ω relationship is determined from the Pochammer-Chree equations. The Pochammer-Chree equations do not give $C_p(\omega)$ directly and must be solved numerically, which is described in detail in [172]. An example of the $C_p(\omega)$ relationship, for a steel bar of 20 mm diameter, is given graphically in Figure 4.12. The fundamental wave velocity C_o is given by C_p at $\omega = 0$. It should be noted that the shape of $C_p(\omega)$ does not depend on C_o and is solved in dimensionless form, which is multiplied by C_o to give the result shown.

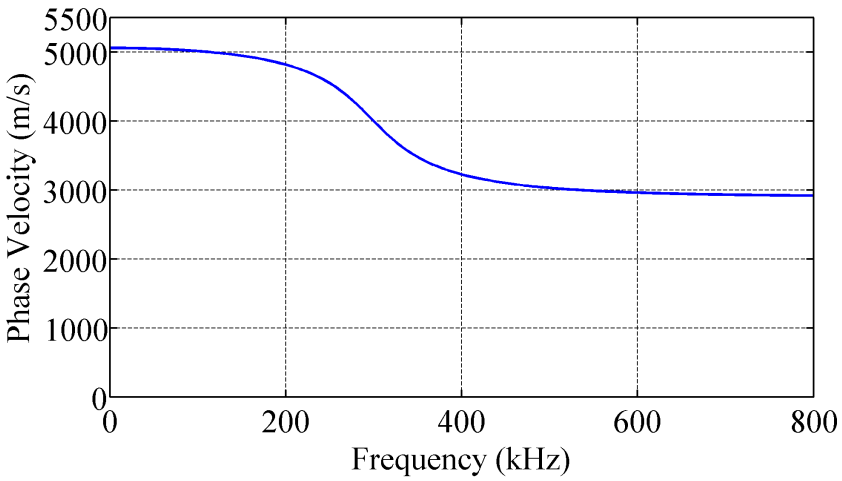

Figure 4.12: Plot of $C_p(\omega)$ relationship determined numerically from Pochamme-Chree equations for a steel bar of 20mm diameter

This correction for geometric dispersion only implements a phase shift which varies with frequency to the frequency components of the wave. As the relationship is derived from linear elastic constitutive law, no dissipation of energy is involved and hence the magnitude of the frequency components is left unchanged. In a polymeric HPB which was used for the impact bend HPB arrangement, the wave propagation is affected by the viso-elastic behaviour of the polymer and experiences both dispersion and attenuation. Visco-elastic wave propagation is discussed in more detail in §5.2.3.3 and Appendix B. The shifted wave is returned to the time domain by the inverse Fourier transform :

$$\varepsilon^i(t) = \int_{\infty}^{\infty} \boldsymbol{\varepsilon^i(\omega)} e^{-j\omega t} dt \tag{4.11}$$

The application of dispersion corrected shifting to the raw signals shown in Figure 4.11 is shown in Figure 4.13.

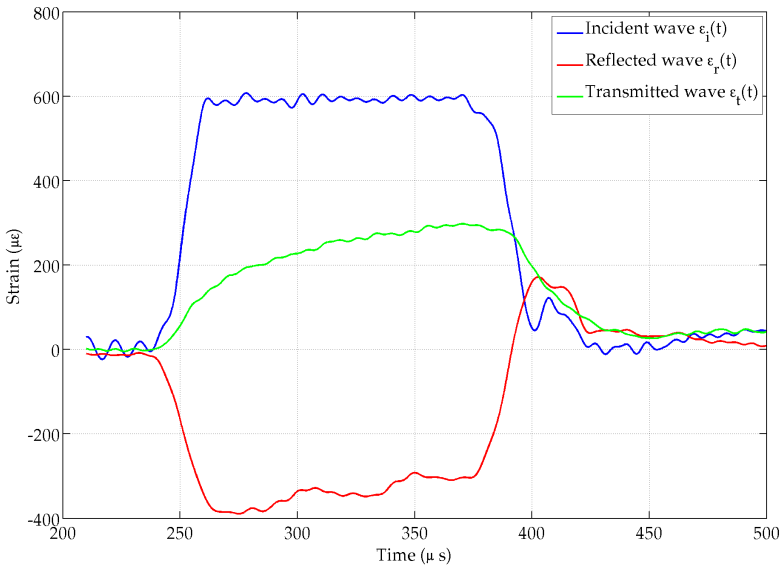

Figure 4.13: Plot of strain waves shifted to bar-specimen interfaces

The force and velocity at the interface of the specimen and input bar are given by:

$$P_{in}(t) = A_{bar}E_{bar}(\varepsilon_i^i(t) + \varepsilon_r^i(t)) \tag{4.12}$$

$$v_{in}(t) = C_o(\varepsilon_i^i(t) - \varepsilon_r^i(t)) \tag{4.13}$$

The corresponding force and velocity at the interface of specimen and output bar are given by:

$$P_{out}(t) = A_{bar}E_{bar}(\varepsilon_t^i(t)) \tag{4.14}$$

$$v_{out}(t) = C_o(\varepsilon_t^i(t)) \tag{4.15}$$

The above relations are dependent on certain conditions, *inter alia*

- The incident and reflected waves must not overlap. If there is wave overlap, then techniques using multiple strain gauge stations are required to separate the signal into incident and reflected waves.

- The magnitude of the stress in the bar does not exceed the elastic limit of the bar material. The calculation of the forces and velocities at the bar ends are based on linearly elastic material behaviour, and any plastic deformation of the bars renders these calculations inaccurate.

- Any radial non-uniformity of the wave has diminished sufficiently by the time the wave reaches the strain gauge station so that the wave can be treated as radially uniform.

- The friction between bar and specimen is sufficiently small such that friction does not constrain the specimen radially.

- The specimen mass is sufficiently small such that the forces required to accelerate the specimen are small in comparison to the forces required to deform the specimen.

It should be noted that the Equations 4.12-4.14 give the forces and velocities *at the interfaces*. Stresses and strains in the specimen are calculated by assuming that the specimen experiences uniform stress and strain. Given a cylindrical specimen of initial area A_o and length l_o, the instantaneous specimen length $l_s(t)$ is given by:

$$l_s(t) = l_o - C_o \int_0^t [\varepsilon_t(\tau) + \varepsilon_t(\tau) - \varepsilon_i(\tau)]d\tau \tag{4.16}$$

The instantaneous true strain is found from the standard relationship:

$$\varepsilon_{spec}(t) = ln(\frac{l_s(t)}{l_o}) \tag{4.17}$$

The average strain rate of the specimen is:

$$\dot{\varepsilon}_{spec}(t) = \frac{C_o}{l_s(t)}[\varepsilon_t(t) + \varepsilon_r(t) - \varepsilon_i(t)] \tag{4.18}$$

If the volume of the specimen is assumed to remain constant, the instantaneous area $A(t)$ is calculated from Eq. 4.3. The stresses at the input and output interfaces are then given by:

$$\sigma_{In}(t) = \frac{A_{bar}E_{bar}}{A(t)}[\varepsilon_i(t) + \varepsilon_r(t)] \tag{4.19}$$

$$\sigma_{Out}(t) = \frac{A_{bar}E_{bar}}{A(t)}\varepsilon_t(t) \tag{4.20}$$

Due to the stress wave propagation within the bars and specimen during a SHPB test, the stresses at the loaded faces of the specimen are not always in equilibrium. However, after a few reflections of waves within the specimen, the input and output face stresses vary by a neglible amount. The results of a compressive or tensile SHPB test

can only be considered valid once the input and output face stresses have reached this state of "quasi-equilibrium".

4.3.2 SHPB Mechanical Details

The SHPB at BISRU is mounted on a 9m long steel I-beam, of depth 300 mm, width 100 mm and web thickness 8 mm. Loading is achieved via strikers propelled from a Nitrogen charged gas gun. The gas gun has a maximum breech pressure of 20 bar, and can accommodate barrels ranging from 10 mm to 50 mm bore diameter. Both the input and output bars for the compression experiments were 20 mm diameter centreless ground silver steel, which has a yield stress in excess of 600 MPa. These bars were selected based on previous experience of testing a Glass Fibre - Vinyl Ester FRP [173]. FRPs may have a relatively low modulus in comparison to metals, but the failure stresses are not low: GFPP has a quasi-static through thickness compressive failure strength ranging from 240 to 270 MPa - see §4.2.1. The input bar should be of sufficient diameter and strength to sustain the input pulse necessary to fail the specimen, without becoming plastic itself. The outptut bar is sized such that the transmitted stress wave is of a magnitude that may be recorded by the data acquisition equipment without increasing uncertainty, again without approaching plasticity in the bar. Based on the range of strengths determined from quasi-static tests, the transmitted stress waves expected from this bar set up would have maxmima in the region of 50 to 100 MPa, which is acceptable.

The input bar has a total length of 1990 mm. The output bar is marginally shorter, at 1950 mm, which is a deliberate decision in order to prevent repetitive loading of the specimen. In compressive SHPB testing with metallic HPB, the stress waves persist in the bars for a relatively long time after the first loading of the specimen. If contact is maintained between the specimen and both bars after the first loading, the specimen will be loaded repeatedly by the waves reflecting within the bars. This can introduce uncertainty as to whether the specimen failed during the first loading, or during the later loading cycles. If the output bar is shorter than the input bar, then the tensile reflected wave in the output bar arrives at the bar-specimen interface before the second wave in the input bar (which is compressive). As the bar-specimen interface cannot sustain any tension, the tensile wave in the output bar separates the output bar from the specimen. Hence when the second compressive wave from the input bar arrives at the specimen, there is no output bar to provide resistance for the compression. As the distal surface of the specimen is free, the second compressive loading wave reflects as tension and separates the specimen from the input bar. Hence the specimen can

no longer be loaded by either input or output bars. If the input bar is longer than the ouput bar, the second compression wave in the input bar arrives at the specimen while the specimen is still in contact with both bars, and repetitive loading ensues, which is undesirable.

4.3.3 Striker and Pulse Shaping Details

For the vast majority of SHPB experiments, the striker is simply a cylindrical bar of similar material to the HPB itself. Loading the HPB with a cylindrical striker produces an approximately trapezoidal incident stress wave, as seen in Figure 4.11. However, this is not always desirable. A desirable feature of a SHPB experiment is an approximately constant strain rate. Once the initial "ring-up" of the specimen has ocurred, and the forces on the input and output faces of the specimen are approximately equal, it may be shown that the specimen strain rate $\dot{\varepsilon}(t)$ is proportional to the magnitude of the reflected wave in the incident bar $\varepsilon_r(t)$:

$$\dot{\varepsilon}(t) = \frac{-2C_o}{l_o}\varepsilon_r(t) \tag{4.21}$$

An approximately constant strain rate would manifest in the raw strain gauge signals as a trapezoidal reflected wave. This is *not* a feature of published data of FRP tests with the SHPB. For example Tarfaoui [174] or Gillespie *et al* [138]) report tests where strain rates may drop from a peak of approximately $1000s^{-1}$ to approximately $300s^{-1}$ during a single test. Frew and colleagues [144, 143] and Vecchio and Jiang [175] noted that a non-trapezoidal incident wave is necessary to achieve an approximately constant strain rate for any materials which do not exhibit close to perfectly plastic behaviour. This may be explained by fact that once force equilibrium on the specimen faces has been reached :

$$\varepsilon_i(t) + \varepsilon_r(t) = \varepsilon_t(t) \tag{4.22}$$

The shape of the transmitted wave $\varepsilon_t(t)$ is determined by the specimen response:

- For a perfectly plastic material, $\varepsilon_t(t)$ will initially rise then maintain a plateau proportional to the specimen flow stress.
- For materials which exhibit strong work hardening or linear brittle behaviour, $\varepsilon_t(t)$ will continue to rise until the material fails.

Thus if a trapezoidal $\varepsilon_r(t)$, indicating a constant strain rate, is desired, a non-trapezoidal $\varepsilon_i(t)$ wave is required for work hardening or brittle materials. Frew *et al* [143, 144], Song

et al [9] and Vecchio [175] achieved the shaping of the incident pulse by using sacrificial elements between a cylindrical striker and the input bar. As these pulse shaping elements deformed plastically, each test required a new pulse shaper, which increases experimental cost. However, Kumar et al [145] proposed changing the shape of the incident by using strikers of non-cylindrical profile. Importantly, the striker remained elastic during impact with the input bar, allowing it to be reused. Pulse shaping via elastic impact has the added benefit that the magnitude of the incident wave scales linearly with striker velocity, giving some flexibility. If pulse shaping is achieved via deformable sacrificial elements, the magnitude of the incident wave does not scale significantly with striker velocity. If a different magnitude of incident wave is desired, the geometry and potentially material of the sacrificial element must be revised. The repeatability of incident waves pulse shaped with sacrificial elements depends on the consistency of material properties and dimensional tolerances of the sacrificial elements. The repeatability of incident waves using a profiled elastic striker depends on the repeatability of the striker velocity, with the wave shape remaining constant.

The author has collaborated with colleagues at BISRU (Mr T.J. Cloete and Dr A. Bekker (*nee* van der Westhuizen)), on the use of conical or tapered strikers for achieving nominally constant strain rates on testing of quasi-brittle, rate dependent materials. The author's work has focussed on FRP [173], while Cloete and Bekker [146] utilised the technique for characterising bovine cortical bone.

A variety of linearly tapered strikers were used during testing, depending on the specimen orientation being tested. The strikers were all machined from the same grade of silver steel as the HPB in use. A straight cylindrical striker and typical tapered striker are shown in Figure 4.14. The different striker geometries are presented in Table 4.1. In addition to shaping the incident wave using different striker profiles, the incident wave was smoothed by use of a small quantity of a pliable, putty like adhesive on the face of the input bar impacted by the striker. The deformation of the putty increases the rise time of the wave, which reduces the effect of Pochammer-Chree oscillations.

4.3.4 Electronics and Data Acquisition

The HPB were instrumented with two diametrically opposed strain gauges, with a resistance of 120Ω and 2 mm gauge length. The Wheatstone bridge was completed with two dummy gauges, mounted on a panel of the same material as the HPB, which eliminates any thermal affects. The Wheatstone bridge was typically energised with a

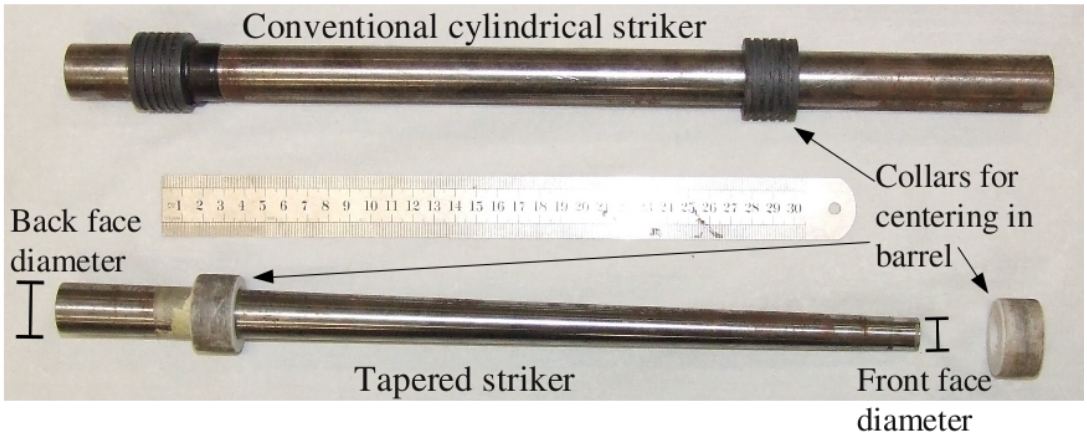

Figure 4.14: Photograph of straight and tapered strikers

Table 4.1: Tapered Striker Geometries

Striker	Front face diameter (mm)	Rear face diameter	Length (mm)
1	18	24	400
2	20	36	400
3	25	36	450

voltage of 4 V, from a DC power supply which fed the current via decoupling capacitors to eliminate any high frequency oscillation. The output of the bridge was balanced before each test. The output voltage of the bridge was amplified via custom amplifiers based on the TI INA110KP amplifier chip, with zero gain drop off to 100 kHz, and gain drop off characterised to 800 kHz. The gain of the amplifiers was set to 1000 for all SHPB tests. The amplified strain signals were captured using an ADLINK^{TM}PCI9826H DAQ card. The signals were recorded at a sampling frequency of 10 MHz, at 16 bit resolution on a $\pm$ 5 V scale. The velocity of the striker was measured using a light trap, consisting of two pairs of infrared LEDs and matched photodiodes monitored on an oscilloscope. The paired LEDs and diodes were separated by 39.7mm.

4.3.5 Specimen Geometry

The through thickness tests were conducted on cylindrical specimens, of nominal diameter 11 mm cut from a 12 mm thick panel. The in-plane tests used square section specimens with a side length of 11 mm, and 12 mm thickness. All specimens were

cut from panels using abrasive water jet cutting. The specimen faces which were in contact with the bars were polished using 220 and 500 grit SiC polishing paper. The faces of the bars and specimens were lubricated with molybdenum grease to minimise frictional effects. At least six specimens were tested for each series of HPB experiments.

4.3.6 Calibration

Calibration of a HPB consists of determining certain material parameters as well as the appropriate conversion factors to transform the voltage measured at the strain gauge station into strain or stress.

The accuracy with which C_o and ρ is determined strongly influences the accuracy of the force and velocity measurements of a HPB experiment. The measured density of the silver steel bars is 7850 $kg.m^{-3}$. C_o was determined experimentally by impacting a single HPB, with no specimen in place, and capturing the incident and reflected waves at the gauge station. As the non-impacted face of the HPB is free, the force at this face must be zero at all times. The procedure followed was that recommended by Marais [176] and Lifshitz and Leber [177]. The signals captured at the strain gauge station $\varepsilon_i^g(t)$ and reflected $\varepsilon_r^g(t)$ are shifted to the free end of the bar by the dispersion correction method described earlier.

Having shifted the incident and reflected waves from the gauge station to the free end of the bar, the two are multiplied by the elastic modulus and summed to give the nett stress acting on the free end. The free end of the bar should experience zero stress at all times. C_o was obtained by iteratively shifting the incident and reflected waves to minimise the resultant stress at the free end of the bar. This value of C_o, in conjunction with the measured density of the bars, was used to calculate the Elastic modulus of the bar E_y from Equation 4.6. Errors in wave speed of less than 1 % can manifest as spurious stresses at the free end with magnitudes up to 20 % of the peak stress of the incident wave. A typical signal from a steel input bar is shown in Figure 4.15, with the incident and reflected waves shifted to the free surface. The waves are still expressed as voltages, which are multiplied by an appropriate conversion factor to obtain stress.

HPB subjected to stresses in the linear stress-strain range, and the relationship between HPB strain and the strain gauge bridge output voltage V_{out} is also linear. Hence there is a linear relationship between HPB stress $\sigma(t)$ and the ratio of ouput bridge excitation voltages $\frac{V_{out}}{V_{BR}}$:

$$\sigma(t) = \kappa_{cal} \frac{V_{Out}}{V_{BR}} \tag{4.23}$$

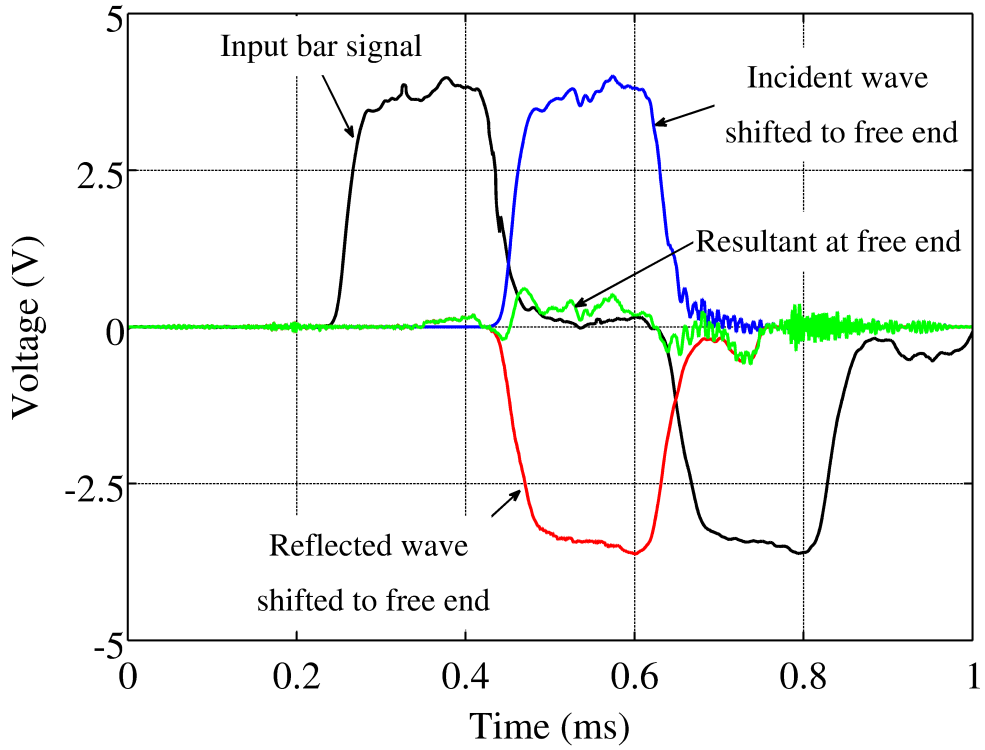

Figure 4.15: Plot of input bar waves, shifted to free end for wave speed measurement

The conversion factor κ_{cal} is determined experimentally, from impact of a HPB and a striker of the same material and diameter. This results in an approximately trapezoidal stress wave, where the amplitude of the wave is related to striker velocity v_s by:

$$\sigma_{Th} = \rho C_o \frac{v_s}{2} \tag{4.24}$$

In practice, the stress wave will be approximately trapezoidal, with the rise times dependent on the accuracy of alignment of HPB and striker faces, as well as the smoothness of these faces. If the rise time of the stress wave is very short, or the propagation distance is very long, oscillations may become visible due to Pochammer-Chree dispersion effects. Pulse smoothing, by means of a soft deformable element between the striker and input bar substantially reduces the effect of dispersion. The striker used for calibration is cut from the same stock as the input bar to ensure matched impedance, and is relatively long (500 mm) to ensure that the plateau of the stress wave is well defined. The captured incident wave is shifted from the strain gauge station, back to the bar face impacted by the striker. The conversion factor κ_{cal} is adjusted until the plateau of the wave matches the stress level σ_{Th} calculated from the measured striker

velocity. Figure 4.16 shows the typical trapezoidal incident wave, multiplied by κ_{cal} to match the plateau stress to σ_{Th}.

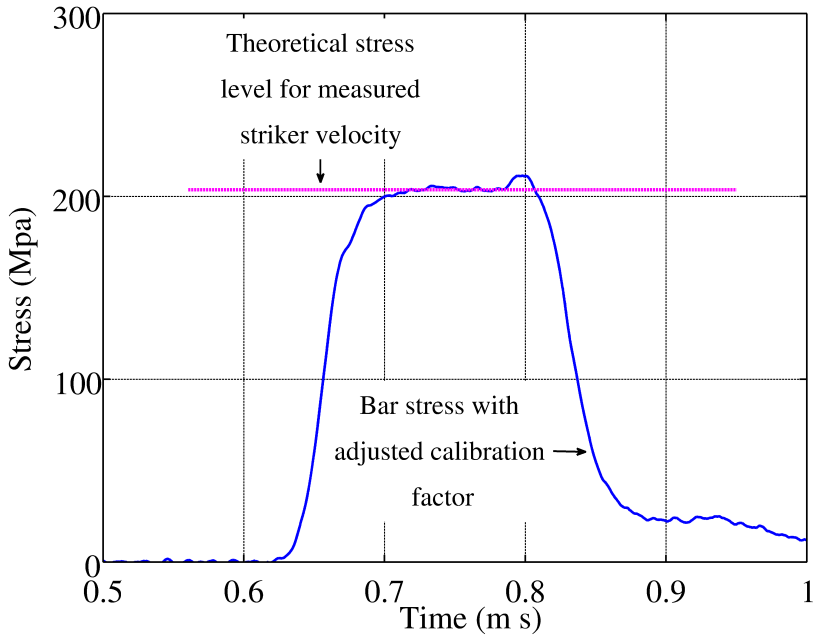

Figure 4.16: Plot of incident wave from calibration test, adjusted to match σ_{Th}

The input and output bars were calibrated independently. The calibration was conducted at $V_{Br} = 4.01\,V$, with V_S ranging from 7 to 11 m/s. The parameters, averaged over the 6 tests, are shown in Table 4.2. The difference in C_o for the input and output bars is less than 0.4 %, which is negligible. The difference in κ_{cal} is fractionally more than 1 %. This difference is most likely due to the strain gauge stations on the input and output bars have slightly different alignment relative to the bar axis, and hence producing small differences in output voltages.

Table 4.2: Steel SHPB Bar Parameters

Parameter	**Input Bar**	**Output Bar**
Wave Speed $C_o(m/s)$	5120	5100
Elastic Modulus $E_y(GPa)$	205.8	204.2
$\kappa_{cal}(MPa)$	192.24	194.16

4.4 Direct Impact HPB Testing

Direct Impact HPB (DIHPB) testing dispenses with the input bar, and compresses the specimen directly between the striker and a single HPB, illustrated in Figure 4.17. The DIHPB was proposed by Gorham *et al* [178, 179] as a means of testing very high strength metals, at rates higher than permitted with a SHPB arrangement.

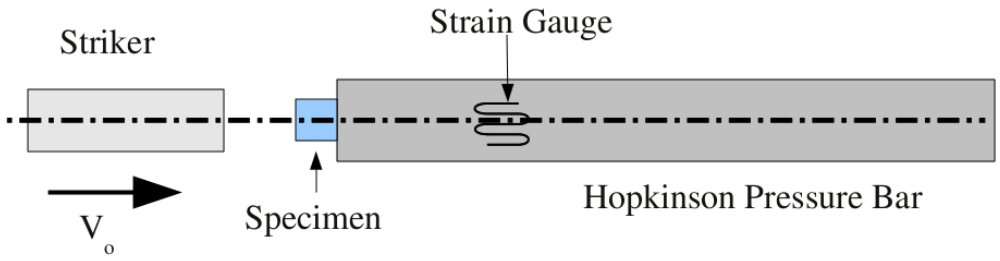

Figure 4.17: Schematic of Direct Impact HPB

As no input HPB is used, the instantaneous specimen length is calculated based on the instantaneous velocities of the HPB face and the striker. The velocity of the HPB face is readily obtained via Eq. 4.14. The transmitted strain in the HPB $\varepsilon_t(t)$ is measured, along with the the striker initial velocity v_s. The instantaneous striker velocity is calculated assuming the force exerted by the specimen on the striker is equal to the force exerted by the specimen on the HPB i.e. specimen equilibrium is assumed.

Assuming that the striker and HPB have the same area and material properties, the instantaneous specimen length $l_s(t)$ is :

$$l_s(t) = l_o - v_s t + \int_0^t \frac{2E_y}{C_o \rho} \varepsilon_t(\tau) d\tau \tag{4.25}$$

As with a conventional SHPB, the specimen is assumed to deform uniformly and with constant volume. Hence the instantaneous specimen area is calculated using Eq. 4.3. Thus specimen true stress is calculated via:

$$\sigma_s(t) = \frac{A_{bar} E_y}{A_s(t)} \varepsilon_t(t) \tag{4.26}$$

True stress-strain results calculated from the above are very sensitive to the initial striker velocity V_o. As the specimen length, and hence strain, are a function of instantaneous striker velocity, which changes during the test, it is not possible to maintain a

constant specimen strain rate during a DIHPB test. The nominal specimen strain rate quoted for the DIHPB tests is given by :

$$\dot{\varepsilon}_s(t) = \frac{V_o}{L_o} \tag{4.27}$$

The DIHPB arrangement used the input bar described in §4.3.6. The specimen dimensions were identical to those used for the quasi-static and SHPB compression tests.

4.5 High Rate Testing Results

4.5.1 SHPB Through-Thickness Results

During processing of SHPB results, it is important to check that the specimen has reached dynamic equilibrium. This is achieved by comparing the stresses calculated for the input and output face of the specimen, as seen in Figure 4.18. The stress at the input and output face will never be precisely equal at all times during an experiment. If the difference between the two is small, the test may be considered valid. In order to facilitate equilibration, the specimen dimensions were revised to a nominal diameter of 15 mm and length of 6 mm, and new specimens were cut from the same panel as the original specimens. The increased specimen area reduces the impedance mismatch between the bars and specimen. Reducing the length decreases the wave transit time of the specimen. Both of these improve the likelihood of earlier specimen equilibrium. The resulting reduced variation between the input and output face stresses, may be seen in Figure 4.18. There is a difference at the peak, of less than 4%, which was considered acceptable. An example of a SHPB test on GFPP which did not achieve acceptable equilibrium is shown in Appendix A.1.2. In all tests conducted on GFPP using the SHPB, the peak stress at the input face was slightly higher than at the output face. The specimen strength reported is based on the output face stress, as this is the more conservative measure.

The true stress-true strain curves for the tests with acceptable equilibrium are shown in Figure 4.19. The SHPB results exhibit greater non-linearity than the quasi-static tests. Similar behaviour has been reported by Song *et al* [9] and Gama *et al* [10] for SHPB testing of other GFRP. Typical variation of strain rate as with specimen strain is shown in Figure 4.20. The peak strain rate for the test shown has a maximum of 820 $/s$ and falls to 520 $/s$ at failure. The reported strain rate for each test is taken to be the average strain rate between the peak rate and failure, which for this test is 630 $/s$. This is far

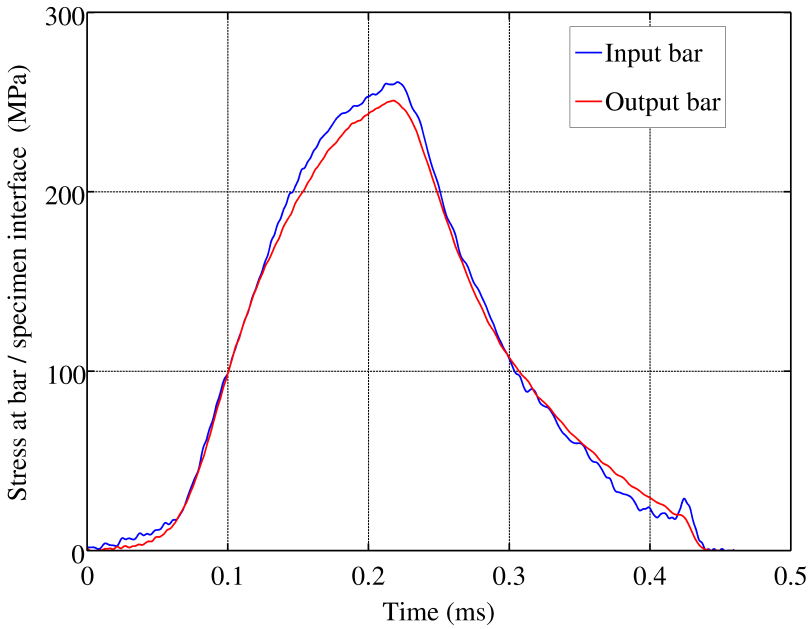

Figure 4.18: Plot of specimen input and output face stresses during SHPB test showing acceptable equilibration

less variation in strain rate for a single test than that reported by Gama *et al* [10] where no pulse shaping was used, where an average rate of 473 $/s$ is reported for test where the rate falls from a peak of approximately 1000 $/s$ to 250 $/s$.

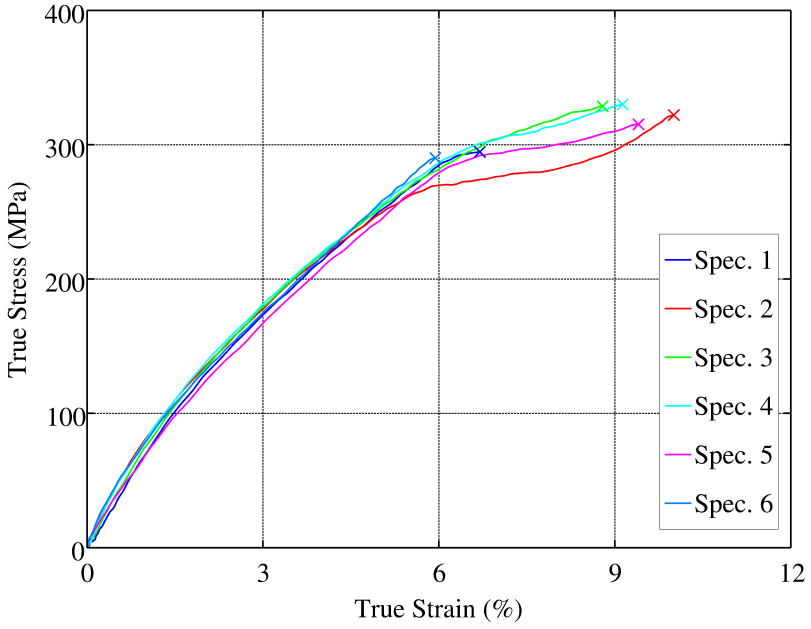

Figure 4.19: Plot of true stress-strain response for SHPB compression testing of GFPP in through thickness direction

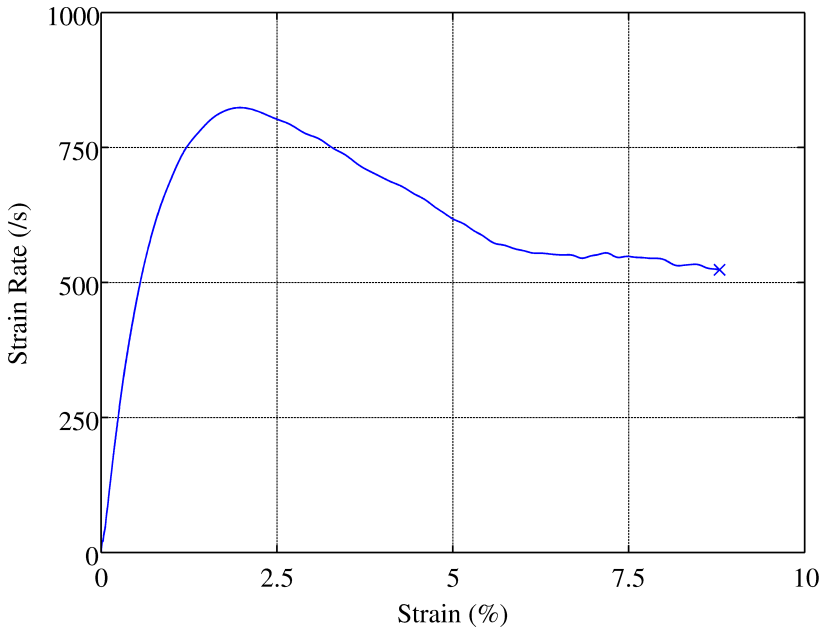

Figure 4.20: Plot of strain rate response for SHPB compression testing of GFPP in through thickness direction

The dominant failure mode was a spreading failure at the loaded surfaces as shown in Figure 4.21 respectively. The majority of spreading failure was observed in the laminae closest to the loaded faces.

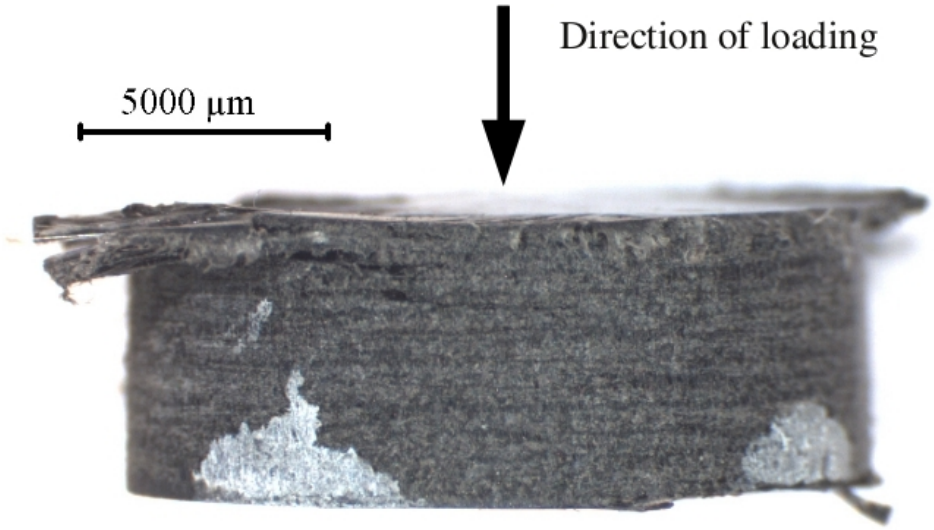

Figure 4.21: Photograph of typical GFPP specimen showing spreading failure after SHPB test

4.5.2 Direct Impact HPB Through-Thickness Results

Typical HPB stress-time data captured from a Direct Impact HPB (DIHPB) test is shown in Figure 4.22(a). The abrupt drop in bar stress after the peak is indicative of gross specimen failure. The striker velocities ranged from 12.5 to 14.9 m/s. Typical true stress-strain results from a DIHPB test are shown in Figure 4.22(b). As with the SHPB results, the response shows some non-linearity and minor oscillations. The stress reported is the peak stress prior to the abrupt drop.

Due to the nature of the DIHPB test, it is unusual to recover a specimen unless the striker velocity is very close to that required to cause failure. As there is no means of arresting the striker, other than the specimen, the specimen is loaded repeatedly (beyond the first pulse shown in Figure 4.22(a)) and is consequently pulverised into small fragments. One specimen, from the test conducted at the lowest striker velocity, was recovered post-test and is shown in Figure 4.23. Spreading failure is clear on both the input and output faces. The degree of damage is greater than observed in the SHPB tests, due to the higher velocities associated with the DIHPB test.

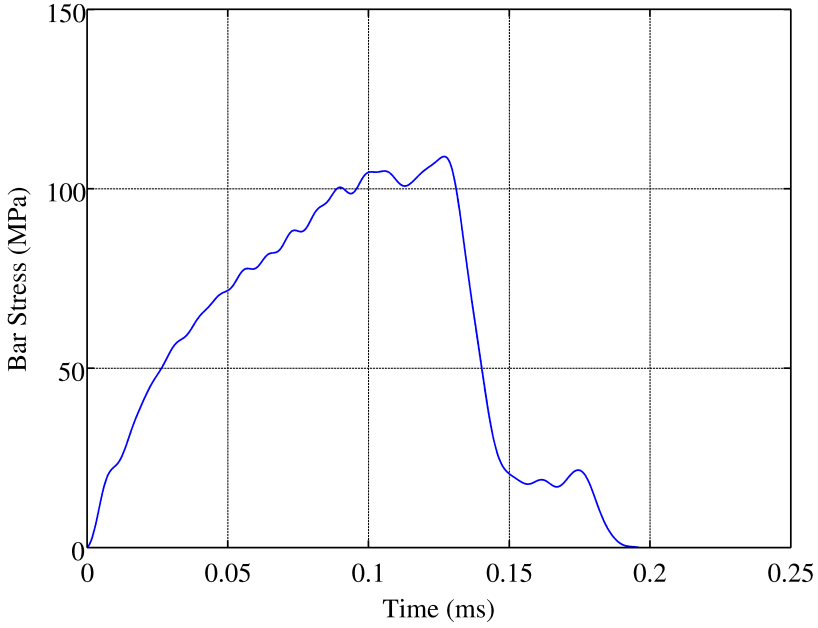

(a) Plot of bar stress

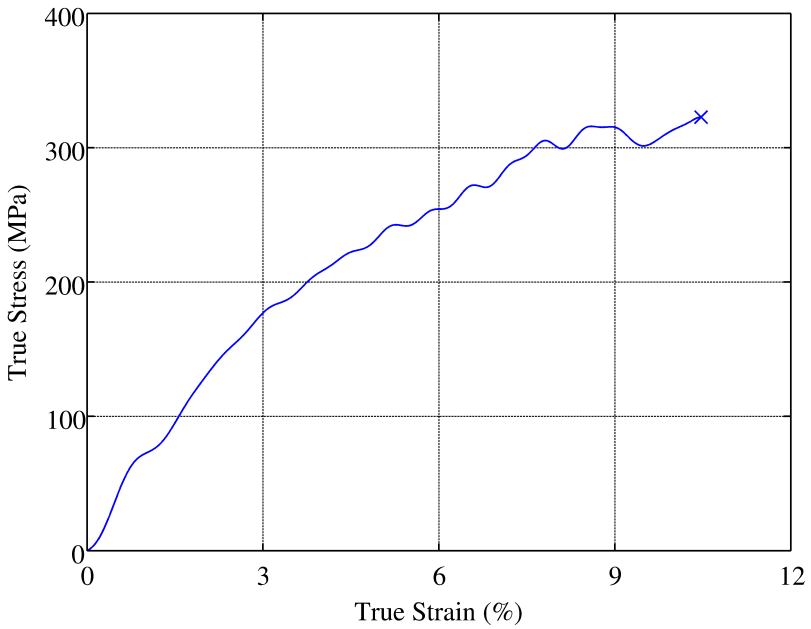

(b) Plot of specimen true stress-strain

Figure 4.22: DIHPB results for through thickness testing of GFPP

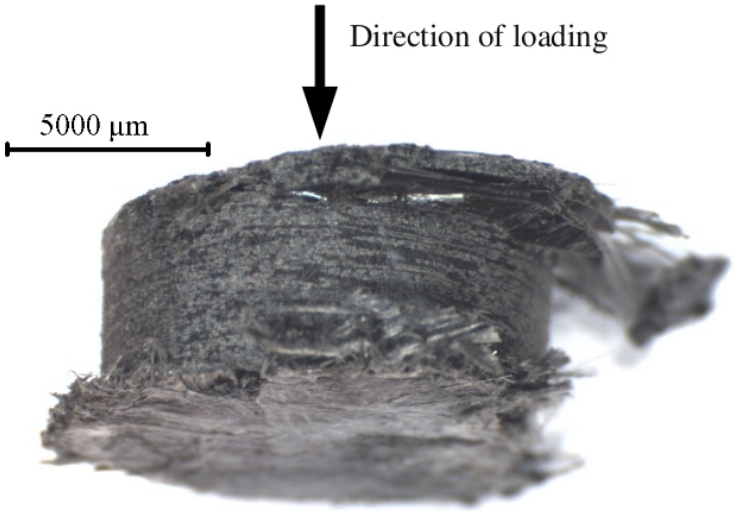

Figure 4.23: Specimen recovered from DIHPB test

4.5.3 Comparison

A summary of true stress at peak load, for the tests conducted at different rates is presented in Table 4.3. The peak stress results across all strain rates tested are plotted in Figure 4.24. With the exception of the direct impact HPB results which showed more scatter than the other tests, the peak stress increases almost linearly with the logarithm of strain rate. The increase in peak stress with increasing strain rate agrees with the results for other GFRP systems, for example [140, 9, 132, 139]. This rate dependence may be modelled with Eq 4.28, adapted from the Johnson-Cook model.

Table 4.3: Summary of through thickness compression results for GFPP

Rate	0.1 mm/min	1 mm/min	10 mm/min	SHPB	DIHPB
Peak True Stress (MPa)	242.2	256.0	271.3	313.8	293.5
Std. Dev. (MPa)	11.9	7.9	18.0	16.7	20.9
C.O.V (%)	4.9%	3.1%	6.6%	5.3%	7.1%
Mean Strain Rate ($/s$)	1.4×10^{-4}	1.4×10^{-3}	1.4×10^{-2}	5.3×10^{2}	1.2×10^{3}

$$\sigma' = \sigma_o(1 + c_1\, ln(\frac{\dot{\varepsilon}}{\dot{\varepsilon}_o})) \tag{4.28}$$

$\dot{\varepsilon}_o$ is a baseline strain rate, chosen here to be unity. σ_o is the corresponding peak stress at this rate. Fitting the above model yields constants of $\sigma_o = 280$ MPa and $c_1 = 0.013$. The fit has a correlation coefficient of $R^2 = 0.89$.

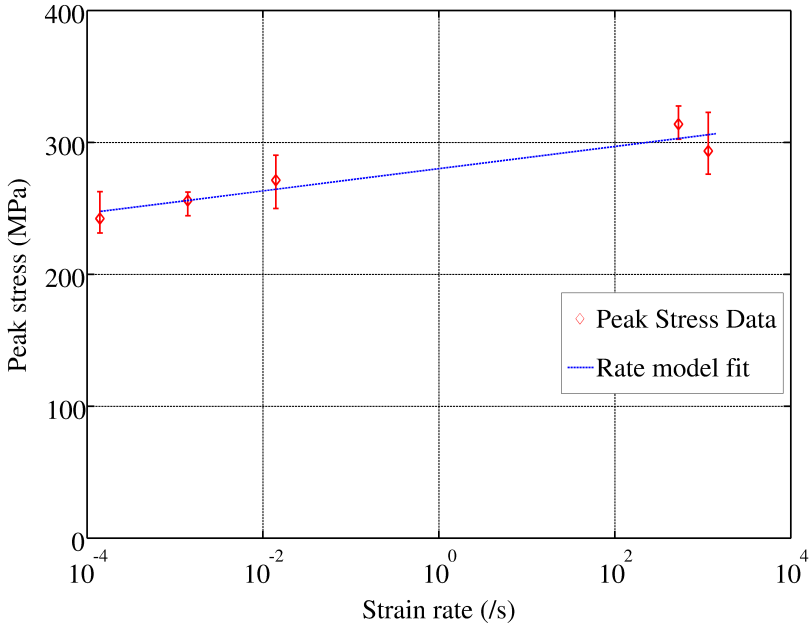

Figure 4.24: Plot comparing peak stresses at different strain rates for through thickness compression of GFPP

4.5.4 SHPB In-Plane Results

The SHPB tests on GFPP in the in-plane direction did not produce acceptable equilibrium, as shown by a typical result in Figure 4.25. The stress at the input bar is always greater than at the output bar, with a difference of 21% at the peak stress. The abrupt drop after the peak stress indicates a catastrophic specimen fracture. Failure for the in-plane SHPB tests occurred approximately 60-70 μs after the incident wave arrived at the specimen, in comparison to approximately 150 μs for the through thickness tests. Revising the specimen dimensions for the in-plane specimens, in order to improve equilibration, would have been problematic due to the relatively coarse weave of the Twintex® fabric used to make the GFPP specimens. In order to facilitate equilibration, the specimen length would have to be reduced to less than the length of one weave unit, making the specimen not representative of a unit volume. The results are included in the summary presented in Table 4.4, with a cautionary note. A representative specimen is shown in Figure 4.26. The brooming failure mode is exaggerated, and large scale delamination is present. Fibre buckling is visible, but has not resulted in the localised kink bands observed in the quasi-static in-plane tests. In-plane SHPB testing of GFPP specimens was not pursued further due to the specimen geometry limitations on equilibration.

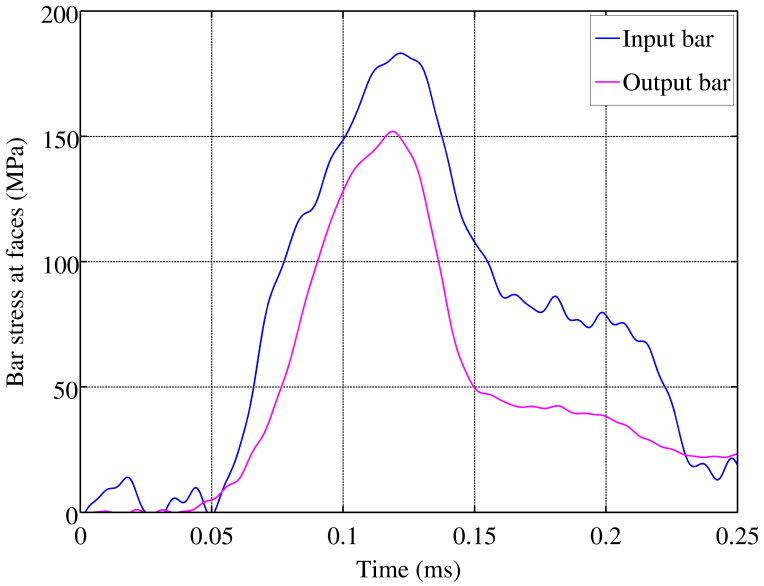

Figure 4.25: Poor equilibration of SHPB test on GFPP, in-plane loading

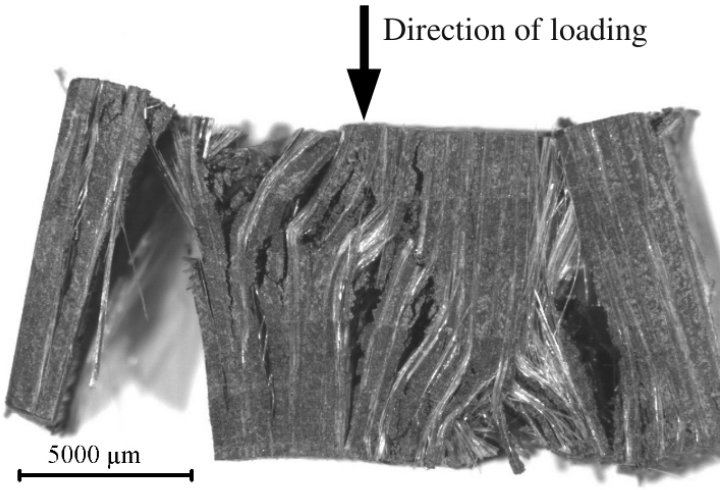

Figure 4.26: Failed GFPP specimen, after in-plane SHPB test at striker velocity of 8 m/s

4.5.4.1 Direct Impact HPB In-Plane Results

The typical bar stress captured during an in-plane DIHPB test on GFPP is shown in Figure 4.27, with the corresponding specimen engineering stress-strain curve in Figure 4.28. As with the SHPB tests, an abrupt drop in bar stress after the peak marks gross specimen failure. Striker velocities for the in-plane DIHPB tests ranged from 10.8 to 11.7 m/s. The peak engineering stress results for the in-plane DIHPB tests are summarised in Table 4.4. The in-plane DIHPB tests invariably resulted in complete specimen fragmentation. Inspection of the recovered fragments showed that delamination was the dominant failure mode.

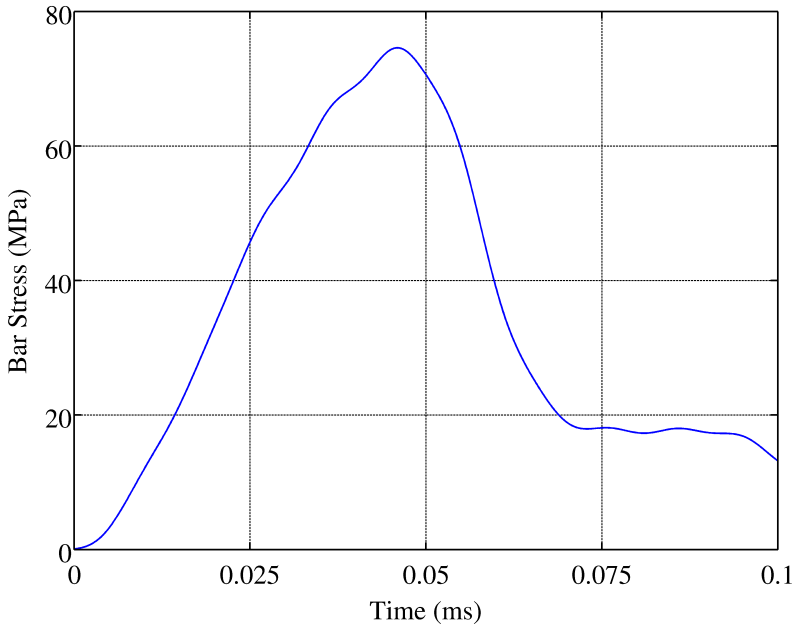

Figure 4.27: Plot of bar stress from a Direct Impact HPB test of GFPP in the in-plane direcation, for a striker velocity of 11 m/s

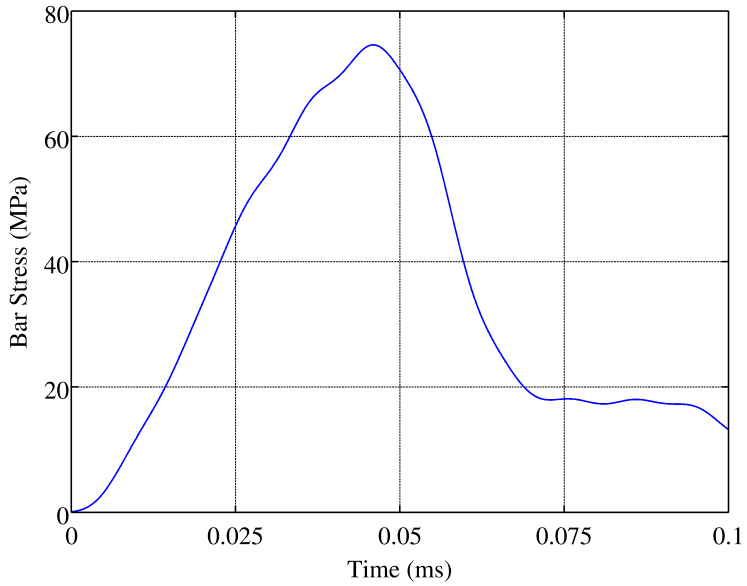

Figure 4.28: Plot of specimen engineering stress-strainfrom a Direct Impact HPB test of GFPP in the in-plane direction, for a striker velocity of 11 m/s

4.5.4.2 Comparison

The engineering stress results for the in-plane loading of GFPP are summarised in Table 4.4, and plotted in Figure 4.29. Please note that the in-plane SHPB tests did not have acceptable equilibrium, and were excluded from the curve fitting, but are plotted for completeness. As with the through thickness testing, the in-plane compression tests on GFPP showed an increase in peak stress as strain rate increased. The logarithmic rate model applied earlier to the through thickness results (§4.5.3) is applied here, excluding the SHPB data. For in-plane compression, the rate dependence model is given by Eq. 4.29. The correlation coefficient R^2 is 0.97 when the SHPB data is excluded. The quasi-static in-plane compressive strength quoted by the manufacturer lies in the range of 137 to 170 MPa [19]. The experiments conducted at 10 mm/min yielded results comparable to the manufacturer's values, but the experiments at lower rates (0.1 and 1.0 mm/min) produced slightly lower strength values. However, lower values of strength at lower strain rates are consistent with the other experiments conducted in this thesis.

$$\sigma_{IP} = 152.7(1 + 0.035\, ln(\dot{\varepsilon})) \quad MPa \tag{4.29}$$

Table 4.4: Summary of in-plane compression results for GFPP

Rate	0.1 mm/min	1 mm/min	10 mm/min	SHPB	DIHPB
Peak Eng. Stress (MPa)	108.8	112.0	133.9	160.6	189.8
Std. Dev. (MPa)	5.5	3.9	7.4	17.2	6.8
C.O.V (%)	5.1%	3.5%	5.5%	10.7%	3.6%
Mean Strain Rate ($/s$)	1.6×10^{-4}	1.6×10^{-3}	1.6×10^{-2}	5.7×10^{2}	1.1×10^{3}

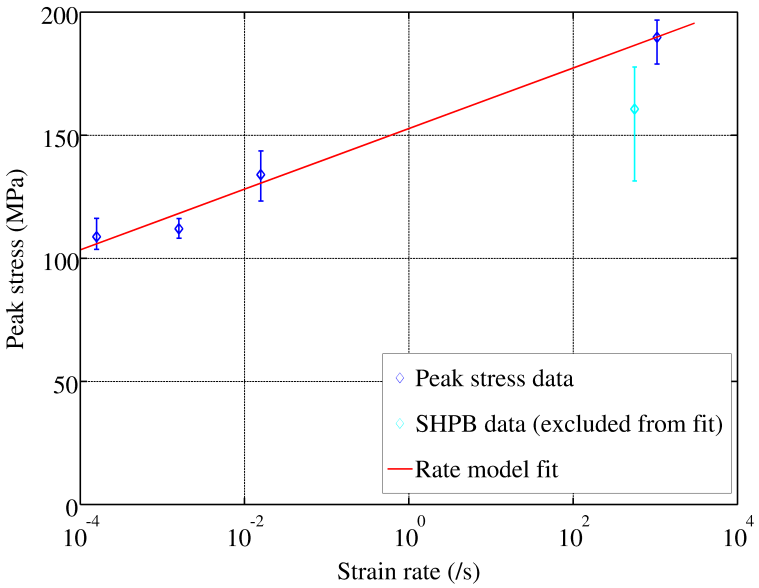

Figure 4.29: Comparison of peak engineering stress for all rates for in-plane compression of GFPP

4.6 Through-Thickness Modulus Determination

The in-plane tensile modulus of GFPP was provided in the manufacturer's data sheet [19], and had been confirmed locally by Zengeni [180], to lie in the range of 11 to 15 GPa (Table 2.4). No values for the through thickness modulus (E_{33}) of GFPP were found in the literature, making it necessary to investigate E_{33} experimentally.

Cubic specimens were instrumented with 2 strain gauges, on opposite faces, aligned in the through thickness direction. The gauges used were the smallest locally available, which had a 2 mm gauge length, and total length of 6 mm, with integrally mounted leads. Due to the practical problems associated with accurately aligning and bonding gauges to specimens of 12 mm thickness, larger specimens were obtained from a panel of 20 mm nominal thickness. These specimens were cubic, with nominal width and breadth of 20 mm. The strain gauge Wheatstone bridge was completed using two dummy gauges bonded to an unloaded block of GFPP, to avoid thermal effects. The applied bridge voltage was 5 V, and the bridge output was amplified by a gain of 100 before being captured on a 12 bit data recorder.

Cyclic compression tests were conducted in the through thickness direction, with force and strain being captured simultaneously. A lower stress limit of 0.75 MPa, correspoding to a nominal force of 300 N, was chosen to avoid unloading the specimen completely, and an upper stress limit of 5 MPa (nominal force of 2 kN) was chosen

to avoid approaching the failure strength. Tests were conducted under displacement control at a CHS of 1 mm/min.

4.6.1 Modulus Determination From SHPB Tests

Conventional SHPB test data is seldom useful for determining the modulus of the specimen. The stresses acting on the input and output faces of the specimen generally only reach equibilibrium some time after the specimen has deformed plastically, making the data in the elastic portion of the test inadmissable. However, work by Frew and colleagues [144, 143] has shown that the specimen stress equilibrium can be dramatically improved in the early part of the test by careful pulse shaping. The rise time of the incident loading wave needs to be increased substantially, typically by adding a deformable element between the striker and input bar. SHPB tests were conducted on the block specimens instrumented with strain gauges, described in §4.6. The specimen strain gauge bridges were completed using dummy gauges on unloaded GFPP blocks. The bridge excitation voltage for the specimens was 4 V, and the bridge output amplified using the same amplifiers as for the bar strain gauges, but with a gain of 10. The pulse shaping was achieved using the tapered strikers described in §4.3.3, and a 4-5 mm ball of putty between the striker and input bar. This increased the pulse rise time sufficiently for acceptable specimen equilibration to occur.

4.6.2 Results of Through-Thickness Modulus Investigation

In this section, true strain always refers to a measured value from a strain gauge on the specimen. The quasi-static true stress and strain data used to obtain the through thickness modulus (E_{33}) of GFPP is shown in Figure 4.30. The mean value of E_{33} obtained from all the tests is 1.94 GPa, with a coefficient of variation (COV) of 4.1%. The nominal strain rate for the quasi-static tests was $1.4 \times 10^{-3}/s$.

The determination of modulus from SHPB tests requires more careful examination. An important requirement is that the stresses acting on the specimen faces reach equilibrium during the early part of the test. The stresses at the input and output faces for a typical modulus test on GFPP using a SHPB are shown in Figure 4.31. There is little variation as the load increases, with a maximum variation of 6% at peak load. The variation at peak load is not important, as this portion of the data in not included when calculating modulus from the slope. The good equilibration during the modulus tests may be attributed to:

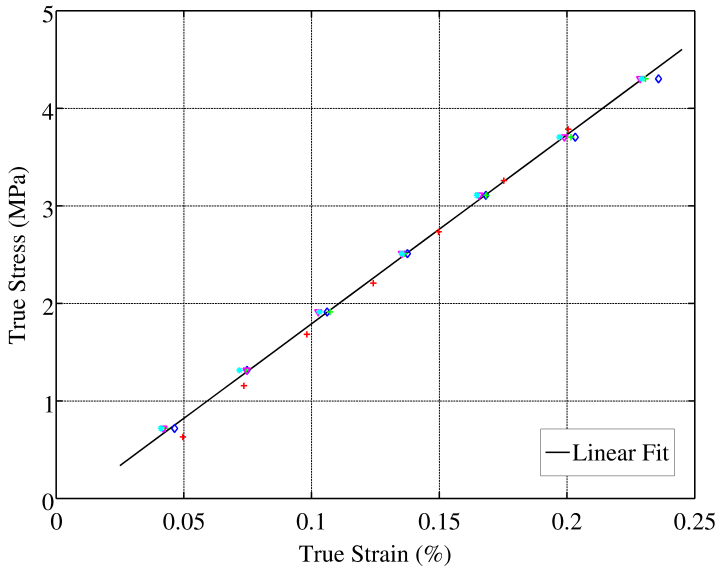

Figure 4.30: Plot of GFPP true stress-strain data for modulus determination

- The rise time of the incident loading pulse in the modulus SHPB test is approximately 150 μs due to the additional pulse shaping, which is approximately double the rise times during the SHPB tests to failure. As the rise time of loading is increased, the likelihood of specimen equilibration improves, but the strain rates achieved during the test decrease.
- The specimens used for the modulus SHPB tests had cross sectional areas approximately 4 times greater than those used for the SHPB tests to failure. This reduces the impedance mismatch between bars and specimens, which greatly facilitates equilibration.

A hindrance to equilibration in the modulus SHPB tests is the relatively long specimen length of 20 mm, compared to 6 mm for the specimens tested to failure. It is apparent that specimen equilibration benefits more from the increased rise times and specimen area, than is detracted by the increased specimen length. The specimen stress is taken to be that experienced at the back face, and may be combined with the measured strain to obtain the true stress-strain relationship shown in Figure 4.32. The data at peak load has some non-linearity as the specimen is unloading. The data used for the linear fit excludes the very early loading, and the non-linear region near the peak load.

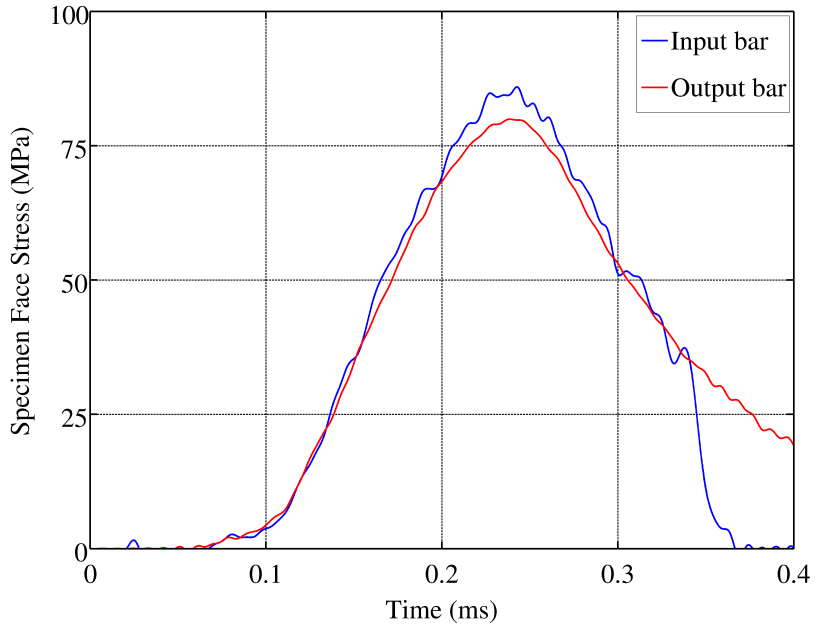

Figure 4.31: Plot of specimen input and output faces stresses, showing equilibration of GFPP specimen during SHPB modulus test

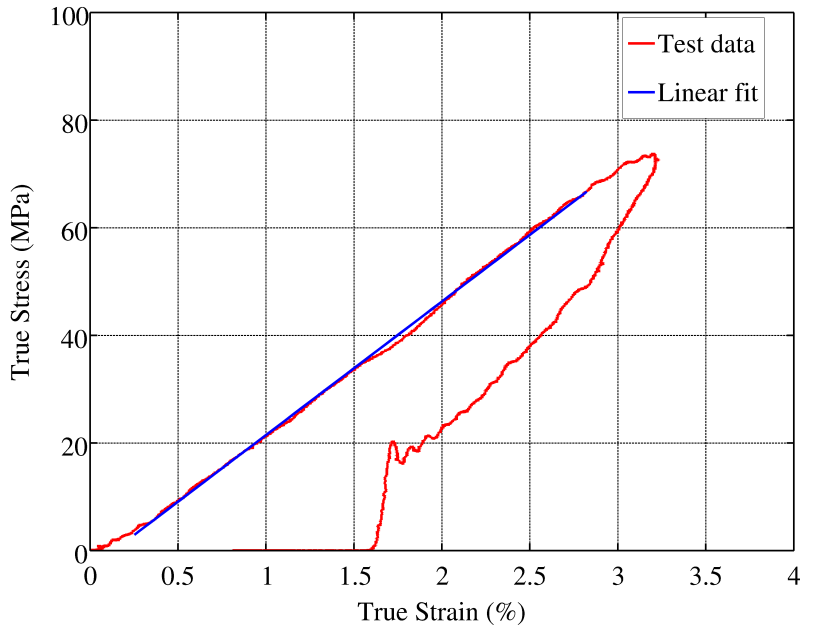

Figure 4.32: Plot of linear fit to sub-failure SHPB test of GFPP in the through-thickness direction

The mean value for E_{33} obtained from eight SHPB tests is 2.47 GPa, with a COV of 6 %. The strain rate history for a typical test is shown in Figure 4.33. It was evident that obtaining a constant strain rate for the partial loading would require susbtantial work on the pulse shaping, which was not within the scope of this thesis. The average strain rate over the range of interest, for all the tests was $2 \times 10^2/s$.

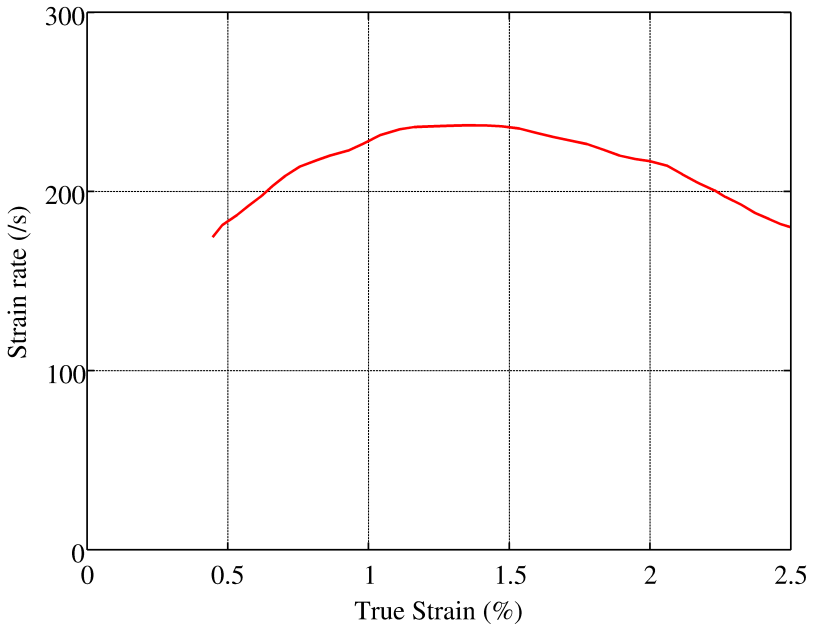

Figure 4.33: Plot of strain rate history for SHPB modulus test of GFPP

E_{33} for GFPP increased from 1.94 to 2.47 GPa as strain rate increased from 10^{-3} to $10^2/s$ - an increase of 27 %. The compressive modulus for polypropylene is approximately 1.5 GPa [181]. It is not surprising that E_{33} is similar to the modulus of the matrix, but slightly higher due to the presence of the fibres. The strain rate dependency of E_{33} is likely due to visco-elastic effects in the polypropylene.

4.7 Summary

Compression tests of GFPP in the through thickness and in-plane directions showed that the peak stress increases with strain rate. The rate dependence was modelled using a logarithmic rate law, adapted from the Johnson-Cook model. Through thickness failure modes were either spreading failure at the loaded faces, or macroscopic shear. Both of these failure modes appear to be linked to the in-plane fibre failures, caused by transverse tensile strain. The in-plane failure modes involved brooming, fibre kinking and delamination. The SHPB tests in the in-plane direction did not result in acceptable specimen equilibrium.

Chapter 5

Bend Tests

This chapter describes the quasi-static and high strain rate bend testing of GFPP and FMLs based on aluminium and GFPP. All quasi-static tests were conducted on a Zwick™ Model 1484 Universal Testing Machine. The impact bend tests were conducted on a novel test arrangement, of the author's design, based on a Hopkinson Pressure Bar. A number of delamination tests are based on three or four point bend geometry. Hence the implementation of a high strain rate bend test rig is of great benefit to developing the high strain rate delamination test geometry and methodology.

5.1 Quasi-static Bend Tests

5.1.1 GFPP

The 3-Point bend tests followed ASTM D 7264 [25]. A span to thickness ratio of 16:1 was followed as closely as possible. The parameters for the different test specimens are shown in Table 5.1:

Table 5.1: GFPP Three Point bend test parameters

Thickness (mm)	2.7	4.0
Span (mm)	50	64
Width (mm)	20	20
Cross head speed (mm/min)	1 & 20	1 & 20
No. of tests	4 (each rate)	4 (each rate)

The supports and central loader for the bend tests utilised 10mm diameter silver steel rollers. The force-displacement data was normalised to stress data using the standard Euler-Bernoulli equations for a monolithic beam [25]:

$$\sigma_{11} = \frac{3PS}{2wt^2} \tag{5.1}$$

Where P = force applied at centre span, S = span, w =specimen width and t = specimen thickness.

Strain at the outer fibre at centre span is obtained from:

$$\varepsilon = \frac{6\delta t}{S^2} \tag{5.2}$$

Where δ is the specimen deflection at center span.

The elastic modulus E_{11} is determined from the slope of the force-deflection plot, given that the deflection at centre span δ_c is given by:

$$\delta_c = \frac{PS^3}{48E_{11}I_{22}} \tag{5.3}$$

E_{11} is the modulus parallel to the support span and I_{22} is the second moment of area about the relevant axis. The equations are only valid for linear elastic materials. As the behaviour of GFPP up to peak load is essentially linear, this is a reasonable approximation. The post peak reponse may only be characterised using non-linear computational models.

5.1.2 Fibre Metal Laminates

No international standards exist for testing of FMLs. The appropriate standard for FRPs [25], as well as publications on testing of similar FMLs [91], were used as a basis for the test configurations.

The FML bend specimens were cut from a panel with a 2/1 lay up, consisting of two 1.2 mm thick outer skins of aluminium and a central layer of GFPP, which was nominally 1.6 mm thick, giving a nominal specimen thickness of 4 mm. The specimen nominal width was 25 mm. 3 point bend tests were conducted with a span of 64 mm, at cross head speeds of 1 and 20 mm/min.

5.1.3 Results of Quasi-static Bend Tests of GFPP

The force-displacement results for the tests conducted on the 2.7 mm thick GFPP specimens, at 20 mm/min are shown in Figure 5.1. The results of the tests conducted at 1 mm/min, and on the 4 mm specimens, are qualitatively similar, differing only in the magnitudes of forces and displacements to failure. The first departure from the the initial linear response is associated with local buckling of the fibres on the compression side, under the central loading roller, as shown in Figure 5.2. The departure from linearity occurs between 85% and 97% of the peak force. The force drops briefly, before progressing in an approximately linear manner, on a lower slope than the initial response, up to the peak. The peak force, followed by an abrupt drop, concurs with brittle fibre failure on the tensile side.

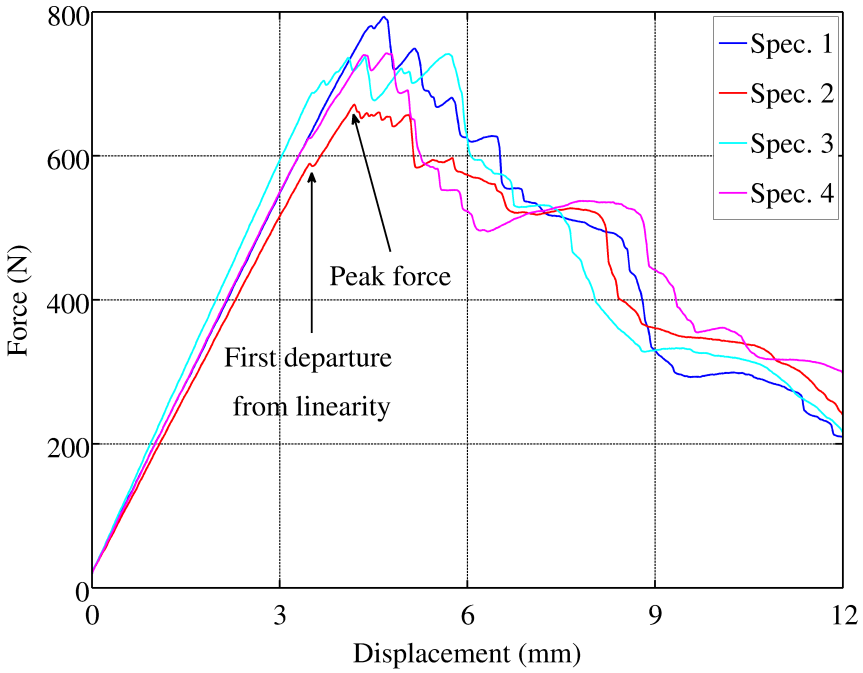

Figure 5.1: Force-displacement response of Three Point bend tests on GFPP

The tensile fibre failure is accompanied by visible whitening in the region of failure, as shown in Figure 5.3. This whitening is due to sudden localised cracking of the matrix, as the matrix cannot sustain such high stresses once the fibres have failed. After the peak force, the resistance of the specimen decreases as failure progresses from the outer fibres towards the neutral axis.

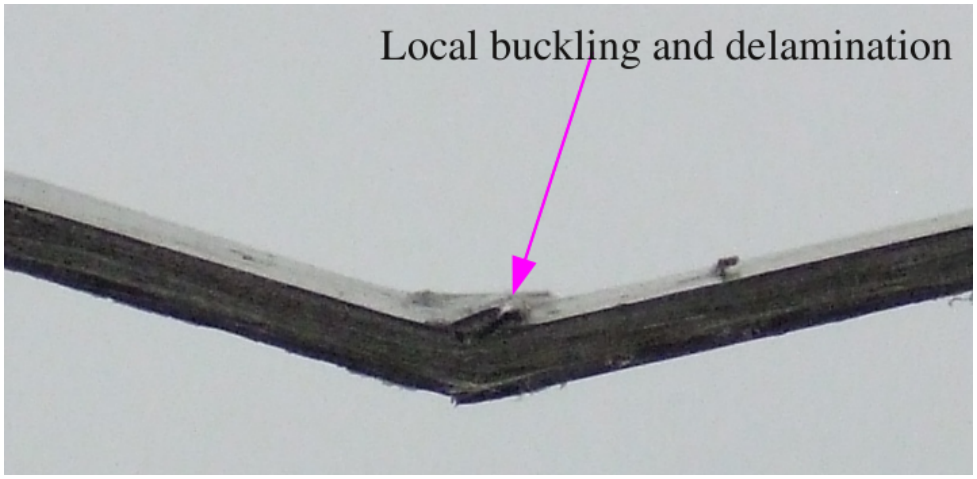

Figure 5.2: Photograph of typical GFPP specimen after bending test (side view), showing

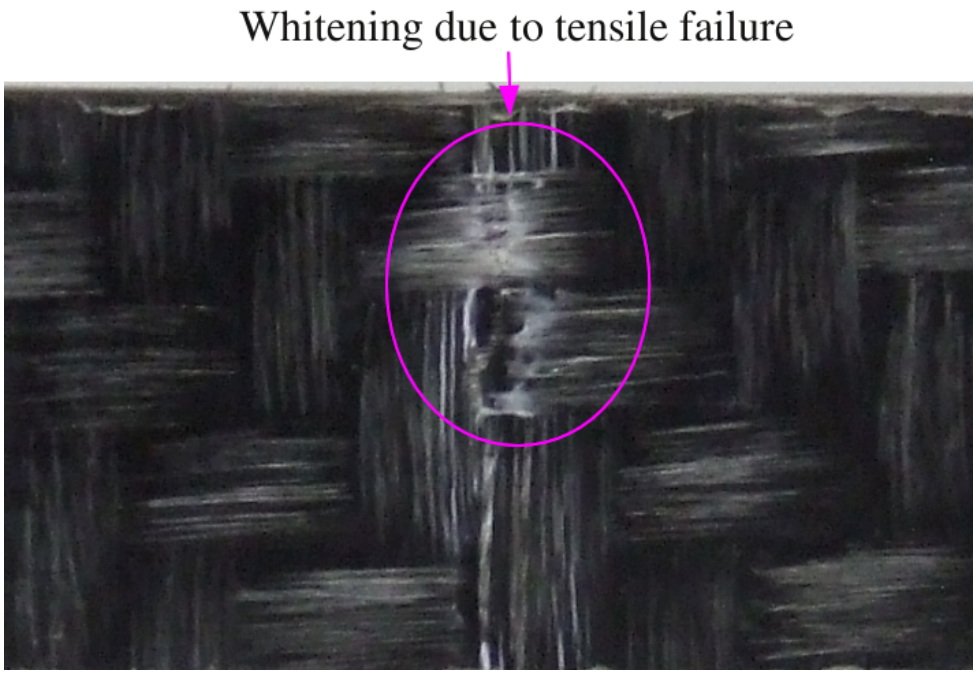

Figure 5.3: Photograph of typical GFPP specimen after bending test (tensile damage)

The results of all the quasi-static tests on GFPP are summarised in Table 5.2. The stresses and strains quoted are for the peak force of each test, calculated using the equations described in §5.1.1. The elastic moduli are calculated using the slope of the force-displacement curve between 10 % and 60 % of the peak force, to avoid any non-linearity at the start of the test or approaching failure. Bending tests have inherently non-uniform stress and strain fields. Hence the strain rate quoted is based on the outer fibre, at the centre of the loading span, as this experiences the highest stresses and strains.

Table 5.2: Summary of quasi-static bend test results for GFPP

Parameter	Series 1	Series 2	Series 3	Series 4
Mean Thickness (mm)	2.7	2.7	4.0	4.0
Mean Width (mm)	24.7	24.6	24.8	24.7
CHS (mm/min)	1.0	20.0	1.0	20.0
Mean Peak Stress (MPa)	273.1	291.1	274.9	300.1
COV of Peak Stress (%)	5.2%	9.9%	6.0%	7.8%
Mean Strain at peak (%)	2.78%	2.94%	2.84%	3.16%
COV of Strain at Peak Stress	8.1%	5.8%	5.5%	7.3%
Flexural Modulus (GPa)	10.0	10.5	10.8%	11.1
COV of Flexural Modulus (%)	3.5%	5.2%	2.4%	5.9%
Strain Rate at outer fibre (/s)	1.09×10^{-4}	2.19×10^{-3}	0.98×10^{-4}	2.01×10^{-3}

The tensile strength determined from the bending tests lies in the range 273 to 300 MPa, which correlates well with the manufacturer's quoted tensile strength of 288 MPa [19] and the range of values published in the open literature (Table 2.4). The modulus in the warp direction E_{11} was in the range 10 to 11.1 GPa, which is at the lower end of the published range (Table 2.4). The two different thicknesses of panel exhibit almost insignificant variation in strength, strain at failure and modulus, for tests conducted at similar strain rates. Of greater interest is the fact that for both panels, there is an increase in strength and strain to failure for the tests conducted at the higher rate. The quantitative analysis of this rate dependence is discussed with the impact bending test results, in §5.3.1.

5.1.4 Results of Quasi-static Bend Tests of FMLs

The force-displacement response of FML specimens in 3 point bending, at a cross head speed of 20 mm/min, are shown in Figure 5.4. The response is essentially linear until the onset of plasticity in the aluminium layers. The post-yield behaviour is stiffer than monolithic aluminium, as the GFPP layers continue to resist with their initial modulus. Small drops in the force are noticeable at displacements of approximately 7 mm and 10 mm - these coincided with audible cracking noises, which are assumed to be fibre rupture.

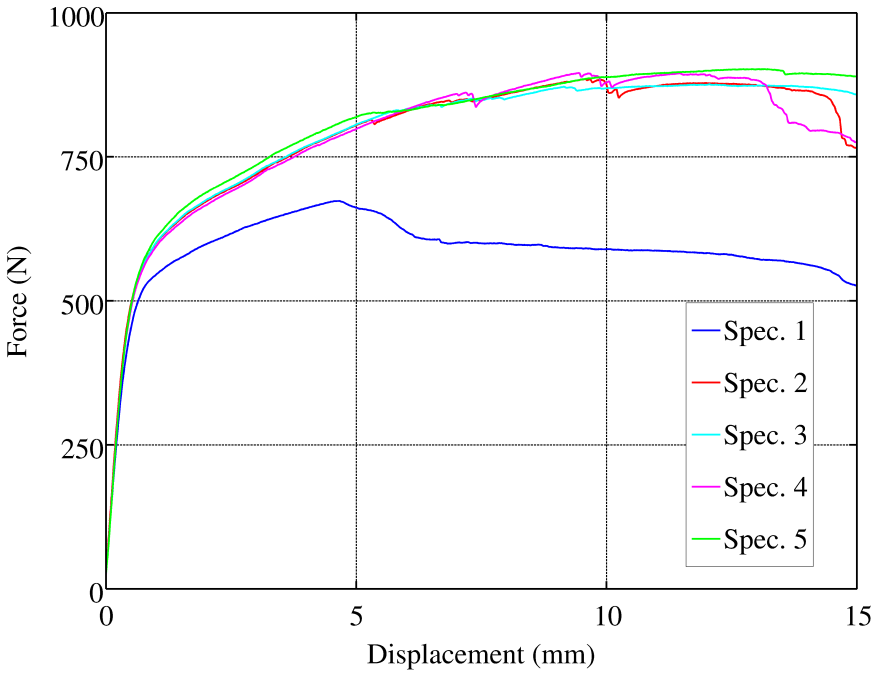

Figure 5.4: Force-displacement response of 3 point bend tests on FML

The response of Specimen 1 is clearly different to that of Specimens 2 to 5, which are closely grouped. Specimen 1 developed delamination in the GFPP layer, close to the upper aluminium-GFPP interface, as shown in Figure 5.5. It is not debonding, as a thin layer of matrix and fibres are still adhered to the upper Aluminium layer. As the failure mode of Specimen 1 was substantially different to the other specimens, it was excluded from any further quantitative analysis.

The 3 point bend tests on FML specimens at a cross head speed of 1 mm/min are very similar, with only minor differences in magnitude. The comparison of both quasi-static series and the impact bend tests is discussed in §5.3.2.

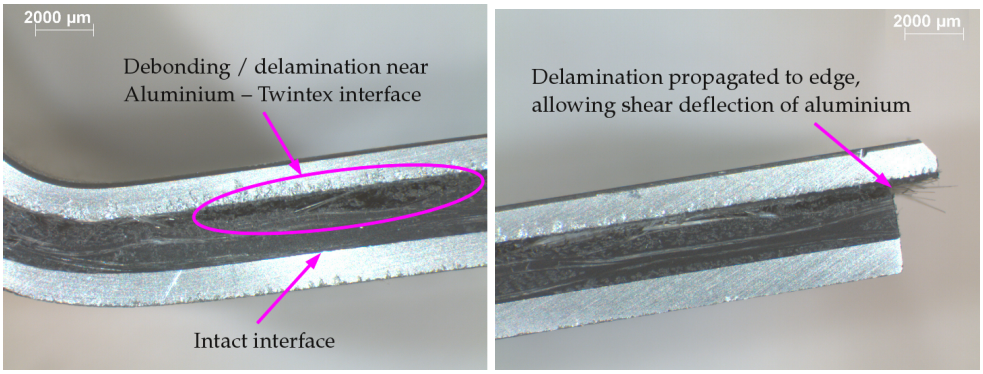

(a) Centre span (b) Edge

Figure 5.5: Delamination of FML Specimen 1

5.2 Impact Bend Testing

As with other impact experiments, impact bend tests require careful experimental design for the specific materials or structures being tested. The primary output of a bend test is typically a force-deflection curve. The instruments used to measure these parameters must be chosen such that the maximum values recorded during experiments do not exceed the capacity of the instrument, while not being so small as to compromise the resolution and accuracy of the measurement. Impact experiments must also consider the effect of the stress waves generated by impact, and how these might affect the instrumentation.

Laminates based on GFPP have relatively low stiffness in comparison to carbon fibre based laminates, or glass fibre-epoxy systems. Hence the deflections to failure during bend testing are relatively large. The anticipated deflections to failure are of significant consideration while designing the impact bend experiments.

5.2.1 Motivation for Using HPB

Commercial impact testing equipment based on drop testers, is widely available. However, such equipment suffers from two main limitations:

- As loading is achieved via drop testing, the impact velocity is limited by the height of the test frame. Certain designs offer additional loading springs to increase the impact velocity [27], but these come at a significant cost. Gas gun driven impact experiments allow testing at much higher impact velocities.
- The impact event induces stress waves in both the specimen and loading structure. The short length of strain gauge based load cells results in reflection of the stress waves before loading has finished, which manifests as oscillations in the force histories (for example [92]). Filtering of these signals is possible, but the filtering may remove some of the specimen response which is highly undesirable.

The HPB is based on stress wave propagation, which allows the capture of force histories for impact events, without requiring filtering that may obscure specimen response. A significant limitation of using a HPB is the duration of the event that may be recorded, which is determined by the distances from the strain gauge station to the bar ends and the wave speed of the bar material. This duration may be increased by using multiple strain gauge stations and wave deconstruction techniques. However,

the experiment could also be designed such that the failure occurs within the duration limitation of the HPB in use, avoiding the more complicated analyses involved with multiple reflections.

5.2.2 Important Considerations for Bend Tests Employing the HPB

HPB based bend tests using a single input bar (for example [153, 154, 155]) to both impact the specimen and measure the force, are compromised by several features. The force applied to the specimen by the bar is proportional to the difference in magnitudes of the incident and reflected waves (Eq. 4.12). The flexural stiffness of the specimen is generally small in comparison to the axial stiffness of the bar, which causes the majority of the incident wave to be reflected. Hence the applied force at the interface is a small fraction of that associated with either the incident or reflected waves at the strain gauge station. As the bridge voltages and amplification must be set up to capture the maximum magnitude of the incident and reflected waves, the resolution of small stresses (and hence forces) will be poor. The uncertainty in the force measurement was noted by Bacon *et al* [153], who used a steel bar to fracture PMMA and glass specimens. Martins [154] investigated the fracture of polyethylene specimens, which would be relatively flexible in bending, and chose a polycarbonate input bar to reduce the impedance mismatch and hence reduce these effects.

The loading wave must also produce sufficient deflection to fail the specimen. The specimen deflection achievable is limited by two parameters: the duration of a stress wave transit, and the maximum velocity of the bar-specimen interface. The duration is limited by the bar wave speed and length, as well as a striker of sufficient length to produce the required stress wave. The bar length is limited by practical considerations such as available laboratory space, or the maximum length of suitable bar material that is commercially available. The velocity at the bar-specimen interface may not exceed the striker velocity just prior to impacting the bar. The striker velocity is in turn limited by the need to maintain elastic stress wave behaviour in the bar. Given a striker and HPB of equal diameter and material, the maximum striker velocity $V_S(max)$ is limited by the yield stress σ_y:

$$V_S(max) = \frac{2\sigma_y}{\rho C_o} \tag{5.4}$$

Consider the case where the specimen is of negligible stiffness and the bar end behaves as a free surface. This permits the calculation of the maximum deflection

obtainable from the single bar set up, assuming perfect impact with a striker of the same material and diameter, which results in a square loading wave. This provides an upper bound on the deflection for a given bar material. Table 5.3 compares several options for bar materials [1] in terms of maximum duration of incident wave Δt and bar tip deflection δ. A striker length of 1 m is assumed, which would require a bar length of 2 m. The limitation here is the striker length, as the gas gun at BISRU can only accomodate strikers up to 1 m in length. The bed on which the gas gun and HPBs are mounted is approximately 9 m long, so a longer HPB may be used if necessary.

Table 5.3: Typical bar materials, striker velocities and total deflections

Parameter	ρ	C_o	σ_y	$V_S(max)$	Δ t	δ
Material	kg/m^3	m/s	MPa	m/s	ms	mm
Silver steel	7830	5100	600	30	0.196	6
Maraging steel	8000	4800	1600	83	0.208	17
Aluminium 6061 T6	2700	5000	200	30	0.200	6
Titanium 6 Al 4 V	4500	5100	800	70	0.196	17
Polycarbonate	1200	1400	50	60	0.714	43

It is immediately evident that common bar materials such as silver steel and aluminium alloy do not permit large deflections for this configuration. More expensive alloys such as maraging steel or titanium fare better, but the largest deflection is obtained by using a polycarbonate bar. As specimen stiffness increases, the accuracy of the above analysis decreases. However, as the focus of this thesis is on laminates of relatively low stiffness, the above results inform the choice of bar material while designing the experiments.

The use of both an input and output bar, such as by Nwosu *et al* [158, 159], does not necessarily provide more accurate measurement of the forces. The presence of heavy fixtures on the output bar (see Figure 2.43) makes it difficult to determine whether the forces measures are attributable to specimen response or inertia of the fixtures. Replacing the supporting fixtures by twin output bars, as reported in Rubio-Gonzalez *et al* [13], Ogawa *et al* [152] or Delvare *et al* [161], removes the fixture inertia from the problem and allows measurement of the reaction forces directly on the specimen. While this

[1] Polycarbonate is strictly speaking a visco-elastic material. However, Rao and Shim [182] have shown that HPB experiments using polycarbonate may be analysed using linear elastic equations with little error.

is beneficial, it is not without further complications. Quasi-static three point bending experimental results are presented in terms of the force and deflection at the mid-span of the specimen. While the summed reaction forces equal the central force for a quasi-static experiment, in an impact experiment this is not true for the entire duration of the experiment. The input bar of this configuration must still be long enough to achieve sufficient deflection of the specimen for failure to happen. The output bars need not be as long as the input bar, but must still be long enough to capture the failure event before wave overlap occurs at the strain gauge stations. If the specimens being tested have large deflections to failure, the transmitted stress waves have longer durations. This requires longer output HPB and hence a relatively long support bed.

The necessary measurements of a three point bending impact experiment are the displacements (or velocities) of the three loading / reaction points. Force measurement at either the central point, or both outer points, is necessary. Of these, accurate force measurement at the central point is most desirable. The force at the outer points is seldom reported, and would require correction for delay due to the time taken for the bending wave to travel to the outer points.

5.2.3 Implemented Configuration for Impact Bending Experiments

As noted in §5.2.2, the force measurement using an input HPB is compromised by the need to provide a velocity boundary condition of sufficient magnitude. In addition, the force measurement at the outer supports is generally not useful in an impact bend experiment due to the delay in the bending waves reaching the outer supports. It is easier to measure the central impact force accurately with an output HPB. To achieve this the traditional configuration is reversed, with the two outer supports on the input side and the central force measured on the output side with a HPB. Thus the input HPB may be dispensed with, and the required velocity boundary condition provided by a short impacter with appropriate specimen supports.

A photograph of the rig implemented herein is shown in Figure 5.6. A schematic of the configuration is explained with the aid of Figure 5.7. A specimen is supported at two outer points on an impacter. The impacter is supported by axial guides (omitted from figure for clarity) and its position is monitored throughout the experiment using a Reflective Object Sensor (ROS). The details of the ROS are described in §5.2.3.1. The impacter and specimen are accelerated from rest via a pusher bar driven by a gas gun barrel (Figure 5.7(a)). The pusher bar is larger in diameter than the impacter, and

is arrested by a stopper once the impacter has achieved the desired velocity (Figure 5.7(b)).

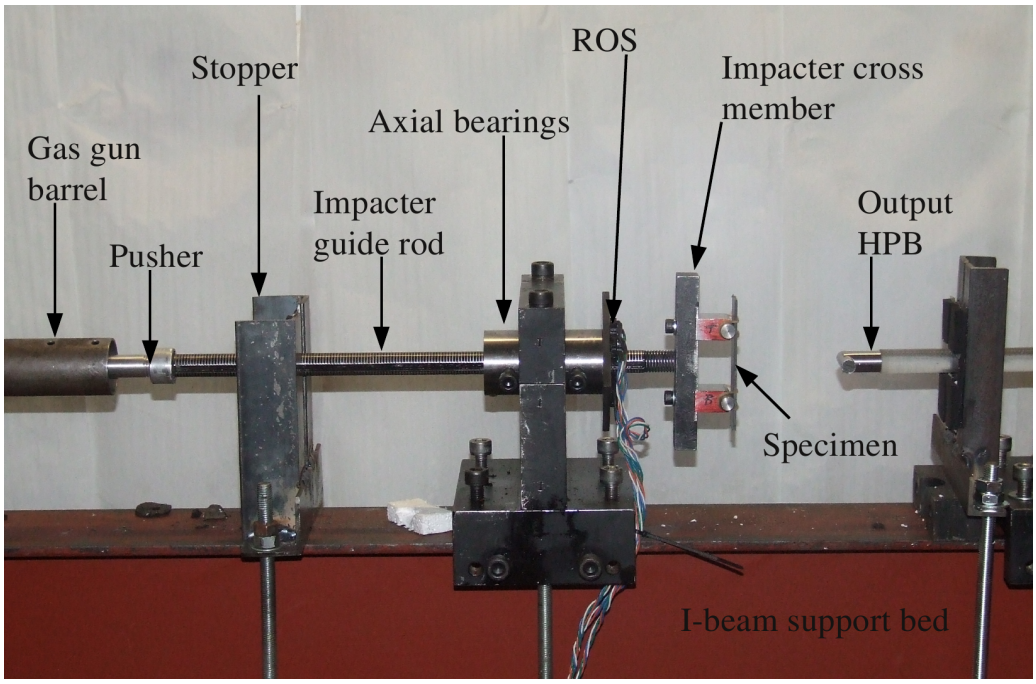

Figure 5.6: Photograph of bending HPB apparatus

The specimen impacts on a centrally located HPB, which is an output bar (Figure 5.7(c) - bar length not shown to scale). The inertia of the impacter continues driving the outer points of the specimen forwards, while the HPB at the central point resists the motion. The force and velocity at the central point are determined from a strain gauge station on the ouput HPB, using Eq. 4.14. The velocity is simply integrated to obtain displacement of the central point. The cross member of the impacter has a flexural stiffness $E_y I_{22}$ value of $1.1 \times 10^3 Nm^2$, while the typical specimens described in Table 5.1 have $E_y I_{22}$ ranging from 0.5 to 1.7 Nm^2. As the cross member is 3 orders of magnitude stiffer than the specimen, it may be assumed to have negligible deflection relative to the central guide. Hence the displacement of the two outer points is the same as the central guide, which is recorded using the ROS. Thus all the necessary parameters for a three point bend impact experiment are measured.

The output HPB is primarily used for force measurement, and is only required to measure the first passage of the compressive wave accurately. As the approximate force required to fail the specimen may be determined from quasi-static bending tests, the bar material and diameter may be chosen such that the stress wave arising from the impact is of sufficient magnitude to be accurately captured by the available data aquisition system. This is a substantial improvement in accuracy of the force measurement

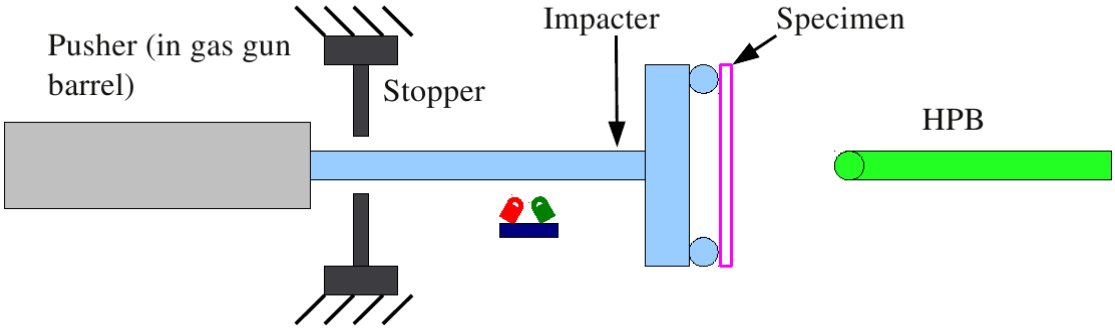

(a) Pusher and impacter being accelerated by gas gun toward HPB

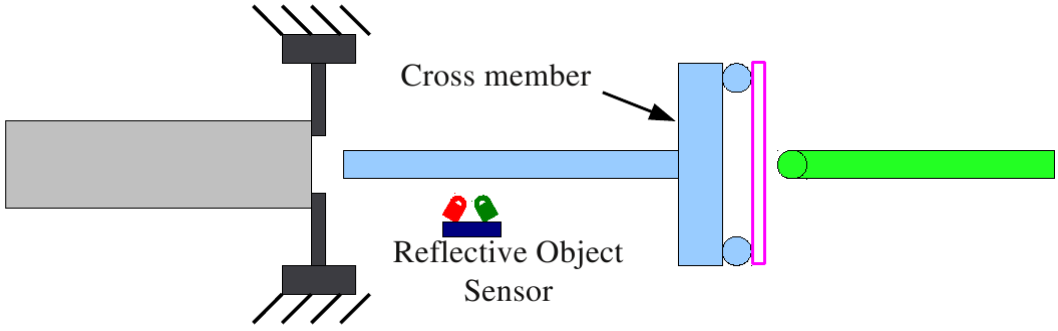

(b) Pusher arrested by stopper; impacter travelling at constant velocity towards HPB

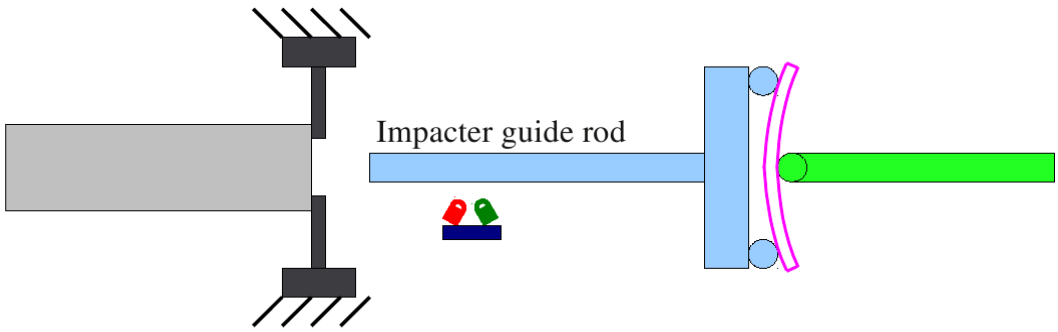

(c) Specimen impacts centrally against HPB; inertia of impacter keeps outer supports moving, causing specimen to deform; force measured by HPB

Figure 5.7: Schematics explaining HPB Impact Bend test configuration

over the bending configuration with a single input HPB, acting as both an impacter and force measurement.

The inertia of the impacter does not negatively affect the force measurement, as there are no large fixtures between the specimen and output HPB. In fact, it is better for the impacter to be heavier rather than lighter - greater inertia means the impacter velocity will decrease less during impact, hence giving a more uniform rate of loading. The gas gun providing the initial push to the impacter is of sufficient capacity that an impacter of 1 kg mass is easily accelerated to velocities of the order of 10 m/s in a distance of less than 200 mm.

The pusher bar is of length 400 mm, and remains largely inside the gas gun barrel, except for the short portion protruding after it is arrested. The impacter, supports and the space required for acceleration occupy relatively little space in front of the gas gun - approximately 600 mm for the final iteration of the design. Thus less than 1 m of the bed is occupied by the bending rig, and the remainder of the HPB bed may be used for the output bar. Thus the duration of the force measurement is only limited by the output bar length and wave speed. As HPB apparatus at BISRU are mounted on a 9 m long bed, the output bar length is limited by the maximum length of the appropriate material that is commercially available.

5.2.3.1 Reflective Object Sensor

The position or displacement of the impacter is measured using a Reflective Object Sensor (ROS) and a graduated light and dark scale. The ROS consists of a matched light source (in this case an LED) and receiver (in this case a phototransistor). When pointed at a surface, the voltage measured across the photodiode arm will be high for very reflective surfaces and low for non-reflective surfaces. Thus if a scale of alternating light and dark regions is passed at constant velocity in front of the ROS, the output voltage will be a sinusoid as shown in Figure 5.8. The wavelength corresponds to a displacement equal to one pitch of the scale. The ROS is a non-contact sensor and therefore does not affect the motion of the impacter in any way, nor is it affected by any vibrations of the impacter as an LVDT or linear potentiometer would be. The range of displacement of an ROS based system is limited by the total length of the light and dark scale provided. The ROS is not damaged by exceeding the range of displacement, unlike a LVDT or linear potentiometer. The disadvantage of using the ROS is that it provides displacement data in discrete intervals, unlike LVDTs or linear potentiometers, which are analogue instruments.

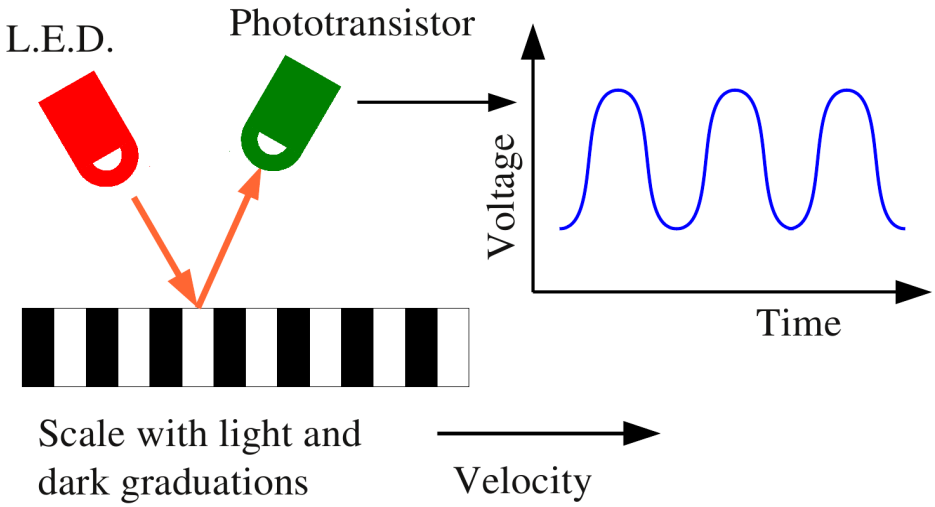

Figure 5.8: ROS operating principle

The ROS utilised is the Fairchild QRB 1134 as this provides the LED and phototransistor in a single, easily mountable package. The central guide rod of the impacter was CNC machined with shallow grooves (depth of 0.06 mm) at a 2 mm axial pitch. The guide rod was then sprayed black and polished to provide alternating light and dark stripes. To improve the resolution of displacement measurement, two sensor packages were mounted with a nominal axial separation of 0.5 mm. Careful measurement with a digital Vernier height gauge and oscilloscope showed the sensor offset to be 0.48 mm. The output voltages of the ROS were captured on two channels of the same DAQ card used to capture the HPB strain gauge signals. All channels were sampled at 10 MHz, at 16 bit resolution.

The Fairchild QRB 1134 has rise and fall times of 8 μs. Given the scale pitch of 2 mm, this gives a theoretical maximum velocity of 125 m/s. However, as the pitch is reduced to improve resolution, the amplitude of the sinusoidal voltage output decreases. Investigations by Stander [183] and Merrett [184] showed that for a 2 mm pitch, the practical limit of measured velocity is 20 m/s. This was acceptable as the anticipated impacter velocities were less than 15 m/s. The resolution of the ROS is 0.48 mm. The algorithm and scripts used to obtain displacement histories from the raw ROS output are provided in Appendix D.1.

5.2.3.2 Impacter Details

The impacter requires the following features for a successful impact bend test:

- The cross member which supports the specimen at the two outer points must be sufficiently rigid that its deflection during the experiment is negligible in comparison to the specimen.
- The guides for the impacter must allow free axial movement, while maintaining axial alignment with the HPB and preventing any rotation about the HPB axis.

The cross member of the impacter has a flexural stiffness $E_y I_{22}$ of approximately $1.1 \times 10^3 Nm^2$. The specimens tested in this thesis have $E_y I_{22}$ values ranging from 0.5 to 1.7 Nm^2, making the impacter three orders of magnitude stiffer than the specimens. Hence treating the impacter as perfectly rigid should have a negligible effect on the results.

The first iteration of the impacter design is described in Appendix E.1. The final version of the impacter is shown in Figures 5.6 and 5.9. The cross member of the impacter permitted the support span to be adjusted, within a range of 35 mm to 100 mm. The specimen supports permit a maximum specimen deflection of 24 mm, which is more than required for the specimen tested in this thesis. The axial guide rod has a length of 300 mm. The support for the impacter has two bushes separated axially by 50 mm, to prevent any vertical sag of the impacter. Rotational constraint is provided by screws with ends profiled to match the keyway in the guide, which does not restrict the axial motion in any way.

The specimen is held in place by looping two elastic bands over the support rollers as shown in Figure 5.9.

The M6 hole in the centre of the cross member is coaxial with the guide rod of the impacter. This threaded hole was used for attaching a jig that aided precise axial and angular alignment of the impacter and output HPB between tests.

5.2.3.3 Output HPB Details

The quasi-static tests indicated peak forces would be in the region of 500 N to 1000 N. This is relatively small in the context of HPB, where typical tests produce forces on the kN scale. Initial tests were conducted with a 10 mm diameter, 5 m long Aluminium 6061 bar. This bar was limited to a capture time of 1.8 ms, was unwieldy due to its length and had a poor signal to noise ratio. The aluminium HPB was rejected in favour of a polymeric HPB. The implemented output HPB was a polycarbonate (PC) bar of 16.7 mm diameter, and length 1987 mm. The choice of polycarbonate for the output HPB was based on the findings of Curry [185], who investigated polycarbon-

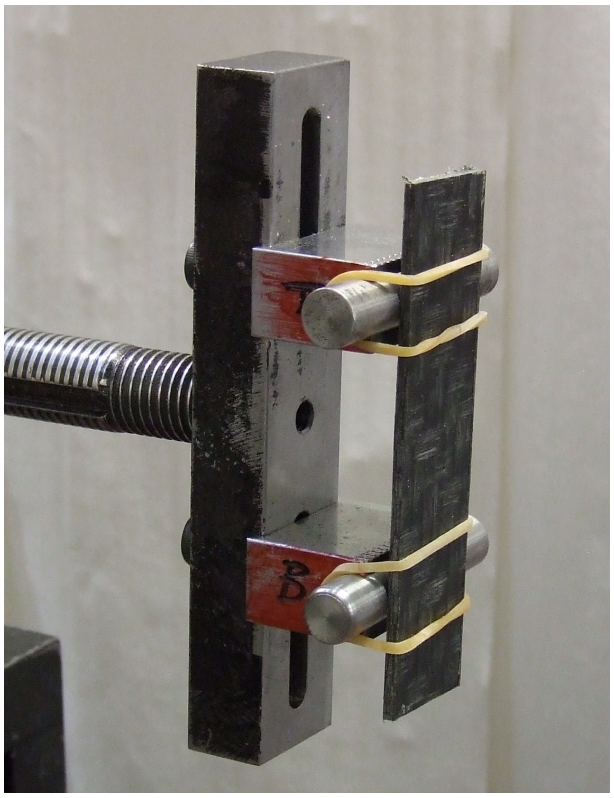

Figure 5.9: Adjustable cross member of impacter

ate, polymethyl methacrylate and nylon as candidate materials for polymeric HPB and found polycarbonate to have the lowest attenuation. A very attractive feature of PC is its wave speed of approximately 1480 m/s. Thus a 2 m PC HPB, with the gauge station located 200 mm from the impact face, has a capture duration limit of almost 2.4 ms before wave reflections superimpose. The PC bar used had density ρ of 1196 kg/m^3. The bar was instrumented with two diametrically opposed 350 Ω foil strain gauges, of gauge length 2 mm, at an axial location 233 mm from the shoulder of the impact end. The strain gauges are Kyowa KFP-2-350-C1-65L1M2R gauges, which provide the closest match to the PC thermal expansion coefficient of 65 to 70 $\times 10^{-6}/^{\circ}C$. The strain gauge bridge was completed with two dummy gauges mounted on a piece of PC. Due to the relatively high strains experienced by the PC bar, bridge excitation voltages of 1 to 2 V were used to prevent clipping of the signal.

The impacter end of the bar had a threaded attachment, made of Aluminium 6061, which supported a transverse ϕ 10 mm steel cylinder. This cylinder served as the central impacter, shown in Figure 5.10. In order to provide a lip to retain the cylinder, the attachment had an outer diameter of 15 mm. The impacter attachment had a total length of 16 mm. The cylinder and threaded attachment had a total mass of 45 g.

This mass was considered sufficiently small for inertia effects to not obscure the force measurements. The wave transit time for this attachment is approximately 3 μs. A cylindrical object typically requires 4 to 6 reflections of a stress wave before the forces on its ends vary by less than 5 % [186]. Thus the attachment should be equilibrated within 18 μs. Given that the bending impact events were expected to exceed 1 ms durations, a "ring-up" time of 18 μs is negligible. The transverse cylinder was press fitted into the attachment head, to ensure good contact and which facilitates stress wave transmission with minimal disruption.

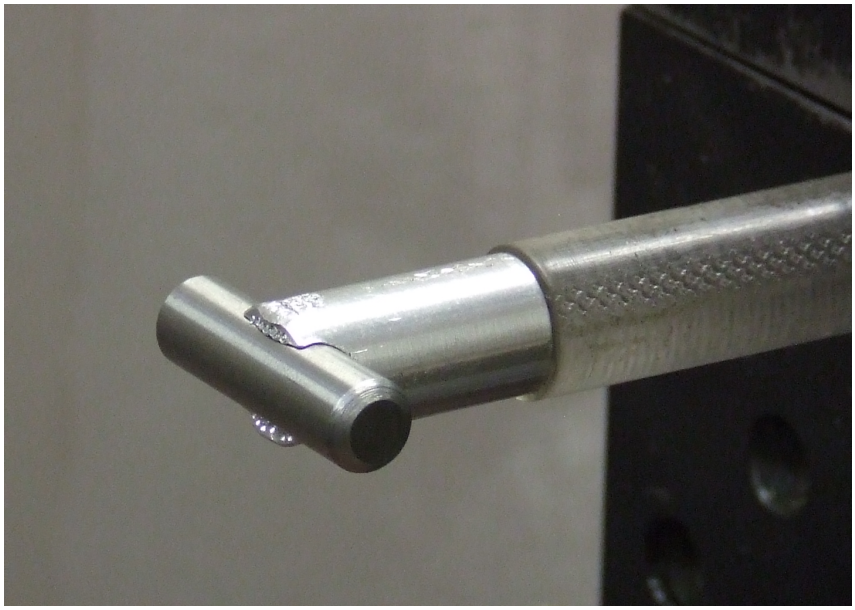

Figure 5.10: Head attachment of HPB

In order to account for the visco-elastic wave propagation in a PC HPB, a dispersion and attenuation correction technique was implemented. This technique was originally reported by Bacon [187] and investigated at BISRU by Curry [185]. An explanation of these techniques may be found in Appendix B, along with the author's implementation as scripts. The correction for visco-elastic effects follows a similar process to that of dispersion correction in a linear elastic HPB, as described in §4.3.6. Dispersion correction for linear elastic bars corrects for the variation in phase velocity C_p with frequency ω by applying a phase shift which varies with frequency, to the Fourier components of a given wave (Eq. 4.9). Correction for visco-elastic wave propagation also applies a phase shift to the Fourier components. In an elastic HPB, the variation in C_p with respect to ω is due to radial inertia. In a polymeric HPB, the visco-elastic nature of the material causes C_p to vary with ω. The relationship between C_p and ω for the PC bar used is shown in Figure 5.11. In addition, the viscous effects cause an attenuation of the magnitude of the waves, which also varies with ω. The attenuation coefficient $\alpha(\omega)$,

which is a logarithmic ratio of the magnitude of the Fourier components, is shown in Figure 5.12.

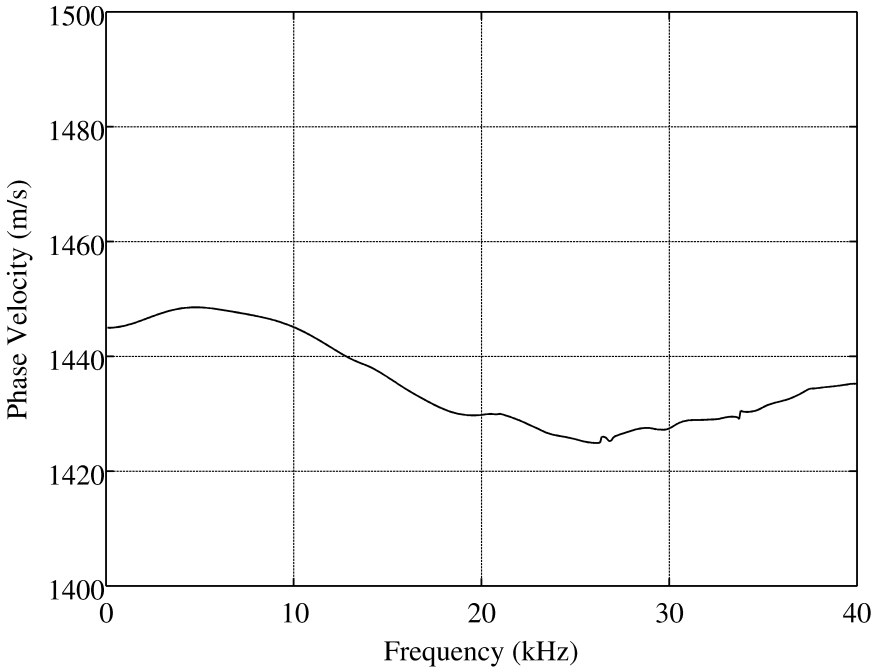

Figure 5.11: Variation of C_p with ω for polycarbonate HPB

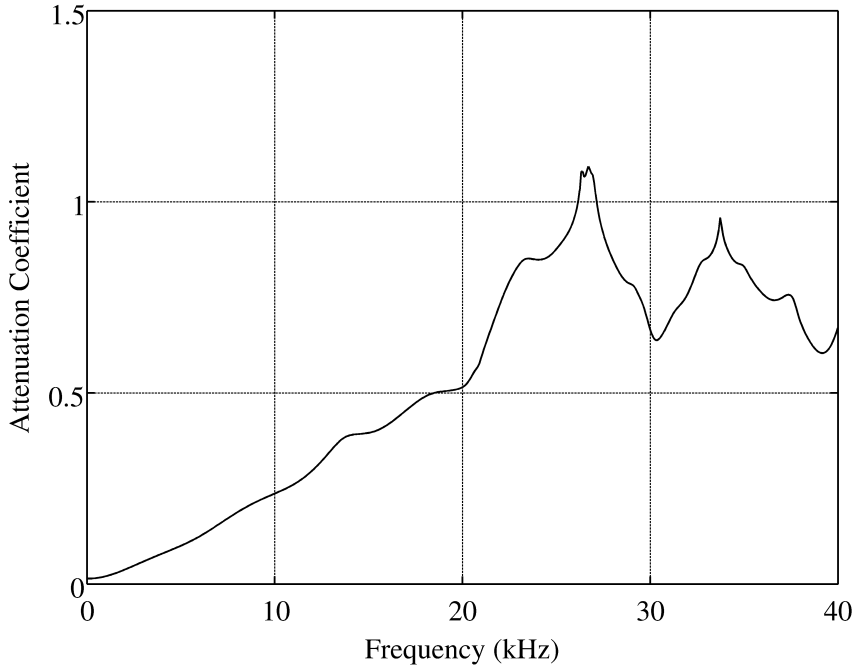

Figure 5.12: Variation of attenuation coefficient α with ω for polycarbonate HPB

The correction for dispersion and attenuation are applied simultaneously to the Fourier components by :

$$\boldsymbol{\varepsilon^i(\omega)} = \boldsymbol{\varepsilon^g(\omega)} e^{\alpha(\omega)+i\omega\frac{Z}{C_p(\omega)}} \tag{5.5}$$

The calibration for stress level in the PC HPB is achieved in a similar manner to that for a elastic HPB. However, it is essential that the wave is shifted from the gauge station back to the impact face to correct for attenuation. The details of the calibration tests may be found in App. B.4. The important parameters for the PC HPB are summarised in Table 5.4.

Table 5.4: Polycarbonate HPB Bar Parameters

Parameter	**Value**
Wave Speed $C_o(m/s)$	1450
Density kg/m^3	1196
Elastic Modulus $E_y(GPa)$	2.52
$\kappa_{cal}(MPa)$	2.432

5.2.4 High Speed Video

High speed video of the experiments was essential for the delamination tests, to monitor crack propagation, and desirable for simple bend tests to monitor specimen response and impacter velocity. Video of the impact bend experiments was recorded using a Photron APX-RS high speed camera, mounted with a Nikon Nikkor f1.4 50 mm fixed focal length lense. The APX-RS has a 1 MegaPixel CMOS sensor. However, data transfer limitations restrict the resolution of image captured as the frame rate is increased. The window containing all areas of interest was 384 pixels wide, by 256 pixels high. This permitted a frame rate of 22 500 frames per second (fps), which translates to 44.4 μs between frames. Available lighting allowed a shutter speed of 33 μs. The camera was positioned perpendicular to the bar axis, level with the bar. The camera was operated via the Photron FPV software.

The video recorded by the camera was stored both as AVI video for qualitative assessment, and as a sequence of JPEG images for any quantitative analysis. The JPEG images were annotated with the frame number and a time stamp. The frame showing initial impact between specimen and HPB was easily distinguishable from the frames

prior to impact. This meant that the uncertainty in time of impact was 44.4 μs, the time between frames. The duration of the measured force was almost 2400 μs which gives a syncronisation uncertainty between the video and DAQ time bases of less than 2%, which was considered acceptable.

5.2.5 Impact Bend Test Specimens

The relevant dimensions of the specimens tested with the Impact Bend HPB are given in Table 5.5:

Table 5.5: Bend test specimen dimensions

Material	Width (mm)	Thickness (mm)	Support Span (mm)
GFPP	25	2.7	50
GFPP	25	4.0	64
FML (2/1)	25	4.0	64

The specimen dimensions and lay-ups are the same as described in §5.1. The impact velocity required to induce failure in the different specimens was not known *a priori*. To minimise specimen wastage, the initial test of each series was conducted at a relatively high velocity, to maximise the probability of specimen failure within the duration limitations. Based on high speed video of each initial test, and a quick visual assessment of the degree of failure within the specimen, impacter velocities were adjusted appropriately for the remaining specimens in the series.

5.2.6 Data Processing of a Typical HPB Impact Bend Test

A plot of the typical signals captured during an impact bend test is shown in Figure 5.13. The first step is to shift the HPB strain gauge voltage from the axial position of the strain gauge to the impact tip of the bar, using the procedures described in App. B. The time of impact is determined from the time at which the strain gauge voltage is 50% greater than the typical noise amplitude.

As the distance from the strain gauge to the distal free end of the bar is 1753 mm, and the C_o in the PC bar is 1450 m/s, the time taken for the reflected wave to reach the strain gauge is 2.42 ms, referred to as the wave transit time. Hence the strain gauge

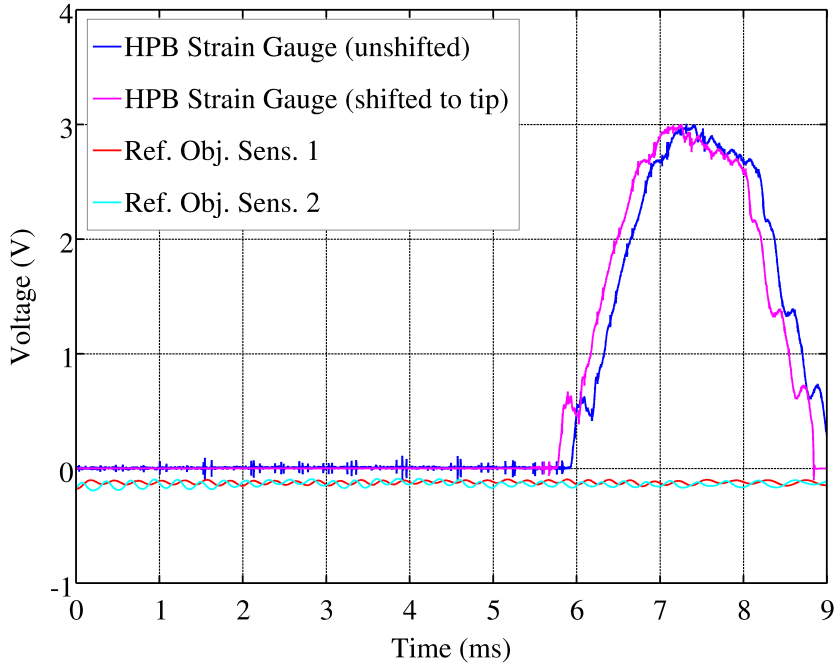

Figure 5.13: Plot of shifted and original strain gauge voltages

signal from 2.42 ms after the time of impact is discarded, as this represents a superimposition of the incident and reflected waves. [2] The strain gauge voltage is converted to axial stress using an experimentally determined conversion factor (detailed in App. B.4) and then to axial force at the HPB tip. A typical force-time response is shown in Figure 5.14. This force is used to calculate bending stresses in the specimen, using the simple quasi-static, linear elastic form of Eq. 5.1. The initial oscillations are probably due to bending waves - these are discussed further in §7.2.1. However, the force from approximately 30% of the peak magnitude follows a linear trend, with some minor superimposed oscillations.

The peaks and troughs of the ROS voltage are located using the script detailed in Appendix D.1. The displacement-time response of the impacter is determined for the entire signal capture of 9 ms, as shown in Figure 5.15. The blue data points are the discrete displacement-time points for the impacter over the entire signal. The magenta data points show the response during impact. The green linear trend line is based on the 20 data points immediately preceding impact, which corresponds to approximately 15 mm of travel. As the impacter has approximately 25 mm of travel, between the posi-

[2]The addition of a second strain gauge station a short distance from the first, and the application of wave deconstruction techniques, would permit capture durations exceeding the wave transit time. This was unnecessary for the specimens tested in this thesis, and is thus left for future work.

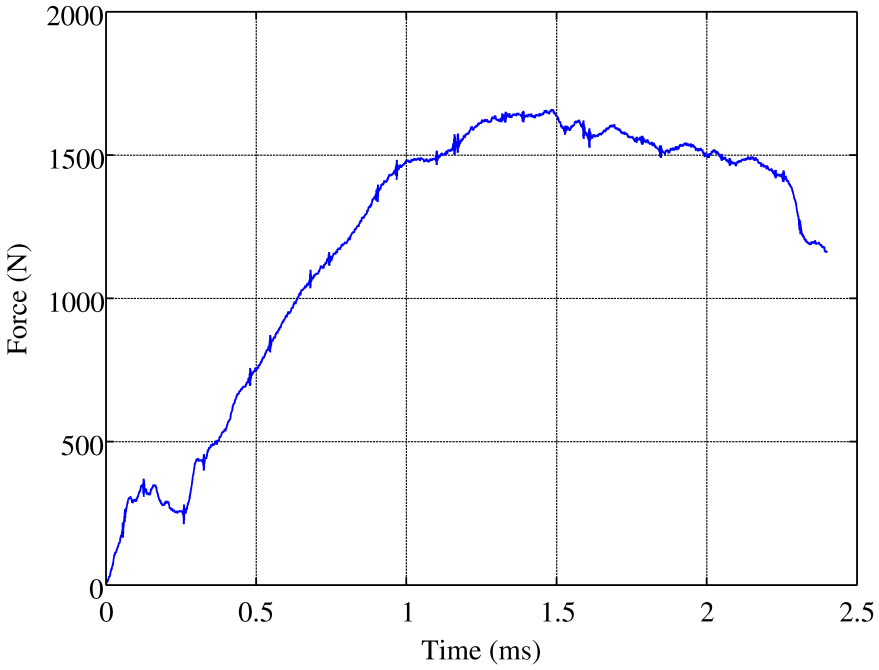

Figure 5.14: Plot of force at the HPB tip, on a zeroed time scale

tion where the pusher bar is arrested and impacting the HPB, these 20 points represent the impacter in as close to "free flight" as practically obtainable. The slope of this line is used to determine the velocity of the impacter. In this region of travel prior to impact, the close fit between the data points and the trend line indicate that the impacter is travelling at relatively constant velocity. Hence the effect of any friction between the impacter and its axial guides is negligible.

The discrepancy between the linear trend and the data below 2.5 ms is because the impacter is still being accelerated by the pusher at this point. The deceleration during impact is shown by the deviation of the impacter displacement from the linear trend line. The decrease in velocity of the impacter is less than originally expected. This necessitated the addition of a secondary stopper to arrest the impacter before the first bar support.

The specimen deflection is the difference between the displacements of the impacter and the HPB tip. The velocity of the HPB tip is obtained from Eq. 4.14, which is integrated to obtain displacement. The displacements and resulting specimen deflection are plotted in Figure 5.16. The HPB tip displacement is plotted as a solid line, as it uses the original time step of the DAQ system, with 0.1 μs between data points. The time steps between displacement points obtained from the ROS are larger due to the finite

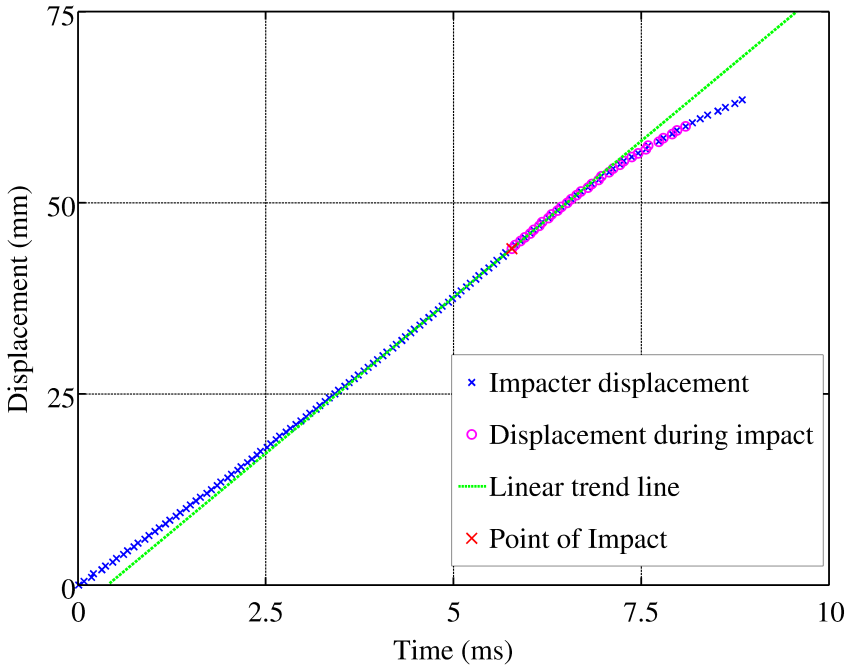

Figure 5.15: Plot of displacement history of the impacter

pitch of the light and dark graduations. The midpoint deflection-time response of the specimen will be a continuous, smooth function after the initial impact. The specimen deflection data on the ROS time base are fitted with a cubic polynomial using the finer time base of the HPB tip displacement. The small variations between some of the discrete ROS displacement data points and the polynomial are artefacts of the ROS data processing. If an individual peak is particularly noisy, the peak finding algorithm employed would report a time that was offset slightly from the actual peak. The error in reported displacement-time for the individual datum point does not affect other data points in the same signal. While one cannot interrogate an individual displacement-time point from the ROS with great accuracy, the response over an experiment shows a clear trend.

The polynomial fit for the displacement-time response is easily differentiated to obtain the acceleration of the impacter. Differentiation of the original ROS displacement data on the coarse time base would result in a very noisy acceleration signal, with spurious large spikes. Differentiating the polynomial fit yields a smooth, continuous acceleration curve. The force associated with specimen deflection is obtained by subtracting the inertial force of the impacter:

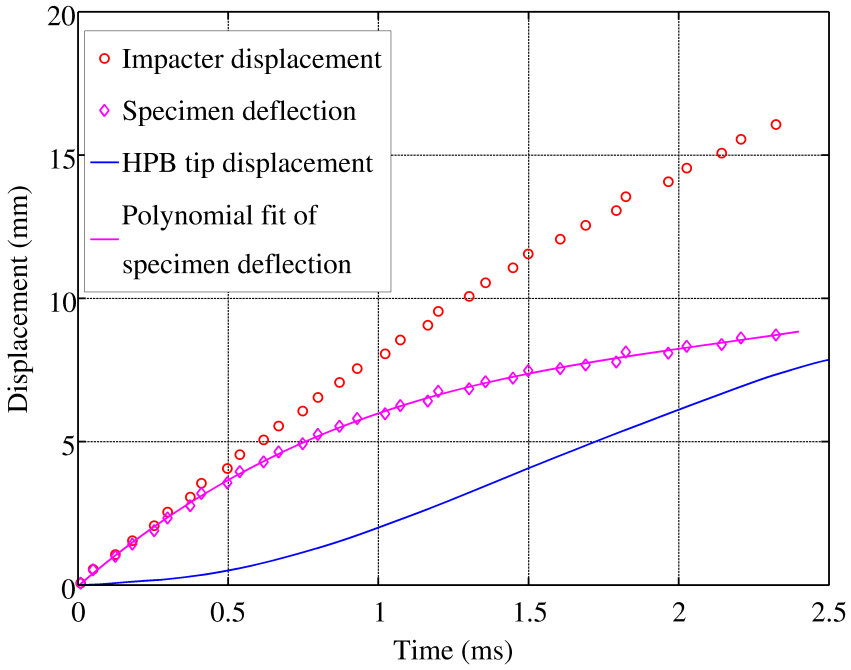

Figure 5.16: Plot of deflection of specimen, obtained from impacter and HPB displacments

$$F_{Spec}(t) = F_{Bar}(t) - m_{Imp}a_{Imp}(t) \tag{5.6}$$

It should be noted that maximum acceleration of the impacter occurs at the point of impact, and is approximately 10 - 15 m/s^2. By the time the specimen reaches maximum force, the impacter acceleration has reduced to 2-4 m/s^2. As the impacter mass is fractionally less than 1 kg, and the peak forces during a test range from several hundred to more than one thousand Newtons, the impacter inertial force is negligible.

The specimen force-displacement response may be obtained by two means:

- The displacement-time response from the polynomial fit, shown in Figure 5.16, is calculated over the original, fine time base of the DAQ system.
- The force signal is interpolated to the reduced, relatively coarse time base of the ROS output.

The specimen force-displacement response from both methods is shown in Figure 5.17. There is close correlation for the majority of the data. It should be noted that the coarse time base of the ROS output may result in features (such as early peaks or

oscillations) of the force signal being missed. Hence the force-displacement response on the fine time base is always plotted to ensure these features are visible.

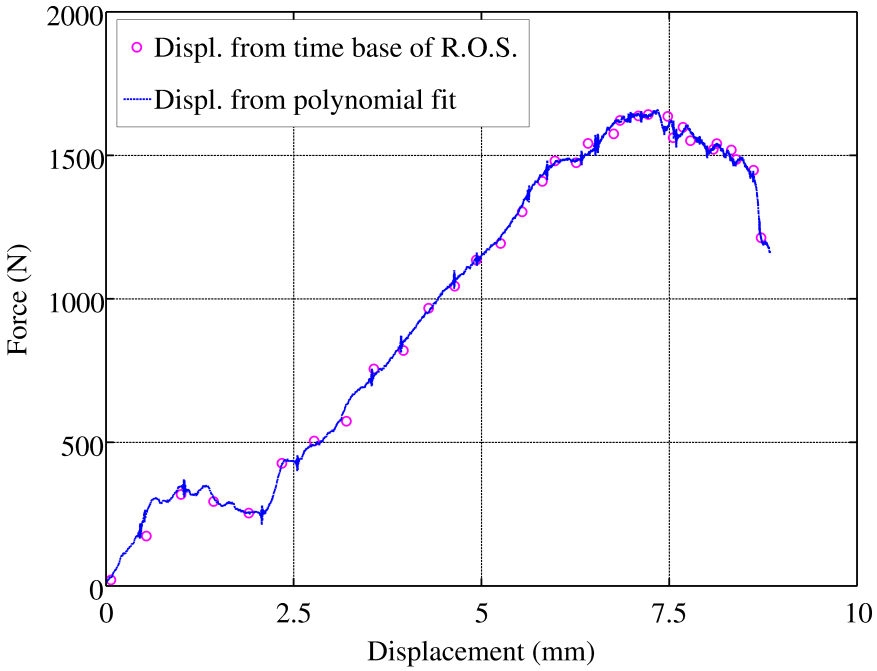

Figure 5.17: Force displacement response of a typical impact bend test

5.3 Results of HPB Impact Bend Tests

5.3.1 HPB Impact Bend Test of GFPP

Typical force-displacement responses for the 2.7 mm and 4.0 mm GFPP specimens, using the HPB based impact bending rig, are shown in Figure 5.18 and 5.19 respectively. A common feature of both series is the initial oscillation of the force, followed by an approximately linear region. Possible reasons for the oscillations are discussed below. The reported strength is calculated from the first local peak in the force, after the departure from a linear response (indicated by a red X). The force-displacement responses for all specimens in both series are shown in Figures 5.20 and 5.21 respectively.

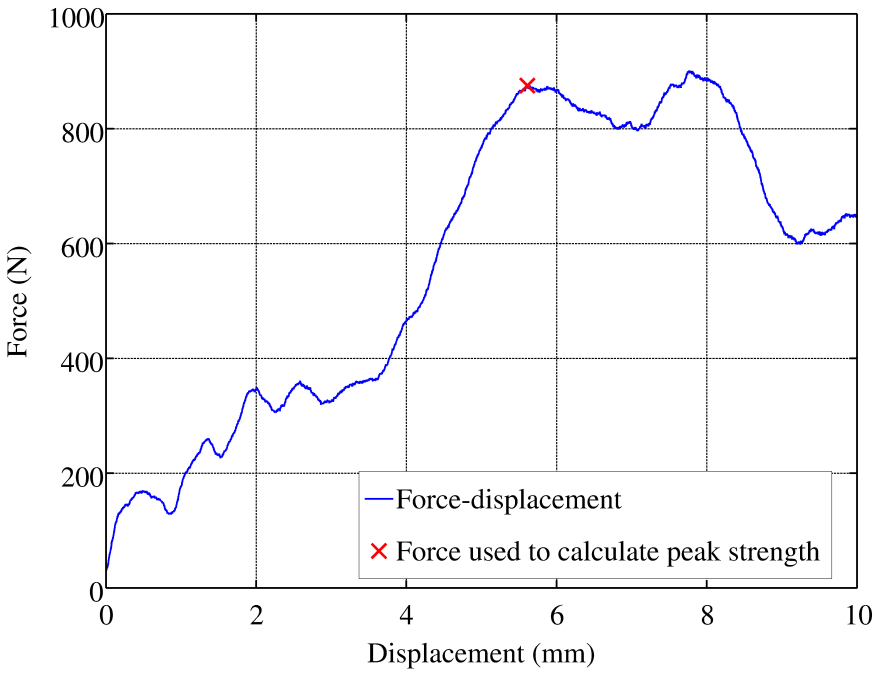

Figure 5.18: Plot of unfiltered force-displacement response for a typical HPB Impact Bend test of 2.7 mm thick GFPP specimen

The early oscillations present for both sets of specimens do not persist beyond a force of approximately 400 N, and therefore do not affect the the peak force which is used to calculated flexural strength. This is a substantial improvement over signals obtained from instrumented drop weight rigs, where the superimposed oscillations persist for the duration of the test (see Figure 2.33). The oscillatory behaviour is discussed in detail in §7.2.1.

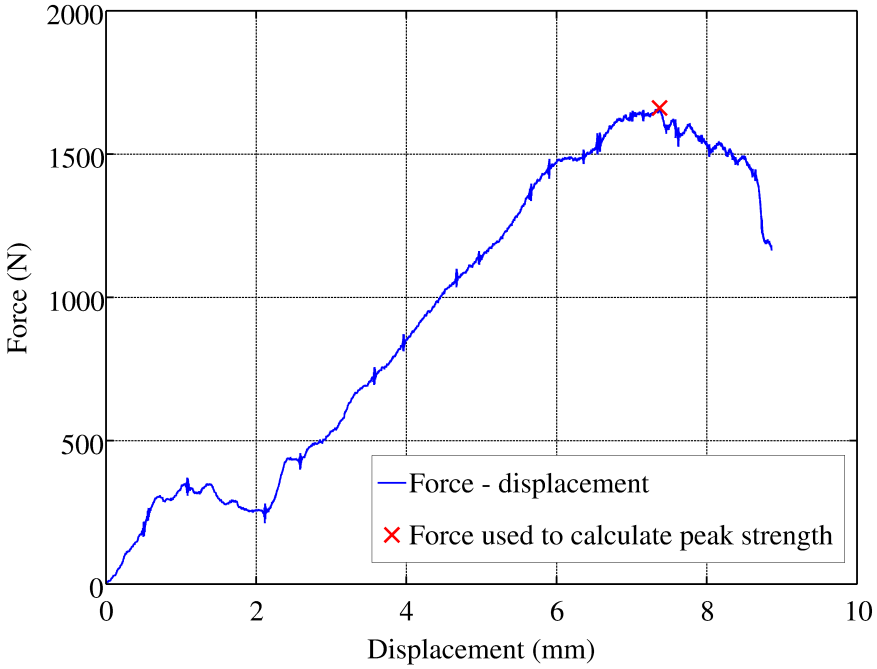

Figure 5.19: Plot of unfiltered force-displacement response for a typical HPB Impact Bend test of 4 mm thick GFPP specimen

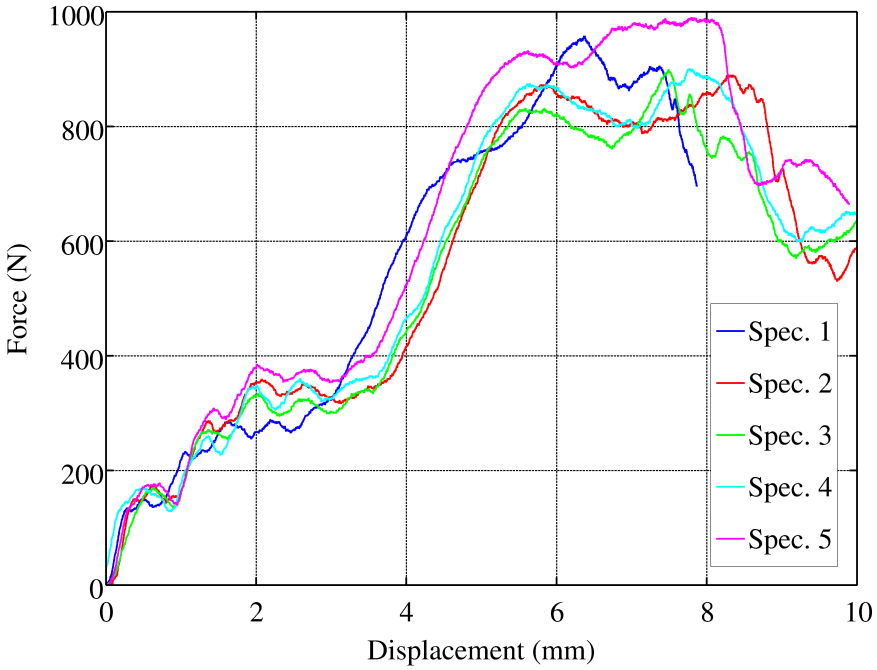

Figure 5.20: Plot of force-displacement response for HPB Impact Bend tests of 2.7 mm thick specimens

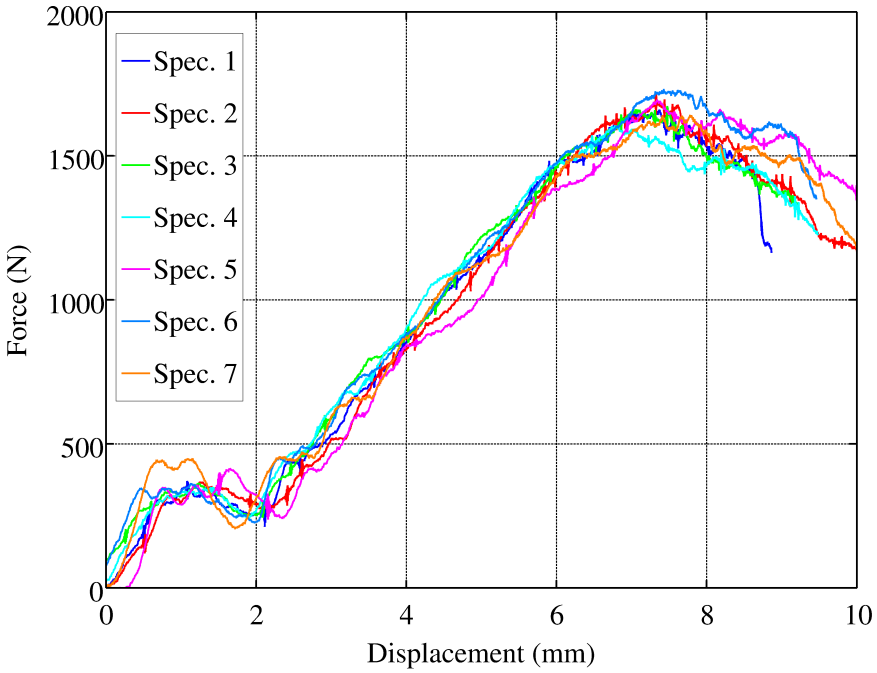

Figure 5.21: Plot of force-displacement response for HPB Impact Bend tests of 4 mm thick specimens

f

Frames from high speed video of a HPB Impact Bend test on a 2.7 mm thick GFPP specimen are shown in Figure 5.22. There is a marked difference in shape of the specimen between Figure 5.22(c) and 5.22(d): the specimen deflection profile changes from a smooth, parabolic form to a relatively straight sided 'V', with a sharp corner under the impact point. The sharp V-profile indicates that significant fibre failure has occurred by this time, which is approximately 1.96 ms after impact. Figure 5.22(c) corresponds to the peak indicated by the red X in Figure 5.18 at a displacement of approximately 6 mm, while Figure 5.22(c) corresponds to the drop after the second peak approximately 8 mm of displacement. It should be noted that the second peak is 2.0 % higher than the first peak. However, the flexural strength is calculated from the first peak as :

- The first peak is lower and therefore the more conservative measure of strength
- There has definitely been failure of a substantial portion of the fibres by the second peak, suggesting the the initiation of failure corresponds to the first peak

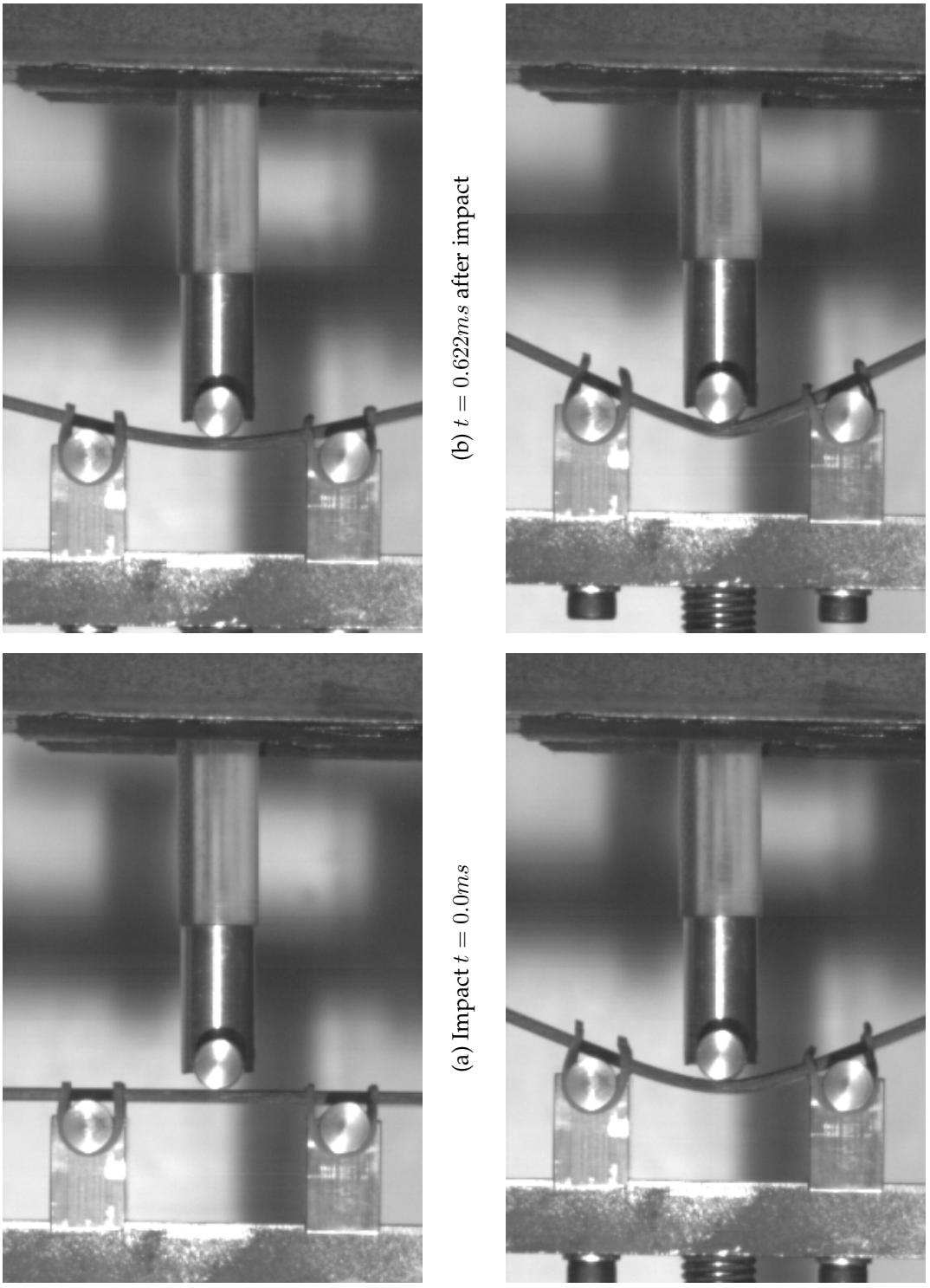

(a) Impact $t = 0.0ms$ (b) $t = 0.622ms$ after impact

(c) $t = 1.289ms$ after impact (d) $t = 1.956ms$ after impact

Figure 5.22: Frames from high speed video of HPB Impact Bend test of 2.7 mm GFPP specimen

The results of the HPB Impact Bend tests on GFPP are summarised in Table 5.6. A range of initial impacter velocities are reported and it is noted that the impacter velocity decreases during individual tests. The stresses calculated are based on the quasi-static, linear elastic relationships described in §5.1.1. Strain at the outer fibre can be determined from Eq. 5.2, and differentiated with respect to time to obtain strain rate. An example of strain rate for a typical test is shown in Figure 5.23. The strain rate varies with impacter velocity, and hence is maximum at the start before decaying as impacter velocity decreases during the test. The strain rate reported is the mean value for the duration of impact.

Table 5.6: HPB impact bend test results for GFPP

Parameter	2.7 mm Thickness	4.0 mm Thickness
Mean Width (mm)	24.6	24.6
Impact Velocity (m/s)	5.7 - 6.7	7.8 - 8.5
Mean Flexural Strength (MPa)	373.4	386.9
Peak Stress COV (%)	2.9 %	4.4 %
Flexural Modulus (GPa)	X	11.3
Flexural Modulus COV (%)	X	5.2 %
Mean Strain at Peak Force (%)	X	3.7%
Strain at peak COV (%)	X	3.5%
Mean Strain Rate ($/s$)	26.4	24.9

Due to the relatively small region with a linear reponse of the tests on 2.7 mm specimens, it was not possible to determine a sensible flexural modulus from this data. As the 4.0 mm specimens exhibit a linear response over a much longer section of the test (Figure 5.24), it was possible to estimate a flexural modulus from the test data. The initial oscillations in the test data cause the intercept of any linear fit to be offset from the origin. This offset is taken into account when determining the failure strain reported in Table 5.6.

The results of the flexural strength for all rates and thicknesses is shown in Figure 5.25. The logarithmic, Johnson-Cook type rate model used for the compression data (§4.28) was fitted to the data, and is also plotted in Figure 5.25. For flexural strength, the model becomes:

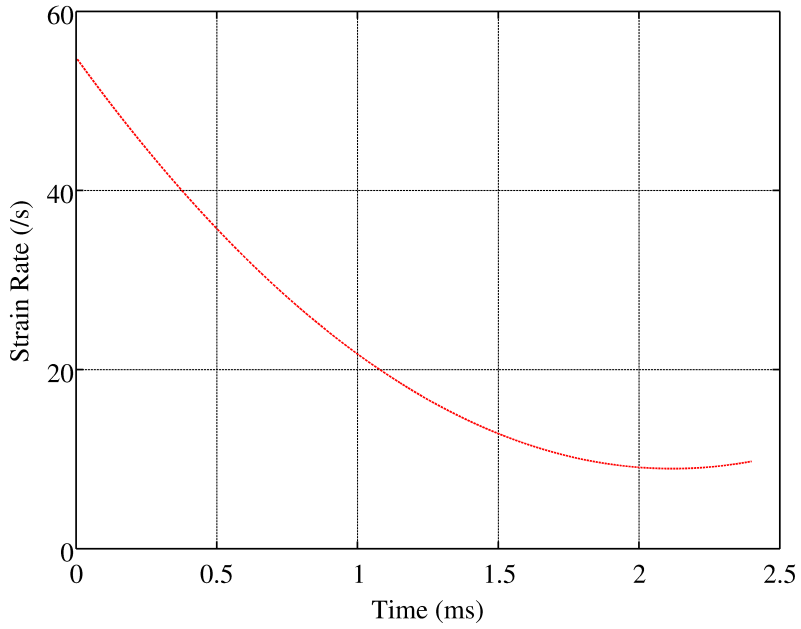

Figure 5.23: Plot of strain rate variation during a typical HPB Impact Bend test on GFPP

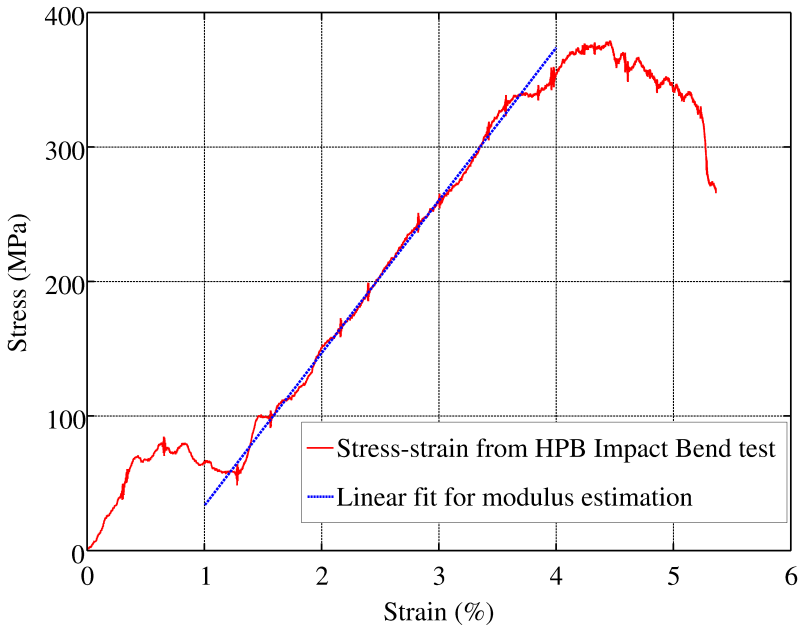

Figure 5.24: Plot of HPB Impact Bend test stress-strain response, with linear fit for modulus estimation

$$\sigma_{Flex} = 352.6(1 + 0.0238\, ln(\dot{\varepsilon})) \quad MPa \tag{5.7}$$

The correlation coefficient R^2 for this fit is 0.98.

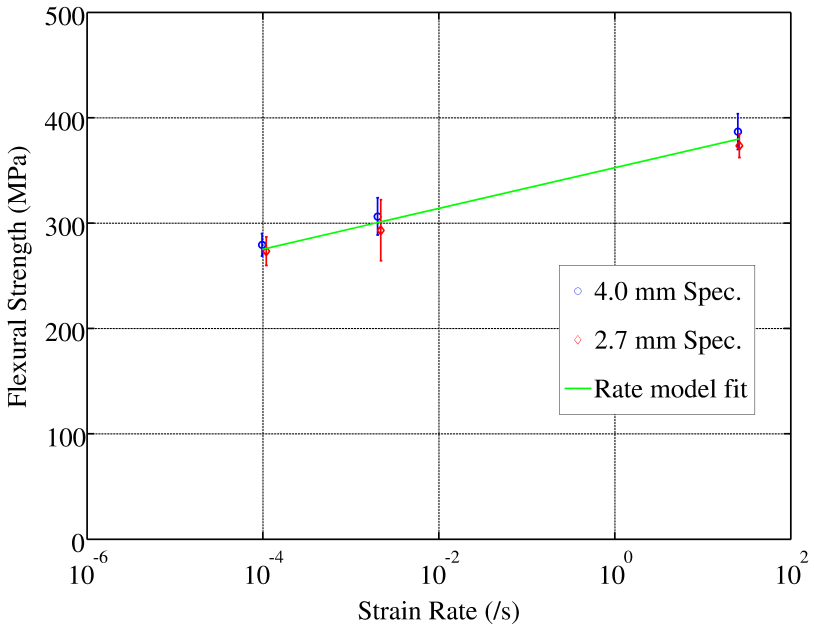

Figure 5.25: Plot comparing flexural strength of GFPP specimens at all rates

A similar fit was performed for the flexural failure strain data for the 4 mm thick specimens. The rate dependence model for the failure strain is:

$$\varepsilon_{Flex} = 3.45(1 + 0.0207\, ln(\dot{\varepsilon}))\% \tag{5.8}$$

The slope of the failure strain model (0.0207) is comparable to that of the flexural strength model (0.0238). As GFPP behaves in a linear elastic manner up to failure, it is not surprising that the rate dependence of the flexural strength and flexural failure strain correlate. The flexural modulus data is presented in Figure 5.26. For the range of strain rates examined, the variation in modulus is smaller than one standard deviation of the data. *Hence the flexural modulus of GFPP may be considered insensitive to strain rate.*

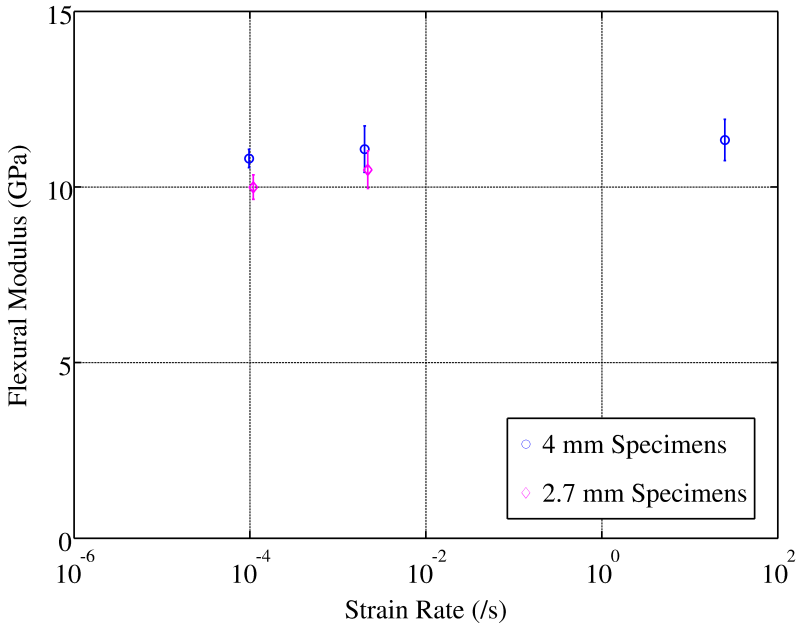

Figure 5.26: Plot comparing flexural modulus of GFPP specimens at all rates

5.3.2 HPB Impact Bend Tests of FMLs

The force-displacement results for HPB Impact Bend tests of aluminium-GFPP FMLs are shown in Figure 5.27. As with the other impact bend tests, there is oscillation in the initial portion of the data, due to bending waves. Once the oscillations settle, the response follows a similar trend to the quasi-static tests. Unfortunately, the oscillations obscure the transition from the linear, elastic deformation regime, to the regime driven by plasticity in the aluminium layers.

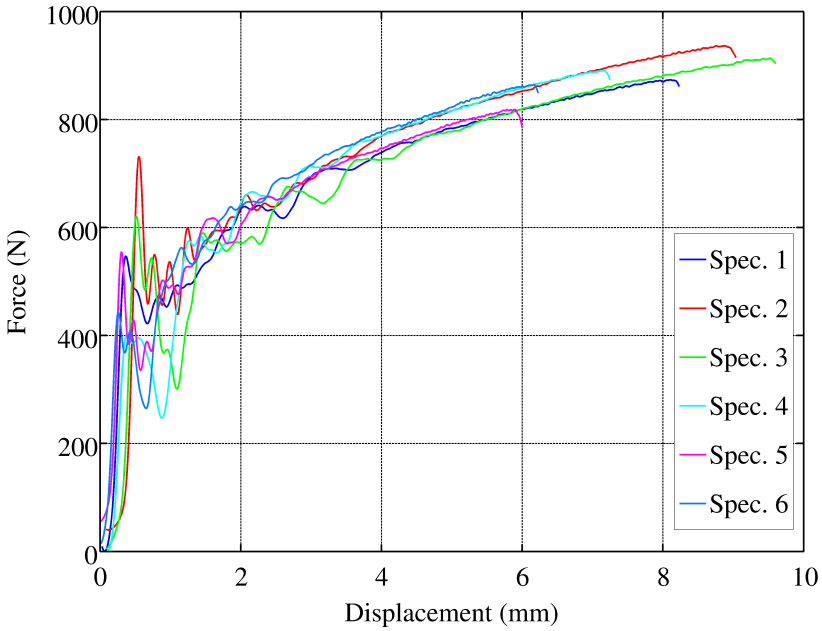

Figure 5.27: Plot of force-displacement response of FML specimens to HPB Impact Bend test

The mean force-displacement response, as well as the envelope of all the data, is plotted for the quasi-static and HPB tests in Figure 5.28. The data for the initial, oscillatory portion of the HPB Impact Bend tests is omitted for clarity. Very little rate dependence may be observed in Figure 5.28. The mean response for tests at 1 mm/min is slightly lower than the mean for 20 mm/min, but lies within the minimum envelope of the 20 mm/min data. The HPB Impact Bend test data is initially lower than both quasi-static tests, but rises to marginally above the maximum envelopes for the quasi-static data.

The weak dependence of the FML's response with respect to strain rate is not surprising as the specimen's flexural response is governed largely by the material furthest from the neutral axis, which in this case is Aluminium 1200 H4. Stander [188] found

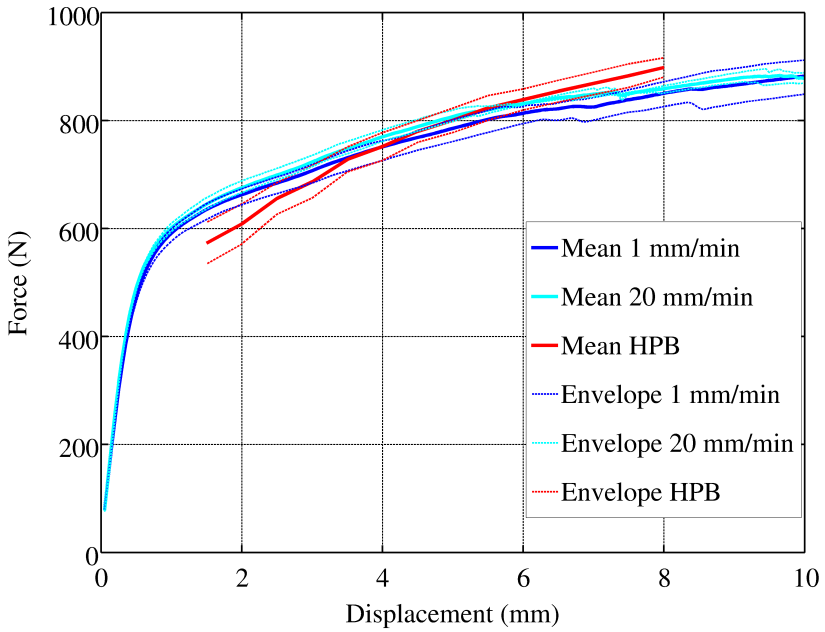

Figure 5.28: Plot of force-displacement response of FML specimens for quasi-static and HPB tests

the response of similar aluminium alloys at strain rates ranging from $10^{-3}/s$ to $10^{3}/s$ in compression to be insensitive to strain rate. The GFPP layers are closer to the neutral axis and therefore the rate dependence of the GFPP has less influence on the macroscopic response of the specimen.

The FML specimens under bending display insignificant dependence on strain rate for strains exceeding the elastic limit. The transition from elastic to plastic response for the HPB Impact Bend tests is obscured by oscillations in the data.

5.4 Summary

A novel impact bend test apparatus based on a HPB is presented. This arrangement permits higher impact velocities than drop weight apparatus, and is capable of measuring greater specimen deflections than bend apparatus using an input HPB to load the specimen. The use of an output HPB as opposed to an input HPB to measure the central force on a bend test provides better resolution of the force measurement. The absence of large support fixtures on the output HPB mean the force measurement is not obscured by fixture inertia.

Bend tests at displacement rates ranging from 1 mm/min to approximately 8 m/s (corresponding to peak strain rates ranging from $10^{-4}/s$ to approximately $2 \times 10^{1}/s$) were conducted on GFPP and Aluminium-GFPP FML specimens. The flexural strength of GFPP increased with strain rate, and was fitted using the linear logarithmic rate model. The flexural modulus of GFPP was insensitive to strain rate for the range investigated. The flexural response of the FML specimens was rate insensitive, due to the low rate sensitivity of the aluminium outer skins of the FML.

Chapter 6

Delamination Tests

The delamination test program is described in this chapter. Part of the scope of this thesis was to develop a high strain rate / impact test where properties pertinent to delamination, such as interlaminar shear strength or delamination fracture toughness could be measured. Several candidate test methods were first evaluated as quasi-static tests. Each test method was evaluated in terms of:

- Simplicity of specimen manufacture and required loading fixtures
- Validity of results - the presence of failure modes other than delamination would invalidate the test
- Repeatability of results
- Potential for adaptation to higher rate testing

The reasons for rejection of some of the test methods and geometries is detailed in the description of the results for those tests. The implemented high rate delamination test method, as well as the results of its application of GFPP and FML specimens, is presented. The results for quasi-static and high rate delamination tests are compared.

6.1 Interlaminar Shear Strength Tests

6.1.1 Lap Shear

6.1.1.1 Experimental Details

Lap shear tests had been adapted to high strain rate testing by Harding and colleagues [40, 41, 42] as reviewed in §2.3.1.2 and §2.7.5.2. FEA in these publications showed that a specimen with a Z-profile in lateral view minimised variation in shear stress across the gauge section. The profile and dimensions of the specimen, detailed in [42], were used as a starting point for this investigation, and are shown in Figure 6.1. The gauge section is nominally 12 mm long, and the entire specimen is 20 mm wide.

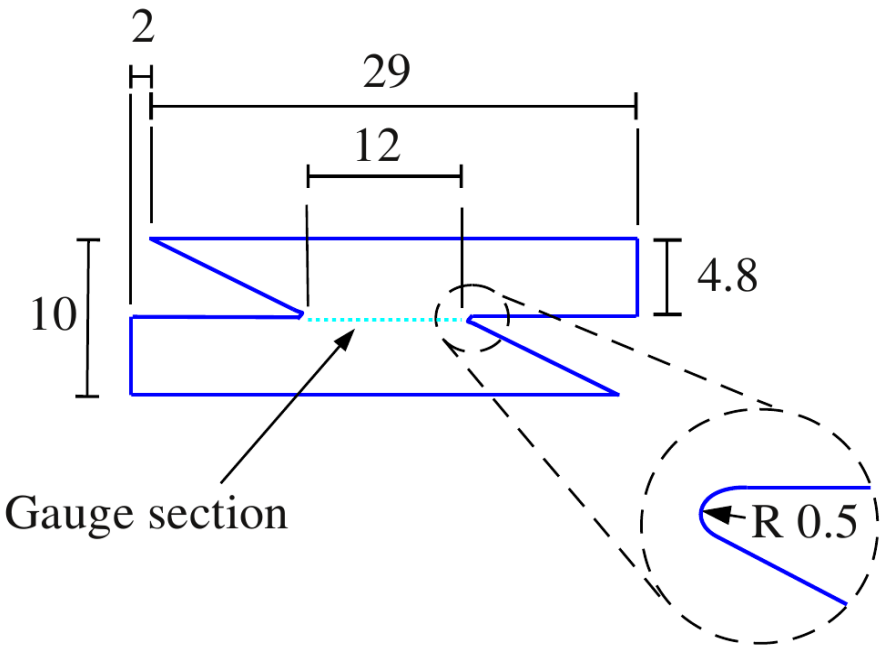

Figure 6.1: Schematic showing dimensions of Z-Shear specimen

Manufacture of these specimens was a non-trivial exercise. 44 plies of GFPP fabric were required to produce the 20 mm thick laminate, which required very careful lay-up to ensure a panel of even thickness. The specimens were cut using a two-stage water jet cutting process. The laminate was firstly cut into strips of 20 mm width. These strips were rotated through 90 °, and stacked side by side on a flat surface such that the fibre plane was now perpendicular to the surface. The strips were clamped together to prevent relative movement, and the entire strip and clamp assembly was positioned on the water jet cutting table. The Z-profile of the specimens was then cut, providing the

desired specimen geometry with the fibre planes appropriately aligned. The specimen end and side faces were polished using 500 grit SiC polishing paper.

The specimens were loaded using a custom adapter in the Zwick testing frame, shown in Figure 6.2. The ends were compressed together as this required the simplest loading adapters, as opposed to being pulled apart which would have required more complicated grips or glueing the specimen to the adapters. The specimen was constrained laterally by shoulders on the adapters. Ten specimens were tested at a cross head speed of 1 mm/min. The nominal interlaminar shear stress σ_{13} is calculated from Eq. 6.1.

$$\sigma_{13} = \frac{P}{wl_g} \tag{6.1}$$

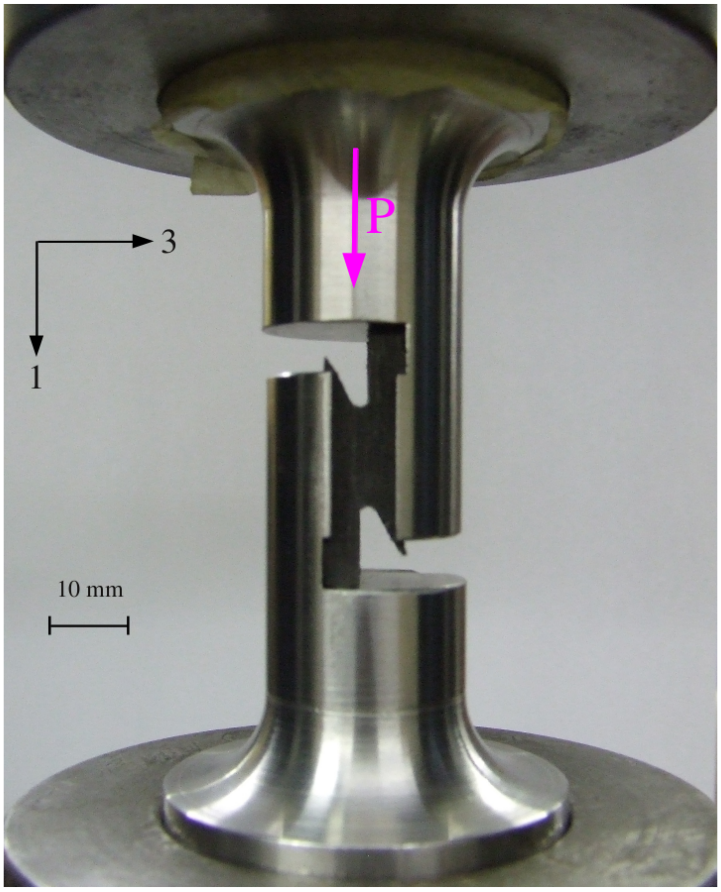

Figure 6.2: Z-Shear specimen, mounted in adapter in test frame

6.1.1.2 Results

All specimens tested exhibited clear interlaminar failure, with no other noticeable failure modes. The nominal shear stress of all the Z-Shear tests is shown in Figure 6.3. The scatter is unacceptable, with the peak stress having a COV of 59 %. Furthermore, even the peak value of σ_{13} for all tests was 3.8 MPa - less than a third of the 13 MPa value quoted in the GFPP data sheet [19]. Possible reasons for the substantial scatter and lower than expected shear strength are:

- The notch radius at the gauge section was limited by the jet diameter in the water jet cutting process. It is uncertain how well controlled the jet diameter is at a sharp corner, but some variation in notch radius would be expected. Varying notch radii would lead to variations in stress concentration, and hence scatter in the perceived interlaminar shear strength.
- The two stage water jet cutting process, necessary to achieve the desired profile and fibre orientation, had never been attempted before by the company contracted to machine the specimens. The author was unable to find reference to similar machining processes. It is plausible that being subjected to two stages of water jet cutting, with the second stage having the jet parallel to the fibres, caused microscopic damage to the laminate. This would manifest as premature failure and lower shear strength. The specimen geometry makes visual inspection of the corner (where failure initiates) extremely difficult. Ultrasonic scanning of this region would be problematic due to the scattering of waves by the corner and angled face. Hence identifying machining damage at the critical location prior to testing is difficult, and would only eliminate the specimens that fail prematurely.
- This specimen geometry had in the past [41, 42, 40] only been applied to unidirectional CFRP laminates, prepared from prepreg. These specimens would have much flatter interlaminar profiles than those prepared from woven GFPP. The yarn width of 4 to 5 mm, is relatively large in comparison to the gauge length of 12 mm. This is a high degree of crimp which could contribute to scatter, as the gauge section will start at different points along the weave.

It should be noted that the two stage water jet cutting process was the only option locally available for machining the Z-profile from GFPP, and the manufacturing cost per specimen was relatively high. Specialised grinding tool profiles would be necessary to machine the required profile on a milling machine, which were not available. Laser cutting of a thermoplastic such as GFPP would be unlikely to produce

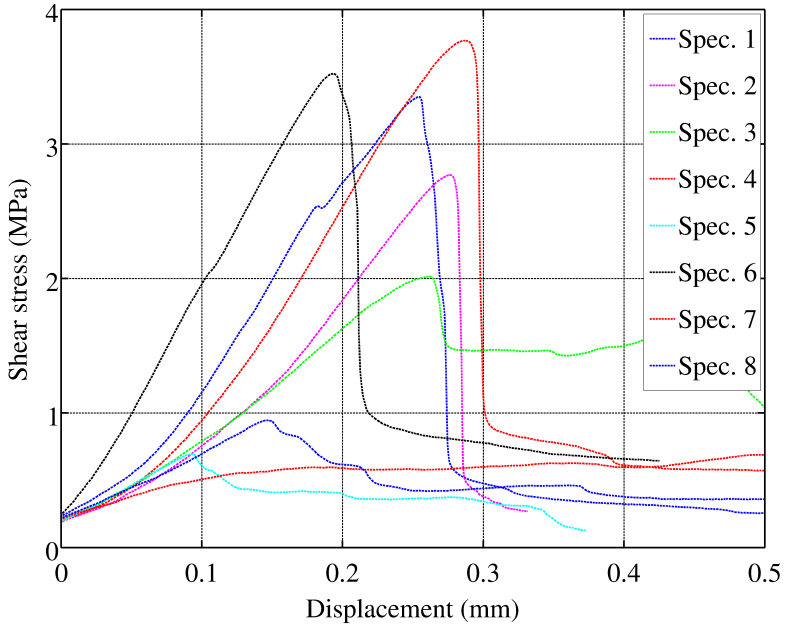

Figure 6.3: Shear stresses for Z-Shear tests

the tolerances and surface finish required due to differential melting of the matrix and fibres.The temperature gradients associated with laser cutting would also affect the matrix properties in an unknown manner.

Any further investigation of similar specimen geometries, with adjusted gauge lengths and differing notch radii, would still involve uncertainties in specimen integrity due to the machining process. Hence the Z-Shear test method was eliminated as a suitable delamination test method for woven GFPP at quasi-static or higher rates.

6.1.2 Short Beam Shear

6.1.2.1 Experimental Details

Short Beam Shear (SBS) testing has simple specimen and test geometry perspective, making it an obvious candidate for delamination testing. The SBS tests were conducted in accordance with ASTM D 2344 [31]. The test geometry is simply a Three Point bend test, with a very short support span, as shown earlier in Figure 2.7, in §2.3.1.3.

The specimens were of nominal thickness 7 mm and width 17 mm. The initial investigation showed that tests performed at a span-to-thickness ratio of 4.4 (span of 30 mm) performed better than the span-to-thickness ratio of 5.5 (span of 38 mm), which was recommended by Xie and Adams [45] based on FEA. All tests were conducted at a cross head speed of 1 mm/min. The modified SBS fixture with a rubber pad between specimen and central loader [47], was not used as it affects stress wave propagation as discussed in §2.3.1.3. The nominal interlaminar shear stress σ_{13} is calculated from [31]:

$$\sigma_{13} = \frac{3P}{4wt} \tag{6.2}$$

6.1.2.2 Results

The shear stresses derived from the Short Beam Shear (SBS) tests are plotted in Figure 6.4. The two dashed lines are the first two tests, conducted at a span of 38 mm. The solid lines are the remaining tests, which had a span of 30 mm and hence have a slightly stiffer response. The results are relatively closely grouped. The average apparent peak interlaminar shear strength of 20.5 MPa is substantially larger than the value of 13 MPa quoted in the data sheet [19], which was obtained via the Iosepescu test method. Santulli *et al* [86] reported apparent interlaminar shear strengths in the range of 25 to 30 MPa for SBS tests on GFPP, but did not present force-displacement curves or discuss other failure modes. The stress-displacement curves of all specimens developed non-linearities before reaching the respective peaks. During the tests, failure modes such as indentation, fibre buckling and kink banding were observed as well as the desired delamination as shown in Figure 6.5. The presence of these undesirable failure modes means the shear strength derived from these tests cannot be attributed exclusively to interlaminar shear. Hence the SBS test was eliminated as a candidate for delamination testing of woven GFPP at quasi-static and higher rates.

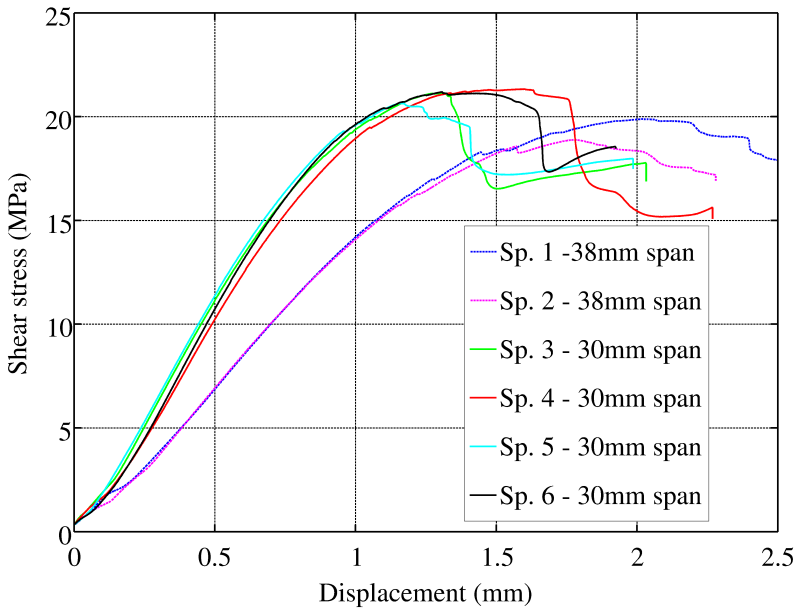

Figure 6.4: Plot of interlaminar shear stresses from Short Beam Shear tests of GFPP

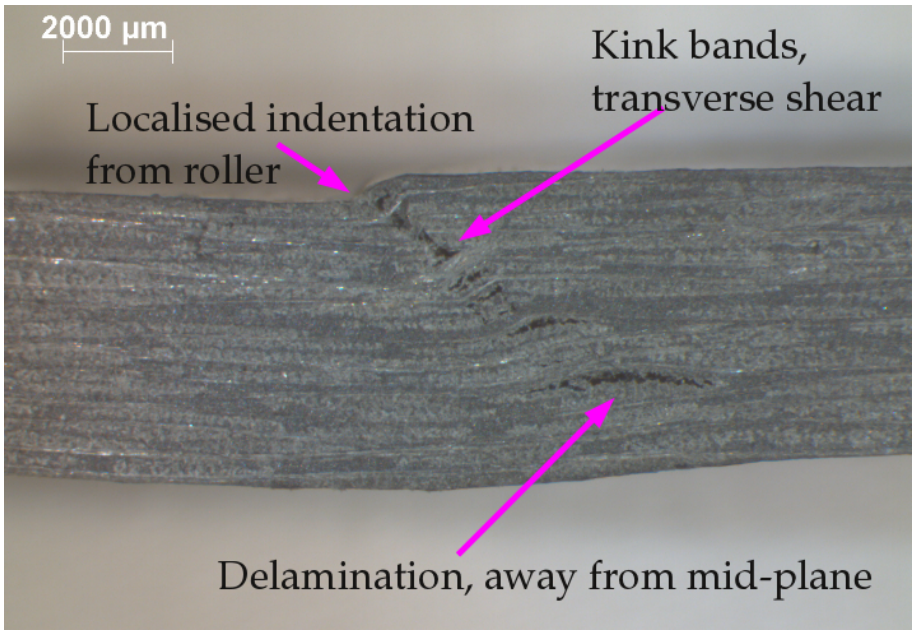

Figure 6.5: Photograph of failure modes present in typical SBS test (Specimen no. 4)

6.2 Fracture Mechanics Based Delamination Tests

The tests described in §6.1.1.1 and §6.1.2.1 attempt to measure the shear stress associated with delamination failure, with no predefined flaw. Fracture mechanics delamination tests aim to measure the fracture toughness or energy release rate associated with growth of a delamination from a known initial flaw.

6.2.1 Mode II Delamination via End Notch Flexure

6.2.1.1 Experimental Details

Mode II End Notch Flexure (ENF) testing has been the subject of much debate in the literature (for example [70]) and at present an ASTM standard is still under consideration. The test configuration followed commonalities of prior publications [55, 91, 66] as closely as possible.

ENF testing is based on 3 Point bend loading, as shown in Figure 6.6. The ENF specimens required a laminate with an induced flaw. This was achieved by inserting a folded piece of aluminium foil to the desired crack length, at the mid-plane during lay up. The nominal laminate thickness was 5 mm and specimen width w was 32 mm. All ENF testing was conducted at a support span of 120 mm, and a cross head speed of 1 mm/min. ENF tests were conducted on 4 specimens.

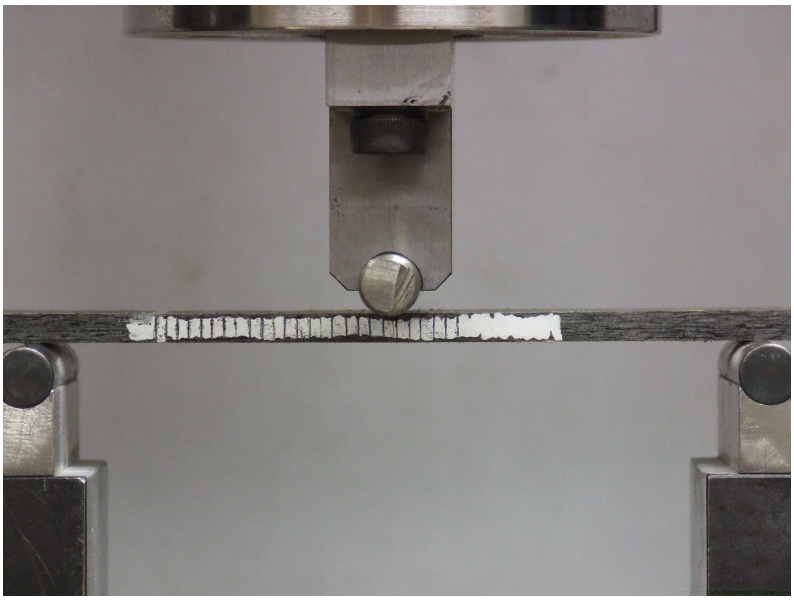

Figure 6.6: Photograph of End Notch Flexure specimen in Three Point bend fixture, prior to test

The strain energy release rate G is calculated from :

$$G = \frac{P^2}{2w}\frac{\partial C}{\partial a} \tag{6.3}$$

P is the applied force, C is the specimen compliance, a is the crack length and w is the specimen width.

The specimen compliance C as a function of crack length a was determined experimentally for each specimen. The specimen was positioned on the supports, with the crack tip at a known distance from one support. A relatively small (200 N) load was applied to the specimen and then removed. The inverse of the slope of the force-deflection curve gives the compliance, for the given crack length. By shifting the specimen laterally on the supports, a different effective crack length is obtained. This process was repeated from $a = 0$ (i.e. the crack tip outside the supports), in increments of 10 mm, to a total crack length of 50 mm. The experimentally measured compliance was then fit to a third order polynomial shown in Eq. 6.4.

$$C(a) = C_3^a a^3 + C_2^a a^2 + C_1^a a + C_0^a \tag{6.4}$$

The function $C(a)$ is differentiated for application in Equation 6.3, which gives the following relationship for G_{II}:

$$G_{II} = \frac{P^2}{2w}(3C_3^a a^2 + 2C_2^a a + C_1^a) \tag{6.5}$$

Crack position for all compliance calibration and delamination tests was measured from digital photographs. It was noted in [54] that this approach resulted in less scatter of the crack position data, but also less accuracy in comparison to measurements taken using either ultrasound (C-scan) or direct visual assessment. The following reasons motivated the use of measurement from digital photographs:

- During the high strain rate tests, high speed ($20000 fps$) digital photography is the only means available to the author to measure crack position. The tests cannot be interrupted, and the test durations of a few milliseconds totally preclude any direct visual assessment, ultrasonic or eddy current techniques.

- Fahr *et al* [189] noted that the eddy current method could not detect delamination in FMLs. Ultrasonic techniques could detect cracks if the FML specimen was

still flat, but any dent for example due to impact, obscured the delamination measurement.

Photographs of the ENF tests were taken with a Fuji S5000 camera, resulting in an image 2048 x 1536 pixels in size. Photographs were taken every 20 seconds, which was sufficient given that the ENF tests lasted approximately 20 minutes. The straight edges and corners of the central loading attachment were used to calibrate the images for size and any angular offset of the camera in the plane of the specimen. As the camera did not move relative to the central loading point, the same calibration could be applied to all the photographs from one test. This process was automated in a script, which may be found in App. D.2. The script also obtained the time stamp of each image, which accounted for variation in time steps between photographs due to the operator. The script output was an array of position and time.

The edge of the specimen was painted with white water based fluid, to increase contrast and aid crack tip identification. The edge was also marked with vertical graduations 2 mm apart, which were not used for length measurements but to aid crack tip identification. In Figure 6.7, the line markings under the central loader remain continuous as the crack has not reached this region yet. The line markings closer to the left hand support show a clear step at the crack plane. The line markings permit the crack tip position to be determined to within one line spacing (2 mm). However, more accurate measurement can become subjective, as Mode II crack tips appear fuzzy under high magnification, due to the presence of microcracks around the crack tip.

6.2.1.2 Unsymmetric End Notch Flexure Testing on FMLs

All FML delamination specimens were cut from a 1/1 panel, which consisted of a single, 3 mm thick aluminium layer and a single nominally 3 mm thick GFPP layer. The procedure for preparing fracture specimens with an initial flaw is described in §3.3. The side of the specimen was painted with white correction fluid to aid crack tip location. The FML ENF specimens were nominally 24 mm wide and 120 mm long. The support span chosen was 60 mm. Exploratory tests, which are not included in the reported data, indicated that the aluminium layers would develop plastic strains very early in the test at longer spans. The validity of the LEFM calculations decreases as the presence of plasticity in the specimen increases, hence the need to avoid plastic deformation.

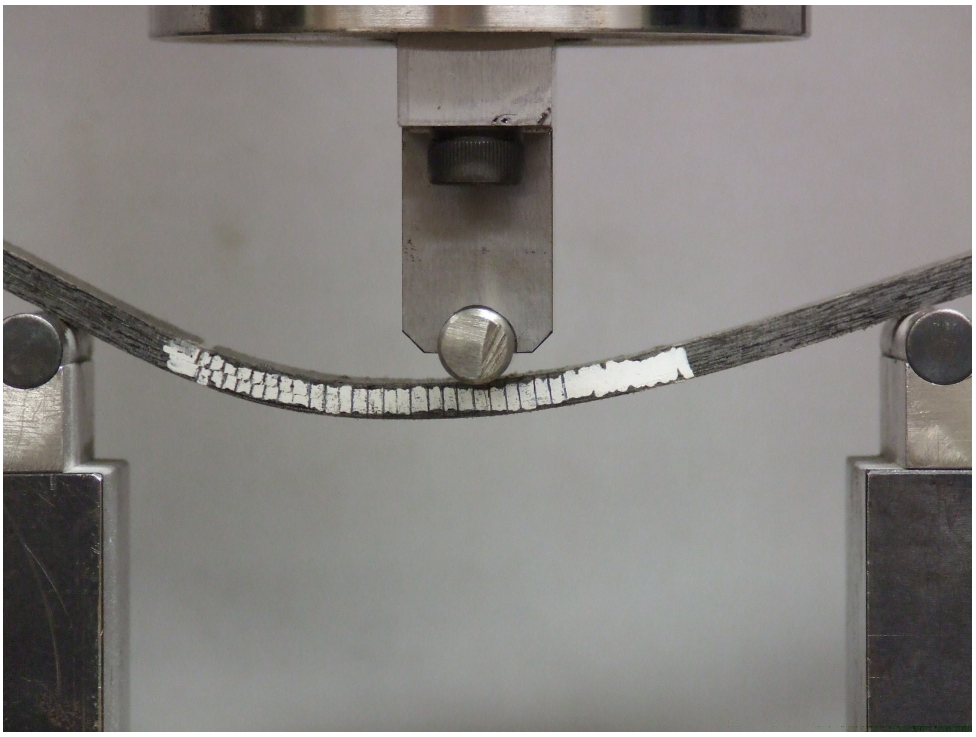

Figure 6.7: Photograph of loaded End Notch Flexure specimen showing progression of crack, via step in line markings

Other than the specimen dimensions, the procedure for the FML ENF tests was identical to that of the GFPP ENF tests described in §6.2.1.1. The specimens were oriented with the aluminium layer on top (i.e. in contact with the central loading roller).

The crack for the FML ENF specimens was positioned at the interface of the aluminium and GFPP layers. Due to the different materials, and hence stress and strain fields, on either side of the crack plane, this does not yield a pure Mode II crack. The equations presented by Sundararaman and Davidson [190] were used to calculate the mode mixity ratio.

6.2.1.3 Results

The force-displacement response of GFPP to ENF tests is shown in Figure 6.8. The data is exhibits very little scatter for tests of this nature. The average peak force is 1025 N and has a COV of only 2.3 %. The initial response is linear, before a gradual softening. Even after the peak load, the force decreases on a smooth curve. Abrupt drops in the force only occurred some 3 to 4 mm of deflection after the peak force. However, after unloading, the specimens recovered almost completely - the maximum permanent deflection was less than 0.2 mm, despite being subjected to deflections in excess of 15 mm. As the specimen experienced little permanent deformation other

than the crack propagation, it is reasonable to apply LEFM principles. The quasi-static ENF tests on GFPP produced a rather surprising result - the crack propagation was relatively stable. The expected result for an ENF test is unstable crack growth [60, 63], with crack propagation too rapid for visual tracking and an abrupt drop in the meaured force. The crack growth, shown in Figure 6.9, does make small jumps, but generally progresses in a stable manner.

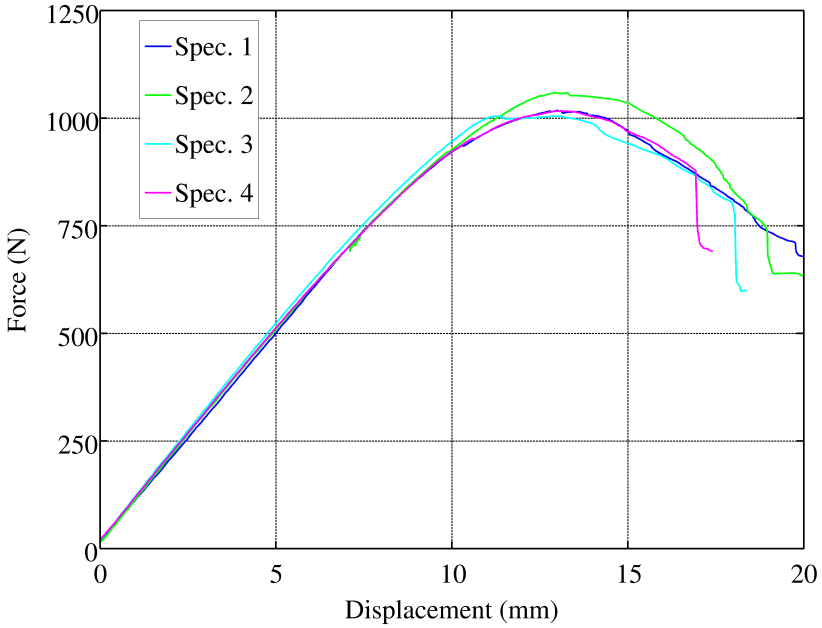

Figure 6.8: Plot of force-displacement response for End Notch Flexure tests of GFPP

The compliance as a function of initial crack position data is presented in Figure 6.10. The coefficients of the cubic polynomial used to fit the data are applied to Eq. 6.5 to obtain G_{II}, which is shown in Figure 6.11. The average initiation value of G_{II} is 0.88 kJ/m^2, with C.O.V of 36%. The initiation value for each test was determined from the intercept of a linear fit through the first 10 data points after the crack began propagating. G_{II} appears to be reaching a plateau after approximately 22 mm of crack extension. The value of this plateau is 5.25 kJ/m^2, with C.O.V of 7 %, based on the average of the last 5 data points for each specimen. At peak force in these experiments, the average value of G_{II} is 3.7 kJ/m^2. This compares well with the values of G_{II} reported in the literature based on the peak force value, which lie in the range 3.5 to 4.0 kJ/m^2 [91].

After the test was completed, the specimens were sectioned and the fracture surfaces inspected using an optical microscope. A typical specimen is shown in Figure

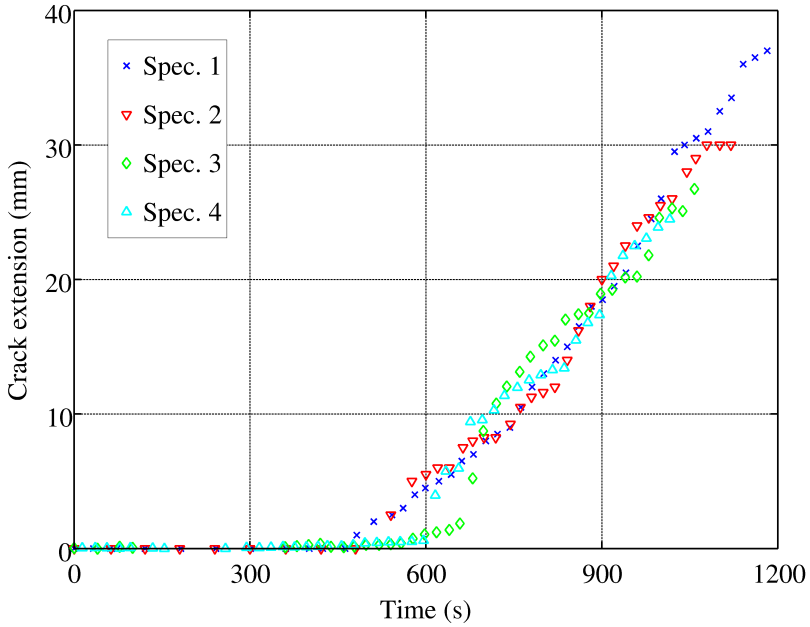

Figure 6.9: Plot of End Notch Flexure crack growth

6.12. It appears that failure is dominated by loss of adhesion between the fibres and matrix - the exposed fibres are relatively clean, with no lumps of matrix material adhering to fibres at this magnification. The loss of adhesion between fibres and matrix seems to switch between fracture faces when encountering a boundary between warp and weft in the weave pattern.

6.2.1.4 FML

The force-displacement response for the ENF tests on FML specimens is shown in Figure 6.13. An initial linear rise is followed by a non-linear region prior to the peak force. The peak force coincided with crack initiation, as shown by typical results in Figure 6.14. The crack growth was unstable, hence permitting only an initiation value for G to be calculated. It was unclear as to whether the non-linearity preceding the peak force was due to plasticity in the aluminium, which would render LEFM calculations inaccurate. Nonetheless, the initiation values for G were calculated using LEFM as a starting point. Monitoring the aluminium layer for the onset of plasticity during the test is unfeasible, due to the relatively short length of the region that deforms plastically and uncertainty as to where plasticity will develop first. The onset of plasticity can be predicted easily using FEA. Hence this set of experiments was modelled via FEA, and is discussed further in §7.3.5.

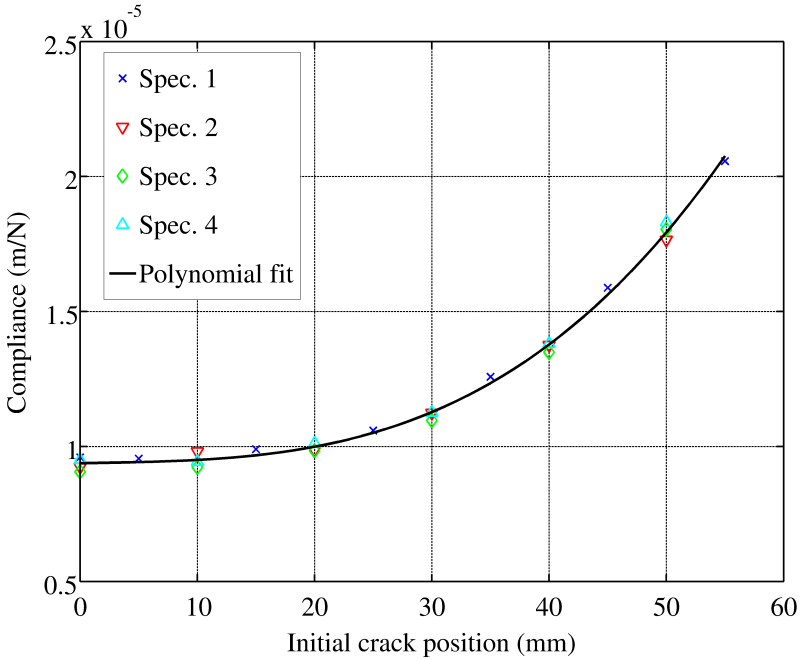

Figure 6.10: Plot of crack position - compliance data for GFPP End Notch Flexure specimens

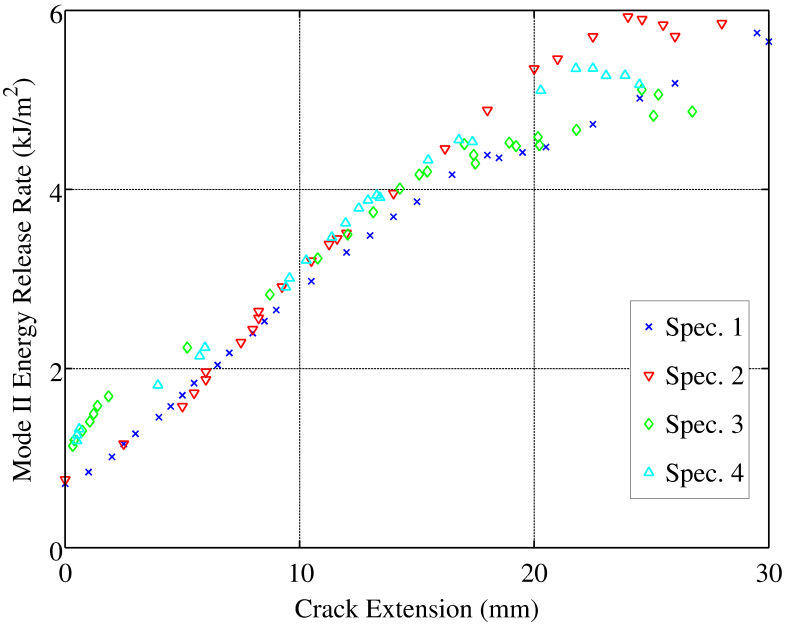

Figure 6.11: Plot of Mode II strain energy release rate for GFPP

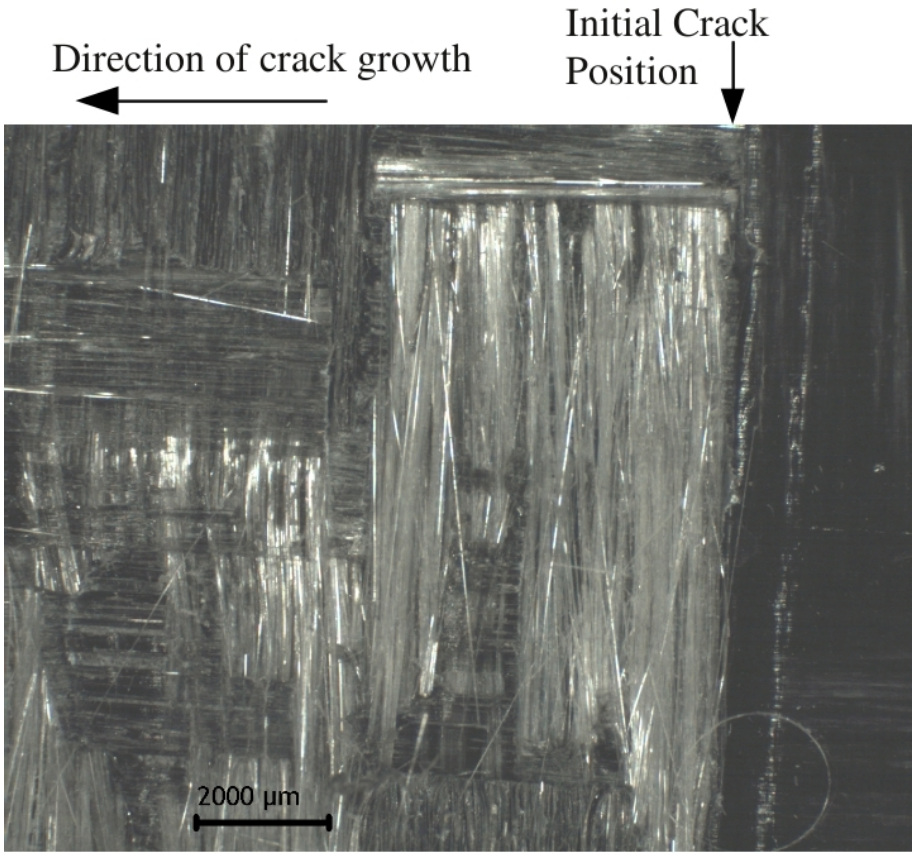

Figure 6.12: Photograph of fracture surface of GFPP specimen, post ENF test

The mean initiation value for G_{I-II} obtained from the unsymmetric ENF tests on FMLs is 0.22 kJ/m^2, with C.O.V. of 6.4%. The mode mixity ratio $\frac{G_I}{G_{II}}$ for specimens of this particular lay-up was determined from FEA, described in §7.3.4.1. The ratio $\frac{G_I}{G_{II}}$ has an approximate value of 0.25, for the initial crack length. However, as the crack propagates towards the central load, the Mode I component decreases.

6.2.1.5 Rejection of the ENF test for High Strain Rate Testing

During the processing of the photographs, it became apparent that the fuzzy crack tip associated with Mode II was already difficult to identify clearly, even at the comparatively high resolution. The high speed video of the impact bend tests would result in images of a much lower resolution (see §5.2.4). Hence crack measurement for ENF specimens in the impact experiments would be practically impossible. Consequently, ENF tests were eliminated for high rate delamination testing of GFPP and FMLs.

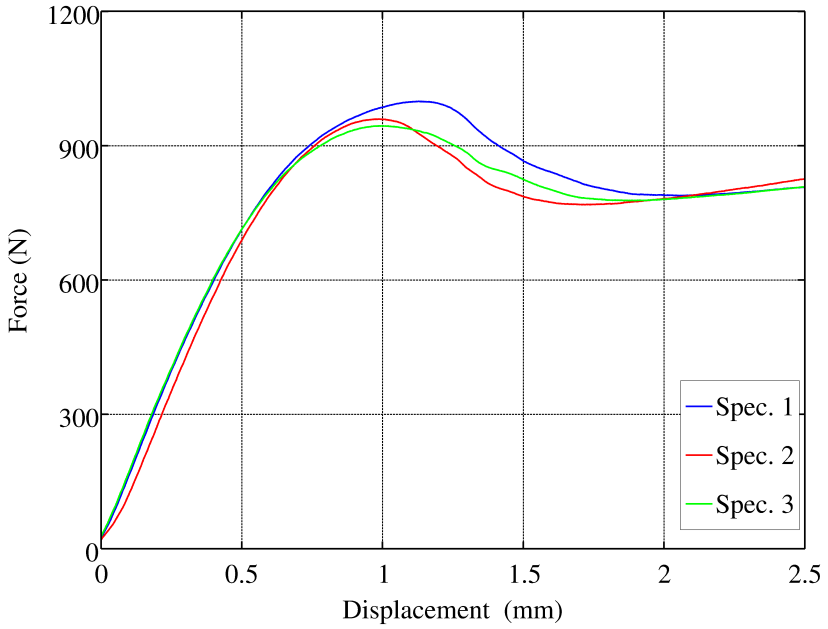

Figure 6.13: Force-displacement results for ENF tests on FMLs

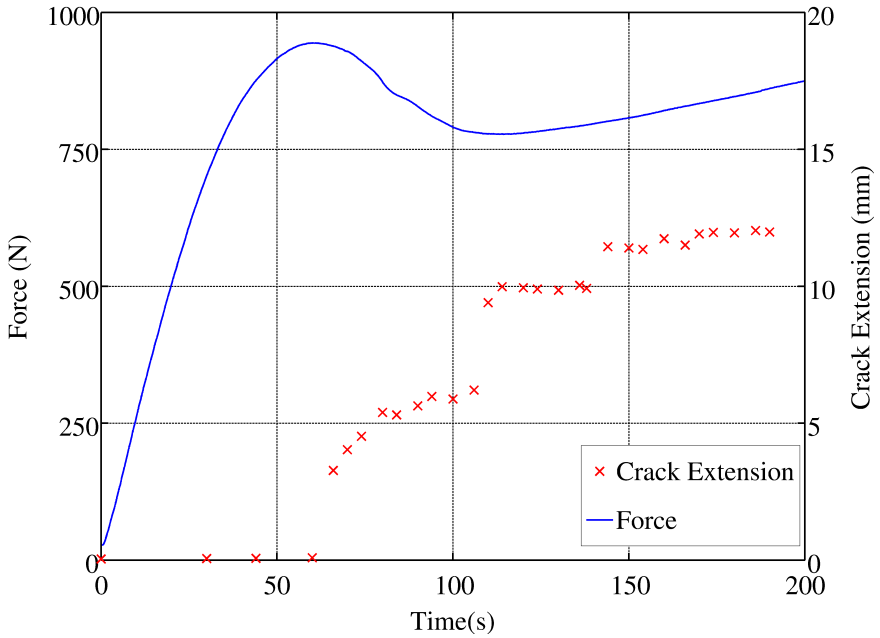

Figure 6.14: Force and crack extension histories for a typical ENF test on an FML specimen (Specimen 3)

6.2.2 Mixed Mode Delamination via Single Leg Bending

6.2.2.1 Experimental Details

The Single Leg Bend (SLB) test is a mixed Mode I-II test based on a Three Point bend geometry, shown in Figure 6.15. The partial removal of the lower leg requires that the support on that side be raised by the thickness of the lower leg to level the specimen upper surface. This was easily achieved by inserting a spacer of appropriate thickness below the support (not visible in Figure 6.15).

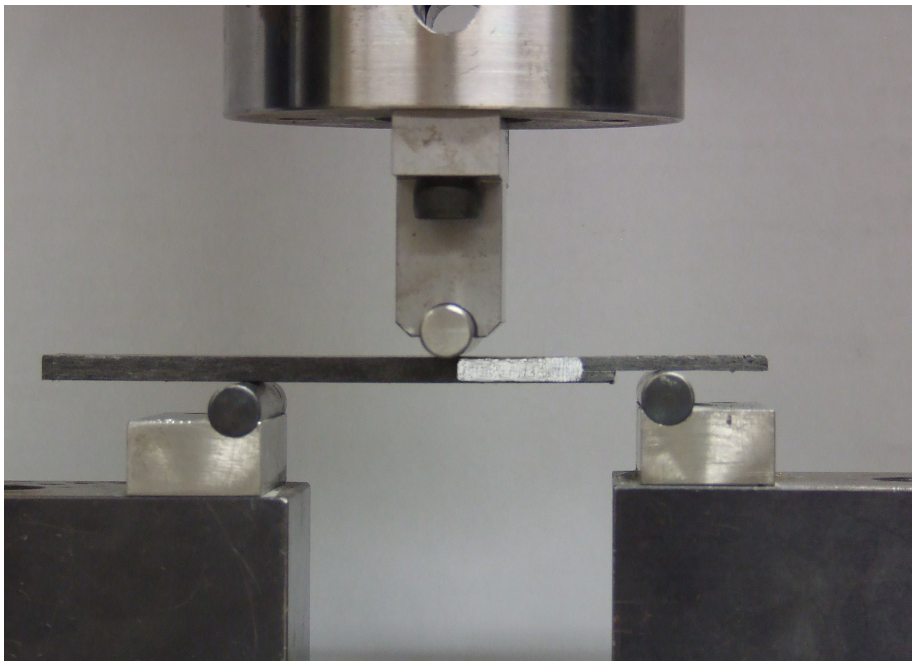

Figure 6.15: Photograph of Single Leg Bend specimen in test fixture

The GFPP SLB specimens were cut from a 5 mm thick GFPP panel manufactured in the same manner as that for ENF specimens. The initial flaw was nominally 50 mm from the edge of the panel, at the mid-plane of the laminate. Strip specimens of 25 mm width and 140 mm length were cut from the panel and a 30 mm section removed from the lower leg. The support span for the SLB tests was 80 mm. The side of the specimens was painted with white correction fluid to aid crack tip identification.

The data processing for an SLB test is identical to that of the ENF test, described in §6.2.1.1. The difference is that the energy release rate G calculated from a SLB test is a mix of Mode I and II, whereas for the ENF test (on symmetric specimens) provides a pure Mode II value.

The crack length-compliance relationship was experimentally determined as discussed in §6.2.1.1. The range of crack lengths for compliance calibration were limited by the length of leg removed, to between 20 and 45 mm. Thus the increment of crack length between compliance tests was reduced to 4 mm, so that sufficient data was collected to fit a cubic polynomial. The load during compliance calibration was limited to 150 N as slight opening of the legs was noted for the longer crack lengths.

The SLB tests were conducted at a cross head speed of 1 mm/min.

6.2.2.2 Results

The force-displacement curves for the six quasi-static SLB tests conducted on GFPP specimens are shown in Figure 6.16. Due to inconsistencies in the machining process, it was not possible to position the specimens with the crack tip in the same initial position. The crack initial position varied from 12 mm to 19 mm over the different tests. The differing initial position of the crack results in different apparent stiffnesses of the specimens, which is evident in Figure 6.16.

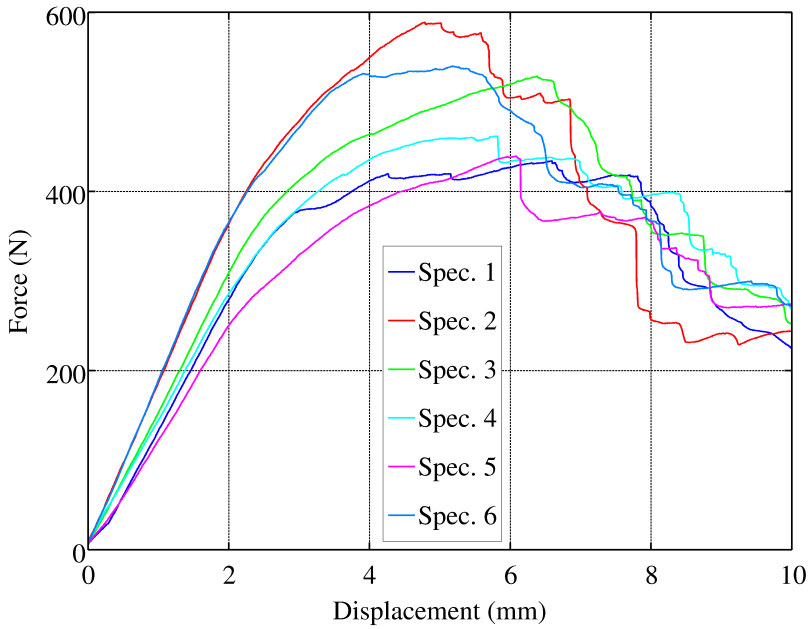

Figure 6.16: Plot of Single Leg Bend quasi-static force-displacement response of GFPP

The crack progation of all the specimens is shown in Figure 6.17. The crack propagation in each specimen was initially stable. However, after displacements of 5 mm, corresponding to crack extensions of 6 to 8 mm, stick-slip crack growth was exhibited. Minor fibre bridging was visible in most specimens, but did not obscure the crack tip.

Local fibre buckling was noted on the compression side of the upper leg above the crack tip, in some tests. This manifested visibly as a whitening of the specimen surface, accompanied by a sudden drop in the force-displacement curve. The onset of local buckling was recorded for each test, and typically occurred after 8 mm of displacement which is after peak force was reached. As the local buckling is a non-linear process, the energy release rate, which is based on LEFM, is only calculated up to the onset of buckling.

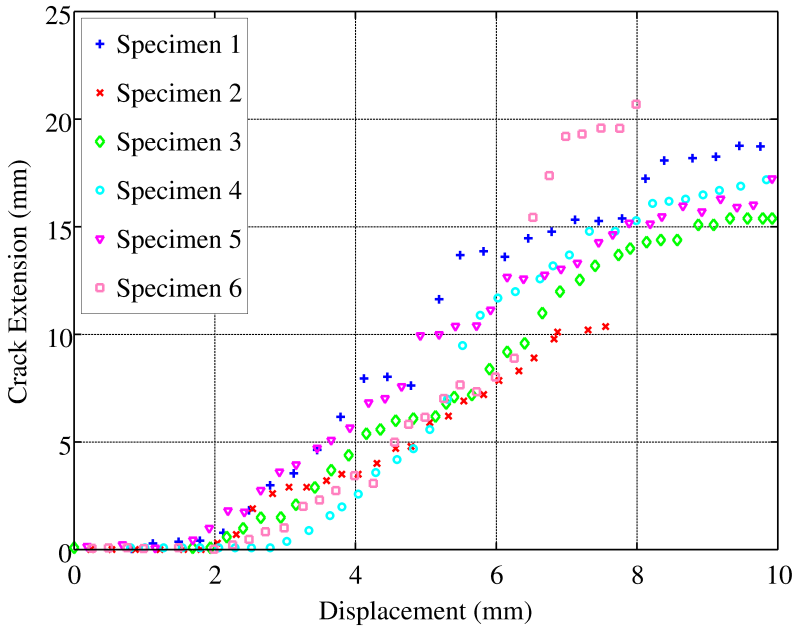

Figure 6.17: Plot of crack extension-displacement response of quasi-static Single Leg Bend tests on GFPP

The force and crack extension,for a typical SLB test on GFPP, are compared as functions of displacement in Figure 6.18. The crack initiation precedes the peak force substantially. The initiation value of G_{I-II} is calculated based on the visual crack measurement exceeding 0.5 mm greater than the initial value. The ASTM standard for the DCB test [33] suggests two alternatives for determining the initiation value of G: the non-linear (NL) point and 5% offset methods. Determining the NL point is very subjective for results such as these, which transition very smoothly. The 5% offset line, shown in magenta in Figure 6.18, intersects the force-displacement trace at a higher force than that corresponding to the visual assesment of crack initiation. Hence the initiation value of G_{I-II} determined from the visual crack measurements is the most conservative and consistent measure for these experiments.

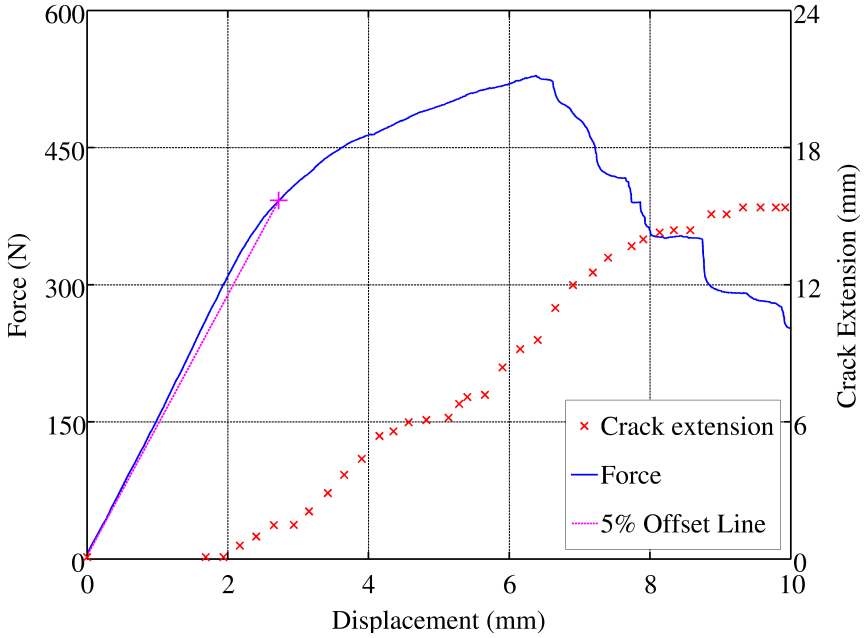

Figure 6.18: Plot of force and crack extension for a typical quasi-static Single Leg Bend test on GFPP

G_{I-II} as a function of crack extension for all the quasi-static SLB tests on GFPP is shown in Figure 6.19. The mean initiation value of G_{I-II} is 0.53 kJ/m^2, but the certainty of this value is very low, as the COV is 45 %. From initiation, G_{I-II} increases approximately linearly with crack extension, and appears to be reaching a stable plateau of 3.2 kJ/m^2 for crack extensions greater than 10 mm. As noted above, the response of Specimens 2 and 6 was excluded for displacements greater than 8 mm, due to the presence of local fibre buckling. The stable propagation (plateau) value of G_{I-II} is based on the mean of those specimens with valid data at these crack extensions. The propagation values for G_{I-II} are comparable to those reported by Reyes Villanueva [91], for SLB tests on unidirectional GFPP, with propagation values of G_{I-II} ranging from 3 to 5 kJ/m^2 for displacement rates in the range 0.1 to 10 mm/min.

The maximum crack extension is limited by the initial crack length, and the support span - all specimens showed a slowing of the crack growth as the crack tip approached mid-span, where the load is applied. A larger support span would permit larger crack extensions, which should increase the certainty of the stable propagation value of G_{I-II}.

The mode mixity ratio often quoted for SLB tests with equal thickness upper and lower legs is $1.3\dot{3}$. However, the relationship for determining SLB mode ratio, presented by Yoong and Hong [79], is very sensitive to small thickness ratio changes

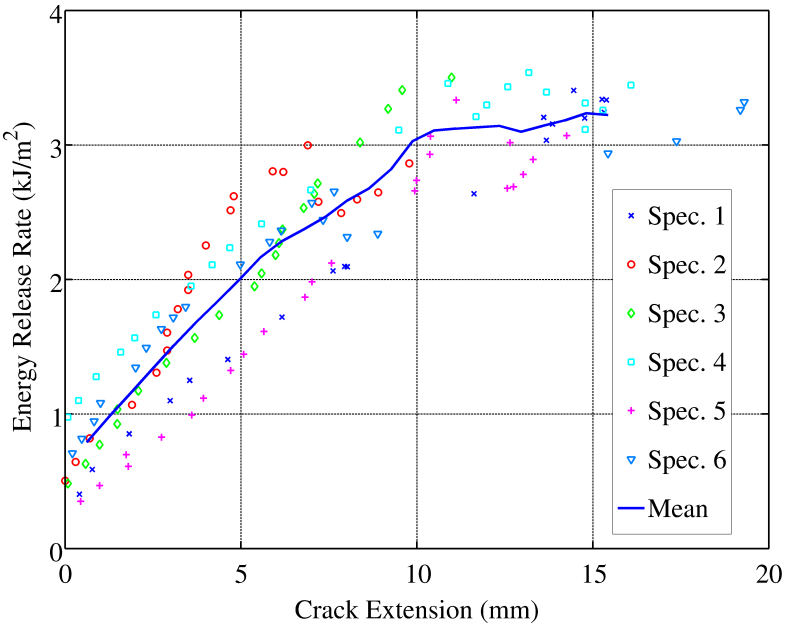

Figure 6.19: Plot of energy release rate G_{I-II} at a function of crack extension for QS SLB tests on GFPP

around 0.5. The mode mixity ratio (G_I/G_{II}) for these specimens is determined by the ratio of thickness of the upper half leg, to total specimen thickness. The mean value of this ratio is 0.53, which based on Yoong and Hong's data, gives a mode mixity ratio G_I/G_{II} of 1.05.

The quasi-static SLB tests produced the desired delamination failures, without being obscured by other failure modes. The loading geometry required for the SLB was easily achievable with the Impact Bend HPB setup described in §5.2. The SLB tests produced a crack with both Mode I opening and Mode II sliding - the presence of crack opening aids crack tip identification from photographs greatly. The only means of crack tip identification for high speed tests, available to the author, was by processing images obtained from high speed video. Hence high strain rate delamination tests were conducted using SLB specimens on the HPB Impact Bend setup.

6.2.3 High Rate Single Leg Bend Delamination Tests of GFPP

6.2.3.1 Experimental Details

Specimens from the same batch prepared for the quasi-static SLB tests, described in §6.2.2.1, were used for the HPB SLB tests. The Impact Bend HPB setup required minimal modification for the SLB tests: a spacer of appropriate thickness was inserted between one support and the impacter cross member to accomodate the asymmetric SLB specimen.

All SLB tests on the Impact Bend HPB setup were filmed with the high speed camera, described in §5.2.4.

6.2.3.2 Results

The force-displacement and crack extension-displacement results for the eight HPB SLB tests on GFPP are shown in Figure 6.20 and Figure 6.22 respectively. The force rises rapidly due to the initial impact, followed by some oscillations. The force-displacement curves for HPB Impact Bend tests on GFPP and delamination SLB specimens are compared in Figure 6.21. In an HPB Impact Bend test on GFPP bend specimen, the force rises substantially after the initial impact and associated oscillations, as the specimen has not lost any flexural stiffness. Oscillations due to wave propagation in the specimen become less significant at higher deflections, due to the higher forces being measured. In a HPB Impact Bend test with a fracture specimen, the specimen loses flexural stiffness as the crack propagates. Thus the measured force during a delamination test will not increase as rapidly as for a bend specimen, and may even decrease due to large losses in stiffness. Any oscillations in the measured force due to wave propagation in the specimen are therefore more noticeable for a fracture specimen. Rather than analysing the vibrational modes and stress wave propagation for the more complicated geometry of an SLB specimen in the same manner as for the bend specimens (§5.3.1), the impact SLB tests were simulated using explicit FEA, which is presented in §7.3.3. Nonetheless, the data analysis applied to the quasi-static SLB tests was used to provide estimates of energy release rates for the impact SLB tests, and allows observation of any trends between the quasi-static and HPB SLB tests.

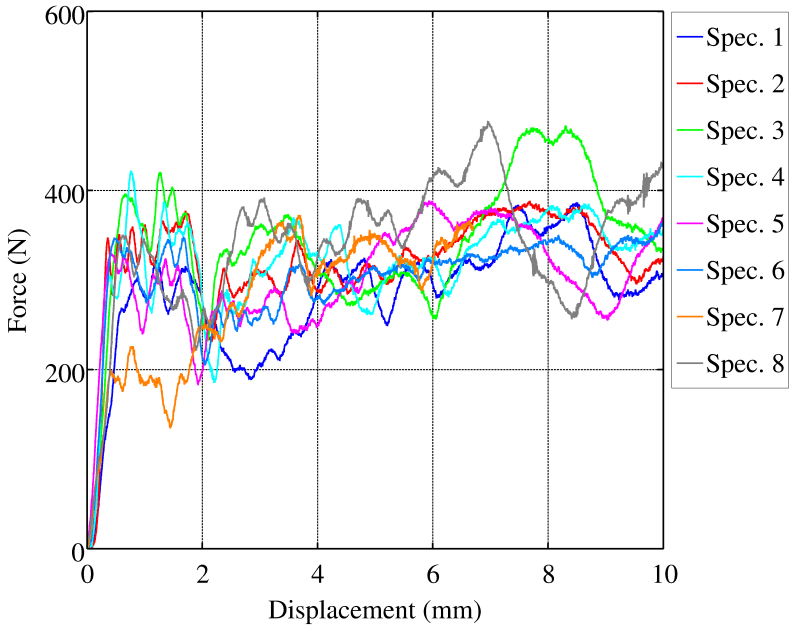

Figure 6.20: Plot of force-displacement data for HPB Single Leg Bend tests on GFPP

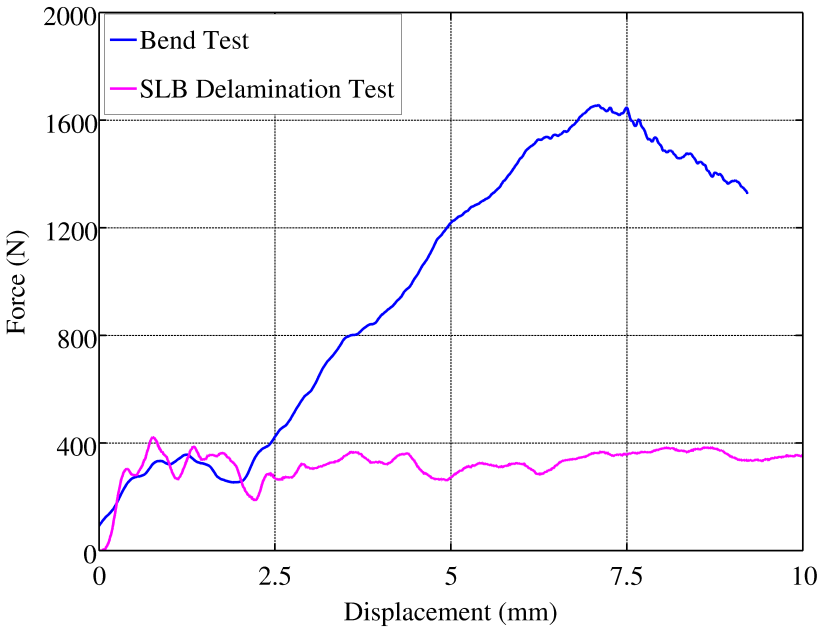

Figure 6.21: Plot of force-displacement data for HPB Impact Bend tests on GFPP bend and Single Leg Bend delamination specimens

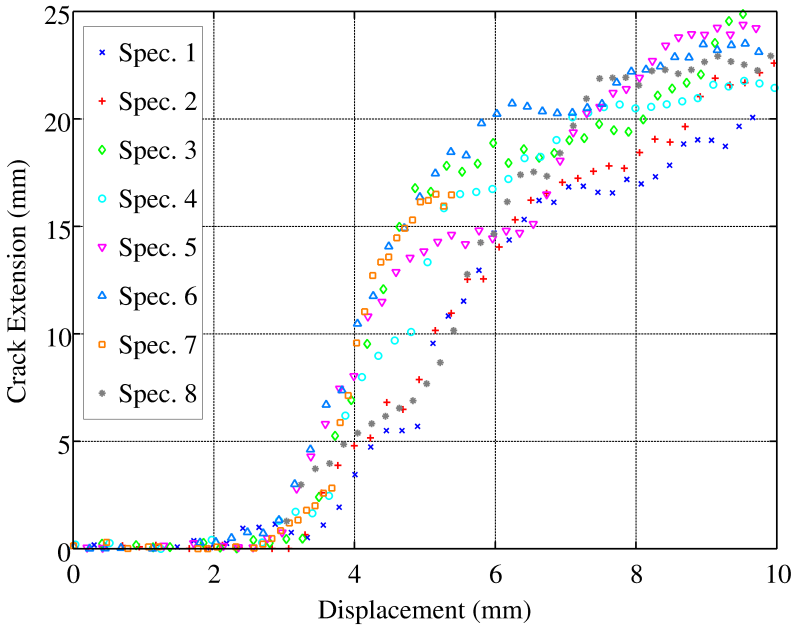

Figure 6.22: Plot of crack extension-displacement data for HPB Single Leg Bend tests on GFPP

The force and crack extension data for a typical test are plotted on the same time axis in Figure 6.23. In general, crack initiation does *not* align with a major drop in the force measurement. Crack initiation corresponds with a major drop in force for only one of the eight tests. In the quasi-static SLB tests, crack initiation preceded any non-linearities in the force response. In the HPB SLB tests, the force departs from a linear response approximately 0.6 to 0.7 ms before visible crack growth is observed.

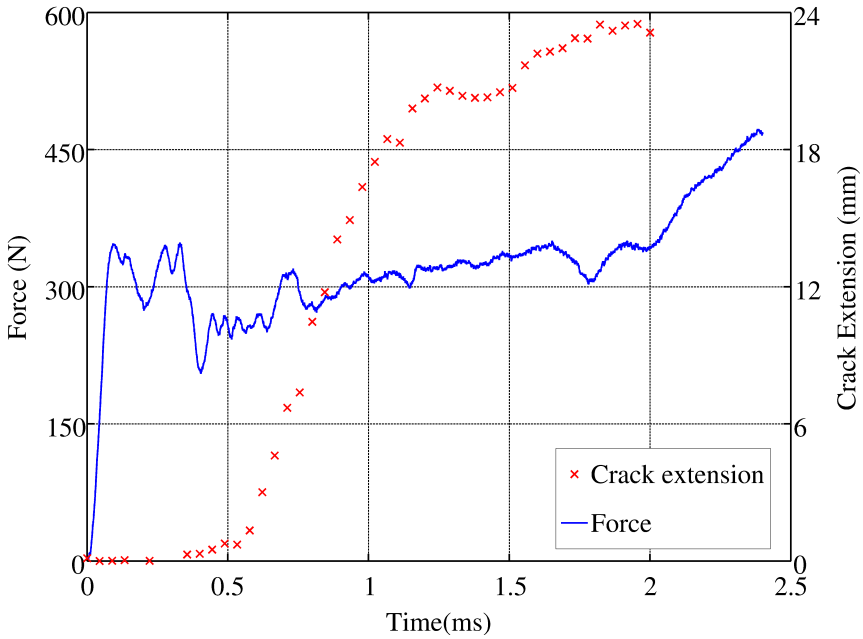

Figure 6.23: Plot of force and crack extension data for an HPB Single Leg Bend test on GFPP

The energy release rate data obtained from the HPB SLB tests is presented in Figure 6.24. The average initiation value of G_{I-II} is 0.50 kJ/m^2, with C.O.V = 28%. This is practically equal to the quasi-static initiation value of 0.53 kJ/m^2. The data does not indicate a stable propagation value, for the range of crack extension investigated.

6.2.3.3 Comparison

The force-displacement, crack extension-time and G_{I-II} data are compared for the quasi-static and HPB SLB tests in Figure 6.25, 6.26 and 6.27 respectively. The thick solid lines indicate the mean data for all tests at that rate, while the dashed lines indicate the maximum and minimum envelopes.

The force-displacement response for the HPB tests is initially higher than for the quasi-static tests. However, during the initial part of any HPB bend test, the force oscillates due to stress waves in the specimen, so this data cannot be relied on greatly.

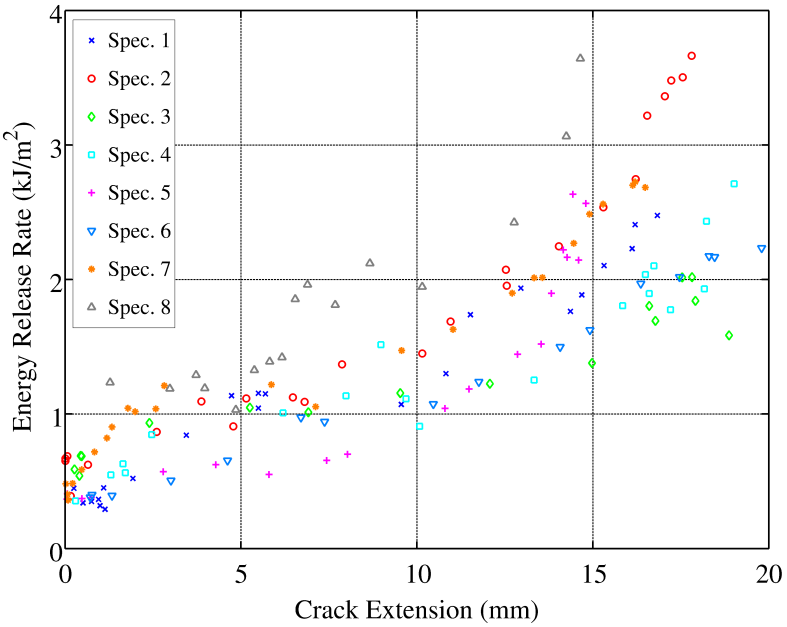

Figure 6.24: Plot of energy release rates for HPB Single Leg Bend tests on all GFPP specimens

The peak force for the quasi-static tests is definitely higher than that of the HPB tests, by approximately 30 % based on the mean curves. Crack initiation begins at slightly lower displacements for the quasi-static tests than the HPB tests. However, crack growth is faster for the HPB tests. Beyond displacements of of approximately 3.5 mm, the crack extension for the HPB tests exceeds that of the quasi-static tests but is less stable.

The initiation values of G_{I-II} for the quasi-static and HPB tests are approximately equal, with mean values of 0.53 and 0.50 kJ/m^2 respectively. However, for larger crack extensions, the resistance to crack growth is higher for quasi-static tests than HPB tests. This is consistent with the lower peak forces and faster crack growth in the HPB tests.

The fracture surfaces of both sets of specimens were inspected under an optical microscope. No differences could be observed, at magnifications up to 20×. A typical fracture surface is shown in Figure 6.28. As with the ENF specimen (Figure 6.12), loss of adhesion between fibres and matrix is prominent. The fracture surface follows the weave pattern, with loss of adhesion more likely to occur where the fibres run transverse to the direction of crack growth.

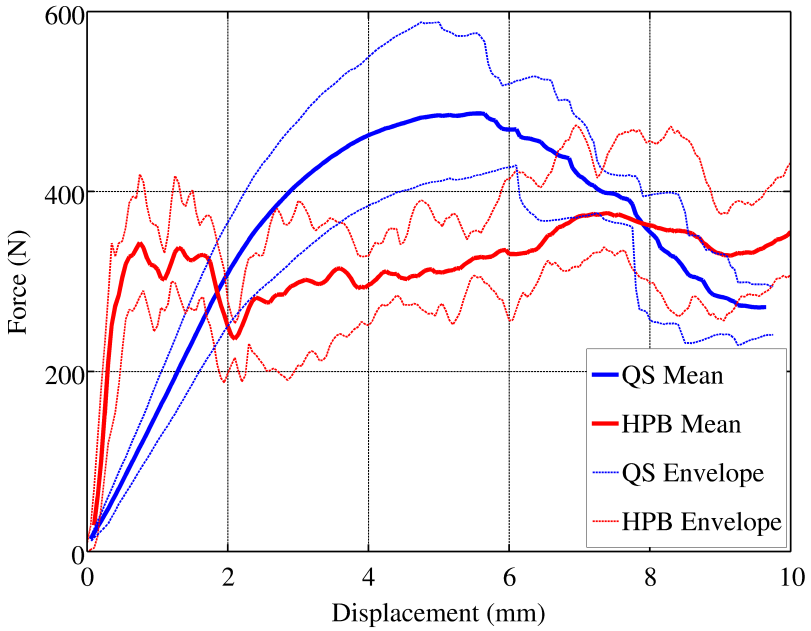

Figure 6.25: Force - displacement data for quasi-static and HPB Single Leg Bend tests on GFPP

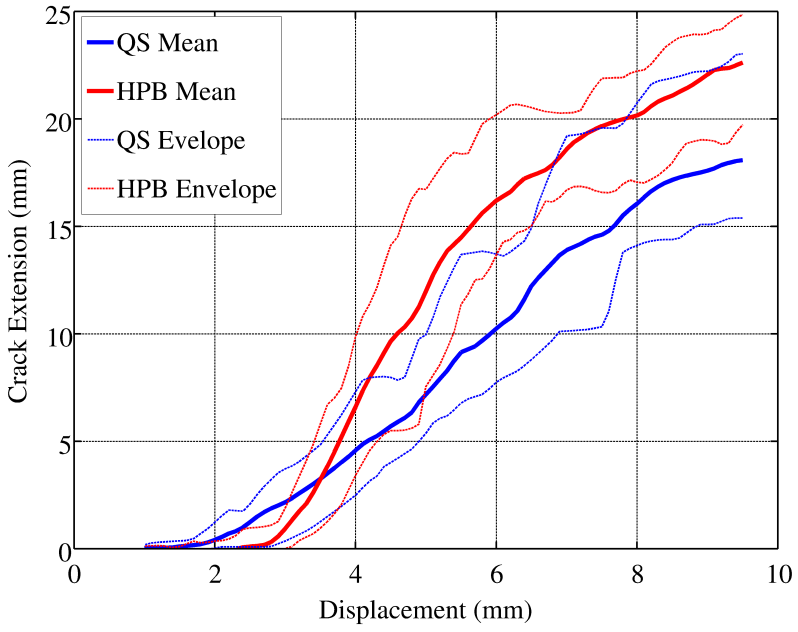

Figure 6.26: Plot of crack extension - displacement data for quasi-static and HPB Single Leg Bend tests on GFPP

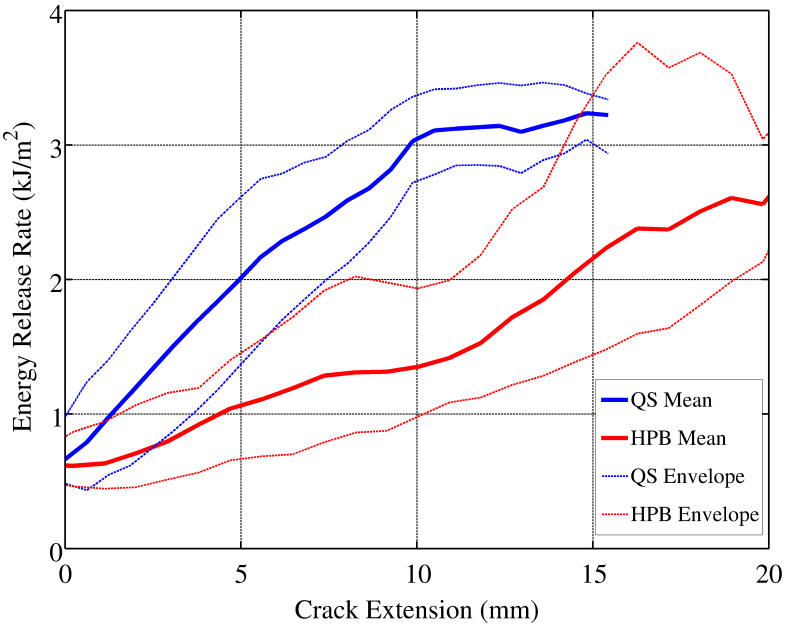

Figure 6.27: Plot of energy release rate - crack extension data for QS and HPB Single Leg Bend tests on GFPP

6.2.4 Quasi-static SLB Tests of FMLs

6.2.4.1 Experimental Details

Asymmetric SLB specimens were prepared from the same FML panel as used for the ENF tests (§6.2.1.2). The specimens were nominally 24 mm wide and 120 mm long. A 30 mm long segment of the lower aluminium layer was removed from the side of the specimen with the initial flaw to produce the desired SLB geometry. The support span for the FML SLB tests was 80 mm. The specimen compliance was calibrated experimentally as for the SLB tests on GFPP. The force limit for these specimens was 150 N. The fracture tests were conducted at 1 mm/min, and photographs of the specimen were taken at 10 s intervals.

6.2.4.2 Results

The force-displacement results for the quasi-static SLB tests on FML specimens are shown in Figure 6.29. The force-displacement response of a typical test, along with the crack extension, is shown in Figure 6.30. Crack initiation occurs while the force-displacement response is still linear, as was the case for the quasi-static SLB tests on GFPP. The force-displacement curve then decreases in slope. For this specimen, the

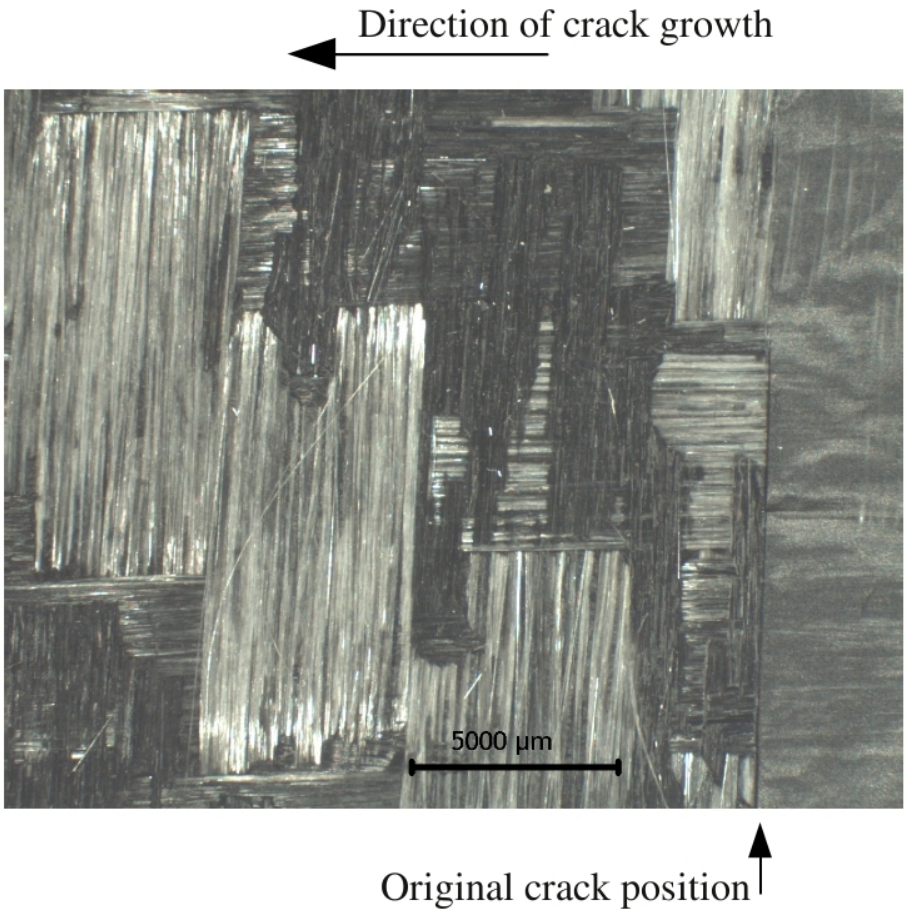

Figure 6.28: Photograph of fracture surface of a GFPP Single Leg Bend specimen

peak force is approximately coincident with an increase in the rate of crack growth. Crack growth then slows as the crack approaches the mid-span. This is associated with an increase in force, as the GFPP layer is now bearing the load almost entirely. The crack extension response for all the admissable specimens is shown in Figure 6.31.

The results are follow a similar trend, except for Specimen 5. Specimen 5 developed a interlaminar crack in the GFPP layer, as well as the interfacial crack between the aluminium and GFPP, which is shown in Figure 6.32. As the aim of these tests was to assess interfacial fracture, Specimen 5 was excluded from the analysis.

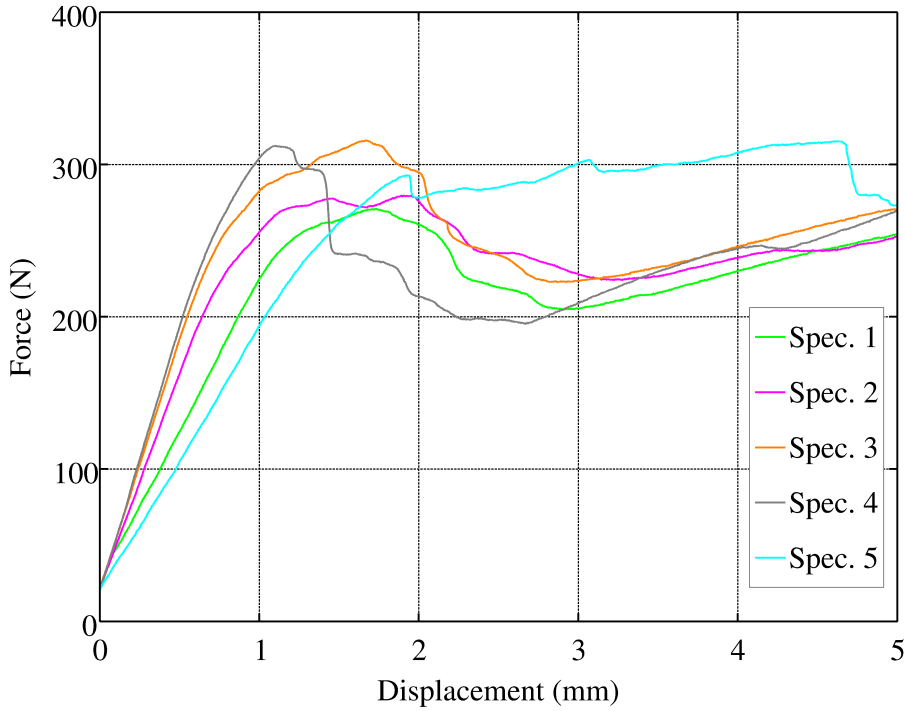

Figure 6.29: Plot of force-displacement results for quasi-static Single Leg Bend tests on FMLs

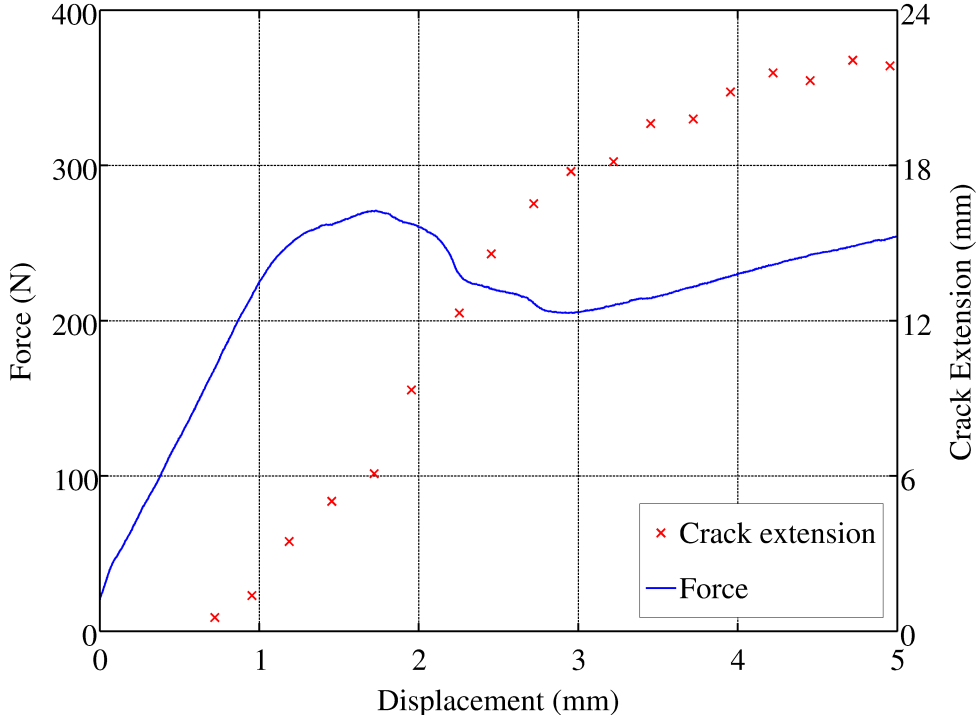

Figure 6.30: Plot of force and crack extension response of a typical quasi-static SLB test on FML

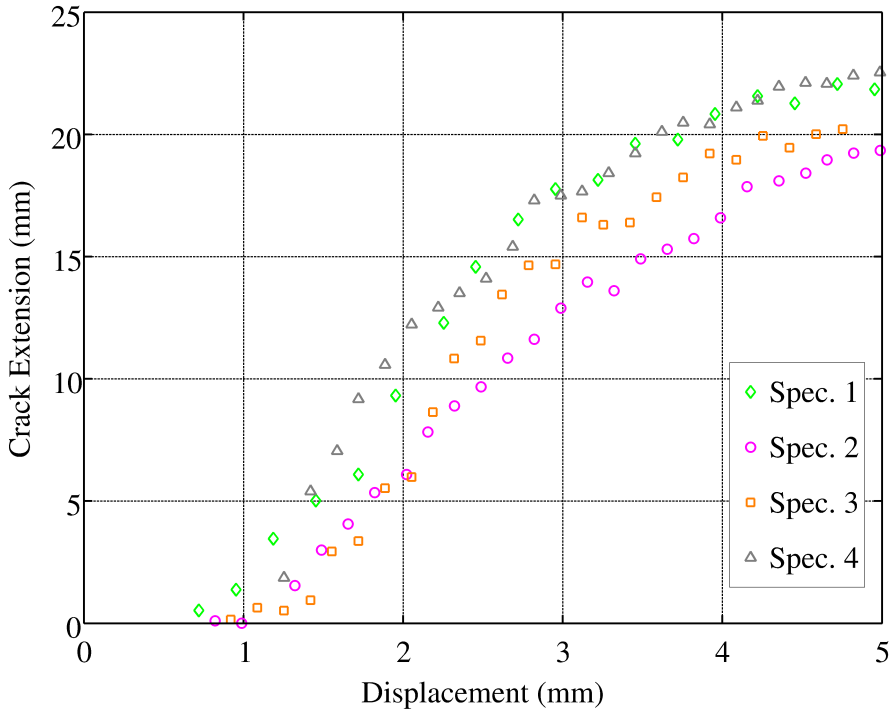

Figure 6.31: Plot of crack extension response of all quasi-static Single Leg Bend tests on FMLs

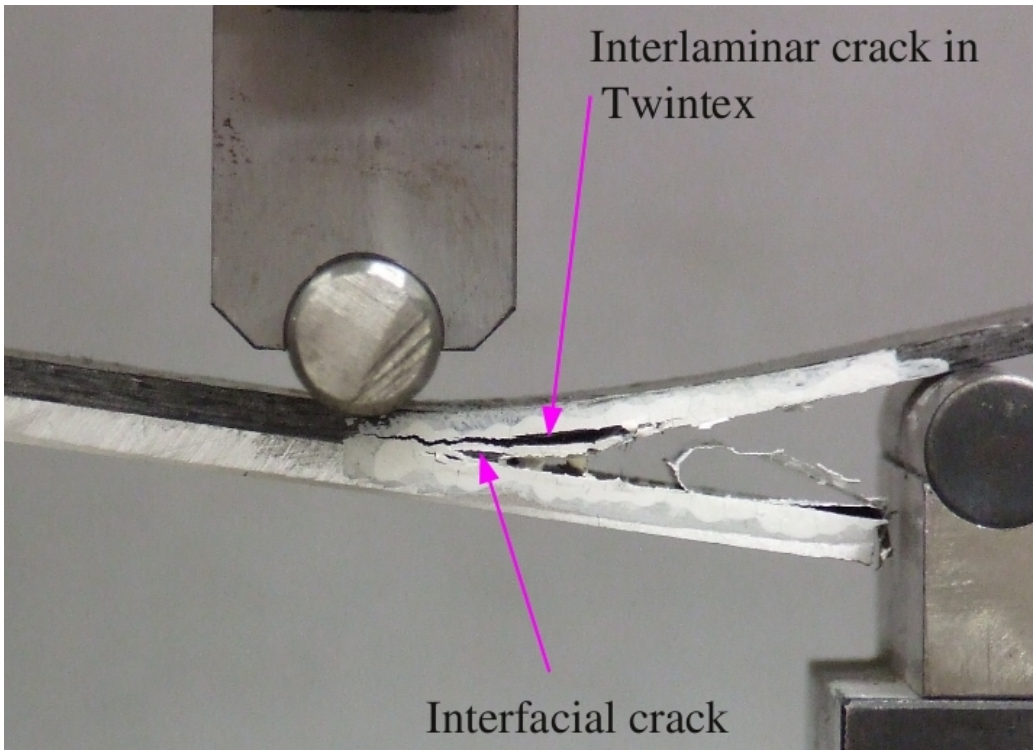

Figure 6.32: Photograph of interlaminar and interfacial cracks in rejected FML specimen

The energy release rate G_{I-II} is plotted in Figure 6.33. After crack initiation, G_{I-II} rises but then falls (due to the relatively large drop in force), which makes identification of a stable propagation value problematic. The average initiation value of G_{I-II} is 0.6 kJ/m^2, with C.O.V. of 23%. For a SLB specimen of this geometry and lay up, the mode mixity ratio $\frac{G_I}{G_{II}}$ tends towards 0.3. This ratio was determined via finite element analysis, which is detailed in §7.3.4.

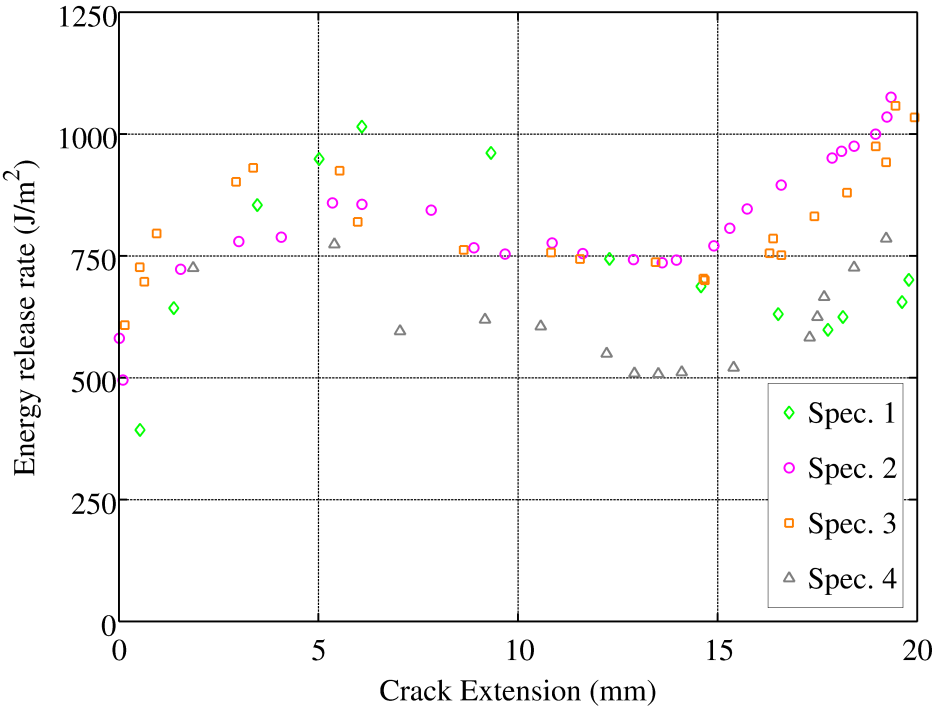

Figure 6.33: Plot of G_{I-II} for all quasi-static Single Leg Bend tests on FML

6.2.5 High Rate SLB Delamination Tests of FMLs

The force and crack extension histories for a typical HPB SLB test are shown in Figure 6.34. The force history, shown in Figure 6.34, exhibited an initial spike, followed by a drop to approximately 20% of the peak force. The force then rrose rapidly to approximately 65% of the peak, before increasing at a much slower rate with some oscillations superimposed. Crack initiation, which occurred at approximately 0.7 ms after impact, *does not coincide with the major drop in force*. In a similar manner to the HPB SLB tests on GFPP, the force response becomes non-linear prior to visible crack initiation. Crack growth is not stable, with stick-slip behaviour very prominent. There is no correlation between the stick-slip events and any notable increase or decrease in the force.

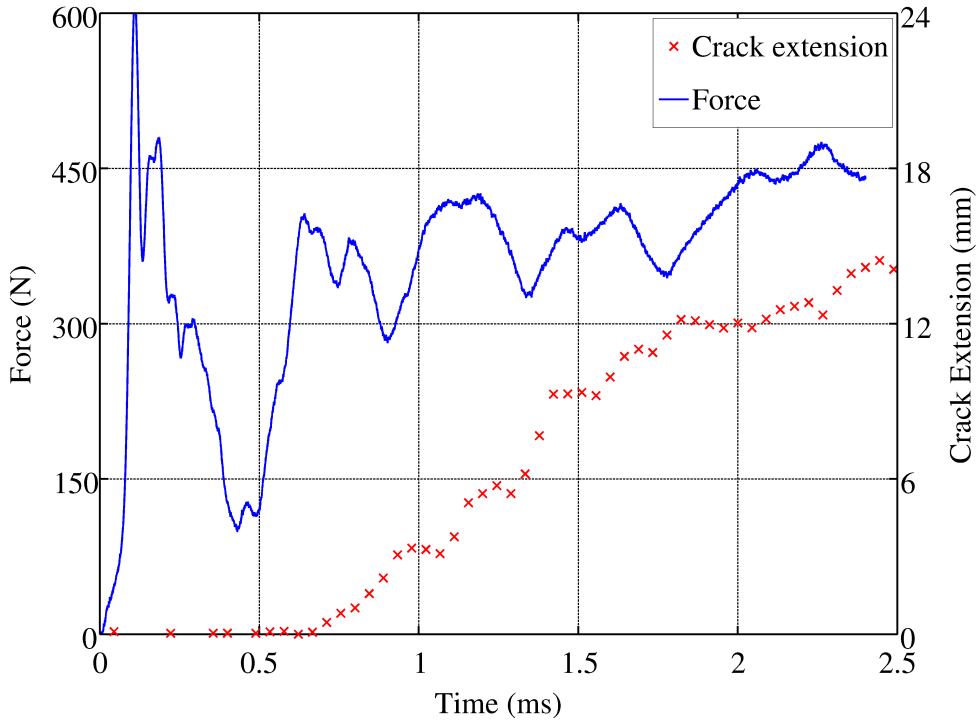

Figure 6.34: Plot of force and crack extension histories for a HPB Single Leg Bend test on FML, with crack tip at quarter-span

Frames from the high speed video for this test are shown in Figure 6.35, with impact corresponding to Figure 6.35(a). The drop in force after the initial peak corresponds to Figure 6.35(b) - in this frame, the upper and lower legs of the specimen were visibly open, but there was no visual indication that crack has grown beyond its initial position. The visual onset of crack growth coincided with Figure 6.35(c) (0.71 ms after impact). Figure 6.35(d) shows the specimen 1.067 ms after impact, when the upper and lower legs had opened appreciably and the crack had grown approximately 3 mm

beyond its original position. The specimen is very clearly in contact with the impact head of the HPB throughout all four frames, so the drop in force is unlikely to be due to a loss in contact between the specimen and HPB. It is possible that the crack growth at the mid-plane of the specimen precedes crack growth at the visible surfaces. Verification of sub-surface crack growth would entail specimens from interrupted impact tests being subjected to non-destructive testing such as ultrasonic scanning. The current version of the HPB Impact Bend apparatus would need to be modified to allow interrupted impact testing.

(a) Impact $t = 0ms$ (b) $t = 0.356ms$ after impact

(c) $t = 0.711ms$ after impact (d) $t = 1.067ms$ after impact

Figure 6.35: Frames from high speed video of high rate Single Leg Bend test on FML specimen using HPB Impact Bend apparatus

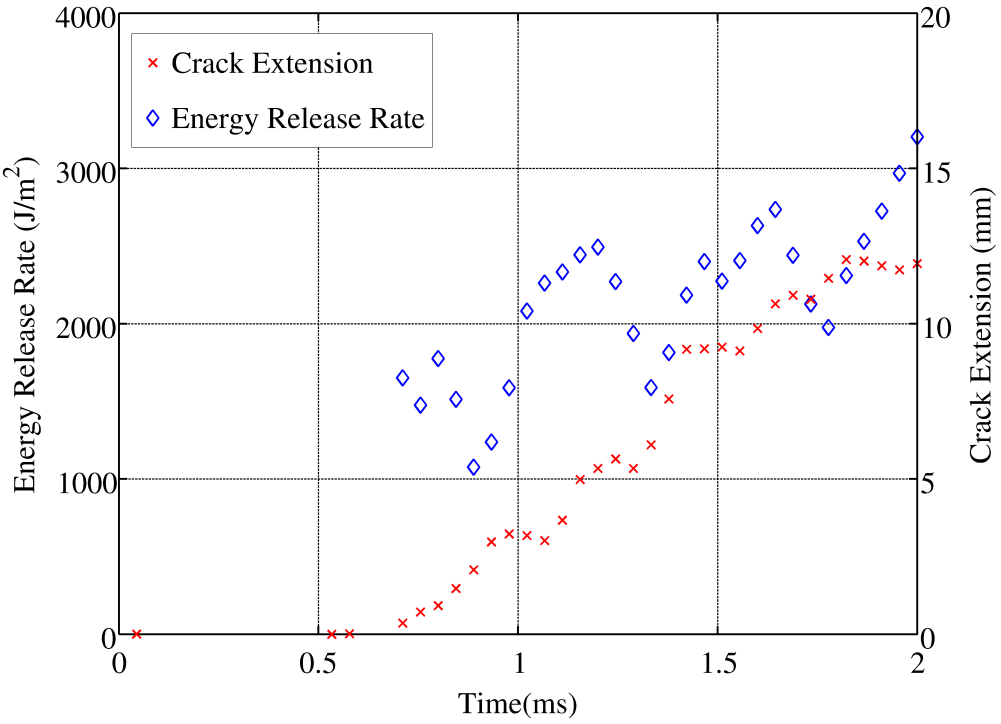

Figure 6.36: Plot of energy release rate and crack extension histories for a HPB Single Leg Bend test on FML, with crack tip at quarter-span

The initiation value of G_{I-II} for this test is approximately 1.6 kJ/m^2. The energy release rate, plotted on the same axes as crack extension in Figure 6.36, displays oscillations which are due to the oscillations in the force measurement. These oscillations make it difficult to ascertain whether a stable propagation value of G_{I-II} has been reached. Three specimens were tested, with the crack tip positioned half way between the outer support and the central impact point [1] , and yielded an average initiation value of G_{I-II} of 1.8 kJ/m^2.

To investigate the sensitivity of the test to initial crack position, further tests were conducted with the crack tip closer to the mid-span. However, crack growth in these tests was more unstable - please see Appendix A.3.1 for the results.

[1]This point is one quarter of the span from the centre, and is referred to as quarter-span in captions for brevity.

6.3 Summary

Several delamination test methods were evaluated, and compared according to the criteria summarised in Table 6.1. The SLB test was found to be the most suitable test method for characterising delamination of GFPP at higher rates. High rate SLB tests were conducted on GFPP and FML specimens, using the HPB Impact Bend apparatus, at impact velocities ranging from 5 to 8 m/s.

Table 6.1: Summary of delamination test methods investigated

Test Method / **Criteria**	Z-Shear	Short Beam Shear	End Notch Flexure	Single Leg Bend
Ease of specimen manufacture	N	Y	Y	Y
Results repeatable	N	Y	Y	Y
Results comparable to literature	N	Y	Y	Y
Delamination only (No other failure modes present)	Y	N	Y	Y
High rate measurements feasible	Y	Y	N	Y

SLB tests on GFPP showed insignificant variation in the initiation values of G_{I-II} between the quasi-static and higher rate tests. Both the force-displacement and energy release rate-crack extension results indicated that after crack initiation, the resistance to crack propagation was lower for tests at the higher rate.

The initiation value of G_{I-II} was higher for the HPB SLB tests on FML specimens that the quasi-static tests. Crack growth in FML specimens was unstable during the HPB SLB tests.

Chapter 7

Discussion

7.1 Compression Testing of GFPP

Through thickness and in plane compression testing of GFPP was conducted at quasi-static strain rates ($10^{-4} - 10^{-2}/s$), and higher rates ($5 \times 10^2 - 10^3/s$) using a SHPB and direct impact HPB. Previous investigations of compression of GFPP had published data at rates less than $1.5 \times 10^2/s$. The through thickness and in plane compression testing of GFPP showed that peak stress increases approximately linearly with the logarithm of strain rate. A logarithmic strain rate dependence law, based on the Johnson-Cook rate law, was used to describe the increase in strength with strain rate. Identifying the mechanisms responsible for the rate dependency would entail an extended experimental program involving detailed microstructural investigation and interrupted tests to observe the evolution of failure. This is recommended for future research.

The through thickness modulus of GFPP was measured quasi-statically and with the SHPB, which has not been previously reported in the literature. The SHPB test was modified such that the forces acting on the specimen achieved acceptable equilibrium while the specimen was still deforming elastically. The tests revealed that the through thickness modulus E_{33} increased by approximately 25% while strain rate increased by 5 orders of magnitude, from $10^{-3}/s$ to $10^2/s$.

Through thickness compression produced two failure modes: spreading and macroscopic shear. Both of these failure modes exhibited in-ply failures and associated delaminations. It is likely that the in-ply failures precede the delaminations, as the compressive stress perpendicular to the plies will suppress any Mode I delamination. The in-ply failures can only be attributed to transverse tensile strain, as there is no applied

stress in this direction. The applied compressive force is perpendicular to the plies, and any friction at the end faces would resist transverse expansion. If the in-ply failure is strain dominated, the failure criterion must be linked to the failure strain in that direction, namely ε_{11}^f. ε_{11} is given by [191]:

$$\varepsilon_{11} = \frac{\sigma_{11}}{E_{11}} - \nu_{21}\frac{\sigma_{22}}{E_{22}} - \nu_{31}\frac{\sigma_{33}}{E_{33}} \tag{7.1}$$

The applied stresses in the ply directions, namely σ_{11} and σ_{22} are both zero. Hence the above reduces to :

$$\varepsilon_{11} = -\nu_{31}\frac{\sigma_{33}}{E_{33}} \tag{7.2}$$

$$= -\nu_{31}\varepsilon_{33} \tag{7.3}$$

The mean through thickness failure strain ε_{33}^f for the quasi-static tests was 13.1%, with a standard deviation of 0.9%. The SHPB tests produced a mean value of ε_{33}^f of 12.8% with a standard deviation of 0.7%. The interlaminar Poisson's ratio ν_{31}, which relates strain in the 1 and 3 directions, or its reciprocal ν_{13} is *not* reported by either the manufacturer or in the open literature. The in-ply failure strain ε_{11} determined from the quasi-static bend tests is 2.5%, while that from the impact HPB bend tests is 3.3%. The ratio of ε_{11}^f and ε_{33}^f gives a quasi-static value for ν_{31} of 0.19 and a dynamic value of 0.26, which are reasonable values for Poisson's ratio.

The macroscopic shear failure mode has been reported in several other studies on through thickness compression of glass FRP with SHPB [10, 173, 192, 193]. Examples of specimens exhibiting macroscopic shear failure are shown in Figure 7.1. The similarity in failure modes between Figure 7.1 (c) and (d) is striking. Both specimens show the tongue and groove pattern along the macroscopic shear plane, even though these are different composite systems: (c) is glass fibre-epoxy tested by [193] and (d) is the GFPP tested in this thesis. However, none of the prior studies explicity link the through thickness failure to the in-ply failure strain. Gama *et al* [10] reported quasi-static failure properties for a plain weave glass-vinyl ester FRP as shown in Table 7.1.

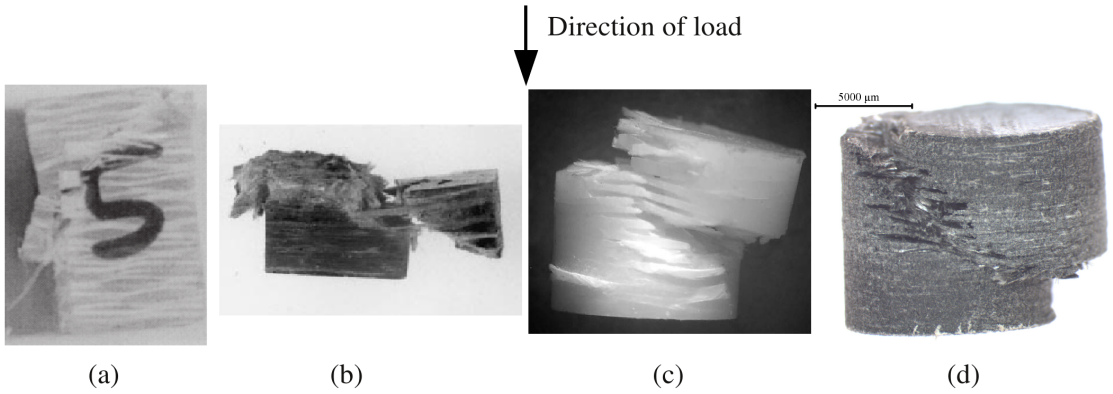

Figure 7.1: Photographs of through thickness compression of GFRP specimens, showing macroscopic shear failure (a) Gama *et al* [10] (b) Shah Khan *et al* [192] (c) Guden *et al* [193] (d) GFPP tested in this thesis

Table 7.1: Compressive failure properties for woven glass-vinyl ester FRP as reported by Gama *et al* [10]

Parameter	Value
E_{11}	28.7 GPa
E_{33}	13.7 GPa
ν_{13}	0.462
ν_{31}	0.220
σ_{11}^f	292 MPa
σ_{33}^f	509 MPa

The in-ply failure strain ε_{11}^f, calculated directly from σ_{11}^f and E_{11} in Table 7.1, has a value of 1.0 %. If ε_{11}^f is calculated using the through thickness properties σ_{33}^f and E_{33} and the appropriate Poisson ratio ν_{31}, the corresponding value is 0.8 %. These values are relatively close, which suggests that the conjecture of through thickness compressive failure being driven by in-ply failure strain has merit. Gama *et al* [10] noted that through thickness compression would cause transverse tensile strains, which would *"promote the development of interlaminar cracks"* and *"the flow of the fiber bundle causes fiber breakage"*. However, Gama *et al* [10] does *not* show via calculation the correlation between ε_{11}^f and ε_{33}^f, as presented above.

The correlation between in-ply failure strain and through thickness failure warrants more detailed investigation. Future work should include measuring the Poisson ratios

linking in-ply and interlaminar strain (ν_{13} , ν_{31}, ν_{23} and ν_{32}). Accurate measurements of relatively large strains ($\varepsilon \geq 10\%$) would be required, which motivates against the use of conventional strain gauges, which are limited to strains less than 5% [194]. High elongation strain gauges [195] may be able to measure such large strains, but require special adhesives to prevent premature debonding and would provide only the average strain over the length of the gauge. Full field strain measurements, obtained via means such as Digital Image Correlation, would greatly assist in the further investigation.

7.2 Bend Testing

A novel configuration of the HPB was developed to perform impact bend testing of GFPP and GFPP based FML specimens. The flexural strength of the GFPP specimens increased with strain rate, while the flexural modulus of GFPP was insensitive to strain rate in the range investigated. A logarithmic rate dependence model was used to describe the increase in flexural strength. The FML specimens did not show a significant rate dependence, as the response of the FMLs was driven by the aluminium outer skins which are not sensitive to strain rate.

The HPB Impact Bend apparatus presented in this thesis is versatile, without compromising the accuracy of force or velocity measurements. The output HPB is selected based on the expected maximum force. Hence specimens with substantially different forces at failure may be accomodated by selecting a different output HPB of appropriate material and diameter. The existing ROS system for measuring impacter displacement was designed for impact velocities of approximately 10 to 15 m/s, and has a measurement resolution of 0.48 mm. This resolution may be insufficient for stiffer specimens, where the displacements to failure are less than 5 mm. In this scenario, displacement measurements may be better obtained with commercially available linear encoder systems based on ROS, which have superior resolution ($\leq 0.01mm$) but are limited to impact velocities less than 10 m/s [196].

7.2.1 Early Oscillations in HPB Impact Bend Tests

The HPB Impact Bend tests on GFPP and FML bend specimens all showed oscillations shortly after impact, which decayed in amplitude as the force increased and were insignificant above forces of approximately 400 N, as shown in Figure 7.2. For the GFPP specimens, the oscillations did not obscure the peak force and hence flexural strength was easily identified. The transition from elastic to plastic response of the FML specimens was obscured, but the large deformation plastic response was easily distinguished. This section examines the early response of the HPB Impact Bend tests, in order to determine the origin of the early oscillations.

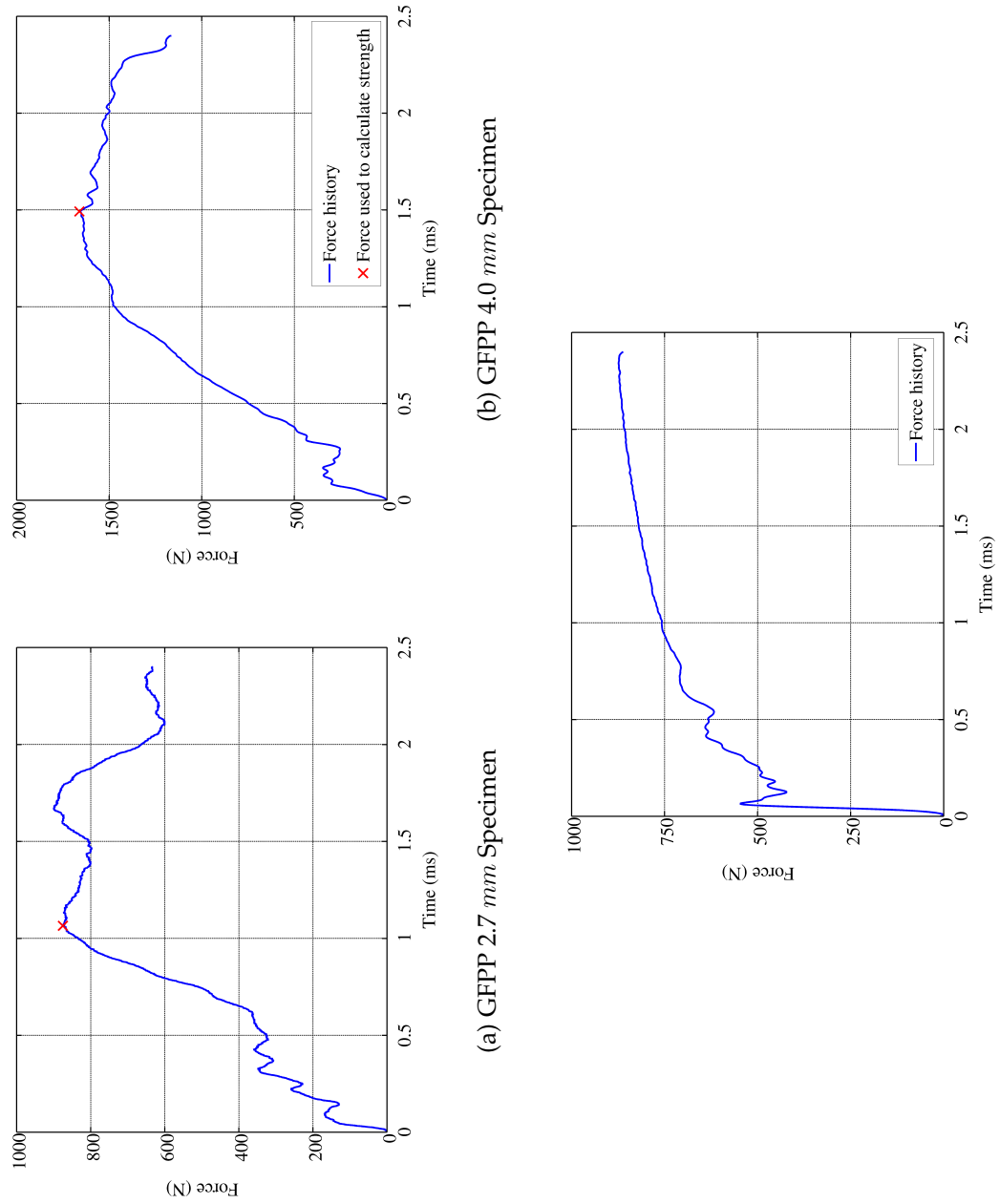

(a) GFPP 2.7 mm Specimen

(b) GFPP 4.0 mm Specimen

(c) A1-GFPP FML Specimen

Figure 7.2: Plots of typical force histories from the HPB Impact Bend apparatus

Only the force signals from the HPB Impact Bend tests on GFPP specimens are considered in this analysis - the FML specimens are not considered. The GFPP specimens remained elastic up to the peak force, when fracture occurred. Hence vibration analysis of the GFPP specimens using linear elastic assumptions is appropriate. The FML specimens exhibited plastic deformation after approximately 0.5 mm of deflection, while the oscillations may still be observed up to deflections of approximately 3 mm. Hence any vibration analysis including the FML specimens would have to consider the effect of plastic deformation. As this complicates the analysis considerably, the FML specimens are not considered in the following analysis.

The initial impact may be exciting the natural flexural modes of the specimen, and or crossmember of the impacter. The specimen may be considered as a simply supported beam, for which the natural frequencies of vibration are given by [197]:

$$f_n = \frac{1}{2\pi}\left(\frac{\pi n}{S}\right)^2 \sqrt{\frac{E_y I_{xx}}{A\rho}} \tag{7.4}$$

S indicates the support span,n the mode of vibration, E_y the modulus of the beam, I_{xx} the second moment of area, A the cross sectional area and ρ the density. The first four natural frequencies of GFPP specimens are given in Table 7.2.

Table 7.2: Natural frequencies of simply supported GFPP beams

Mode Number	**2.7mm Specimens**		**4mm Specimens**	
n	$f\,(kHz)$	$T_o\,(ms)$	$f\,(kHz)$	$T_o\,(ms)$
1	1.35	0.74	1.22	0.82
2	5.39	0.185	4.88	0.205
3	12.14	0.082	10.98	0.091
4	21.58	0.046	19.51	0.051

Fourier transforms were applied to typical force-time signals for both thicknesses, to obtain the frequency spectra shown in Figure 7.3. At the natural frequencies of the first (1.35 and 1.22 kHz) and second (5.39 and 4.88 kHz) mode, the frequency components are of similar magnitudes to their neighbours. This does not exclude the possibility that these natural frequencies are being excited - merely that they do not dominate the response sufficiently to stand out on the frequency spectrum. For both specimens,

the magnitudes of frequency components above 5 kHz are less than 1% of the largest frequency components. At such small magnitudes, it is difficult to discern any differences.

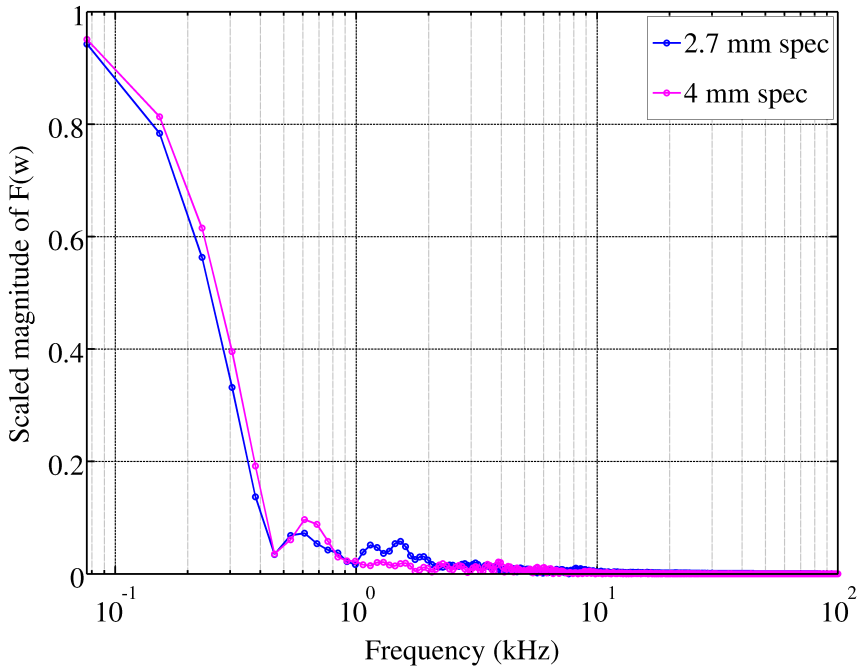

Figure 7.3: Plot of frequency spectra of typical force-time signals from impact bend tests

As Fourier analysis did not reveal a distinct dominant frequency, more detailed examination was conducted in the time domain, where the oscillations are clearly visible. The local peaks and troughs used to determine the period of oscillation were determined by visual inspection. This is not the most precise means of analysis, particularly as superimposition of different frequencies of oscillation will result in the apparent peak being shifted from the true peak. However, more rigorous analysis was beyond the scope of this thesis. Figure 7.4 shows the early portion of a HPB Impact Bend test on a 4 mm GFPP specimen, indicating the "major local peak and trough" and "minor local peak to peak" as referred to in the following discussion.

For both the 2.7 mm and 4.0 mm thick GFPP specimens, the time between the first major local peak and trough ranges from 0.09 and 0.11 ms. For the tests on 4.0 mm thick specimens, the period of the minor oscillations lay between 0.042 and 0.050 ms. which is slightly less than the 4^{th} harmonic period of 0.051 ms. The minor oscillations during tests on 2.7 mm thick specimens do not show a consistent period. The period of the second bending harmonic is 0.185 and 0.205 ms for the respective thicknesses,

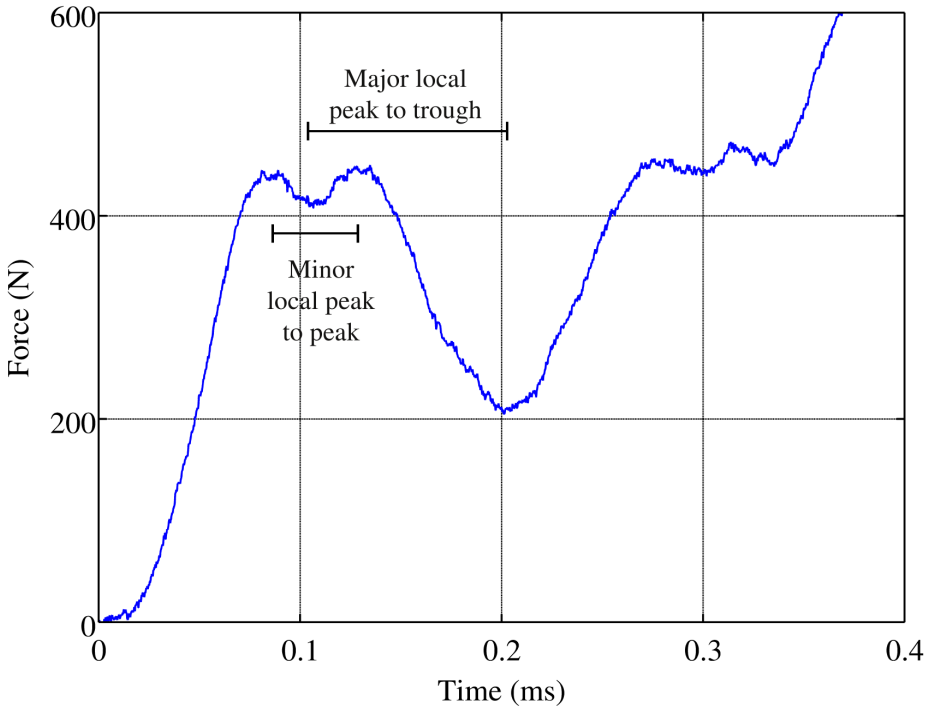

Figure 7.4: Plot of typical force-time signal from an HPB impact bend test, indicating major and minor peaks

which gives a time between the major local peak and trough of 0.092 and 0.102 ms respectively. Hence the major local peak and trough, which are visible for all impact bending tests, may be due to excitation of the second bending mode of the specimen. The 4^{th} bending mode of the 4 mm specimen has a period of 0.051 ms, which is slightly more than period of the minor oscillations for these specimens.

Axial stress waves in the specimen supports of the impacter and the metallic head of the HPB have transit times of the order of 0.003 to 0.005 ms, so may be immediately dismissed as possible causes. Stress waves in the specimen parallel to the direction of impact (i.e. across the thickness) have transit times of approximately 0.007 ms and hence are not responsible for the observed oscillations.

The axial guide rod of the impacter is 350 mm and is made of steel, resulting in the time taken for an axial stress wave to traverse the guide rod and return to the cross member being 0.137 ms. As an axial stress wave would originate as compression, and reflect as tension, this time must be compared with the time between a local peak and the closest local trough (a half period). The corresponding time for the major oscillations lies between 0.09 and 0.11 ms. Hence axial stress waves in the impacter are unlikely to be the sole cause of the oscillations.

The deflection of the cross member of the impacter was considered to be negligible when calculating the deflection of the specimen, as the cross member has a flexural stiffness three orders of magnitude greater than the typical specimens tested during this thesis. While the deflections may be of negligible magnitude, the vibrational modes of the impacter and its cross member may contribute to the observed oscillations. When set at a span of 50 mm, as used for the 2.7 mm thick specimens, the first flexural vibration mode of the cross member has a period of 0.054 ms. This period does not correlate with any of the oscillations observed. The 4 mm thick specimens used a span of 64 mm, corresponding to a period of 0.088 ms. This is slightly less than the half period measured from the first major peak to trough.

The periods of the observed oscillations and the potential causes are summarised in Table 7.3 for the 2.7 mm specimens and Table 7.4 for the 4 mm specimens.

Table 7.3: Summary of oscillation periods and potential causes for 2.7 mm GFPP specimens

Oscillation	Period (ms)	Potential Cause	Period (ms)
Major (Half period)	0.09 to 0.11	2^{nd} bending mode of specimen	0.092

Table 7.4: Summary of oscillation periods and potential causes for 4 mm GFPP specimens

Oscillation	Period (ms)	Potential Cause	Period (ms)
Major (Half period)	0.09 to 0.11	1^{st} bending mode of cross member	0.088
		2^{nd} bending mode of specimen	0.102
Minor	0.042 to 0.050	4^{th} bending mode of specimen	0.051

This type of analysis does not take into account the combined effect of stress waves reflecting from multiple surfaces, nor the resultant of two or more simultaneous vibration modes. The initial impact will generate stress waves in the impacter and HPB, and is likely to excite flexural vibrations of the specimen and cross member of the impacter. Hence the HPB Impact Bend test was modelled using ABAQUS / Explicit, in order to examine the combined effect of the stress waves and vibrational modes of the specimen, impacter and HPB. All moving components (specimen, impacter and HPB) of the experiment were modelled as 3D deformable parts. To reduce computational expense, a quarter-symmetry model was created with the appropriate symmetry boundary conditions applied to the relevant planes. The real impacter consists of several components

with threaded and bolted joints. The complication of modelling each component, including bolt preloads, was considered unnecessary as these components do not move relative to each other. Hence the impacter was modelled as a single part, using a linear elastic material model with $E_y = 210GPa$, $\rho = 7800kg/m^3$ and $\nu = 0.3$. The HPB was also modelled as a single part, but partitioned appropriately to allow different material properties to be applied to the steel roller, aluminium head and polycarbonate bar. The aluminium was modeled using the linear elastic material model with $E_y = 69GPa$, $\rho = 2700kg/m^3$ and $\nu = 0.33$. The polycarbonate was also modelled as a linear elastic material [1] with $E_y = 2.5GPa$, $\rho = 1200kg/m^3$ and $\nu = 0.37$. The specimen material model incorporated the anisotropic elastic properties of GFPP, as shown in Table 7.5. No failure criteria or rate dependency was included in the GFPP material model, as the aim of this analysis was to investigate the early oscillations.

Table 7.5: GFPP anisotropic model parameters

Parameter	E_{11}	E_{22}	E_{33}	ν_{12}	ν_{13}	ν_{23}	G_{12}	G_{13}	G_{23}
Value	11 GPa	11 GPa	2 GPa	0.11	0.11	0.11	1.7 GPa	1.7 GPa	1.7 GPa
Source	§4.6.2 and §5.1.3			Manufacturer's data sheet [19]					

Contact surfaces were defined between the specimen, impacter and HPB. The contact model applied the penalty contact method, with a friction coefficient of 0.2 between the surfaces. The impacter and specimen were assigned an initial velocity of 8 m/s. The entire model was meshed with 3D, 8 noded, reduced integration continuum elements (C3D8R) with appropriate refinement of the rollers and specimen as shown in Figure 7.5. The stress and strain histories were recorded at the elements in the HPB coincident with the axial location of the strain gauges.

Force histories from the FEA prediction and experimental results for the 4 mm thick specimen are compared in Figure 7.6. The force history was determined from the simulation by extracting the HPB strain at an element in the model coincident with the strain gauge in the experiments. This "virtual strain gauge" data was then treated in the same manner as the experimental data (§5.2.6) to calculate the impact force. The FEA prediction has larger superimposed oscillations than the experimental results. Fourier

[1] Polycarbonate is strictly speaking a visco-elastic material, but investigations by Curry [185] and Rao and Shim [182] have shown that modelling PC as a linear elastic material gives a good first approximation.

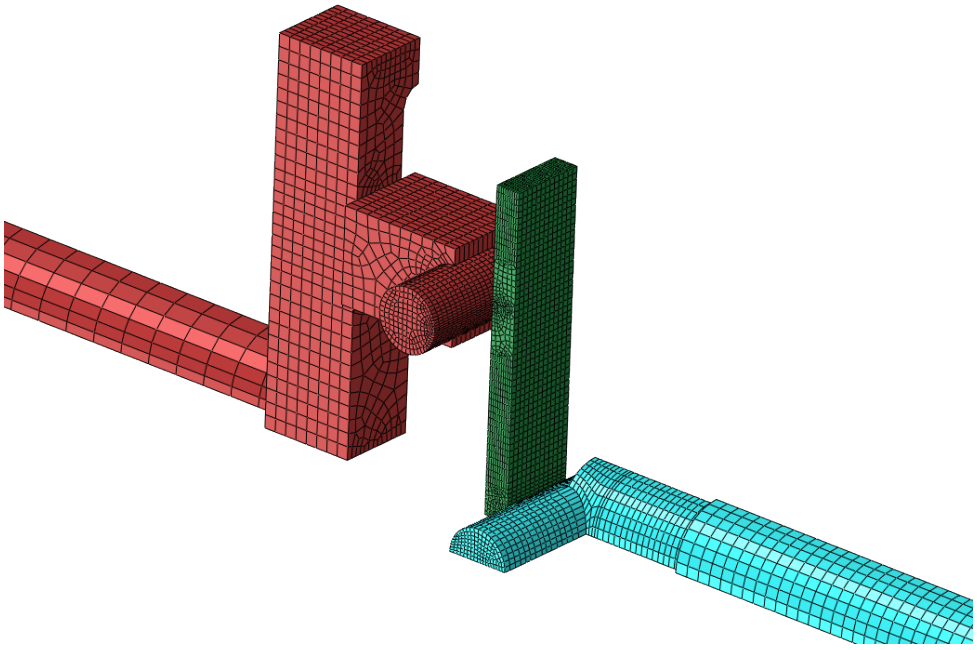

Figure 7.5: Quarter symmetry FEA model of HPB Impact Bend experiment, for a 4 mm thick GFPP specimen

analysis of the FEA force history showed a large frequency component at 18.5 kHz. The analysis of visco-elastic wave propagation in the HPB (Appendix B) indicated that higher frequency osicllations would attenuate in a relatively short propagation distance and hence would not be observed in the experimental force signal. However, the material model for the polycarbonate HPB in the FEA does not incorporate any visco-elastic effects so higher frequencies may propagate without attenuation. Thus the greater oscillations in the FEA force history may be attributed to the use of a purely elastic, non-dissipative material model for the polycarbonate HPB. Fourier analysis of the experimental force histories had indicated that the magnitude of frequency components above 10 kHz was less than 0.5% of the largest frequency component (Figure 7.3). To facilitate comparison, the force prediction from the FEA was filtered using a cut-off frequency of 10 kHz, which is also plotted in Figure 7.6. The filtered FEA force history follows the experimental result and exhibits nonlinearities similar to the experimental results. As the specimen material model in the FEA is purely linear elastic, the nonlinearities in the FEA prediction must be due to something other than the specimen material behaviour. These nonlinearites are most likely due to the interaction of flexural vibrations of the specimen and impacter.

The FEA was also used to verify the assumption that the deflection of the impacter may be neglected when calculating the specimen deflection. Velocities and displace-

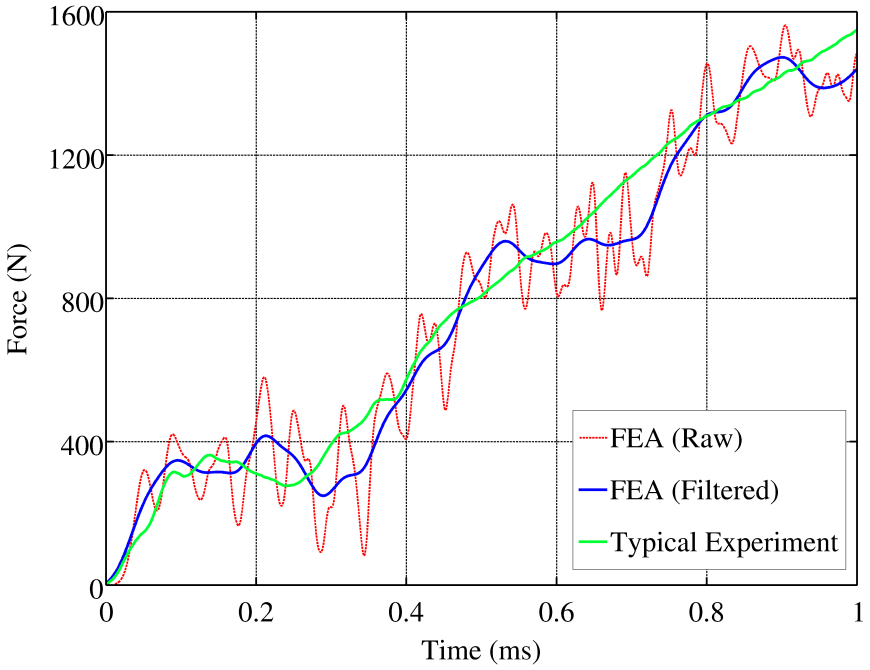

Figure 7.6: Plot of early elastic force histories comparing experimental results and FEA prediction of a HPB Impact Bend test on a 4 mm thick GFPP specimen

ments were extracted from the FEA for points coincident with the roller of the outer specimen support and the axis of symmetry of the impacter. The velocities, compared in Figures 7.7, oscillate about the same trend. When integrated to obtain the displacements, shown in Figure 7.8, the difference is less than 10 μm at any time. As the specimen deflections are several mm, a difference of 10 μm may be safely neglected. Hence treating the impacter as perfectly rigid while calculating specimen deflection is a safe assumption.

The FE simulation of the HPB Impact Bend experiments on monolithic GFPP indicated that the early oscillations in the experimental force histories may be attributed to the interaction of flexural vibrations in the specimen and impacter cross member. The simulations confirmed that the deflection of the impacter may be safely neglected when calculating the specimen deflection.

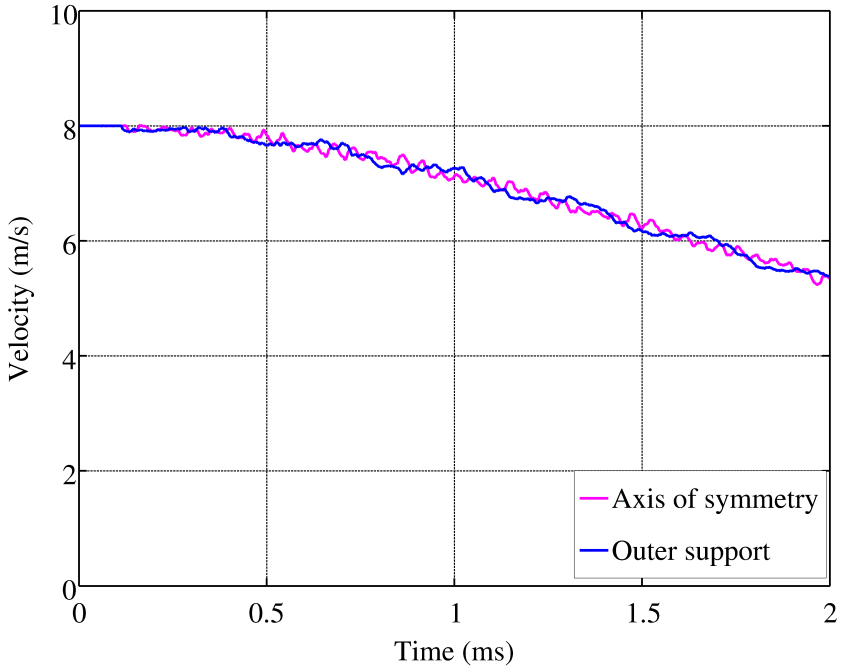

Figure 7.7: Plot of FEA velocity histories for impacter at outer support and axis of symmetry

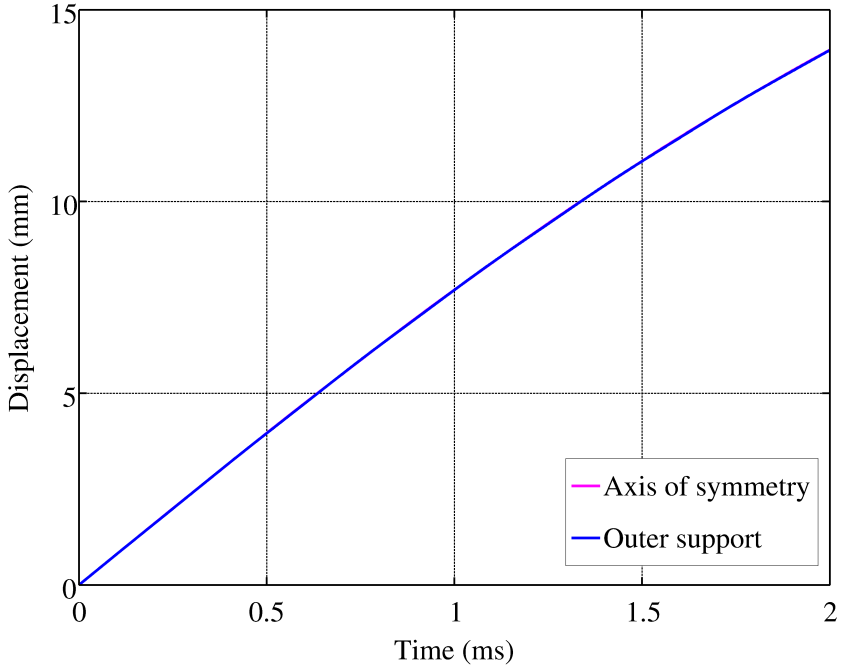

Figure 7.8: Plot of FEA displacement histories for impacter at outer support and axis of symmetry -*N.B. the two plots are indistinguishable at this scale.*

7.3 Delamination Testing

Several methods for delamination testing were evaluated as candidates for high strain rate delamination testing, before selecting the Single Leg Bend test. The impact bend HPB set up was used to test GFPP and FML SLB specimens at impact velocities ranging from 5 to 8 m/s.

The quasi-static delamination tests are interrogated further with the aid of computational models implemented in the finite element code ABAQUS / Standard v6.10. Only the relevant results are discussed in this section , with the details of the specimen geometry, material models, boundary conditions and meshing presented in Appendix C. Delamination is modelled using cohesive elements, which are available in both ABAQUS/Standard and ABAQUS/Explicit. In order to capture the rate dependence observed in the impact delamination experiments, the constitutive model for the cohesive elements would require a rate dependence option, which is not currently available in ABAQUS [198]. The development of a user subroutine for rate dependence of a cohesive element is beyond the scope of this thesis, and hence modelling of the impact delamination experiments was not attempted.

7.3.1 End Notch Flexure tests on GFPP

The ENF tests on GFPP (§6.2.1.1) produced a surprising result by exhibiting relatively stable crack growth, with a gradual softening of the force response. ENF tests normally produce relatively linear force response up to sudden unstable crack growth, coinciding with a rapid drop in force. A FE simulation of the ENF tests was generated to ascertain whether the nonlinear force response was due to progressive delamination, or a combination of delamination and in-ply failure. The ENF tests on GFPP were modelled using a 2D, plane strain model in ABAQUS/Standard. To account for the relatively large deflections, the non-linear geometry option was selected. The initial model (FEA 1) was run using material parameters as summarised in Table 7.6. The force-displacement response extracted from FEA 1 was reasonable in comparison to the experimental results, as shown in Figure 7.9(a). However, the peak force exceeded the experimental value slightly and the drop in force after the peak was more abrupt that that observed experimentally. The predicted force response for the ENF tests is sensitive to the following constitutive parameters:

- Initial slope is proportional to the elastic modulus E_{11}

- Peak force is proportional to the Mode II critical stress σ_{2c}
- The softening behaviour after the peak force is determined by the Mode II fracture energy G_{IIc}

These three parameters were adjusted to obtain closer correlation between the experimental and FEA force-displacement response. The combinations of parameters investigated are detail in Table 7.6.

Table 7.6: Constitutive parameter variation for ENF tests on GFPP

Parameter Model Number	E_{11} GPa	σ_{2c} MPa	G_{IIc} kJ/m^2
FEA 1	11	12	5.3
FEA 2	12.5	12	5.3
FEA 3	12.5	9.5	5.3
FEA 4	12.5	9.5	6.0

In each of the consecutive models, one constitutive parameter was adjusted to improve one aspect of the correlation:

- The initial slope is corrected by increasing E_{11} (Figure 7.9(b)). The initial value E_{11} of 11 GPa was the average measured experimentally in specimens of similar thickness at similar rates (Table 5.2). The revised value of 12.5 GPa lies between the average values measured in this thesis and those reported by the manufacturer [19] and so is within norms.
- The peak force was reduced to within the experimental bounds by decreasing σ_{2c} from 12 to 9.5 MPa, as shown in Figure 7.9(c). The original estimate for σ_{2c} was obtained from the manufacturer [19]. The response post peak force does not drop as abruptly as FEA 1, but is still below the experimental bounds.
- FEA 4 has an increased value of G_{IIc}, which gives very good correlation as shown in Figure 7.9(d). The initial G_{IIc} value of 5.3 kJ/m^2 was the average propagation value of G_{II} from the ENF tests conducted (§6.2.1.3). The revised value of 6.0 kJ/m^2 is at the top of the experimentally observed range.

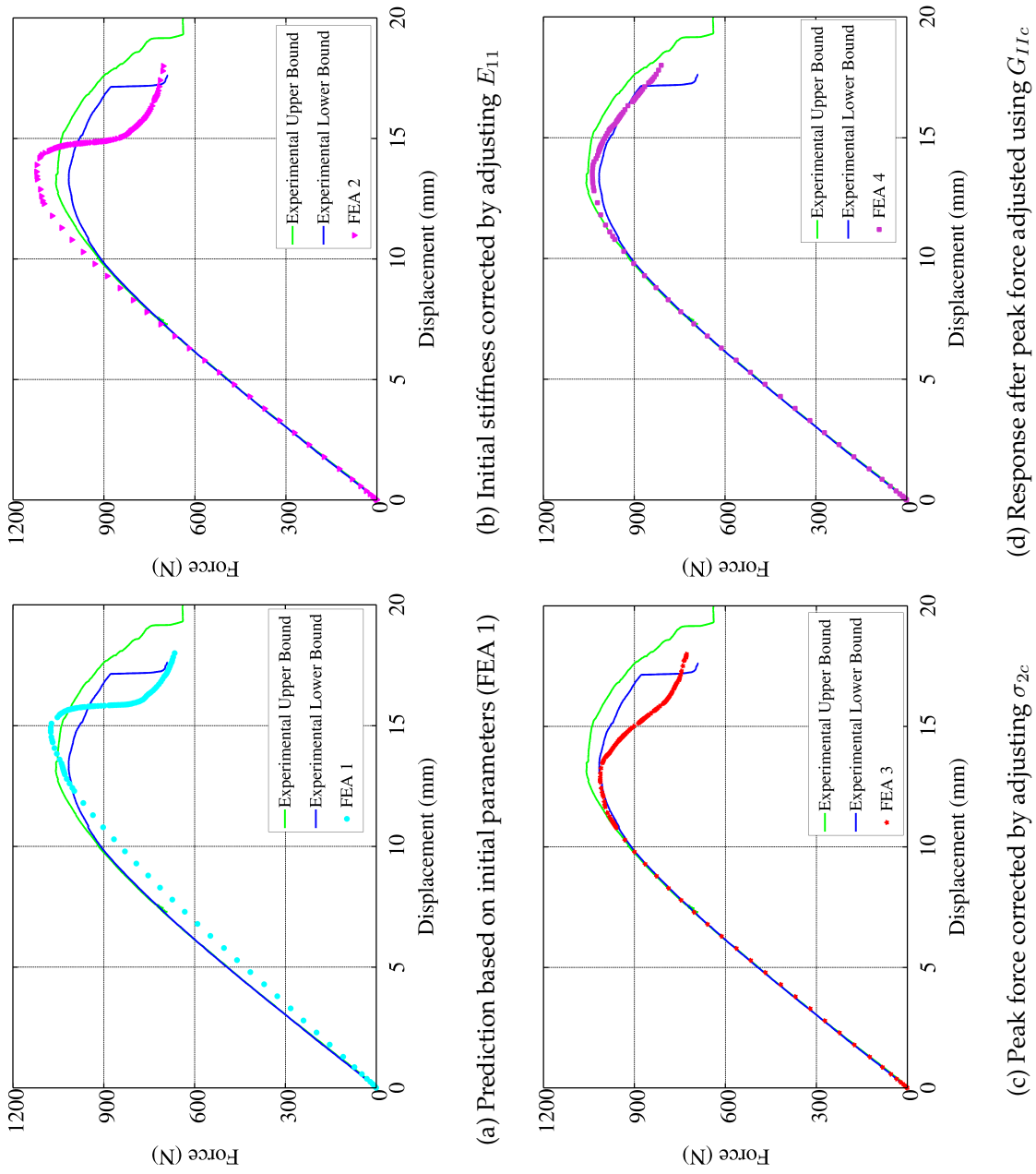

(a) Prediction based on initial parameters (FEA 1)

(b) Initial stiffness corrected by adjusting E_{11}

(c) Peak force corrected by adjusting σ_{2c}

(d) Response after peak force adjusted using G_{IIc}

Figure 7.9: Plots comparing force-displacement response for experiment and FEA

The aim of the FE simulation was to confirm that the nonlinear force response of the ENF test was due to delamination growth, rather than in-ply failures. A contour plot of the in-plane stress S_{11} at maximum displacement is shown in Figure 7.10. The maximum tensile stress is 235 MPa, while the maximum compressive stress is 256 MPa, both of which are lower than the measured quasi-static flexural strength of 273 MPa (Table 5.2). The experimental force response became nonlinear at a deflection of approximately 8 mm. At the corresponding deflection in the FE simulation, the maximum tensile stress is 169 MPa and the maximum compressive stress is 190 MPa. The quasi-static bend tests produced linear responses at stresse well above those expected to cause damage to the matrix material. Hence it is unlikely that localised matrix damage at the outer fibres is contributing to the nonlinearity. As the flexural stresses are substantially lower than the flexural strength when the force becomes nonlinear, the nonlinearity observed can only be attributed to loss of stiffness from accumulated damage in the cohesive elements. At this stage in the FE simulation, the damage initiation criteria had been reached in a band of cohesive elements starting at the crack tip and ending 9 mm closer to central load. It should be noted that the experimentally observed crack tip is not meant to coincide with a cohesive element that has just reached the damage initiation criteria - the cohesive zone model smears the crack tip over a fracture process zone.

This analysis showed that FE simulation using a cohesive zone model can provide good agreement with the macroscopic force-displacement response of experiments. The FE simulation further confirmed that LEFM principles were valid throughout the ENF experiments.

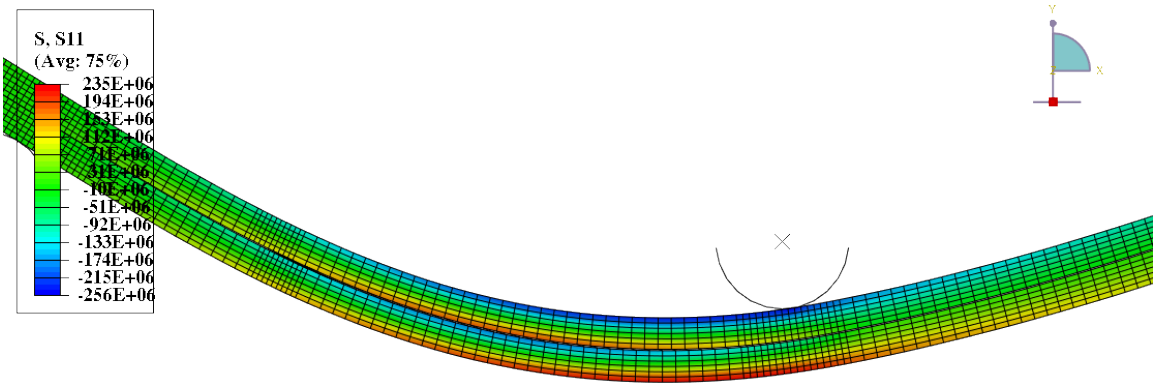

Figure 7.10: Contour plot of S_{11} at maximum displacement for ENF test of GFPP

7.3.2 Single Leg Bend Tests on GFPP

The SLB tests on GFPP exhibited more scatter than the ENF tests. Some of this scatter can be attributed to variation in the thickness of the upper leg, which has a strong effect on the overall stiffness of the specimen. To facilitate comparison, a single SLB test (Specimen 2) was selected for comparison to simulation, which replicated the specific specimen dimensions exactly. The GFPP material model used the parameters detailed in Table 7.5, while the delamination was modelled using cohesive elements with parameters as shown in Table 7.7, which are the same as the initial estimate FEA 1 as used for the ENF simulations. The Mode III (interlaminar cross shear) parameters were assumed to be equal to the Mode II (interlaminar in-line shear) parameters.

Table 7.7: FEA Cohesive zone parameters for Single Leg Bend test of GFPP

Parameter	σ_{1c}	G_{1c}	σ_{2c}	G_{IIc}	σ_{3c}	G_{3c}
Units	MPa	kJ/m^2	MPa	kJ/m^2	MPa	kJ/m^2
Value	5	1.5	10	5.3	10	5.3

The damage initiation criteria was based on a quadratic stress criteria:

$$\left(\frac{\sigma_1}{\sigma_{1C}}\right)^2 + \left(\frac{\sigma_2}{\sigma_{2C}}\right)^2 + \left(\frac{\sigma_3}{\sigma_{3C}}\right)^2 \leq 1 \tag{7.5}$$

The damage evolution was based on a power law:

$$\left(\frac{G_I}{G_{Ic}}\right) + \left(\frac{G_{II}}{G_{IIc}}\right) + \left(\frac{G_{III}}{G_{IIIc}}\right) \leq 1 \tag{7.6}$$

Figure 7.11 compares the force-displacement prediction from FEA with the experimental result. The FEA follows the experimental result closely until the force becomes nonlinear. The experimental result has a greater decrease in stiffness than the FEA prediction. The FEA overestimates the peak force by 6.6 %. At the departure from linearity, corresponding to a specimen deflection of approximately 2 mm, the flexural stresses in the specimen are less than 103 MPa as shown in Figure 7.12(a), which is substantially less than GFPP's quasi-static flexural strength of 270 MPa. At a deflection of 2 mm, damage had initiated in a 5 mm long band of cohesive elements from the crack tip towards the central load. Hence the softening force response can only be due to accumulated damage in the delamination zone, and not in-ply failure. The first

deletion of a cohesive element occurs just after peak force in the simulation. Even at the peak force, the maximum flexural stress is only 167 MPa so in-ply failure cannot be the cause of the decrease in force immediately after the peak. Thus the decrease in force after the peak may be attributed to advanced delamination, which corresponds to deletion of cohesive elements in the simulation. The flexural stresses in the upper leg of the simulation reach the flexural strength of 275 MPa at a deflection of 8 mm, shown in Figure 7.12(b), at which point the simulation was stopped.

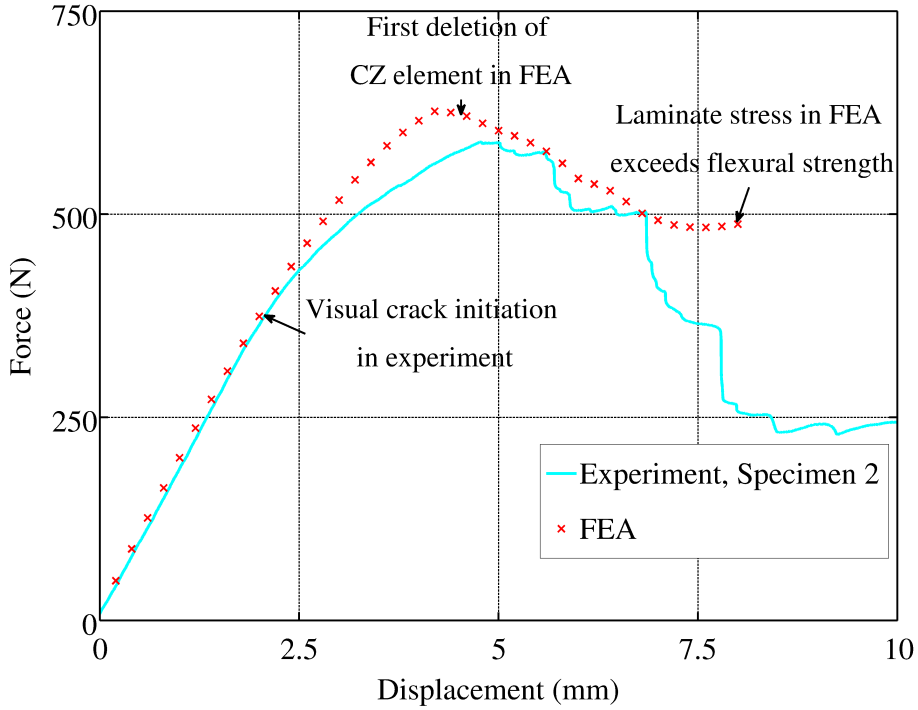

Figure 7.11: Plot comparing force-displacement results for FEA and experimental SLB tests on GFPP (Specimen 2)

The aim of this simulation was to achieve an reasonable agreement, rather than an exact match, of the experimental and simulated force-displacement macroscopic responses, based on constitutive parameters obtained from other experiments and simulations. Refinement of the parameters, as was done for the pure Mode II ENF test, was not pursued for the SLB test. As the SLB is a mixed Mode I-II test, there are four constitutive parameters (σ_{1c}, G_{1c}, σ_{2c} and G_{IIc}) as well as the choice of fracture mode interaction (e.g. linear or quadratic envelope) which will affect the delamination response. Refining this many constitutive parameters with any certainty would require additional experimental data for validation purposes - for example a SLB test conducted at a different fracture mode ratio. The force-displacement for the higher rate SLB tests conducted on the HPB Impact Bend apparatus differ in shape from the

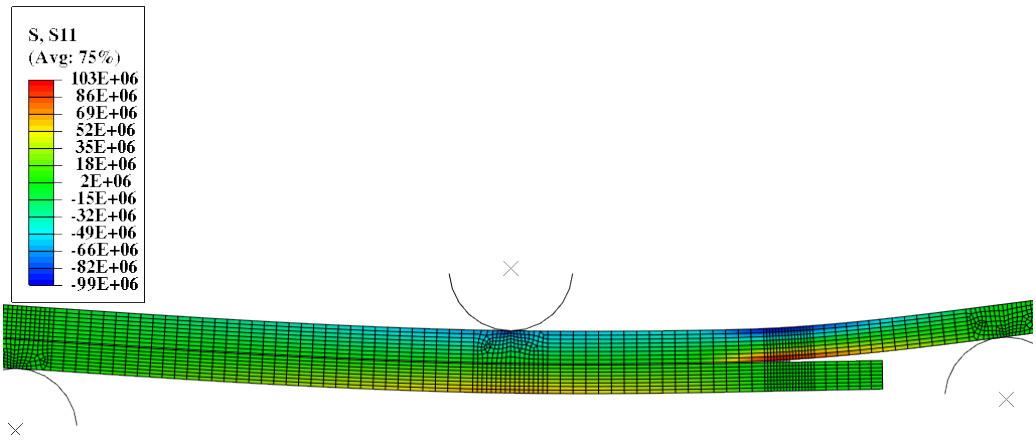

(a) S_{11} at specimen deflection of 2 mm

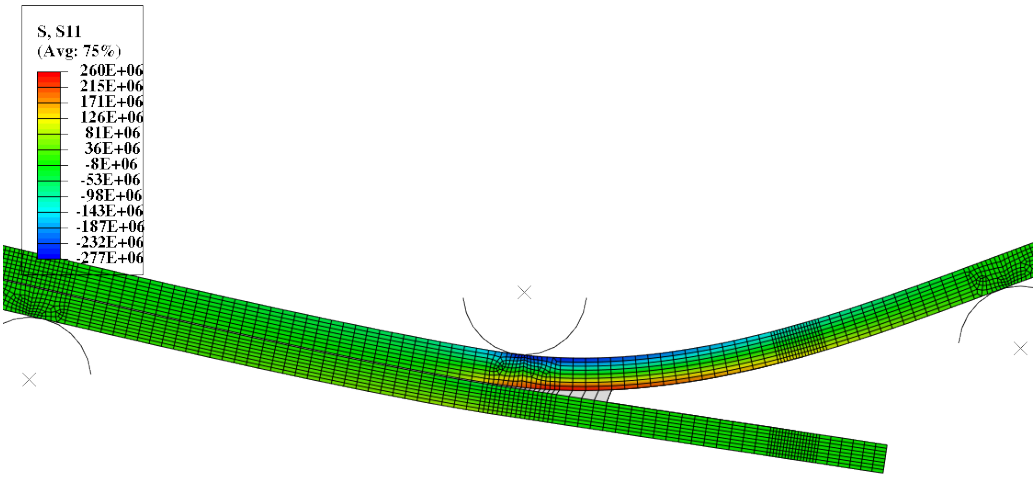

(b) S_{11} at specimen deflection of 8 mm

Figure 7.12: Contour plots of S_{11} from FE simulation of Single Leg Bend test of GFPP

quasi-static SLB tests. Hence before embarking on FEA of the higher rate SLB tests, it was necessary to first establish how well simulations correlated with the quasi-static SLB tests based on the initial estimates for the constitutive parameters. The shape of the quasi-static force-displacement response is predicted accurately by the FEA, with acceptable agreement for the peak force value (6% variation). The FE simulation indicated that the nonlinearity in the SLB force response was due to delamination growth, and not in-ply failure.

7.3.3 High Rate Single Leg Bend Tests Using the HPB Impact Bend Apparatus

The high rate SLB tests on GFPP specimens, using the HPB Impact Bend apparatus, produced force histories that differed not only in magnitude from the equivalent quasi-static tests (see Figure 6.25 in §6.2.3.3), but also in the shape of the force-displacement response. In order to investigate these differences, the high rate SLB tests were modelled using ABAQUS / Explicit, in a similar manner to that for the monolithic HPB Impact Bend tests (§7.2.1). Due to the SLB specimen geometry, the model used half-symmetry. The impacter and HPB were modelled deformable parts assigned the appropriate linear elastic material properties, described in §7.2.1.

Contact interactions were applied to the appropriate surfaces of the specimen, impacter and HPB. In addition, contact interactions were applied to the crack faces, as well as the specimen lower leg which might contact the impacter. The requisite boundary conditions were applied on the plane of half symmetry. The axis of symmetry of the impacter and HPB were constrained to only move axially, as these are supported by axial guide bushes in the experiment. The impacter and specimen were assigned an initial velocity of 8 m/s.

The material model for the specimen used the parameters detail in Table 7.5, while cohesive elements were used to model the delamination. The constitutive models for cohesive elements available in ABAQUS v6.10 do not have options for any rate dependency [198]. Developing the necessary user subroutines for a rate dependent cohesive element in ABAQUS is outside the scope of this thesis. Hence the constitutive parameters used for the quasi-static models, detailed in Table 7.7, were used as an initial estimate for the high rate SLB tests.

The force histories for the experimental results and FEA predications of a high rate SLB test are compared in Figure 7.13. The raw output of the FEA features superimposed high frequency oscillations, as was seen for the FEA predictions for the HPB Impact Bend tests on monolithic GFPP specimens. The FEA prediction was filtered using a cut off frequency of 10 kHz, and the filtered result is plotted. The general shape and trends of the FEA prediction compare reasonably with the experimental results, but there is a clear difference in magnitude once the response becomes nonlinear. The variation over the entire history is difficult to quantify due to the oscillations on both sets of data. At the departure from linearity, which is relatively clear for all the data, the variation between the FEA and the experimental upper bound is 23 %.

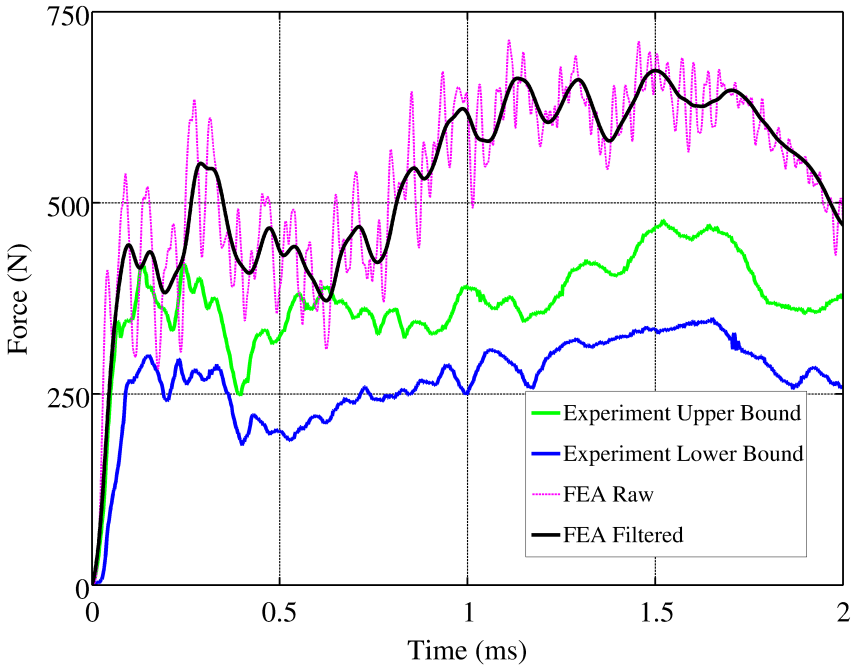

Figure 7.13: Plot of force histories for experiment and FEA predictions of a high rate Single Leg bend test on GFPP

In the FE simulation at the departure from linearity, the highest flexural stresses in the specimen were less than 30% of the quasi-static flexural strength of GFPP. Hence inply failure due to bending cannot be responsible for the departure from a linear force response. The damage initiation criteria along the plane of delamination plane, at the time of departure from a linear force response, is plotted in Figure 7.14.

The elements at the crack tip had reached the damage initiation criteria, as is expected. However, an independent damage zone had also initiated around the midspan, except for directly below the point of impact with the HPB. The initiation of damage on either side of the midspan is due to interlaminar shear stresses, which change direction below the point of impact (and hence are zero at this point). In addition, the through thickness stresses were compressive immediately below the impact point, which suppressed delamination damage initiation to a certain extent. The initiation of damage at multiple locations in the simulated impact experiment is very different from the simulated quasi-static experiment, where damage initiated first at the initial crack tip then propagated towards midspan. As the damage initiated near the midspan was due to interlaminar shear stresses, the corresponding delamination in the experiments would be Mode II or III crack growth. The high speed video of the high rate SLB experiments was reviewed, but has insufficient resolution to determine whether

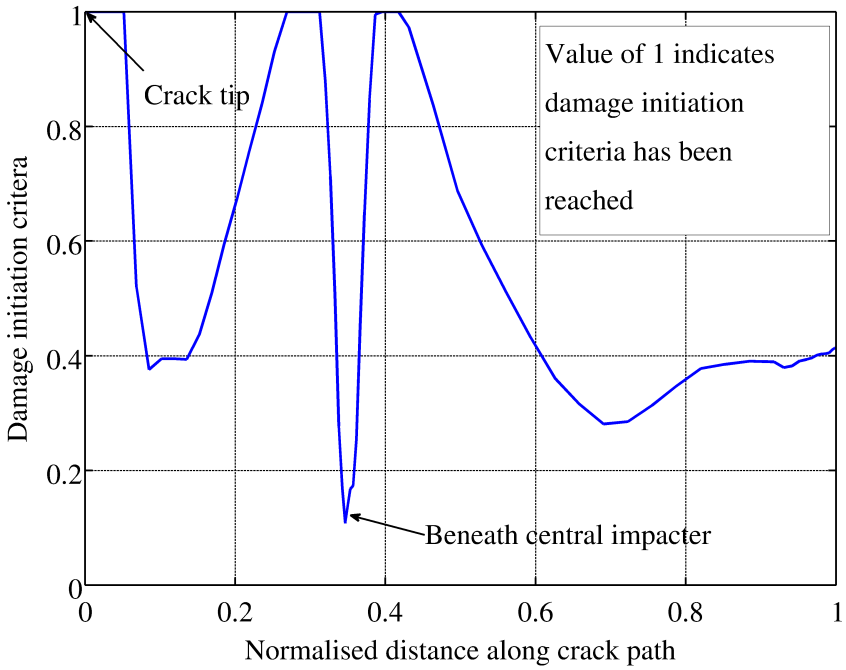

Figure 7.14: Plot of damage initiation critera along plane of delamination

any Mode II or III cracks develop near the midspan. By the end of the test, the delamination growing from the starter defect would merge with any delamination that initiated adjacent to the impacter. Hence it was not possible to confirm whether the multiple delamination sites predicted by the FE simulation also existed in the experiments. Interrupted impact tests may be helpful in confirming the presence of multiple delamination sites. However, this would require significant modification to the existing apparatus to ensure that interruption of the specimen deformation was performed accurately and without damaging the specimen.

If multiple delamination sites were present during the experiments, then the accuracy of the G_c values derived therefrom would be reduced. However, it would be premature to declare the results invalid until the presence of multiple delaminations in the impact experiments is proved.

The simulated force responses for both the quasi-static and high rate SLB tests are greater than experimental results, with the high rate SLB response over-predicted by a greater proportion. The difference in magnitude may be due to some rate dependency in the delamination response. In order to confirm this, a rate dependent cohesive zone model would have to be implemented in an explicit FE code. However, the difference in shape between the predicted force response of the FE simulations of the quasi-static

and high rate SLB experiments cannot be ascribed to rate depedency, as neither the in-ply material model nor the cohesive element consitutive model included any rate dependent terms.

The force-deflection responses of the quasi-static and high rate (HPB) SLB tests on GFPP are compared in Figure 7.15 for the experimental results and in Figure 7.16 for the FE predictions. The FE simulation has predicted the different shapes of the force-deflection responses with reasonable accuracy. Hence the different shape of the force response at high rates must be due to physical phenomena that are included in or captured by the FE simulation. Flexural vibrations and stress wave interaction in the specimen and impacter, which will be captured by FE simulation, are probably contributing to the nonlinearites in the force response, as was the case for the HPB Impact Bend tests of monolithic GFPP specimens. The presence of multiple damage zones in the cohesive elements (at the initial crack tip and on either side of midspan), is likely to induce further nonlinearity in the force response.

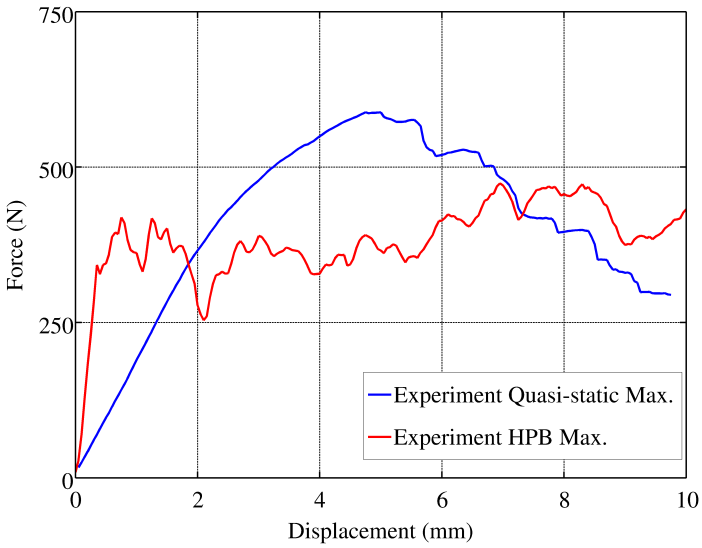

Figure 7.15: Plot of force-deflection for experimental results of quasi-static and high rate Single Leg bend test on GFPP

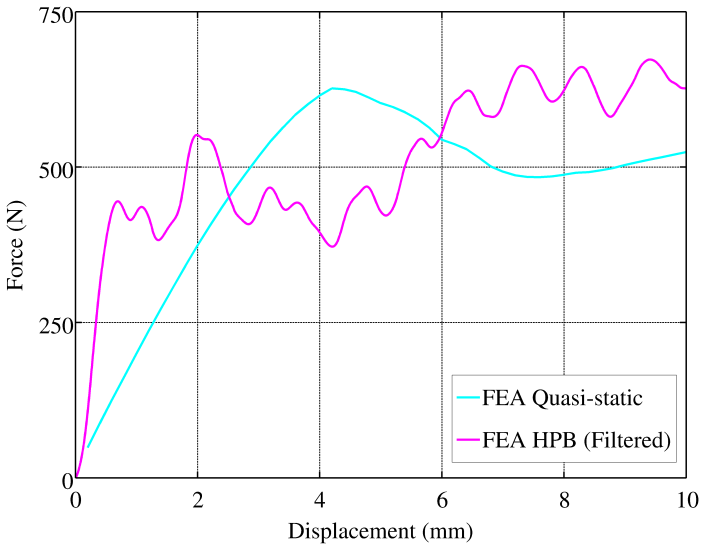

Figure 7.16: Plot of force-deflection for FEA predictions of quasi-static and high rate Single Leg bend test on GFPP

7.3.4 Fracture Mode Analysis of FMLs

The fracture mode ratio of an interfacial crack between different materials depends on both the deformation geometry (as for single material specimens) and the relative moduli of the materials at the interface. The fracture mode ratio may be determined from either analytical solutions using plate or beam theory, or from force and displacement fields obtained from FEA. Sundararaman and Davidson [190, 199] presented analytical solutions for bimaterial ENF and SLB specimens for interfacial fracture, based on plate theory. However, the relationships presented included parameters which were not clearly defined. Furthermore, the results of the analytical solutions for mode mixity ratios were compared to FEA results, and were in good agreement. As FEA can account for geometric and material nonlinearities more easily than analytical approaches, the modal ratios for the interfacial fracture tests on FMLs were determined using FEA. The Virtual Crack Closure Technique (VCCT), descibed in §2.6.2, was used to estimate the contributions of the different fracture modes in unsymmetric ENF tests of FMLs. The analysis performed is for quasi-static experiments, using ABAQUS/Standard and hence no rate depedency was modelled. The experiments were approximated as 2D plane strain problems, as the Mode III contributions were assumed to be negligible.

The VCCT is used to determine the strain energy release rates for the different modes of fracture, based on the forces and displacements of the nodes adjacent to the crack tip. If the increment of crack growth is small, then one may assume that the force and displacement fields around the crack tip do not change significantly. Hence all the required forces and displacements may be obtained from a single model. The VCCT approximations for G_I are explained with the aid of Figure 7.17. Only the vertical forces F_2 and displacements δ_2 are shown in Figure 7.17 for clarity - G_{II} is calculated in the same manner using the horizontal forces F_1 and displacements δ_1. The 2D planar problem shown assumes a out of plane width of b.

G_I may be approximated by:

$$G_I = \frac{1}{2b\Delta a}\left[F_2^{(j+1)}(\delta_2^{U(j-1)} - \delta_2^{L(j-1)}) + F_2^{(j)}(\delta_2^{U(j-2)} - \delta_2^{L(j-2)})\right] \tag{7.7}$$

And G_{II} by :

$$G_{II} = \frac{1}{2b\Delta a}\left[F_1^{(j+1)}(\delta_1^{U(j-1)} - \delta_1^{L(j-1)}) + F_1^{(j)}(\delta_1^{U(j-2)} - \delta_1^{L(j-2)})\right] \tag{7.8}$$

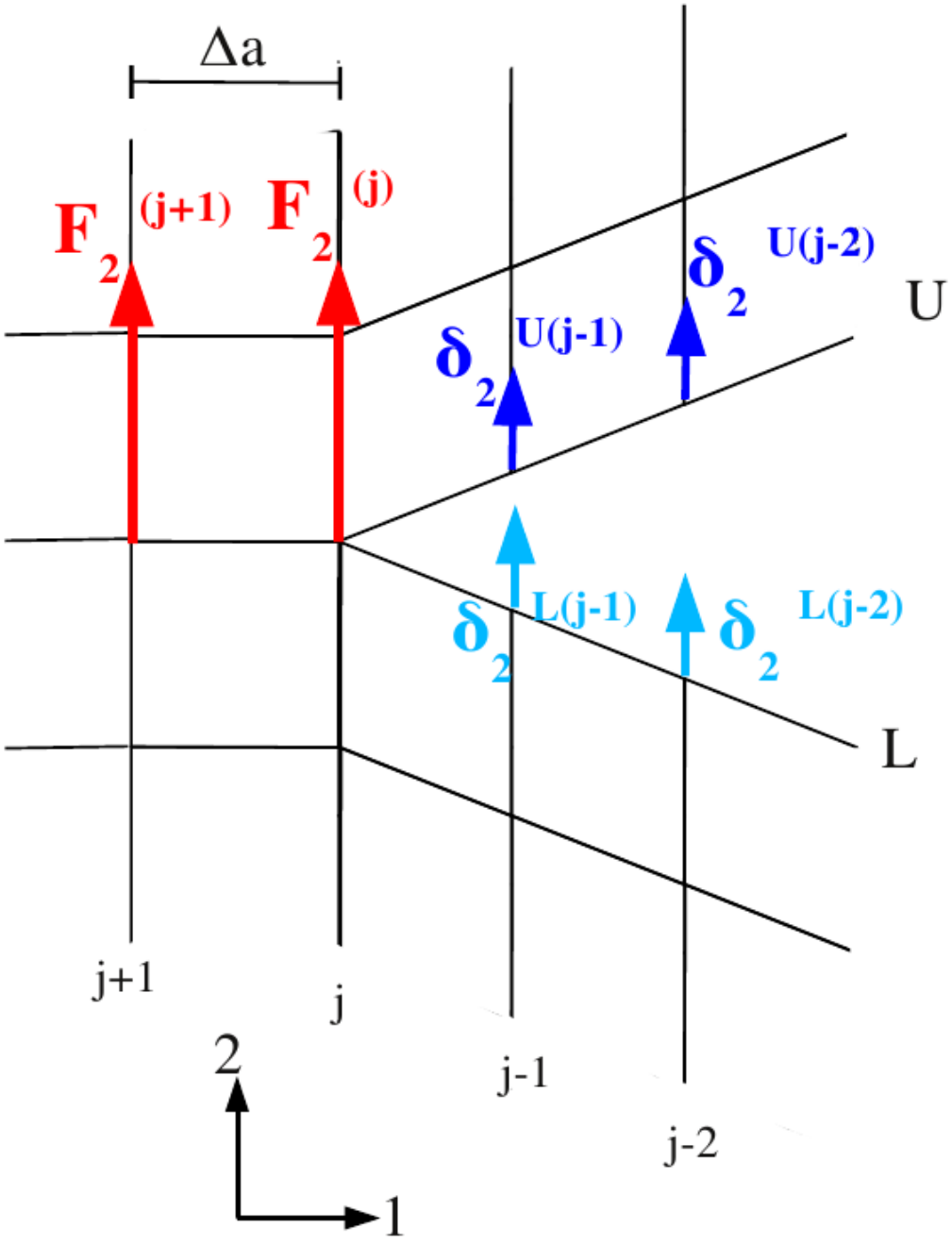

Figure 7.17: Schematic of nodal forces and displacements used to approximate G_I for a 2D problem using the VCCT

The total energy release rate G_T is simply the sum of the modal energy release rates, i.e. for a 2D problem $G_T = G_I + G_{II}$.

While extracting the nodal displacements from an ABAQUS output database (ODB) is straightforward, obtaining the nodal forces requires an intermediate step. The force acting on a particular node, due to one of the adjacent elements, is obtained from the ODB by requesting the field variable "NFORC". For a static problem, the sum of all forces acting on a particular node from all the adjacent elements must be zero for the node to be in equilibrium. For a node with q adjacent elements, the nodal force was taken to be the largest of all the permutations of 1 to $q-1$ of the element force contributions, i.e. the largest out of balance resulant acting on the node.

7.3.4.1 Fracture Mode Analysis of ENF Test of FML

The VCCT was applied to FE simulations of the ENF tests of FML specimens to obtain the fracture mode ratios. To reduce computational expense, the simulations were based on a 2D, plane strain assumption. During the ENF tests on aluminium, permanent deformation of the aluminium layer was noted at the end of the tests. It was unclear at what point in the test the aluminium became plastic, so two fracture mode analyses were conducted for the ENF tests of FMLs:

- Modelling the aluminium layer as a linear elastic material
- Modelling the aluminium layer as an elasto-plastic material

Details of these models may be found in Appendix C. The model was loaded by displacing the central roller vertically by 1.5 mm, which was the maximum deflection recorded in the experiments. The effect of crack growth was simulated by replicating the models, with an increment of 5 mm in the initial crack length for each model.

The modal energy release rate ratios as a function of initial crack position are shown in Figure 7.18, for the models with an elastic response for the aluminium. Results based on an elasto-plastic response for the aluminium are shown in Figure 7.19. For both cases, it is clear the Mode II dominates. For a purely elastic aluminium response, the proportion of Mode I ($\frac{G_I}{G_T}$) decreases steadily as the inital crack position approaches mid-span without converging to an asymptotic value. However, for an elasto-plastic aluminium response, the fracture mode ratios appear to stabilise, with $\frac{G_I}{G_{II}}$ tending towards a value of approximately 0.22.

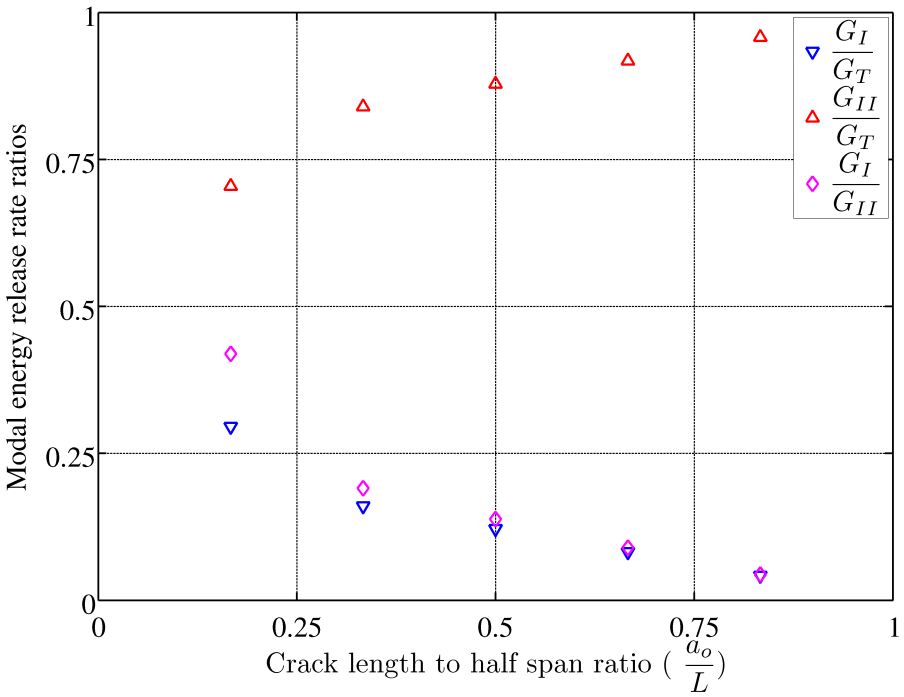

Figure 7.18: Plot of fracture mode ratios for an ENF FML specimen, with elastic aluminium

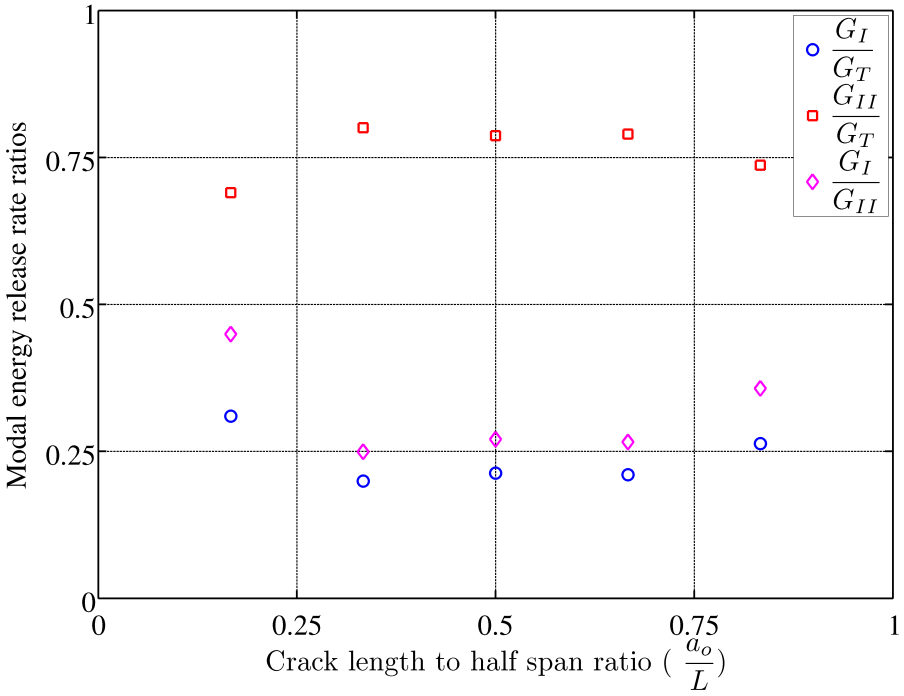

Figure 7.19: Plot of fracture mode rate ratios for an ENF FML specimen, with elasto-plastic aluminium

7.3.4.2 Fracture Mode Analysis of SLB Test of FML

The fracture mode ratios of SLB tests on FML specimens was obtained by application of the VCCT to 2D, plane strain FE simulations. The SLB tests of FML specimens did not exhibit any plastic deformation during the experiments, as the majority of the load is carried by the upper leg which is GFPP. Hence the aluminium layer of the SLB tests of FMLs was modelled as a purely elastic material. The ratios $\frac{G_I}{G_T}$, $\frac{G_{II}}{G_T}$ and $\frac{G_I}{G_{II}}$ for the analyses with an elastic aluminium model are shown in Figure 7.20. The ratio of $\frac{G_I}{G_{II}}$ decreases from approximately 0.55 and appears to converge towards a value of 0.33.

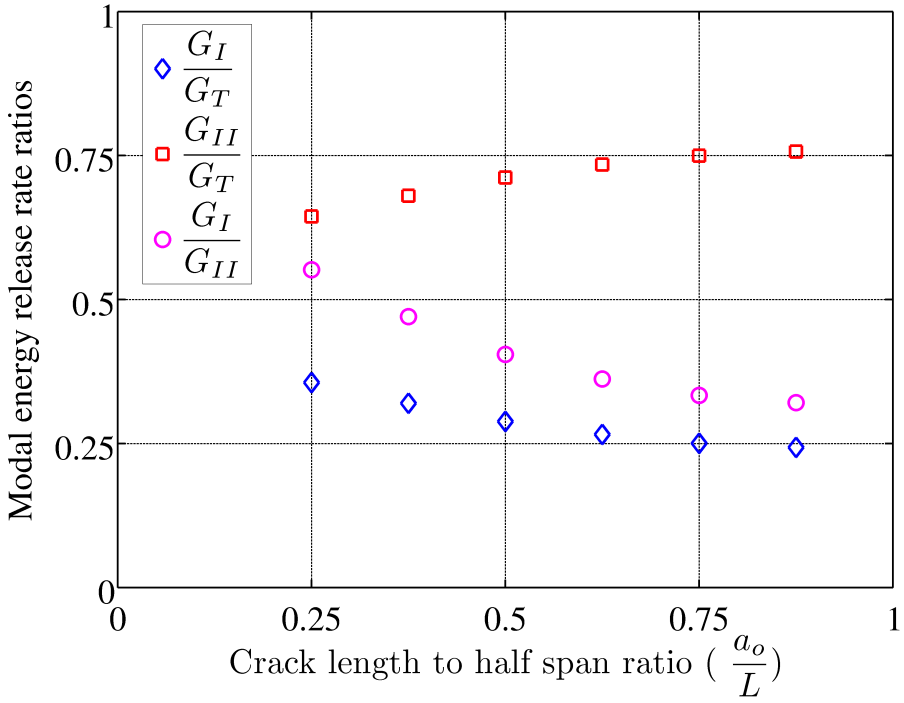

Figure 7.20: Plot of fracture mode rate ratios for a SLB FML specimen, with elastic aluminium

7.3.5 Crack Propagation Analysis of Quasi-Static Delamination Tests of FMLs

The experimental results of the ENF tests of FMLs had some uncertainty, as the aluminium layer of each specimen exhibited some plastic deformation. The LEFM principles used to calculate the energy release rates become less accurate if the area around the crack tip experiences large plastic deformation. FE simulation of these experiments would indicate the onset of plasticity, as well as the degree of plastic deformation once

the crack initiates, which would then either confirm or invalidate the results obtained using LEFM.

The experiment was modelled using a 2D, plane strain assumption. The GFPP layer was modelled using the same anisotropic linear elastic material model as the other simulations, with parameters as detailed in Table 7.5. The aluminium layer was modelled using the Johnson-Cook plasticity model - the parameter identification for this model is detailed in Appendix A.2.2. The interface between the GFPP and aluminium was seeded with a single layer of cohesive elements. The fracture mode ratios obtained in §7.3.4.1 and §7.3.4.2 were used along with the experimentally obtained initiation fracture energies (§6.2.1.4 and §6.2.4.2) to estimate the critical fracture energies for the cohesive element constitutive model, shown in Table 7.8. The critical stresses for damage initiation in the cohesive elements were based on the values used for the delamination of GFPP.

Table 7.8: FEA Cohesive zone parameters for End Notch Flexure test of FML

Parameter	σ_{1c}	G_{1c}	σ_{2c}	G_{IIc}	σ_{3c}	G_{3c}
Units	MPa	kJ/m^2	MPa	kJ/m^2	MPa	kJ/m^2
Value	5	0.4	10	0.8	10	0.8

The force-displacement response of the FE simulation is compared to experiments in Figure 7.21. The FE prediction captures the trend of the experiments well, with the peak force lying between the experimental maximum and minimum. The predicted force response underestimates the displacement to peak force, as well as the stiffness after peak force. However, the difference between the FE prediction and experiment is sufficiently small that the FE simulation may be used to interrogate the plastic behaviour of the aluminium layer without substantial error.

The plastic strains in the specimen, at peak load, are shown in Figure 7.22. While there is plastic deformation near the crack tip, the magnitude of the plastic strains in the crack tip region is less than 0.2%. Hence LEFM calculations are still applicable at this stage of the experiment, and the initiation values of G_{I-II} are admissable. Interrogation of the model at later stages of the experiment showed that plastic strains larger than 2% were present near the crack tip, and the aluminium layer at mid-span was plastic across more than 80% of its thickness. This indicates that LEFM principles are not applicable

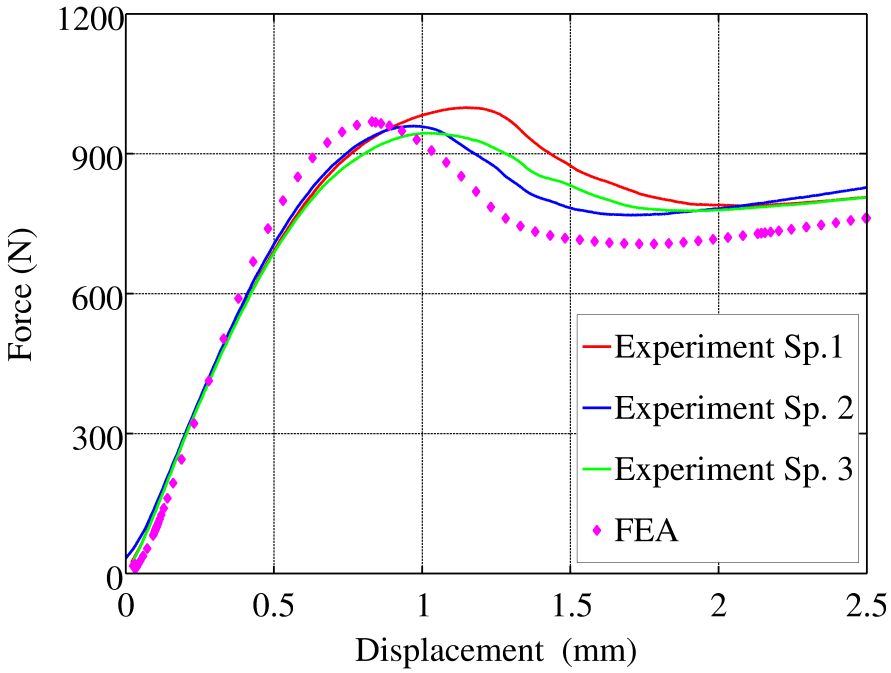

Figure 7.21: Plot comparing force-displacement responses for FEA and experiment for End Notch Flexure test on FMLs

to this portion of the test. However, this is a moot point as only the initiation values of the fracture energies were reported, and LEFM principles were still applicable at crack initiation.

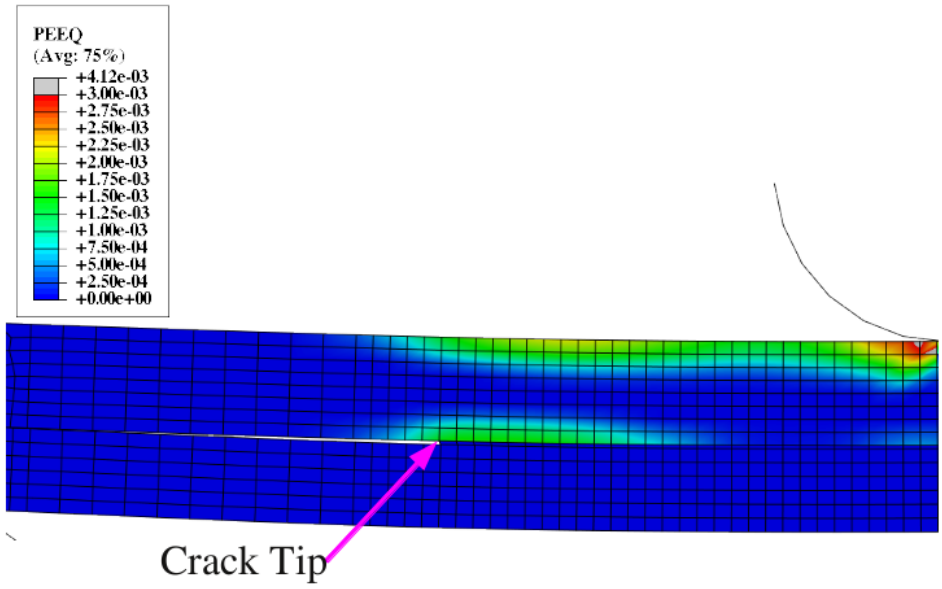

Figure 7.22: Contour plot of plastic strains at peak load from FEA End Notch Flexure test on FML

A similar FE simulation of the quasi-static SLB tests on FML specimens was created, using the cohesive zone parameters detailed in Table 7.8. The force-displacement prediction from the simulation is compared to the experimental bounds in Figure 7.23. The peak force predicted by the FE simulation lies between the experimental upper and lower bounds. However the displacement to peak force for the FE simulation was only 1.1 mm, which underpredicted the experimental value of 1.6 mm substantially. The force predicted by the FE simulation drops more rapidly after the peakthan the experimental results, but follows the trend of the experiments well. The FE simulation indicated that no part of the aluminium layer of the SLB specimen was strained plastically. This is consistent with the absence of any permanent deformation in the experimental specimens.

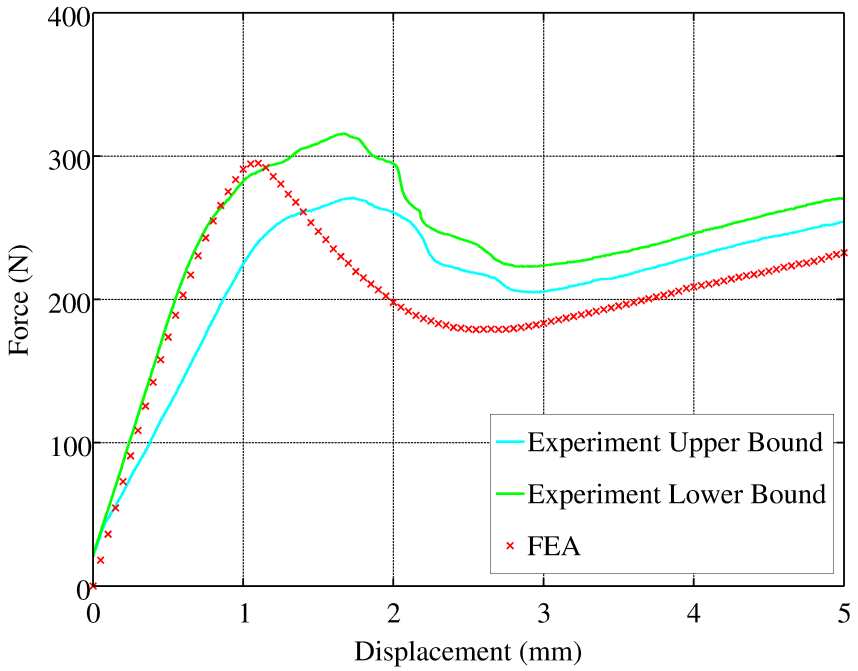

Figure 7.23: Plot comparing force-displacement responses for FEA and experiment for Single Leg Bend tests on FMLs

7.3.6 Summary of FE Simulation of Bending and Delamination Experiments

FE simulation of the HPB Impact Bend tests of monolithic GFPP specimens showed that the early oscillations observed in experimental force histories were most likely due to interaction of different flexural vibrations and stress wave propagation in the

specimen and impacter. In the experiments, these oscillations decayed in magnitude as the force increased, and peak forces were easily identified.

FE simulation of the quasi-static ENF and SLB tests on GFPP, using a cohesive zone approach to model delamination, was able to predict the macroscopic response of the specimen to an acceptable degree of accuracy. The high rate SLB tests were simulated using an explicit FE model, with no rate depedency for either the delamination or in-plane material models. The predicted force response was of similar shape to the experimental results, but overestimated the magnitude of the force. The most likely reasons for the difference in shape of the quasi-static and high rate SLB tests of GFPP are: multiple delamination zones in the high rate tests; and the interaction of flexural vibrations and stress waves in the specimen and impacter.

Chapter 8

Conclusions

The aims of this thesis were to:

- Investigate the compressive and bending response of GFPP at strain rates ranging from quasi-static to impact.
- Adapt a suitable delamination test method to impact loading, and hence investigate the rate dependence of delamination of GFPP and FMLs based on aluminium and GFPP.

The initial hypothesis was that the strength of GFPP increases with increasing strain rate and that the delamination resistance of GFPP and GFPP based FMLs decreases as the rate of loading increases. The experimental program verified that the through-thickness compression, in-plane compression and flexural strengths of GFPP all increase with strain rate. The increase in strength was proportional to the logarithm of the strain rate. Experimental investigation of delamination of GFPP under quasi-static and impact loading, coupled with Finite Element simulation, suggested that there was a slight decrease in delamination resistance of GFPP as loading increased from quasi-static to impact. The crack growth during impact delamination tests of FML specimens was unstable, which prevented sensible comparison to the quasi-static delamination tests.

8.1 Compression Testing of GFPP

Through-thickness and in-plane compression testing of GFPP was conducted at quasi-static strain rates ($10^{-4} - 10^{-2}/s$), and higher rates ($5 \times 10^{2} - 10^{3}/s$) using a SHPB and

Direct Impact HPB. No previous publications had reported strength data for GFPP at rates greater than $1.5 \times 10^2/s$. The SHPB tests made use of pulse shaping in the form of conical strikers, to reduce the variation in strain rate during a test. The through thickness and in plane compression testing of GFPP showed that peak stress increases approximately linearly with the logarithm of strain rate. A logarithmic strain rate dependence law, based on the Johnson-Cook rate law, was used to describe the increase in strength with strain rate. Through-thickness failure appears to be driven by transverse strain leading to in-ply failures, with delaminations spreading from the in-ply failures. The macroscopic form of the through thickness failure will be determined by whether the delamination from any in-ply failure interacts first with an adjacent ply failure, or the outer surface of the specimen. The in-plane failure was dominated by fibre buckling and delamination.

The through-thickness modulus of GFPP was measured quasi-statically and with the SHPB, which has not been previously reported in the literature. The SHPB test was modified such that the forces acting on the specimen achieved acceptable equilibrium while the specimen was still deforming elastically. The tests revealed that the through thickness modulus increased by approximately 25% while strain rate increased by 5 orders of magnitude, from $10^{-3}/s$ to $10^2/s$.

8.2 Bend Testing

A novel configuration of the HPB was developed to perform impact bend testing. The HPB Impact Bend rig implemented in this thesis used an output HPB as the central loading point of a Three Point bend test, resulting in considerable improvement of the force measurement over systems reported elsewhere. The specimen was supported at the two outer points by an impacter, which was accelerated towards the HPB by a gas gun. A polycarbonate HPB was used for the output bar, which permitted force measurements of up to 2.4 ms using a single strain gauge station. This set up permitted testing of relatively flexible laminates (specimen deflections of the order of 5 to 10 mm), compared to other rigs reported in the literature, which were limited to stiffer specimens, where deflections to failure were typically less than 1 mm.

The HPB Impact Bend apparatus was used to test GFPP and GFPP based FML specimens, at impact velocities ranging from 5 to 12 m/s. The flexural strength of the GFPP specimens increased with strain rate. The logarithmic rate dependence model was used to describe the increase in flexural strength. The FML specimens did not show a

significant rate dependence, as the response of the FMLs was driven by the aluminium outer skins which are rate insensitive for the range in which testing ocurred.

The force histories of all HPB Impact Bend tests showed oscillations during the early part of the test. These oscillations decreased in magnitude as the force increased, and the peak forces were easily identified. FE simulation of the early response indicated that these oscillations were probably due to the interaction of flexural vibrations and stress wave propagtion in the specimen and the impacter.

8.3 Delamination Testing

8.3.1 Selection of Test Method

Several methods for delamination testing were evaluated at quasi-static loading rates as candidates for high strain rate delamination testing:

- Short Beam Shear testing produced repeatable results, with interlaminar shear strengths comparable to those in the literature. However, the presence of failure modes other than delamination made Short Beam Shear tests unsuitable for high rate testing.

- Lap Shear testing resulted in clear interlaminar shear, with no other failure modes discernable. However, the measured interlaminar shear strength was substantially less than results reported in the literature, with unacceptably large scatter.

- End Notch Flexure (ENF) testing produced closely grouped results, with the Mode II strain energy release rate G_{II} being comparable to previously reported results. However, End Notch Flexure tests require the crack tip position to the monitored and recorded, which was problematic even at quasi-static rates. At high rates, these problems would be exacerbated, so high rate testing using End Notch Flexure was not pursued.

- Single Leg Bend tests produced repeatable results, in the expected range for mixed Mode I-Mode II delamination. The opening of the crack tip, due to the Mode I loading, aided visual crack tip identification greatly. Hence the Single Leg Bend delamination test was selected for adaptation to high rate testing.

8.3.2 High Rate Delamination Testing

The impact delamination tests on GFPP specimens displayed stable crack growth, but a force response that was notably different from the quasi-static tests. Crack extension measurements obtained from high speed video of the tests indicated that the departure from a linear force response occurred before visible crack growth. The initiation energy release rate for the high rate SLB tests on GFPP was approximately equal to the quasi-static tests, but increased at a slower rate as the crack grew. The quasi-static SLB tests on GFPP appeared to be converging to a stable propagation value, which was not the case for the high rate tests. The force response for impact delamination tests of FML specimens was also different from the quasi-static tests, with the additional complication of unstable crack growth.

8.3.3 Insights From FE Simulations

Finite Element simulation of the End Notch Flexure and Single Leg Bend tests was performed, using the cohesive zone approach to model delamination. Simulation of the End Notch Flexure and quasi-static Single Leg Bend tests showed that the predicted force-displacement response and macroscopic specimen response correlated well with the experimental results. The simulations of high rate Single Leg Bend tests on GFPP predicted a higher force than the experimental results, but the shape of the experimental and simulated force response correlated well. The simulations indicated that delamination initiated at sites other than the initial crack tip, for the high rate tests. The multiple delamination sites, as well as the interaction of flexural vibrations and stress waves, were the most probable causes of the difference in shape of the quasi-static and high rate force responses.

The Virtual Crack Closure Technique (VCCT) was applied to the delamination tests on FML specimens, to estimate the fracture mode ratios. The analysis of the ENF tests considered two cases: purely elastic aluminium and elasto-plastic aluminium. For the purely elastic case, the ratio of $\frac{G_I}{G_{II}}$ decreased steadily without tending towards a distinct value as the crack length was increased, but was clearly dominated by Mode II. For the elasto-plastic case, the ratio $\frac{G_I}{G_{II}}$ tended towards approximately 0.22. The analysis of the Single Leg Bend FML specimen, which only required a purely elastic aluminium response, tended towards a $\frac{G_I}{G_{II}}$ ratio of 0.33.

Chapter 9

Recommendations

The following recommendations are made for future work in this field:

- The link between through-thickness compression and in-ply fibre failure due to transverse tensile strain warrants more detailed investigation. The through-thickness Poisson ratios (ν_{13}, ν_{23}) should be measured experimentally. The relatively high failure strain in the through-thickness direction ($\varepsilon_{33}^{f} \approx 12$ to 13%) and non-uniform strain due to the fabric weave pattern both motivate against measuring the failure strains using strain gauges. A non-contact, full field strain measurement such digital image correlation of speckle patterns would be provide much of the data required.

- The HPB Impact Bend apparatus could benefit from improved resolution of the impacter displacement measurement for testing at lower deflections to failure. The existing Reflective Object Sensor (ROS) system for measuring impacter displacement was designed based on anticipated impacter velocities of approximately 15 m/s. Commercially available ROS systems have better resolution, but are limited to impacter velocities below 8 m/s. This would be appropriate for impact bend testing of more brittle specimens, with smaller deflections to failure that require improved resolution, and would probably be tested at lower impact velocities.

- The duration limit of the HPB Impact Bend apparatus may be increased by either increasing the length of the HPB, or adding additional strain gauges and applying wave reconstruction techniques. Longer duration tests would permit testing at lower impact velocities, which would help bridge the gap between impact tests and quasi-static tests conducted on traditional load frames.

- The possibility of performing delamination tests at velocities between the quasi-static tests and the impact tests presented herein should be investigated. This would aid identification of crack speed and the point at which crack growth becomes unstable.

- The high rate SLB tests on FML specimens, using the HPB Impact bend apparatus, showed less stable crack growth than the quasi-static tests. The effect of parameters such as initial crack position and support span should be investigated further.

- The next iteration of the HPB Impact Bend apparatus should include the capacity to perform interrupted impact tests, which would be of benefit to further delamination studies.

- In order to improve the simulation of delamination using cohesive elements, the delamination failure envelope needs to be investigated further, which necessitates delamination tests at different fracture mode ratios. This could be accomplished by modifying the thickness ratio of the Single Leg Bend specimen, or utilising additional mixed mode delamination tests such as the Single Cantilever Beam. The Single Cantilever Beam specimen would be readily accomodated on the HPB Impact Bend apparatus with minor modifications to the impacter.

- The simulation of the HPB Impact Bend tests and the impact Single Leg Bend tests was hampered by the absence of rate dependency in the anisotropic material model and cohesive zone model available in ABAQUS v6.10. Implementing rate dependency for either involves development and validation of user subroutines, which is not a minor undertaking. Other explicit finite element codes should be investigated as these may include appropriate rate dependence models.

- The FE simulation of the high rate SLB tests on GFPP specimens predicted that delamination grow not only from the initial crack tip, but from sites adjacent to the central impacter. The growth of delamination under the central impacter was undiscernable in the high speed video, due to resolution limitations. The HPB Impact Bend apparatus can be adapted to perform interrupted tests, where the specimen deflection and hence crack growth is limited. Interrupted tests would permit investigating the multiple delamination sites with techniques such as ultrasound that cannot be implemented during the impact test.

References

[1] Vlot A.D. & Gunnik J.W., *Fibre metal laminates - an introduction*, Kluwer Academic Publishers, Dordrecht, 2001.

[2] Vlot A.D., *GLARE - History of the development of a new aircraft material*, Kluwer Academic Publishers, Dordrecht, 2001.

[3] Langdon G.S., Lemanski S.L., Nurick G.N., Simmons M.C., Cantwell W.J. & Shleyer G.K., "Behaviour of fibre metal laminates subjected to localised blast loading: Part I - experimental observations", *Int. J. Impact. Eng.*, vol. 34, (2007), pp. 1202–1222.

[4] Lemanski S.L., Nurick G.N., Langdon G.S., Simmons M.C., Cantwell W.J. & Shleyer G.K., "Behaviour of fibre metal laminates subjected to localised blast loading: Part II - quantitative analysis", *Int. J. Impact Engng*, vol. 34, (2007), pp. 1222–1245.

[5] Langdon G.S., Cantwell W.J. & Nurick G.N., "The blast performance of novel fibre-metal laminates", in: "Structures Under Shock and Impact VIII", , editors Jones N. & Brebbia C.A., 2004, pp. 455–464.

[6] Kolsky H., "An investigation of the mechanical properties of materials at very high rates of loading", *Proc. Phy. Soc. Lond.*, vol. B62, (1949), pp. 676–700.

[7] Nicholas T., "Tensile testing of materials at high rates of strain", *Exp. Mech.*, vol. 21, (1981), pp. 177–185.

[8] Lindholm U.S. & Yeakley L.M., "High strain rate testing: tension and compression", *Exp. Mech*, vol. 8, (1968), pp. 1–9.

[9] Song B., Chen W. & Weerasooriya T., "Quasi-static and dynamic compressive behaviors of a S-2 glass/SC15 composite", *J. Compos. Mat.*, vol. 37, (2003), pp. 1723–1743.

[10] Gama B.A., Gillespie Jr J.W., Mahfuz H., Raines R.P., Haque A., Jeelani S., Bogetti T. & Fink B.K., "High strain-rate behavior of plain-weave S-2 glass/vinyl ester composites", *J. Compos. Mat.*, vol. 35, (2001), pp. 1201–1228.

[11] Lifshitz J.M. & Leber H., "Response of fibre-reinforced polymers to high strain rate loading in interlaminar tension and combined tension/shear", *Compos. Sci. Technol.*, vol. 58, (1998), pp. 987–996.

[12] Ruiz C. & Mines R.A.W., "The Hopkinson pressure bar: an alternative to the instrumented pendulum for Charpy tests", *Int. J. Fract.*, vol. 29, (1985), pp. 101–109.

[13] Rubio-Gonzalez C., Gallardo-Gonzalez J.A., Mesmacque G. & Sanchez-Santana U., "Dynamic fracture toughness of pre-fatigued materials", *Int. J. Fatigue*, vol. 30, (2008), pp. 1056–1064.

[14] McLeod W., "The range of the ancient bow", *Phoenix*, vol. 19, (1965), pp. 1–14.

[15] Barbero E.J., *Introduction to composite materials design*, CRC Press, 2011.

[16] Gay D. & Hoa S.V., *Composite Materials: Design and applications*, CRC Press, 2007.

[17] Boeing, "About the 787 family", Boeing 787 Online Information Brochure, 2011, URL `http://www.boeing.com/commercial/787family/background.html`, most recently accessed: May 2011.

[18] Kerry Desberg, "Owens Corning Twintex reinforcement application in vinyl windows receives JEC Innovation Award", Owens Corning Press Release, 2009, URL `http://www.ocvreinforcements.com/news/`, most recently accessed: May 2011.

[19] Owens Corning Reinforcements, "Twintex T PP data sheet", 2008.

[20] Adams D.F., "Test methods for mechanical properties", in: "Comprehensive Composite Materials", , editors Kelly A. & Zweben C., pp. 113–148, Pergamon, 2000.

[21] ASTM Standard, "D 695 standard test method for compressive properties of rigid plastics", Tech. rep., American Society For Testing And Materials, 2007.

[22] ASTM Standard, "D 3410 standard test method for compressive properties of polymer matrix composite materials with unsupported gage section by shear loading", Tech. rep., American Society For Testing And Materials, 2007.

[23] ASTM Standard, "D 6641 standard test method for determining the compressive properties of polymer matrix composite laminates using a combined loading compression (clc) fixture", Tech. rep., American Society For Testing And Materials, 2007.

[24] ASTM Standard, "D 790 standard test method for flexural properties of unreinforced and reinforced plastics and electrical insulation materials", Tech. rep., American Society For Testing And Materials, 2007.

[25] ASTM Standard, "D 7264 standard test method for flexural properties of polymer matrix composite materials", Tech. rep., American Society For Testing And Materials, 2007.

[26] ASTM Standard, "D 6272 Standard test method for flexural properties of unreinforced and reinforced plastics and electrical insulation materials by four-point bending", Tech. rep., ASTM International, 2007.

[27] Instron, "Drop tower impact systems ceast 9300 series data sheet", 2011.

[28] Zwick-Roell, "Drop weight tester hit230f data sheet", 2011.

[29] ASTM Standard, "D 7291 standard test method for through-thickness "flatwise" tensile strength and elastic modulus of a fiber reinforced polymer matrix composite material", Tech. rep., American Society For Testing And Materials, 2007.

[30] ASTM Standard, "D 3846 standard test method for in plane shear strength of reinforced plastics", Tech. rep., American Society For Testing And Materials, 2007.

[31] ASTM Standard, "D 2344 standard test method for short-beam strength of polymer matrix composites and their laminates", Tech. rep., American Society For Testing And Materials, 2007.

[32] ASTM Standard, "D 5379 standard test method for shear properties of composite materials by the v-notched beam method", Tech. rep., American Society For Testing And Materials, 2007.

[33] ASTM Standard, "D 5528 Standard test method for Mode I interlaminar fracture toughness of unidirectional fibre reinforced polymer matrix composites", Tech. rep., ASTM International, 2007.

[34] ASTM Standard, "D 6671 Standard test method for mixed Mode I-Mode II interlaminar fracture toughness of unidirectional fibre reinforced polymer matrix composites", Tech. rep., ASTM International, 2007.

[35] Hara E., Yokozeki T., Hatta H., Iwahori Y. & Ishikawa T., "Effects of geometry and specimen size on out-of-plane tensile strength of aligned cfrp determined by direct tensile method", *Compos. Part A. Appl. S.*, vol. 41, (2010), pp. 1425–1433.

[36] Hara E., Yokozeki T., Hatta H., Iwahori Y. & Ishikawa T., "Cfrp laminate out-of-plane tensile modulus determined by direct loading", *Compos. Part A. Appl. S.*, vol. 41, (2010), pp. 1538–1544.

[37] Kim J.S. & Yoong H.J., "Structural behaviors of a gfrp composite bogie frame for urban subway trains under critical load conditions", *Engineering Procedia*, vol. 10, (2011), pp. 2375–2380.

[38] Shokrieh M.M. & Lessard L.B., "An assessment of the double notch shear test for interlaminar shear characterization of a unidirectional graphite/epoxy under static and fatigue loading", *Appl. Comp. Mater.*, vol. 5, (1998), pp. 289–304.

[39] May M. & Hallett S.R., "An assessment of through-thickness shear tests for initiation of fatigue failure", *Compos. Part A Appl. S.*, vol. 41, (2010), pp. 1570–1578.

[40] Dong L. & Harding J., "A single-lap shear specimen for determining the effect of strain rate on the interlaminar shear strength of carbon fibre-reinforced laminates", *Comp.*, vol. 25, (1994), pp. 1291–138.

[41] Hiley M.J., Dong L. & Harding J., "Effect of strain rate on the fracture process in interlaminar shear specimens of carbon fibre reinforced laminates", *Comp. Part A*, vol. 28A, (1997), pp. 171–180.

[42] Hallett S., Ruiz C. & Harding J., "The effect of strain rate on the interlaminar shear strength of a carbon/epoxy cross-ply laminate: comparison between experiment and numerical prediction", *Compos. Sci. Technol.*, vol. 59, (1999), pp. 749–758.

[43] Pahr D.H., Rammerstorfer F.G., Rosenkranz P., Humer K. & Weber H.W., "A study of short-beam-shear and double-lap-shear specimens of glass fabric/epoxy composites", *Comp. Part B*, vol. 33, (2002), pp. 125–132.

[44] Harding J. & Li Y.L., "Determination of interlaminar shear strength for glass/epoxy and carbon/epoxy laminates at impact rates of strain", *Compos. Sci. Technol.*, vol. 45, (1992), pp. 161–171.

[45] Xie M. & Adams D.F., "Study of three- and four-point shear testing of unidirectional composite materials", *Comp.*, vol. 26, (1995), pp. 653–659.

[46] Feraboli P. & Kedward K.T., "Four-point bend interlaminar shear testing of uni- and multi-directional carbon/epoxy composite systems", *Comp. Part A*, vol. 34, (2003), pp. 1265–1271.

[47] Abali F., Pora A. & Shivakumar K., "Modified short beam shear test for measurement of interlaminar shear strength of composites", *J. Comp. Mat.*, vol. 37, (2003), pp. 453–464.

[48] Hufenbach W., Langkamp A., Hornig A. & Ebert C., "Experimental determination of the strain rate dependent out-of-plane shear properties of textile-reinforced composites", in: "17th Internationational Conference on Composites Materials", 2009.

[49] Hertzberg R.W., *Deformation and Fracture Mechanics Of Engineering Materials, IVth Ed*, John Wiley and Sons, New Jersey, 1996.

[50] Wilson D.W. & Carlsson L.A., "Mechanical property measurements", in: "Composites Engineering Handbook", , editor Mallick P.K., pp. 1129–1142, Marcel Dekker, 1997.

[51] Zehnder A.T., "Lecture Notes on Fracture Mechanics", Cornell University, 2007, URL `http://ecommons.library.cornell.edu/handle/1813/3075`, course notes made available for download - downloaded Dec. 2010.

[52] Wang Y., Dong Q., Zhang D. & Xu Y., "An acoustic emission study on the fracture behavior of continuous glass fiber/polypropylene composites based on commingled yarn", *Polymer Comp.*, vol. 29, (2000), pp. 728–735.

[53] Czignay T., Marosfalvi J. & Karger-Kocsis J., "An acoustic emission study of the temperature-dependent fracture behavior of polypropylene composites reinforced by continuous and discontinuous fiber mats", *Compos. Sci. Technol.*, vol. 60, (2000), pp. 1203–1212.

[54] Vinciquerra A.J. & Davidson B.D., "Effect of crack length measurement technique and data reduction procedures on the perceived toughness from four-point bend end-notched flexure tests", *J. Reinf. Plast. Comp.*, vol. 23, (2004), pp. 1051–1062.

[55] O'Brien T.K., "Interlaminar fracture toughness: the long and winding road to standardization", *Comp. Part B*, vol. 29B, (1998), pp. 57–62.

[56] Brunner A.J., Blackman B.R.K. & Davies P., "A status report on delamination resistance testing of polymer matrix composites", *Eng. Frac. Mech.*, vol. 75, (2008), pp. 2779–2794.

[57] Kusaka T. & Kurokawa T., "Estimation of Mode I interlaminar fracture toughness of CFRP laminates by using wedge insert fracture test", *J. Soc. Mat. Sci. (Japan)*, vol. 45, (1996), pp. 484–489.

[58] Adams R.D., Cowap J.W., Farquharson G., Margary G.M. & Vaughn D., "The relative merits of the Boeing wedge test and the double cantilever beam test for assessing the durability of adhesively bonded joints, with particular reference to the use of fracture mechanics", *Int. J. Adhes. Adhes.*, vol. 29, (2009), pp. 609–620.

[59] ASTM Work Item, "Wk 22949 New test method for determination of the Mode II interlaminar fracture toughness of unidirectional fibre reinforced polymer matrix composites using the ENF test", Tech. rep., ASTM International, 2009.

[60] Wang W.X., Nakata M., Takao Y. & Matsubara T., "Experimental investigation on test methods for Mode II interlaminar fracture testing of carbon fibre reinforced composites", *Comp. Part A*, vol. 40, (2009), pp. 1447–1455.

[61] Japanese Standards Association, "Testing methods for interlaminar fracture toughness of CFRP K7086", Tech. rep., JSA, 1993.

[62] Tanaka K., Kageyama K. & Hojo M., "Prestandardisation study on Mode II interlaminar fracture toughness test for cfrp in japan", *Comp.*, vol. 26, (1995), pp. 257–267.

[63] Shuecker C. & Davidson B.D., "Evaluation of the accuracy of the four point bend end-notched flexure test for mode ii delamination toughness determination", *Compos. Sci. Technol.*, vol. 60, (2000), pp. 2137–2146.

[64] Sun X. & Davidson B.D., "A direct energy balance approach for determining energy release rates in three and four point bend end notched flexure tests", *Int. J. Frac.*, vol. 135, (2005), pp. 51–72.

[65] Sun X. & Davidson B.D., "Numerical evaluation of the effects of frictions and geometric nonlinearities on the energy release rate in three and four point bend end notched flexure tests", *Eng. Frac. Mech.*, vol. 73, (2006), pp. 1343–1361.

[66] Davidson B.D., Sun X. & Vinciquerra A.J., "Influences of friction, geometric nonlinearities, and fixture compliance on experimentally observed toughnesses from

three and four point bend end-notched flexure tests", *J. Comp. Mat.*, vol. 41, (2007), pp. 1177–1196.

[67] Wang H. & Vu-Khanh T., "Use of end loaded split (ELS) test to study stable fracture behaviour of composites under Mode II loading", *Comp. Struct.*, vol. 36, (1996), pp. 71–79.

[68] Blackman B.R.K., Brunner A.J. & Williams J.G., "Mode II fracture testing of composites: a new look at an old problem", *Eng. Frac. Mech.*, vol. 73, (2006), pp. 2443–2455.

[69] Szekrenyes A. & Uj J., "Approximate interlaminar fracture envelopes for unidirectional E-glass / polyester composite", *Period. Polytech. Mech.*, vol. 49, (2005), pp. 15–24.

[70] O'Brien T.K., "Composite interlaminar shear fracture toughness: Shear measurement or sheer myth?", Special technical publication, ASTM International, 1998.

[71] Crews J.H. & Reeder J.R., "A mixed mode bending apparatus for delamination testing", NASA technical memorandum 100662, NASA Langley Research Center, 1988.

[72] Reeder J.R. & Crews J.H., "Nonlinear analysis and redesign of the mixed mode bending delamination test", NASA technical memorandum 102777, NASA Langley Research Center, 1991.

[73] Reeder J.R., "Refinements to the mixed mode bending test for delamination toughness", NASA technical report NASA-2000-asc15atc-jrr, NASA Langley Research Center, 2000.

[74] Reyes Villanueva G. & Cantwell W.J., "The mechanical properties of fibre-metal laminates based on glass fibre reinforced polypropylene", *Compos. Sci. Technol.*, vol. 60, (2000), pp. 1085–1094.

[75] Guillen J.F. & Cantwell W.J., "The influence of cooling rate on the fracture properties of a thermoplastic-based fibre metal laminate", *J. Reinforced Plastics and Composites*, vol. 21, (2002), pp. 749–772.

[76] Carillo J.G. & Cantwell W.J., "Mechanical properties of a novel fibre metal laminate based on a polypropylene composite", *Mech. Mat.*, vol. 41, (2009), pp. 828–838.

[77] Cortes P. & Cantwell W.J., "Structure property relations in titanium based thermoplastic FMLs", *Polymer Comp.*, vol. 27, (2006), pp. 264–270.

[78] Kiratisaevee H. & Cantwell W.J., "The fracture behaviour of aluminium foram sandwich structures based on fibre reinforced thermoplastics", *J. Sandwich Struct. Mat.*, vol. 5, (2003), pp. 53–75.

[79] Yoon S.H. & Hong C.S., "Modified end notch flexure system for mixed mode interlaminar fracture in laminated composites", *Int. J. Frac.*, vol. 43, (1990), pp. R3–R9.

[80] Cantwell W.J., Scudamore R., Ratcliffe J. & Davies P., "Interfacial fracture in sandwich laminates", *Compos. Sci. Technol.*, vol. 59, (1999), pp. 2079–2085.

[81] Brown. K.A., Brooks R. & Warrior N.A., "The static and high strain rate behaviour of a commingled E-glass polypropylene woven fabric composite", *Compos. Sci. Technol.*, vol. 70, (2010), pp. 272–283.

[82] Bureau M.N. & Denault J., "Fatigue resistance of continuous glass fibre / polypropylene composites: Temperature dependence", *Polymer Comp.*, vol. 25, (2004), pp. 622–629.

[83] Lariviere D., Krawczak P., Tiberi C. & Lucas P., "Interfacial properties in commingled yarn thermoplastic composites. part i: Characterization of the fiber/matrix adhesion", *Polymer Comp.*, vol. 25, (2004), pp. 577–588.

[84] Lariviere D., Krawczak P., Tiberi C. & Lucas P., "Interfacial properties in commingled yarn thermoplastic composites. part i: Part ii: Influence on crack initiation and propagation", *Polymer Comp.*, vol. 25, (2004), pp. 589–600.

[85] Santulli C., Brooks R., Long A.C., Rudd C.D., Wilson M.J. & Warrior N.A., "Impact properties of thermoplastic laminates for automotive applications", in: "Automotive Plastics and Composites Conference", Dunton, 2000.

[86] Santulli C., Drezet D., Brooks R. & Rudd C.D., "Relation between void content and mechanical and impact properties in commingled e-glass / polypropylene thermoplastic composites", in: "EUROMAT Conference", Rimni, 2001.

[87] Reyes G. & Sharma U., "Analysis of woven glass fiber reinforced thermoplastic composites under varying strain rates", in: "Automotive Composites Conference and Exhibition", Society of Plastics Engineers, Troy, MI.

[88] Ding W., *Delamination Analysis of Composite Laminates*, Ph.D. thesis, University of Toronto, 1999.

[89] Perrin F., Bureau M.N., Denault J. & Dickson J.I., "Mode i interlaminar crack propagation in continuous glass fiber polypropylene composites: temperatures and molding condition dependence", *Compos. Sci. Technol.*, vol. 63, (2003), pp. 597–607.

[90] Pattofatto S., Tsitsiris H. & Zhao H., "The instrumented dynamic perforation test applied to a composite shell", in: "9th International DYMAT Conference", 2009.

[91] G. Reyes Villanueva, *Processing and characterisation of the mechanical properties of novel fibre metal laminates*, Ph.D. thesis, The University of Liverpool, United Kingdom, 2001.

[92] Brown K.A., *Finite element modelling of the static and dynamic impact behaviour of thermoplastic composite sandwich structures*, Ph.D. thesis, The University of Nottingham, 2007.

[93] Vermeeren C.A.J.R., "An historic overview of the development of fibre metal laminates", *Appl. Comp. Mat.*, vol. 10, (2003), pp. 189–205.

[94] Fokker Aerostructures, "Glare information page", Official website, URL `http://www.fokker.com/Innovations-Glare?referrer=1189`, last accessed June 2011.

[95] Vogelesand L.B. & Vlot A., "Development of fibre metal laminates for advanced aerospace structures", *J. Mat. Proc. Tech*, vol. 103, (2000), pp. 1–5.

[96] Alderliesten R.C. & Homan J.J., "Fatigue and damage tolerance issues of GLARE in aircraft structures", *Int. J. Fatigue*, vol. 28, (2006), pp. 1116–1123.

[97] Alderliesten R.C., "On the available relevant approaches for fatigue crack propagation prediction in GLARE", *Int. J. Fatigue*, vol. 29, (2007), pp. 289–304.

[98] Alderliesten R.C., Schijve J. & van der Zwaag S., "Application of the energy release rate approach for delamination growth in GLARE", *Eng. Frac. Mech.*, vol. 73, (2006), pp. 697–709.

[99] Shim D.J., Alderliesten R.C., Spearing S.M. & Burianek D.A., "Fatigue crack growth prediction in GLARE hybrid laminates", *Compos. Sci. Technol*, vol. 63, (2003), pp. 1759–1767.

[100] Shim D.J., Alderliesten R.C., Spearing S.M. & Burianek D.A., "Delamination growth in FMLs under variable amplitude loading", *Compos. Sci. Technol*, vol. 69, (2009), pp. 2604–2615.

[101] Hashagen F. & de Borst R., "Numerical assessment of delamination in fibre metal laminates", *Comp. Methods. Appl. Mech. Engrg.*, vol. 185, (2000), pp. 141–159.

[102] de Vries T.J., Vlot. A. & Hashagen F., "Delamination behaviour of spliced fiber metal laminates part 1 experimental results", *Compos. Struct.*, vol. 46, (1999), pp. 131–145.

[103] Hinz S., Omoori T., Hojo M. & Schulte K., "Damage characterisation of fibre metal laminates under interlaminar shear load", *Comp. Part A.*, vol. 40, (2009), pp. 925–931.

[104] Langdon G.S., Cantwell W.J. & Nurick G.N., "Localised blast loading of fibre-metal laminates with a polyamide matrix", *Comp. Part B*, vol. 38, (2007), pp. 902–913.

[105] Reyes Villanueva G. & Cantwell W.J., "The high velocity impact response of composite and fml reinforced sandwich structures", *Compos. Sci. Technol.*, vol. 64, (2004), pp. 35–54.

[106] Hoo Fatt M.S., Lin C., Revilock D.M. & Hopkins D.A., "Ballistic impact of GLARE fibre metal laminates", *Comp. Struct.*, vol. 61, (2003), pp. 73–88.

[107] Hou J.P., Petrinic N., Ruiz C. & Hallett S.R., "Prediction of impact damage in composite plates", *Compos. Sci. Technol.*, vol. 60, (2000), pp. 273–281.

[108] Brewer J.C. & Lagace P.A., "Quadtratic stress criterion for initiation of delamination", *J. Compos. Mater.*, vol. 22, (1988), pp. 1141–1155.

[109] Krueger R., "Virtual crack closure technique: history, approach and applications", *Appl. Mech. Rev.*, vol. 57, (2004), pp. 109–143.

[110] Camanho P.P., Davila C.G. & Ambur D.R., "Numerical simulation of delamination growth in composite materials", Technical report NASA/Tp-2001-211041, NASA, 2001.

[111] Goyal V.K., Johnson E.R. & Davila C.G., "Irreversible constitutive law for modeling the delamination process using interfacial surface discontinuities", *Comp. Struct.*, vol. 65, (2004), pp. 289–305.

[112] Zou Z., Reid S.R., Li. S. & Soden P.D., "Application of a delamination model to laminated composite structures", *Comp. Struct.*, vol. 56, (2002), pp. 375–389.

[113] Jiang W.G., Hallett S.R., Green B.G. & Wisnom M.R., "A concise interface constitutive law for analysis of delamination and splitting in composite materials and its application to scaled notched tensile specimens", *Int. J. Numer. Meth. Engng*, vol. 69, (2007), pp. 1982–1995.

[114] Turon Travesa A., *Simulation of delamination in composites under quasi-static and fatigue loading using cohesive zone models*, Ph.D. thesis, Universitat de Girona, 2006.

[115] Espinosa H.D., Dwivedi S. & Lu H.C., "Modeling impact induced delamination of woven fibre reinforced composites with contact/cohesive laws", *Comput. Methods Appl. Mech. Engrg.*, vol. 183, (2000), pp. 259–290.

[116] Benzeggagh M.L. & Kenane M., "Measurement of mixed mode fracture toughness of unidirection glass epoxy composites with mixed mode bending apparatus", *Compos. Sci. Technol.*, vol. 56, (1996), pp. 439–449.

[117] Blackman B.R.K., Hadavinia H., Kinloch A.J. & Williams J.G., "The use of a cohesive zone model to study the fracture of fibre composites and adhesively bonded joints", *Int. J. Fracture*, vol. 119, (2003), pp. 25–46.

[118] Turon A., Camanho P.P., Costa J. & Renart J., "Accurate simulation of delamination growth under mixed-mode loading using cohesive elements: De[U+FB01]nition of interlaminar strengths and elastic stiffness", *Comp. Struct.*, vol. 92, (2010), pp. 1857–1864.

[119] Blazani C. Wagner W., "An interface element for the simulation of delamination in unidirection fiber reinforced composite laminates", *Eng. Fract. Mech.*, vol. 75, (2008), pp. 2597–2615.

[120] Hallett S.R., Jiang W.G., Khan B. & Wisnom M.R., "Modelling the interaction between matric cracks and delamination damage in scaled quasi-isotropic specimens", *Compos. Sci. Technol.*, vol. 68, (2008), pp. 80–89.

[121] Ye Q. & Chen P., "Prediction of the cohesive strength for numerically simulating composite delamination via CZM based FEM", *Compos. Part B - Eng.*, vol. 42, (2011), pp. 1076–1083.

[122] Chen J., Ravey E., Hallett S.R., Wisnom M.R. & Grassi M., "Prediction of delamination in braided composite T-piece specimens", *Compos. Sci. Technol.*, vol. 69, (2009), pp. 2363–2367.

[123] Overgaard L.C.T., Lund E. & Camanho P.P., "A methodology for the structural analysis of composite wind turbine blades under geometric and material induced instabilities", *Comput. Struct.*, vol. 88, (2010), pp. 1092–1109.

[124] Johnson H.E., Louca L.A., Mouring S. & Fallah A.S., "Modelling impact damage in marine composite panels", *Int. J. Impact Engng*, vol. 36, (2009), pp. 25–39.

[125] Cid Alfaro M.V., Suiker A.S.J., de Borst R. & Remmers J.C., "Analysis of fracture and delamination in laminates using 3D numerical modelling", *Eng. Frac. Mech.*, vol. 76, (2009), pp. 761–780.

[126] Karagiozova D. Langdon G.S., Nurick G.N. & Chung Kim Yuen S., "Simulation of the response of fibre metal laminates to localised blast loading", *Int. J. Impact Engng*, vol. 37, (2010), pp. 766–782.

[127] Hopkinson B., "A method of measuring the pressure produced in the detonation of explosives and by the impact of bullets", *Proc. R. Soc. Lond.*, vol. A213, (1914), pp. 437–456.

[128] Davies R.M., "A critical study of the Hopkinson pressure bar", *Proc. R. Soc. Lond.*, vol. A240, (1948), pp. 375–457.

[129] Verleysen P. & Degrieck J., "Experimental and numerical study of the response of steel sheet hopkinson experiments", *J. Phys. IV France*, vol. 134, (2006), pp. 541–546.

[130] Klepaczko J.R., Nguyen H.V. & Nowacki W.K., "Quasi-static and dynamic shearing of sheet metals", *Eur. J. Mech. A/Solids*, vol. 18, (1989), pp. 271–289.

[131] Rittel D., Lee S. & Ravichandran G., "A shear compression specimen for large strain testing", *Exp. Mech.*, vol. 42, (2002), pp. 58—64.

[132] Vural M. & Ravichandran G., "Transverse failure in thick S-2 glass/ epoxy fiber-reinforced composites", *J. Compos. Mat.*, vol. 38, (2004), pp. 609–623.

[133] Billington E.W. & Brissenden C., "Dynamic stress-strain curves for various plastics and fibre reinforced plastics", *J. Appl. Phys. D: Appl. Phys.*, vol. 4, (1971), pp. 272–286.

[134] Griffiths L.J. & Martin D.J., "A study of the dynamic behaviour of a carbon fibre composite using the split Hopkinson pressure bar", *J. Appl. Phys. D: Appl. Phys.*, vol. 7, (1974), pp. 2329–2341.

[135] Harding J. & Welsh L.M., "A tensile testing technique for fibre reinforced composites at impact rates of strain", *J. Compos. Mat.*, vol. 18, (1983), pp. 1810–1826.

[136] Welsh L.M. & Harding J., "Effect of strain rate on the tensile failure of woven reinforced polyester resin composites", *J. Phys. Colloques*, vol. 46, (1985), pp. C5–405–C5–414.

[137] Saka K. & Harding J., "Behaviour of fibre reinforced composites under dynamic tension", Tech. Rep. AFOSR-85-0218, University of Oxford, 1986, technical Report for Air Force Office of Scientific Research.

[138] Gillespie Jr J.W., Gama B.A., Cichanowski C.E. & Xiao J.R., "Interlaminar shear strength of plain weave S2-glass/SC79 composites subjected to out-of-plane high strain rate compressive loadings", *Compos. Sci. Technol.*, vol. 65, (2005), pp. 1891–1908.

[139] Oguni K. & Ravichandran G., "Dynamic compressive behaviour of unidirectional E glass vinylester composites", *J. Mater. Sci.*, vol. 36, (2001), pp. 831–838.

[140] Ochola R.O., Marcus K., Nurick G.N. & Franz T., "Mechanical behaviour of glass and carbon reinforced composites at varying strain rates", *Compos. Struct.*, vol. 63, (2004), pp. 455–467.

[141] Akil O., Yildirim U., Guden M. & Hall I.W., "Effect of strain rate on the compression behaviour of a woven fabric S2 glass fiber reinforced vinyl ester composite", *Polym. Test.*, vol. 22, (2003), pp. 883–887.

[142] Nemat-Nasser S., *Mechanical Testing and Evaluation*, vol. 8 of *ASM Handbook*, chap. Recovery Hopkinson Bar Techniques, ASM International, 1999.

[143] Frew D.J., Forrestal M.J. & Chen W., "Pulse shaping techniques for testing brittle materials with a Split Hopkinson Pressure Bar", *Exp. Mech.*, vol. 42, (2001), pp. 93–106.

[144] Frew D.J., Forrestal M.J. & Chen W., "Pulse shaping techniques for testing elastic plastic materials with a Split Hopkinson Pressure Bar", *Exp. Mech.*, vol. 45, (2005), pp. 186–195.

[145] Kumar A., Seng L. T. & Pengjun Z., "Design of an impact striker for a Split Hopkinson Pressure Bar test", *J. Institution of Engineers Singapore*, vol. 44, (2004), pp. 119–130.

[146] Cloete T.J., van der Westhuizen A., Kok S. & Nurick G.N., "A tapered striker pulse shaping technique for uniform strain rate dynamic compression of bovine bone", in: "9th International DYMAT Conference", 2009.

[147] Haque A. & Hossain M.K., "Effect of moisture and temperature on high strain rate behavior of S2-glass-vinylester woven composites", *J. Compos. Mat.*, vol. 37, (2003), pp. 627–647.

[148] Tasmerdici A., Kara A., Turan A.K., Tunusoglu G., Guden M. & Hall I.W., "Experimental and numerical investigation of high strain rate mechanical behavior of a [0/45/90/-45] quadriaxial E glass/polyester composite", *Physics Engineering*, vol. 10, (2011), pp. 3068–3073.

[149] Li Y., Lin Z., Jiang A. & Chen G., "Experimental study of glass-fiber mat thermoplastic material impact properties and lightweight automobile body analysis", *Mater. Design.*, vol. 25, (2004), pp. 579–585.

[150] Rubio L., Fernandex-Saez J. & Navarro C., "Determination of dynamic fracture initiation toughness using three point bending testing in a modified HPB", *Exp. Mech.*, vol. 43, (2003), pp. 379–386.

[151] Luo Y., Lv L., Sun B., Qiu Y. & Gu B., "Transverse impact behaviour and energy absorption of three-dimensional orthogonal hybrid woven composites", *Comp. Struct.*, vol. 81, (2007), pp. 202–209.

[152] Ogawa K., Sugiyama F., Pezzotti G. & Nishida T., "Impact strength of continuous carbon fiber reinforced silicon nitride measured by using the SHPB", *J. Am. Ceram. Soc.*, vol. 81, (1998), pp. 166–172.

[153] Bacon C., Farm J. & Lataillade J.L., "Dynamic fracture toughness determined from load point displacement", *Exp. Mech.*, vol. 34, (1994), pp. 217–223.

[154] Martins C.F., Irfan M.A. & Prakash V., "Dynamic fracture of linear medium density polyethylene under impact loading conditions", *Mater. Sci. Eng. A - Struct.*, vol. 465, (2007), pp. 211–222.

[155] Rittel D., Pineau A., Clisson J. & Rota L., "On testing of Charpy specimens using the one point bend impact technique", *Exp. Mech.*, vol. 42, (2003), pp. 247–252.

[156] Jiang F., Rohatgi A., Vecchio K.S. & Cheney J.L., "Analysis of the dynamic responses for a pre-crack three-point bend specimen", *Int. J. Fracture.*, vol. 127, (2004), pp. 147–165.

[157] Park S.W., Zhou M. & Veazie D.R., "Time-resolved impact response and damage of fiber reinforced composite laminates", *J. Compos. Mater.*, vol. 34, (2000), pp. 879–904.

[158] Nwosu S.N., Hui D. & Dutta P.K., "Dynamic mode II delamination fracture of unidirectional graphite epoxy composites", *Comp. Part B*, vol. 34, (2003), pp. 303–316.

[159] Nwosu S.N., Hui D. & Dutta P.K., "Dynamic mixed mode I/II delamination fracture and energy release rate of unidirectional graphite epoxy composites", *Eng. Frac. Mech.*, vol. 72, (2005), pp. 1531–1558.

[160] Yokoyama T. & Kishida K., "A novel impact three point bend test method for determining dynamic fracture initiation toughness", *Exp. Mech.*, vol. 29, (1989), pp. 188–194.

[161] Delvare F., Hanus J.L. & Bailly P., "A non-equilibrium approach to processing hopkinson bar bending test data: Application to quasi-brittle materials", *Int. J. Impact Engng*, vol. 37, (2010), pp. 1170–1179.

[162] Kusaka T., Hojo M., Mai Y.W., Kurokawa T., Nojima T. & Ochiai S., "Rate dependence of Mode I fracture behaviour in carbon fibre epoxy composite laminates", *Compos. Sci. Technol.*, vol. 58, (1998), pp. 591–602.

[163] Sun C.T. & Han C., "A method for testing interlaminar dynamic fracture toughness of polymeric composites", *Comp. Part B*, vol. 35, (2004), pp. 647–655.

[164] Jud K., Personal Communication, Collano Adhesives AG, 2009.

[165] Gray III G.T.(Rusty), *Mechanical Testing and Evaluation*, vol. 8 of *ASM Handbook*, chap. Classic Split-Hopkinson Pressure Bar Testing, ASM International, 1999.

[166] Pochammer L., "On the propagation velocities of small oscillations in an unlimited isotropic circular cylinder", *J. f. Math. (Crelle)*, vol. 81, (1876), pp. 324–326.

[167] Chree C., "The equations of an isotropic elastic solid in polar and cylindrical coordinates, their solutions and applications", *Cambridge Phil. Soc. Trans*, vol. 14, (1889), pp. 250–369.

[168] Gong J.C., Malvern L.E. & Jenkins D.A., "Dispersion investigation in the Split Hopkinson Pressure Bar", *J. Eng. Mat. Tech*, vol. 112, (1990), pp. 309–314.

[169] Lee C.K.B., Crawford R.C., Mann K.A., Coleman P. & Petersen C., "Evidence of higher Pochammer-Chree modes in an unsplit Hopkinson bar", *Meas. Sci. Tech.*, vol. 6, (1995), pp. 853–859.

[170] Gorham D.A., "A numerical method for the correction of dispersion in pressure bar signals", *J. Phys. E. Sci. Intrum.*, vol. 16, (1983), pp. 477–479.

[171] Follansbee P.S. & Frantz C., "Wave propagation in the Split Hopkinson Pressure Bar", *J. Eng. Mat. Tech*, vol. 105, (1983), pp. 61–66.

[172] Govender R.A., *Numerical Investigation of dispersion in Hopkinson Pressure Bars*, M.Sc thesis, University of Cape Town, 2005.

[173] Govender R.A., Louca L.A., Pullen A., Fallah A.S. & Nurick G.N., "Determining the through thickness properties of thick Glass Fibre Reinforced Polymers at high strain rates", *J. Compos. Mater.*, manuscript JCM-10-0590 Accepted for publication, in press.

[174] Tarfaoui M., Choukri S. & Neme A., "Effect of fibre orientation on mechanical properties of the laminated polymer composites subjected to out of plane high strain rate compressive loadings", *Compos. Sci. Technol.*, vol. 68, (2008), pp. 477–485.

[175] Vecchio K.S. & Jiang F., "Improved pulse shaping to achieve constant strain rate and stress equilibrium in Split Hopkinson Pressure Bar testing", *Metallurgical and Material Transactions A*, vol. 38A, (2007), pp. 2655–2665.

[176] Marais S.T., *Development and proving of a Split Hopkinson Pressure Bar used for high strain rate materials testing*, M.Sc thesis, University of Cape Town, 2001.

[177] Lifshitz J.M. & Leber H., "Data processing in the Split Hopkinson Pressure Bar tests", *Int. J. Impact Engng*, vol. 15, (1994), pp. 723–733.

[178] Gorham D.A., "Measurement of stress-strain properties of strong metals at very high rates of strain", *Inst. Phys. Conf. Ser.*, vol. 47, (1979), pp. 16–24.

[179] Gorham D.A., Pope P.H. & Field J.E., "An improved method for compressive stress-strain measurements at very high strain rates", *Proc. R. Roc. Lond.*, vol. A8, (1992), pp. 153–170.

[180] Zengeni T., "Material characterisation of glass fibre polypropylene (twintex)", Final year project report, University of Cape Town, 2007.

[181] MatWeb, "www.matweb.com", 2011.

[182] Rao S., Shim V.P.W. & Quah S.E., "Dynamic mechanical properties of polyurethan elastomers using a nonmetallic Hopkinson bar", *J. Appl. Polym. Sci.*, vol. 66, (1997), pp. 619–631.

[183] Stander M., *Development of an intermediate strain rate tester*, M.Sc thesis, University of Cape Town, 2011.

[184] Merrett R., *High strain rate characterisation of metallic cellular materials using an instrumented direct impact HPB*, M.Sc thesis, University of Cape Town, 2011.

[185] Curry R., *Implementation of polymeric Hopkinson pressure bars*, M.Sc thesis, University of Cape Town, 2011.

[186] Yang L.M. & Shim V.P.W., "An analysis of stress uniformity in split Hopkinson bar test specimens", *Int. J. Impact Engng*, vol. 31, (2005), pp. 129–150.

[187] Bacon C., "An experimental method for considering dispersion and attenuation in a viscoelastic Hopkinson bar", *Exp. Mech.*, vol. 38, (1998), pp. 242–249.

[188] Stander M. ,University of Cape Town, Personal Communication, 2011, Discussion on rate dependency study of Aluminium alloys at BISRU.

[189] Fahr A., Chapman C.E., Laliberte J.F., Forsyth D.S. & Poon C., "Nondestructive evaluation methods for damage assessment in fiber metal laminates", *Polym. Composite*, vol. 21, (2000), pp. 568–575.

[190] Sundararaman V. & Davidson B.D., "An unsymmetric end notch flexure test for interfacial fracture toughness determination", *Eng. Frac. Mech.*, vol. 60, (1998), pp. 361–377.

[191] Hyer M.W., *Stress analysis of fibre reinforced composite materials*, McGraw Hill, 1998.

[192] Shah Khan M.Z., Simpson G. & Gellert E.P., "Resistance of glass-fibre reinforced polymer composites to increasing compressive strain rates and loading rates", *Compos. Part A*, vol. 31, (2000), pp. 57–67.

[193] Guden M., Yildirim U. & Hall I.W., "Effect of strain rate on the compression behaviour of a woven glass fiber/SC-15 composite", *Polym. Test.*, vol. 23, (2004), pp. 719–725.

[194] Kyowa, "Gages for general stress measurement", Data Sheet, 2010.

[195] Kyowa, "High elongation strain gages", Data Sheet, 2010.

[196] Renishaw plc, "Rgh41 Series Readhead (Linear Encoder)", Data Sheet, 2011.

[197] Thomson W.T., *Theory of Vibration with Applications*, Chapman and Hall, London, 4th edn., 1993.

[198] Dassault Systèmes Simulia Corp, Providence, R.I., *ABAQUS v6.10 User's Manual*, 2010.

[199] Davidson B.D. & Sundararaman V., "A single leg bending test for interfacial fracture toughness determination", *Int. J. Fract.*, vol. 78, (1996), pp. 193–210.

[200] Johnson G.R. & Cook W.H., "A constitutive model and data for metals subjected to large strain, high strain rates and temperatures", in: "Proc. 7th Intl. Symp. Ballistics, Netherlands", 1983, pp. 541–547.

[201] Salibsury C., *Spectral analysis of wave propagation through a polymeric Hopkinson bar*, M.Sc thesis, University of Waterloo, 2001.

Appendices

Appendix A

Miscellaneous Experimental Results

Experimental results that were not presented in the body of the report are presented in this appendix.

A.1 Compression of GFPP

A.1.1 Quasi-static Compression in the Through-Thickness Direction

The results of through thickness compression of GFPP, for displacement rates of 1 and 10 mm/min, are shown in Figures A.1 and A.2 respectively.

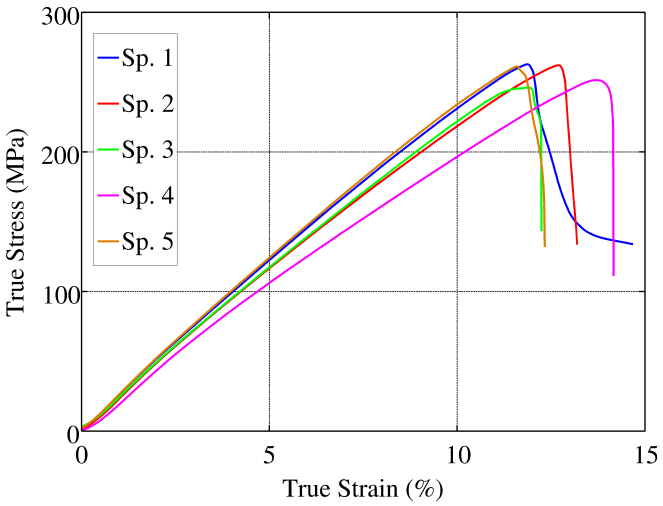

Figure A.1: Plot of true stress-strain response of GFPP for through thickness compression at 1 mm/min

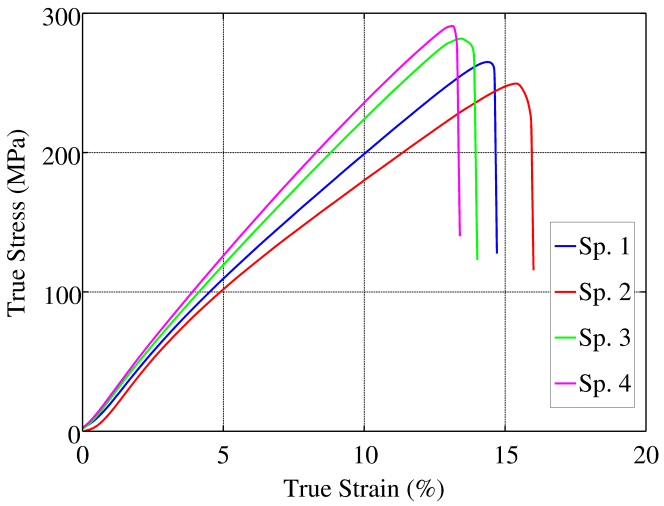

Figure A.2: Plot of true stress-strain response of GFPP for through thickness compression at 10 mm/min

A.1.2 Compression SHPB Tests Showing Poor Equilibration

Initial SHPB tests on through-thickness specimens of the same dimensions as the quasi-static tests (11 mm diameter and 12 mm thickness) resulted in poor equilibration of the input and output face stresses, as shown in Figure A.3. The variation between the stresses at the input and output faces of the specimen was 20% at peak stress, which was considered unacceptable. To improve equilibration during the through-thickness SHPB tests, the specimen diameter was increased to 15 mm and the thickness reduced to 6 mm. The SHPB tests on the original and revised specimens all resulted in the spreading failure mode.

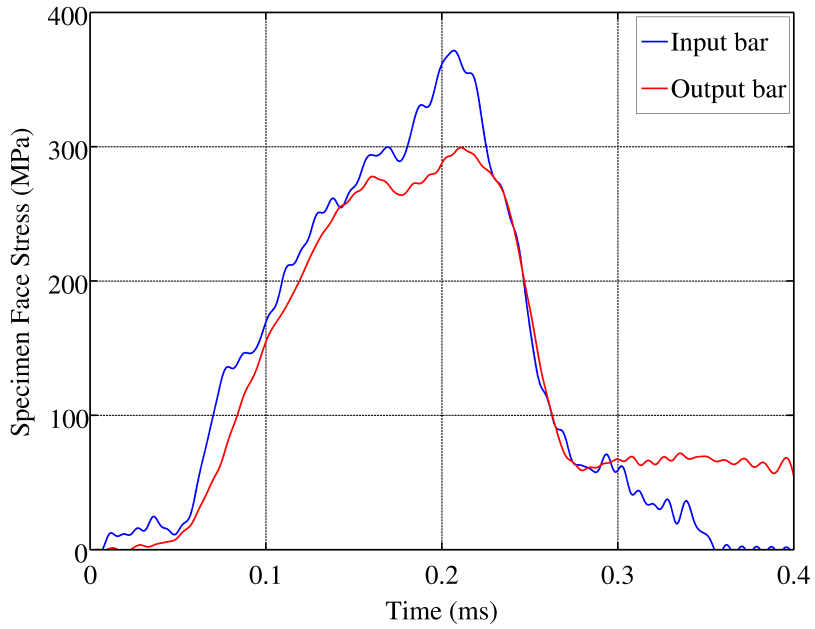

Figure A.3: Plot of specimen stresses at input and output faces during a SHPB test showing poor equilibration

A.1.3 Photographs of Through-thickness Compression of GFPP Specimens

Photographs of all through-thickness compression GFPP specimens, indicating which failure modes were observered, are presented in Figures for cross head speeds (CHS) of 0.1 mm/min, Figures for CHS of 1 mm/min and Figures for CHS of 10 mm/min.

A.1.3.1 CHS 0.1 mm/min

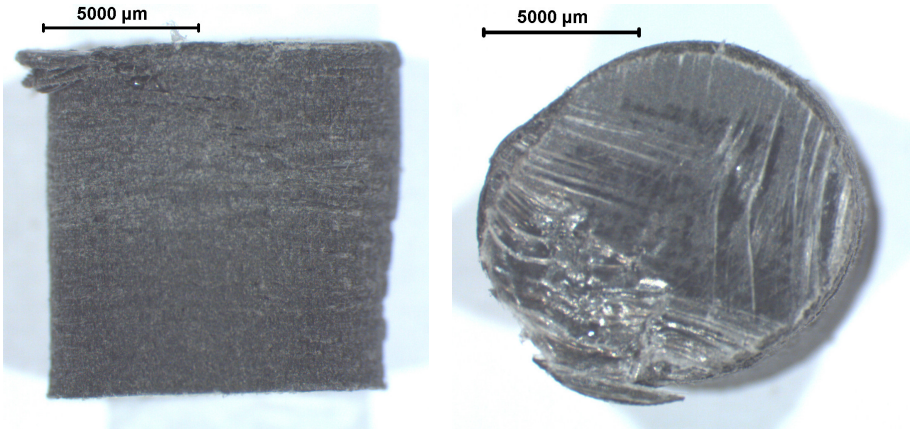

(a) Side View (b) Top View

Figure A.4: CHS 0.1 mm/min, Specimen 1: Spreading on top left

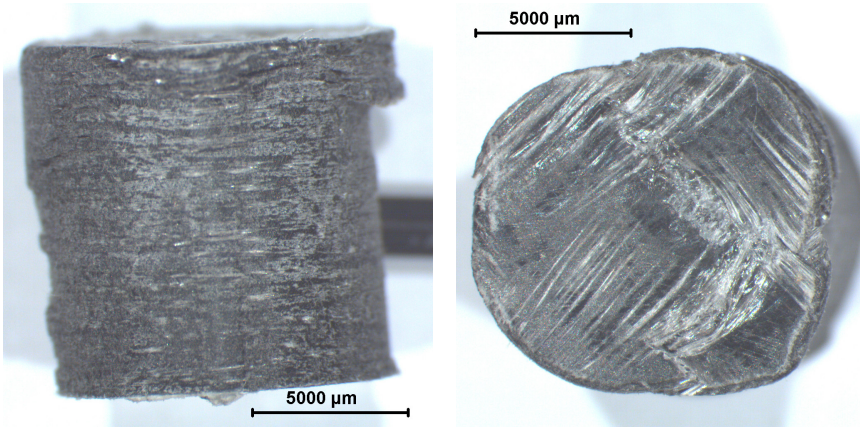

(a) Side View (b) Top View

Figure A.5: CHS 0.1 mm/min, Specimen 2: Spreading on top right

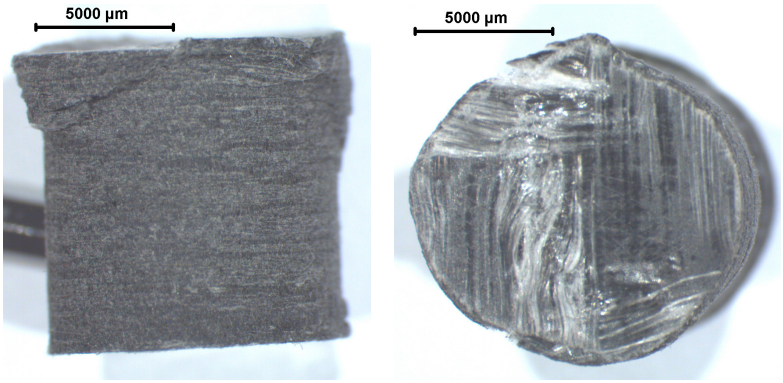

(a) Side View (b) Top View

Figure A.6: CHS 0.1 mm/min, Specimen 3: Macroscopic shear on top left, spreading and bulging on top right

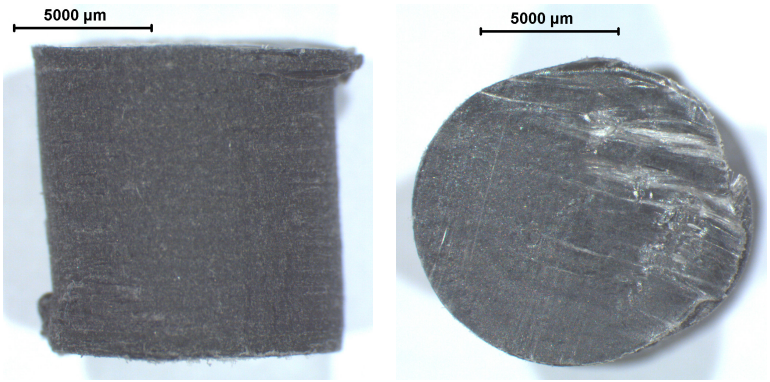

(a) Side View (b) Top View

Figure A.7: CHS 0.1 mm/min, Specimen 4: Spreading on top right and bottom left

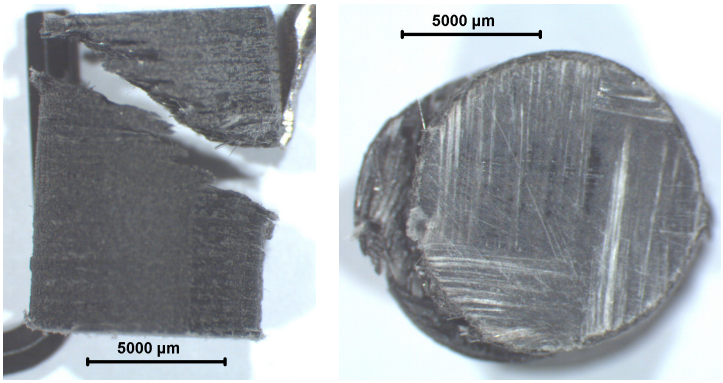

(a) Side View (b) Top View

Figure A.8: CHS 0.1 mm/min, Specimen 5: Macroscopic shear into two fragments

A.1.3.2 CHS 1 mm/min

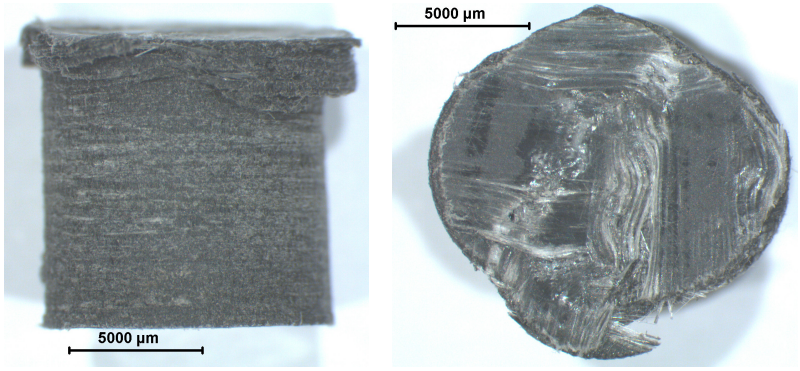

(a) Side View (b) Top View

Figure A.9: CHS 1.0 mm/min, Specimen 1: Spreading of most of top surface

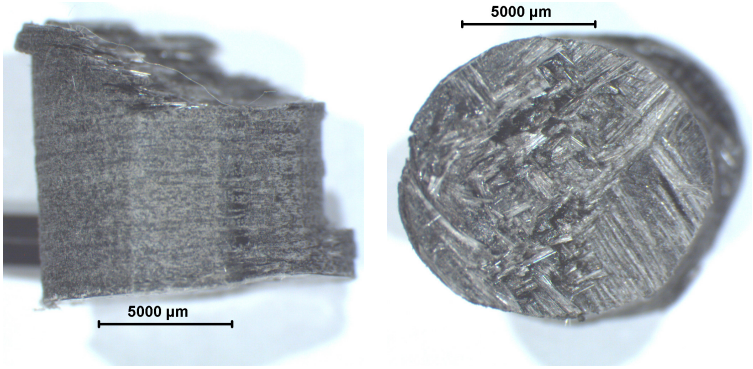

(a) Side View (b) Top View

Figure A.10: CHS 1.0 mm/min, Specimen 2: Macroscopic shear (top surface - fragment not recovered), spreading of bottom right surface

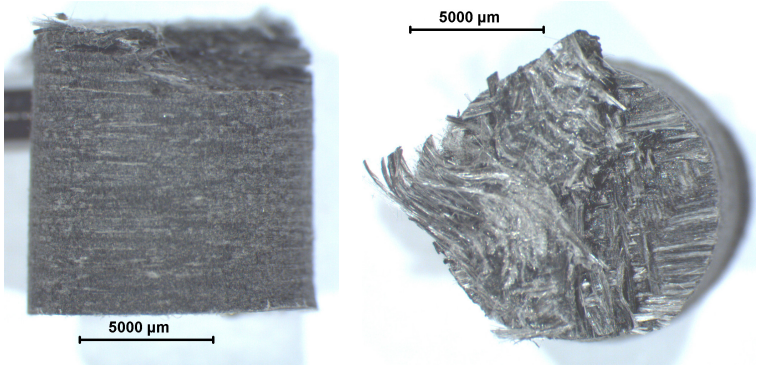

(a) Side View (b) Top View

Figure A.11: CHS 1.0 mm/min, Specimen 3: Fragment ejected on top right, possibly macroscopic shear

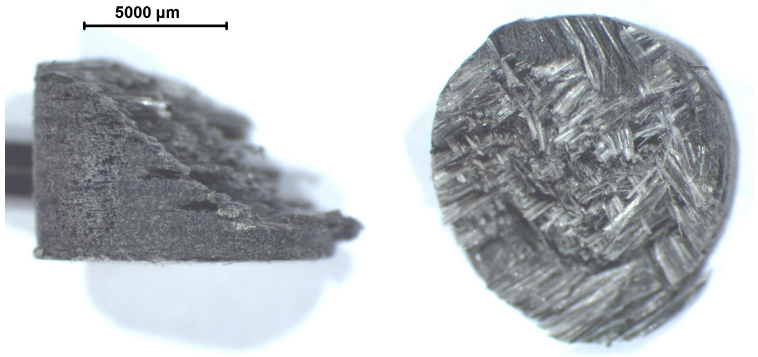

(a) Side View (b) Top View

Figure A.12: CHS 1.0 mm/min, Specimen 4: Macroscopic shear - fragment not recovered

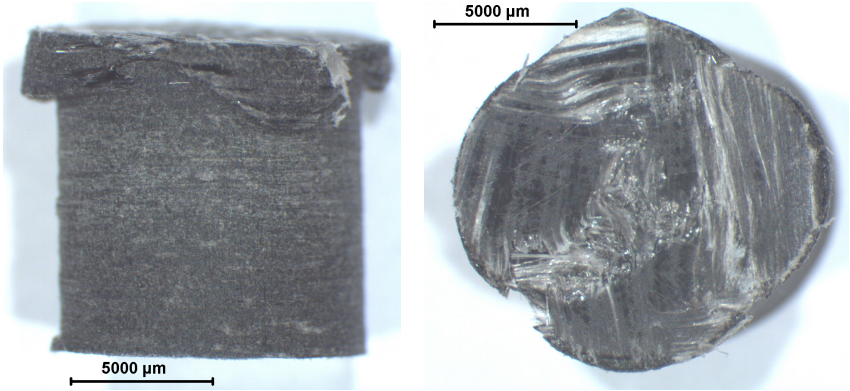

(a) Side View (b) Top View

Figure A.13: CHS 1.0 mm/min, Specimen 5: Spreading with some incipient shear

A.1.3.3 CHS 10 mm/min

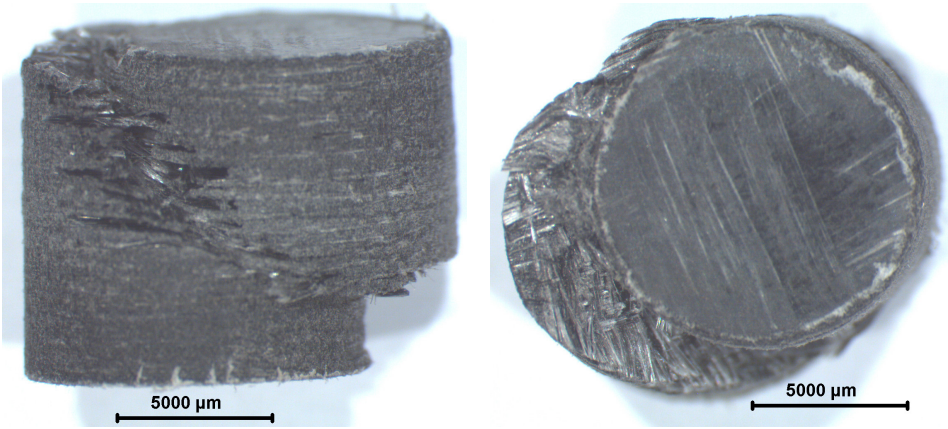

(a) Side View (b) Top View

Figure A.14: CHS 10 mm/min, Specimen 1: Macroscopic shear

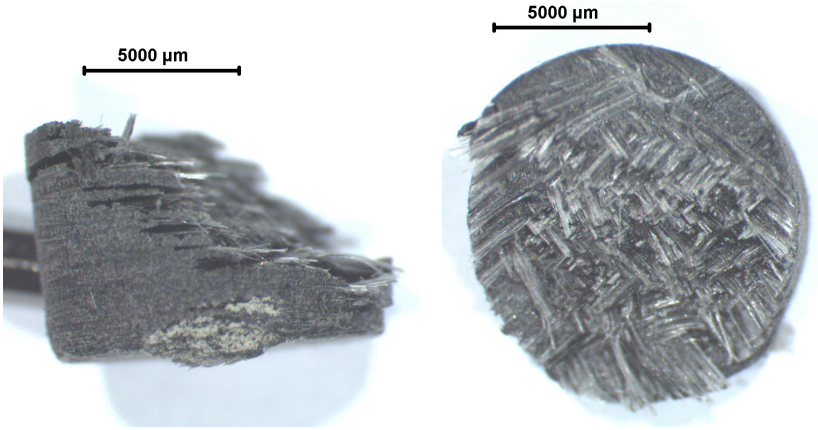

(a) Side View (b) Top View

Figure A.15: CHS 10 mm/min, Specimen 2: Macroscopic shear - fragment not recovered

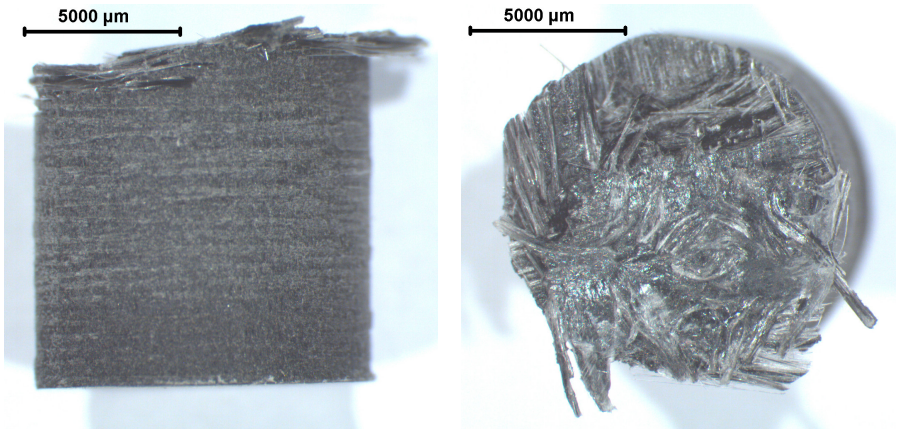

(a) Side View (b) Top View

Figure A.16: CHS 10 mm/min, Specimen 3: Spreading with ejection of a lateral fragment

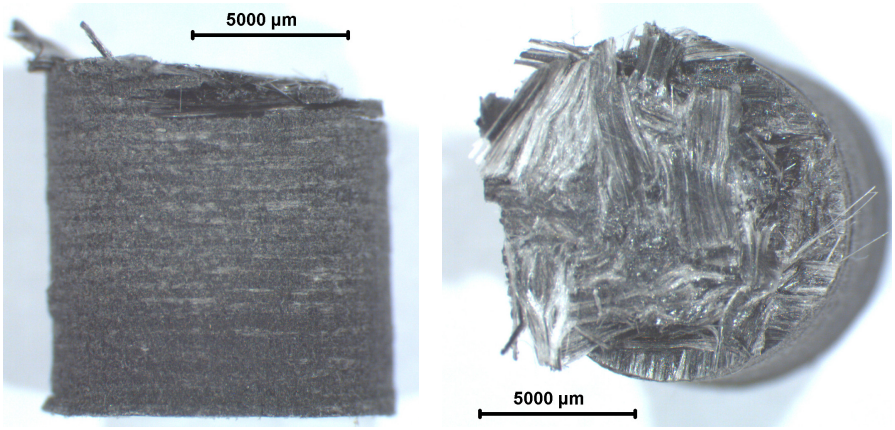

(a) Side View (b) Top View

Figure A.17: CHS 10 mm/min, Specimen 4: Fragment ejected laterally - not recovered

A.1.3.4 SHPB

The patches of white on the specimen were used to mark the face in contact with the input bar.

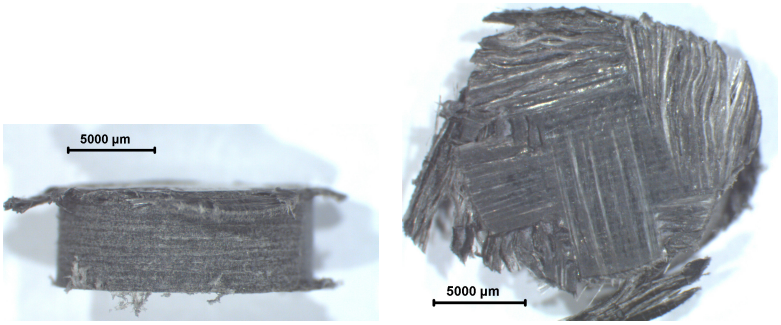

(a) Side View (b) Top View

Figure A.18: SHPB, Specimen 1: Spreading

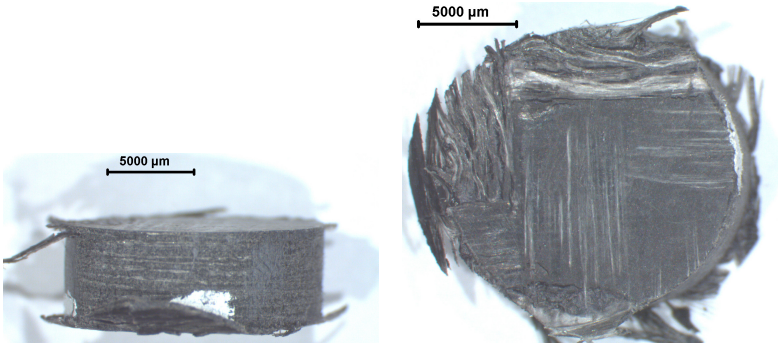

(a) Side View (b) Top View

Figure A.19: SHPB, Specimen 2: Spreading

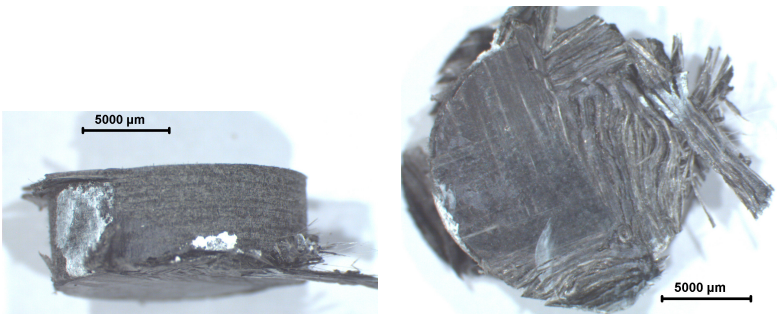

(a) Side View (b) Top View

Figure A.20: SHPB, Specimen 3: Spreading

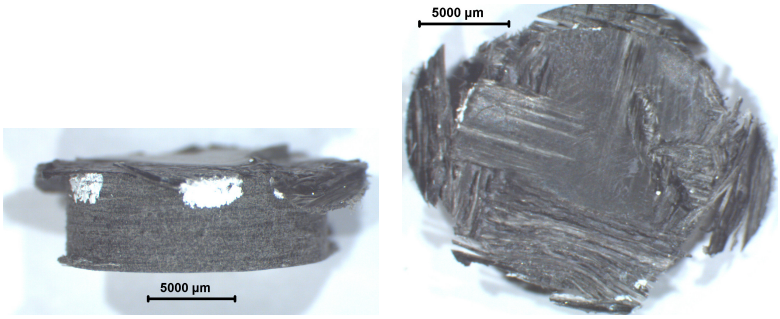

(a) Side View (b) Top View

Figure A.21: SHPB, Specimen 4: Spreading

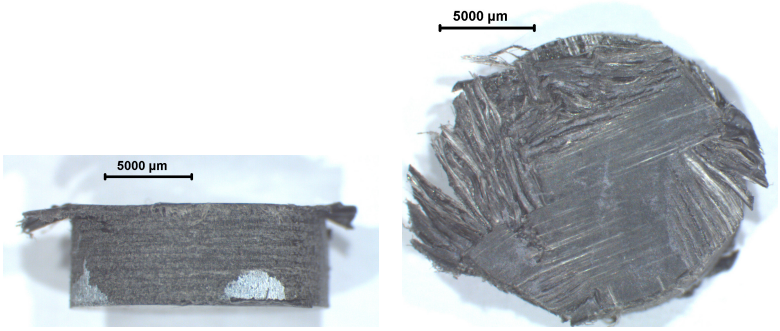

(a) Side View (b) Top View

Figure A.22: SHPB, Specimen 5: Spreading

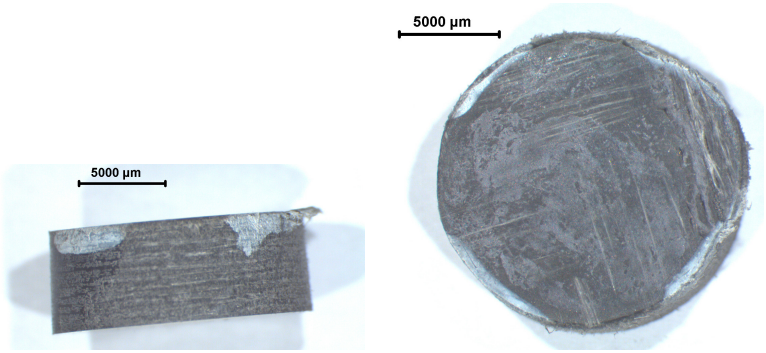

(a) Side View (b) Top View

Figure A.23: SHPB, Specimen 6: Incipient spreading - striker velocity was just sufficient to cause permanent deformation

A.2 Characterisation of Aluminium

A.2.1 Test Configuration

Dogbone tensile test specimens were machined to gauge lengths of 50 mm and width 10 mm. Six specimens of both the 1.2 mm and 3 mm thick sheets were cut in the roll direction, and six of both thicknesses were cut transverse to the roll direction. The tests were run in displacement control, at a cross head speed (CHS) of 1 mm/min. The raw force $P(t)$-displacement $\delta(t)$ data was converted to true stress σ-true strain ε relationships by the standard relationships:

$$\sigma = \frac{P(t)}{A(t)} \tag{A.1}$$

$$\varepsilon = ln\big(\frac{L_o + \delta(t)}{L_o}\big) \tag{A.2}$$

The instantaneous area $A(t)$ was calculated based on the gauge section maintaining constant volume. This assumption is only valid until the specimen begins to neck. It was not necessary to calculate the stress post necking as the strains experienced by the aluminium during the delamination experiments were well below the onset of necking.

A.2.2 Results

The true stress-strain curves for the six 1.2 mm thick specimens, tested in the roll direction, are shown in Fig. A.24. All six specimens exhibited a smooth transition from linear elasticity to plastic flow. The mean 0.2% offset stress was 93 MPa. Two specimens (Sp. 2 and Sp. 4) exhibited lower apparent strains to failure. This was not of any concern as the test data was only used to characterise a plasticity hardening curve. The tests on 1.2 mm thick aluminium in the transverse direction differed by less than 3%. The true stress-strain curves for the 3 mm thick specimens, tested in the roll direction, are shown in Figure A.25. The response of the different thicknesses was similar, with the mean 0.2% offset stress for the 3 mm thick aluminium specimens being 104 MPa.

The aluminium tensile tests were used to obtain the parameters for a Johnson-Cook [200] plasticity model, for use in FEA. The Johnson-Cook plasticity model has the form [200]:

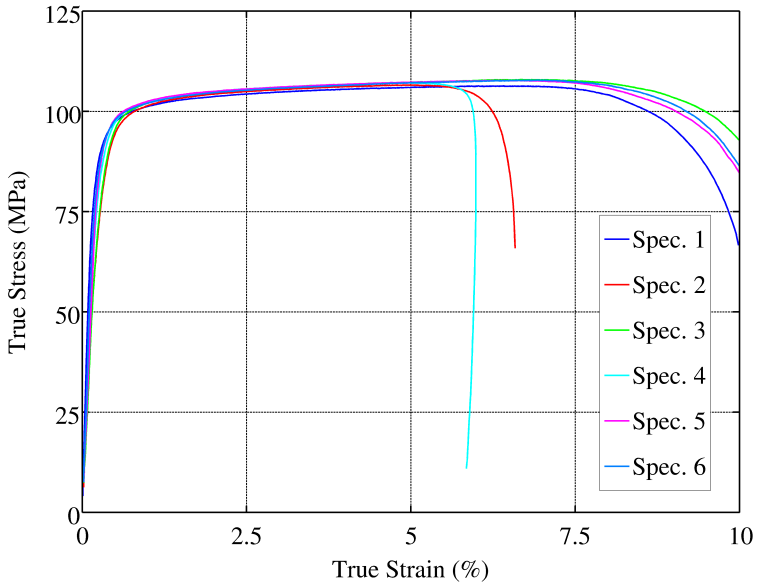

Figure A.24: Plot of true stress vs true strain curves for 1.2 mm thick aluminium in roll direction

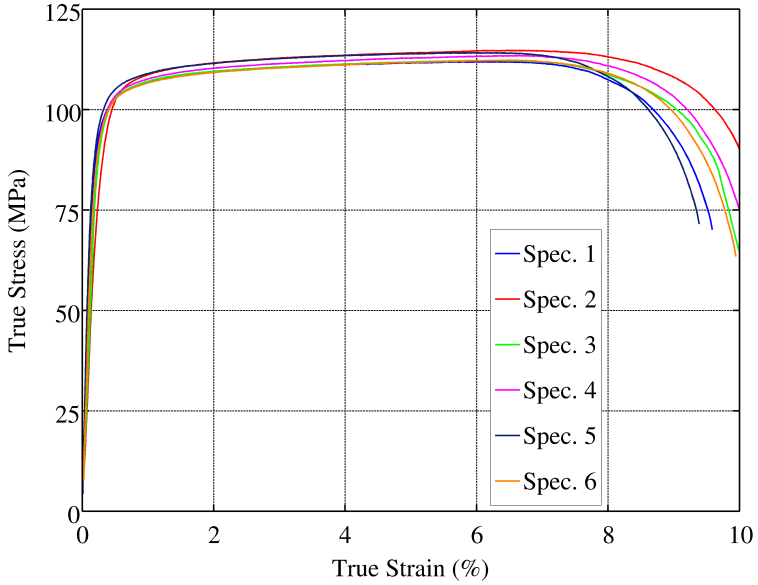

Figure A.25: Plot of true stress vs true strain curves for 3 mm thick aluminium in roll direction

$$\sigma_{vonMises} = [A + B\varepsilon^n] \left[1 + Cln(\frac{\dot{\varepsilon}}{\dot{\varepsilon}_0})\right] \left[1 - \frac{T - T_{ref}}{T_{melt} - T_{ref}}\right] \tag{A.3}$$

The hardening parameters A, B and n were obtained by curve fitting to the quasi-static experimental true stress - true strain curves. These parameters are summarised in Table A.1. Tests by Stander [183] on similar aluminium alloys showed negligible rate sensitivity for the range of strain rates anticipated during testing. Hence the rate dependence parameter C was set to zero for the FE simulations. The temperature dependence exponent m was assumed to have a value of 1.0. The fit for the 1.2 mm thick specimens is shown in Figure A.26.

Table A.1: Johnson-Cook hardening parameters for aluminium

Thickness	A MPa	B MPa	n
1.2 mm	68	50	0.08
3.0 mm	80	49	0.14

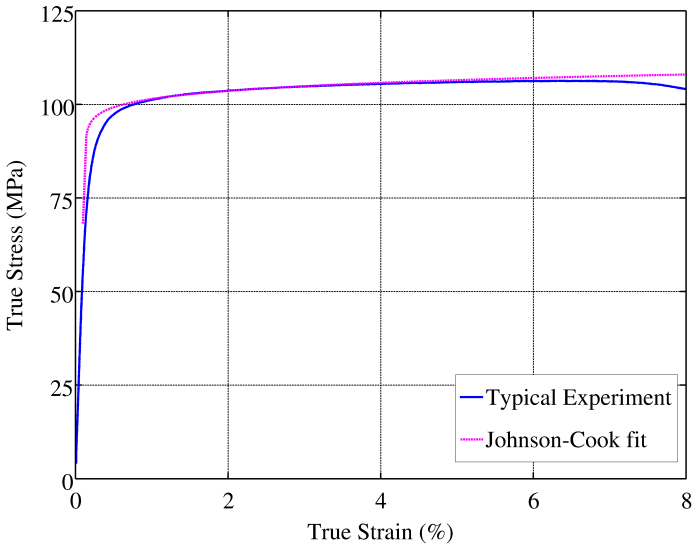

Figure A.26: Plot of experimental and Johnson-Cook true stress -true strain curves for 1.2 mm thick aluminium in roll direction

A.2.3 Quasi-static Bend Tests

A.2.3.1 Test Configuration

The bend tests were performed on a Zwick Universal Testing Machine fitted with adjustable roller supports and a central loading roller. The rollers were all silver steel, with a diameter of 10mm. The specimens were oriented with the roll direction parallel to the span of the support rollers. The test parameters are presented in the table below:

Table A.2: Aluminium 3-Pt bend test parameters

Parameter	**3.0mm Thickness**
Span (mm)	60
Width (mm)	25
Cross head speed (mm/min)	1
No. of tests	6

The six specimens cut from the same 3mm plate were split into two groups. One group was tested in the "as machined" condition. The second group was subjected to the same heating cycle that the aluminium experiences during the manufacture of an FML panel. This was to determine the effect (if any) of the heating cycle on the aluminium, without involving the complications of residual stresses.

A.2.3.2 Results

The force-displacement response for the 3 Point bend tests is shown in Figure A.27. The difference between the "as machined" and "heat treated specimens" is insignificant. The response is almost bi-linear, with the initial stiff response being governed by the elastic modulus and the later response by plastic flow, with very little strain hardening.

A.3 Delamination Testing

A.3.1 High Rate Single Leg Bend Testing of FMLs

The initial set of high rate SLB tests on FML specimens had the initial crack position half way between the outer support and the central impacter (termed quarter-span). To investigate the sensitivity of the SLB test to initial crack position, further tests were

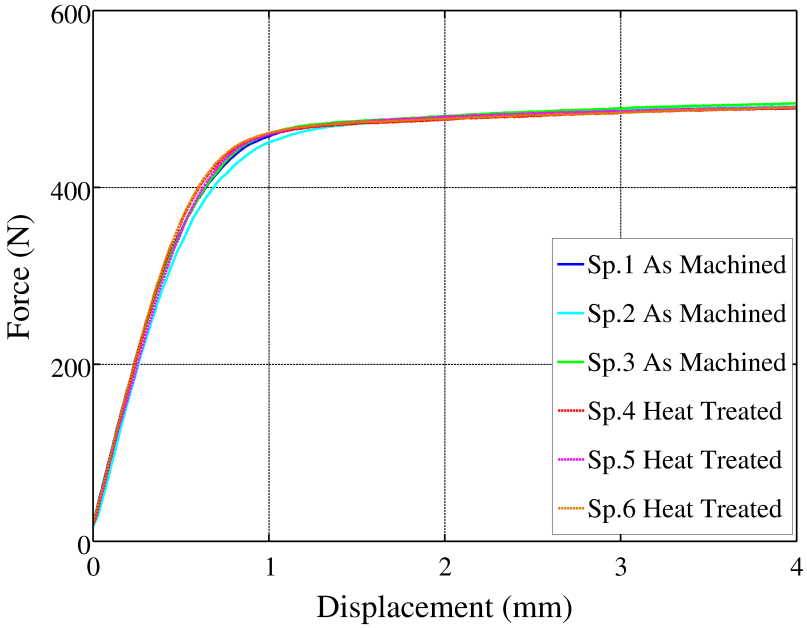

Figure A.27: Plot of force-displacement response for Three Point bend tests on 3 mm thick aluminium

carried out with the initial crack tip closer to the central impacter. Specimen geometry constrainsts prevented tests with the initial crack tip closer to the outer support. The force and crack extension histories for a test, with the repositioned crack tip, is shown in Figure A.28. The force reached a peak very rapidly before dropping with some superimposed oscillations. The peak force preceded visible crack initiation by approximately 0.25 ms. The crack propagation consisted of an initial jump of approximately 5 mm, followed by stick-slip growth. The initial jump in crack length coincided with the measured force dropping to almost zero. The energy release rate relationship calculated for this set of force and crack extension data is shown in Figure A.29. The only sensible data which may be extracted from this set of tests is the initiation value of G_{I-II}, which had an average value of 1.0 kJ/m^2.

While lower than the initiation value of G_{I-II} obtained from the tests with the initial crack tip at quarter span, all of the high rate SLB tests on FML specimens exhibited higher initiation values of G_{I-II} than the quasi-static tests.

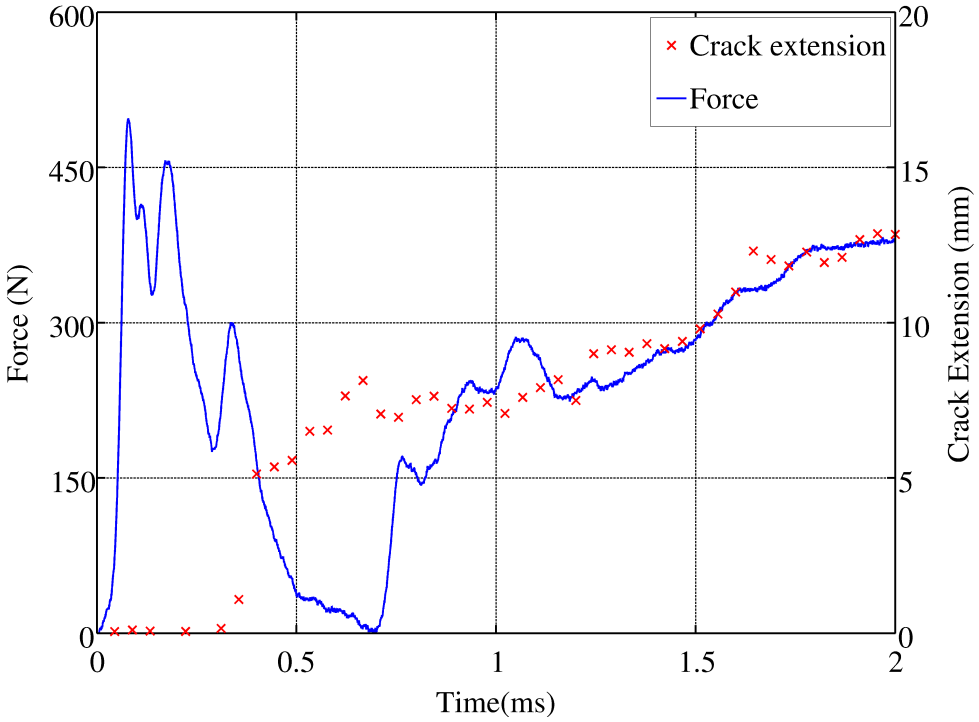

Figure A.28: Plot of force and crack extension histories for a HPB Single Leg Bend test on FML

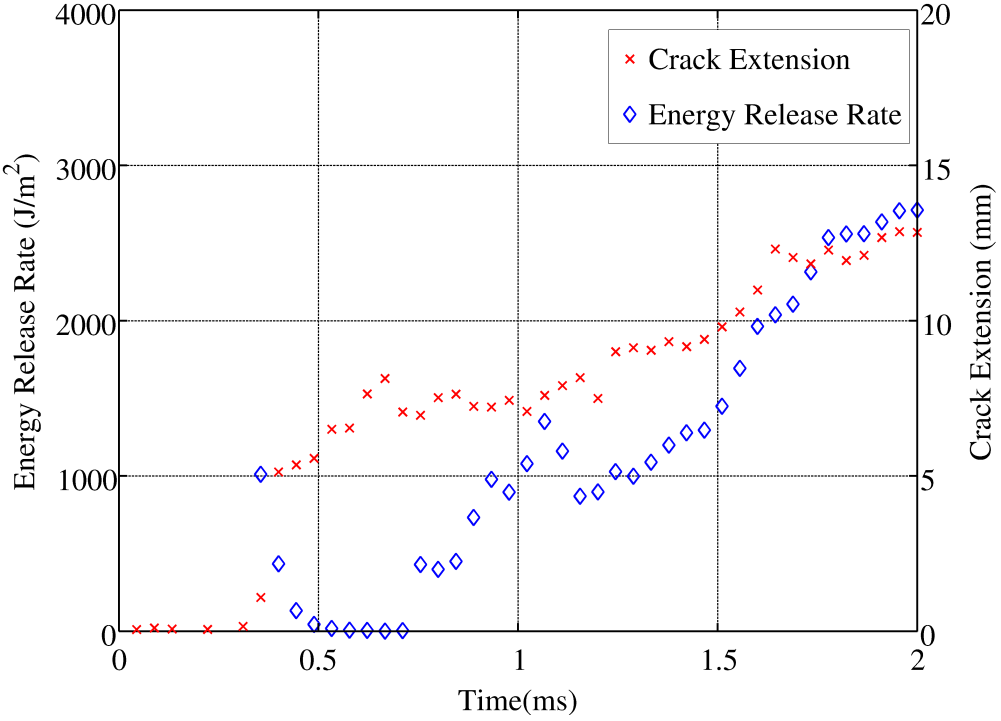

Figure A.29: Plot of energy release rate and crack extension histories for a HPB Single Leg Bend test on FML

Appendix B

Wave Propagation in Polymeric HPB

This appendix describes how to experimentally determine the transfer function for wave propagation in a polymeric HPB. Polymeric HPB exhibit visco-elastic behaviour, which results in both attenuation and dispersion of a wave. This section is based on work published by Bacon [187] and Salisbury [201], and summarises some of the findings of Curry [185], who was co-supervised by the author. The signal processing techniques were based on work by Curry [185], but were the author's own implementation.

B.1 Derivation of Wave Transfer Function

Consider a slender, cylindrical bar subjected to axial impact, that produces a wave propagating axially. If the diameter is small in comparison to length of the wave, the problem may be considered only in terms of the axial coordinate. For dynamic equilibrium, axial stress $\sigma(z,t)$ and displacement $u(z,t)$ are related by:

$$\frac{\partial \sigma(z,t)}{\partial z} = \rho \frac{\partial^2 u(z,t)}{\partial t^2} \tag{B.1}$$

For small displacements, axial strain $\varepsilon(z,t)$ is related to displacement $u(z,t)$ by:

$$\varepsilon(z,t) = \frac{\partial u(z,t)}{\partial z} \tag{B.2}$$

Stress and strain may be transferred to the frequency domain using Fourier transforms, denoted $\tilde{\sigma}(z,\omega)$ and $\tilde{\varepsilon}(z,\omega)$. Eq. B.1 may be re-written using Eq. B.2 in the frequency domain as:

$$\frac{\partial^2 \tilde{\sigma}(z,\omega)}{\partial z^2} = -\rho\omega^2 \tilde{\varepsilon}(z,\omega) \tag{B.3}$$

If the bar material may be described using linear visco-elasticity, stress and strain in the frequency domain are related by the complex modulus $E^*(\omega)$:

$$\tilde{\sigma}(z,\omega) = E^*(\omega)\tilde{\varepsilon}(z,\omega) \tag{B.4}$$

The propagation coefficient $\gamma(\omega)$ is defined by:

$$\gamma^2(\omega) = -\frac{\rho\omega^2}{E^*(\omega)} \tag{B.5}$$

This permits Eq. B.3 to be re-written as:

$$\frac{\partial^2 \tilde{\varepsilon}(z,\omega)}{\partial z^2} - \gamma^2 \tilde{\varepsilon}(z,\omega) = 0 \tag{B.6}$$

The general solution to be above equation is:

$$\tilde{\varepsilon}(z,\omega) = \tilde{P}(\omega)e^{-\gamma(\omega)z} + \tilde{N}e^{\gamma(\omega)z} \tag{B.7}$$

$\tilde{P}(\omega)$ and $\tilde{N}(\omega)$ are the Fourier transforms of strain waves at $z = 0$, travelling in the forward and backward direction, which correspond to the incident $\varepsilon_i(\omega)$ and reflected $\varepsilon_r(\omega)$ waves respectively.

Thus the stress may be expressed as:

$$\tilde{\sigma}(z,\omega) = E^*(\omega)[\tilde{P}(\omega)e^{-\gamma(\omega)z} + \tilde{N}e^{\gamma(\omega)z}] \tag{B.8}$$

Consider the case where the distal end of the bar is free. The stress at a free surface must be zero. Let the strain gauge correspond to position zero, and the distance from the gauge to the free end by z_g. Hence:

$$\tilde{P}(\omega)e^{-\gamma(\omega)z_g} + \tilde{N}e^{\gamma(\omega)z_g} = 0 \tag{B.9}$$

The transfer function $G(\omega)$ from the incident to the reflected wave may be defined as:

$$G(\omega) = -\frac{\tilde{\varepsilon_r}(\omega)}{\tilde{\varepsilon_i}(\omega)} = e^{-2\gamma(\omega)z_g} \tag{B.10}$$

The negative sign is required due to the inversion of the reflected wave. As $\tilde{\varepsilon_{i,r}}(\omega)$ are complex numbers, $G(\omega$ may be rewritten in terms of the complex magnitudes $M_{i,r}$ and phase angles $\theta_{i,r}$:

$$G(\omega) = -\frac{M_r}{M_i}e^{i(\theta_r-\theta_i)} = e^{-2\gamma z_g} = e^{-2(\alpha(\omega)+k(\omega))z_g} \tag{B.11}$$

The real and imaginary parts must be equal, which after minor algebra gives:

$$\alpha(\omega) = \frac{-1}{2z_g} ln\left(\frac{M_r}{M_i}\right) \tag{B.12}$$

$$k(\omega) = \frac{-(\theta_r - \theta_i)}{2z_g} \tag{B.13}$$

Phase velocity C_p is found by :

$$C_p(\omega) = \frac{\omega}{k(\omega)} \tag{B.14}$$

B.2 Experimental Characterisation of Visco-elastic Wave Propagation

As noted in the derivation above, the experimental determination of $\alpha(\omega)$ and $k(\omega)$ requires impacting a polymeric HPB at one end, and leaving the distal end free to give the desired zero stress boundary condition. The technique also requires clear separation between the incident $\varepsilon_i(t)$ and reflected $\varepsilon_r(t)$ waves in the time domain - if there is any overlap between $\varepsilon_i(t)$ and $\varepsilon_r(t)$, the Fourier transform of the waves represents a combination of both waves and the whole analysis collapses. As the strain gauge station was located 1734 mm from the distal free end of the HPB, overlap of the tail of $\varepsilon_i(t)$ and the start of $\varepsilon_r(t)$ would have required an extremely long loading event. However, the distance from the impact face to the gauge station was only 233 mm. Hence the reflection of the reflected wave, termed the 2^{nd} incident wave would overlap with the

tail of $\varepsilon_r(t)$. To prevent this overlap, a aluminium striker of length 30 mm and diameter 10 mm was used. A typical signal from the strain gauge station, with the incident and reflected waves highlighted, is shown in Figure B.1.

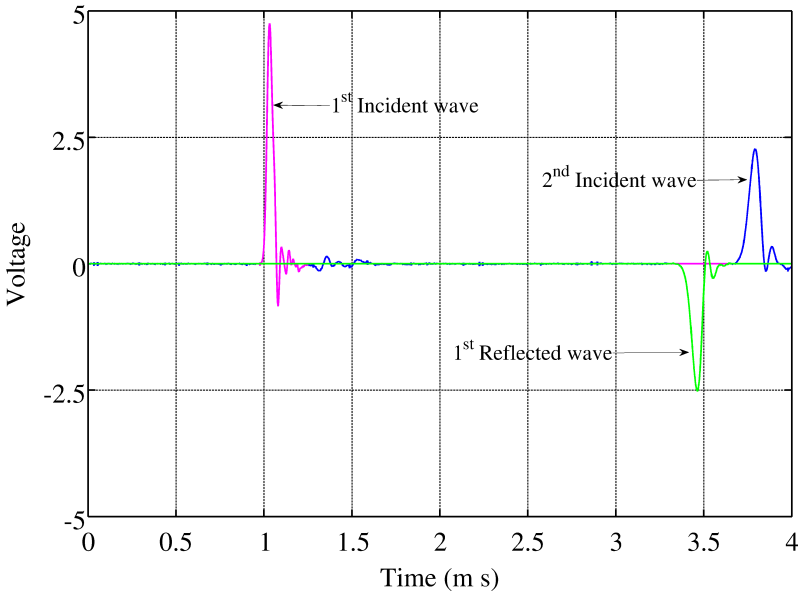

Figure B.1: Typical signal from PC HPB for wave speed determination

A total of 9 tests were performed for wave speed determination, with the striker velocities ranging from 4 to 8 m/s. The variation in attenuation coefficient and phase velocity are shown in Figure B.2 and Figure B.3 respectively.

The results obtained by the author correlate closely with those obtained by Curry [185]. Both attenuation coefficient and phase velocity data are closely grouped up to 15 kHz, before significant scatter arises. The attenuation coefficient increases with frequency in an approximately linear fashion to 20 kHz. This is consistent with increased damping of higher frequencies, as expected. The phase velocity determined from these experiments varies due to a combination of viscous and geometric effects.

The black dashed line in both Figure B.2 and Figure B.3 is the mean of all the data collected. The mean attenuation coefficient and phase velocity curves were used for correcting HPB signals for the bending tests.

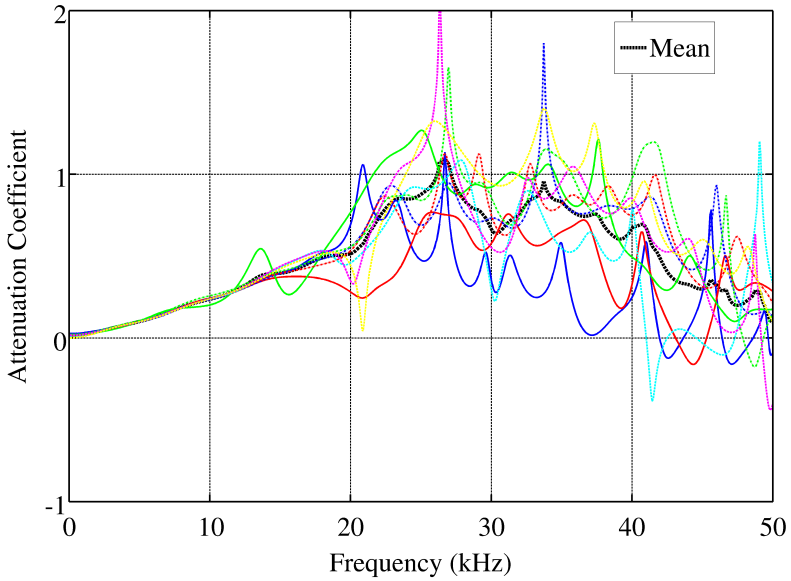

Figure B.2: Attenuation coefficient data for PC HPB

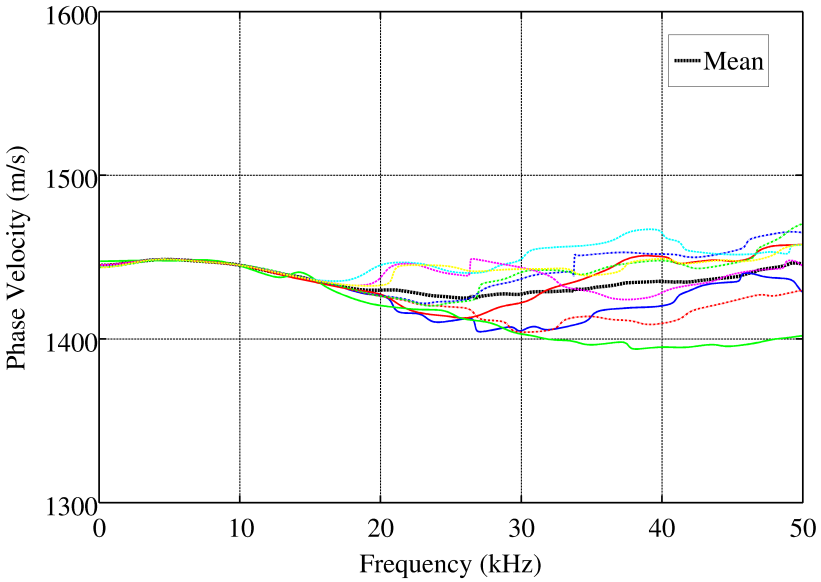

Figure B.3: Phase Velocity data for PC HPB

B.3 Script for Processing Wave Characterisation Experiments

```
clc
clear all

load 'PC_Wave_speed_20110302_10.mat';
Channel1=data(:,1);
N=length(Channel1);
N2=nextpow2(N)+1;
M=2^N2

figure
    hold on;
    box on;
    grid on;
    set(gca,'FontName','urw palladio l','Fontsize',20);
    plot(time,Channel1,'-b');

% ************************************
% Bar inputs
Z_gauge=1.7535 ; % m from gauge to end of bar
Z_Inc2=2*(0.233+0.011);

Freq_CutOff=30e+3;

% Time Inputs
RiseTime=4e-6;

IncBegin=950e-6;
IncEnd=1250e-6;

RefBegin=3300e-6;
RefEnd=3650e-6;

SampleRate=10e+6;
```

```
dt=1./SampleRate;

clear time data

Time=dt.*[0:1:(M-1)]';
TotalTime=Time(length(Time));

Chan1_Offset=mean(Channel1(1:250));
Channel1_Zeroed=Channel1-Chan1_Offset./ones(size(Channel1));
Channel1_Zeroed_Padded=zeros(M,1);

Channel1_Zeroed_Padded(1:N)=Channel1_Zeroed;

% ****************************************
IncPulse=Channel1_Zeroed_Padded....
  .*smoothwindow(Time,IncBegin,IncEnd,RiseTime);
RefPulse=-Channel1_Zeroed_Padded...
  .*smoothwindow(Time,RefBegin,RefEnd,RiseTime);

Fo=1/TotalTime;
Frequency=Fo.*[(-M/2 + 1):1:(M/2)]';
AngFreq=2*pi.*Frequency;

Y_Inc=fftshift(fft(IncPulse));
Y_Ref=fftshift(fft(RefPulse));

Z_Inc=abs(Y_Inc);
Z_Ref=abs(Y_Ref);
Attenuation_Coeff=-log(Z_Ref./Z_Inc)./(2*Z_gauge);

Theta_Inc=angle(Y_Inc);
Theta_Ref=angle(Y_Ref);

Phase_Inc=unwrap(Theta_Inc);
Phase_Ref=unwrap(Theta_Ref);

Phase_Inc_0=Phase_Inc-Phase_Inc(M/2).*ones(size(Phase_Inc));
```

```
Phase_Ref_0=Phase_Ref-Phase_Ref(M/2).*ones(size(Phase_Ref));

Wave_Number=-(Phase_Ref_0-Phase_Inc_0)./(2*Z_gauge);
Phase_Velocity=AngFreq./Wave_Number;

Gamma=Attenuation_Coeff+i.*Wave_Number;
[filename,pathname] = uiputfile('*.mat','Save your Captured Data ');
save(filename,'Frequency','Gamma')
```

B.4 Stress Level Calibration of Polymeric HPB

Calibration tests were conducted using a 500 mm long PC striker, cut from the same stock as the PC HPB in use. As the striker and HPB are of the same material, the following holds true for the stress wave at the impact face:

$$\sigma_{Th} = \rho C_o \frac{V_s}{2} \tag{B.15}$$

The PC bar used has a measured density ρ = 1196 kg/m^3. The value is C_o is taken from the mean of the first 10 points of the $C_p - \omega$ relationship and is 1450 m/s. The incident wave was shifted to the impact face, accounting for attenuation and dispersion. The conversion factor κ_{Cal} was then determined in the same manner as described in §4.3.6. The relevant data for the 17 calibration tests is recorded in Table B.1.

This gives an average κ_{Cal} = 2.432 MPa.

Table B.1: Calibration of PC Bar

Test no.	V_{BR}	Δt	V_S	**Theoret. Conv.**	**Exp. Conv.**	κ_{Cal}
	V	ms	m/s	MPa/V	MPa/V	MPa
1	1.49	5.18	7.67	1.638	1.661	2.475
2	1.48	9.25	4.29	1.649	1.562	2.312
3	1.48	8.89	4.47	1.649	1.663	2.461
4	1.48	9.56	4.15	1.649	1.563	2.314
5	1.48	8.79	4.52	1.649	1.579	2.337
6	1.48	6.69	5.93	1.649	1.638	2.424
7	1.48	6.45	6.16	1.649	1.623	2.402
8	1.48	5.56	7.14	1.649	1.669	2.471
9	1.48	5.51	7.21	1.649	1.681	2.488
10	1.19	4.60	8.63	2.051	2.079	2.475
11	1.19	4.86	8.17	2.051	2.043	2.431
12	1.19	4.13	9.61	2.051	2.082	2.477
13	1.19	4.23	9.39	2.051	2.066	2.459
14	0.99	3.64	10.91	2.466	2.479	2.455
15	0.99	3.75	10.59	2.466	2.473	2.448
16	0.99	3.26	12.18	2.466	2.494	2.469
17	0.99	3.36	11.82	2.466	2.468	2.443

Appendix C

Computational Model Information

Information pertaining to the computational models, that is not discussed in the main body of the thesis, is included here.

C.1 Quasi-static Delamination Simulations

This section presents information that is common to all the simulations of quasi-static delamination. Any parameters that deviate from those described here are discussed in the relevant section.

C.1.1 Material Models

In all instances, the GFPP sections of the specimens were modelled using the anisotropic, linear elastic material model. The elasticity parameters are summarised in Table C.1. The assigned density was 1450 kg/m^3. The GFPP sections were assigned a local coordinate system, with the 1 direction corresponding to the warp fibres, the 2 direction to the weft fibres and the 3 direction to the through-thickness direction.

Table C.1: GFPP anisotropic model parameters

Parameter	E_{11}	E_{22}	E_{33}	ν_{12}	ν_{13}	ν_{23}	G_{12}	G_{13}	G_{23}
Value	11 GPa	11 GPa	2 GPa	0.11	0.11	0.11	1.7 GPa	1.7 GPa	1.7 GPa
Source	§4.6.2 and §5.1.3			Manufacturer's data sheet [19]					

The aluminium portions of any FML specimens were modelled as purely elastic, or elasto-plastic as was appropriate to the experiment being simulated. The constitutive parameters for the aluminium are summarised in Table C.2. The plasticity was described using the Johnson-Cook model, with strain hardening coefficients based on quasi-static tensile tests (§A.2.2).

Table C.2: Aluminium constitutive parameters

Parameter	E_y	ρ	ν	A	B	n	C	m	T_{melt}
Value	69 GPa	2750 kg/m^3	0.33	80 MPa	49 MPa	0.14	0	1	930 K

Any delamination was described using cohesive elements, with the bi-linear traction separation law. The cohesive zone parameters are detailed alongside any simulations presented in the main text.

C.1.2 Element Selection

All the quasi-static simulations were simplified to 2D, plane strain models. Hence the GFPP and aluminium sections (where appropriate) were meshed using the 4 noded, 2D plane strain elements with reduced integration (CPE4R). The delamination regions were meshed with 4 noded, 2D cohesive elements (COH2D4).

C.1.3 Boundary Conditions

All of the quasi-static experiments modelled were based on Three Point Bend geometry. The two outer supports were modelled as analytically rigid surfaces, which were encastred. The central loading roller was also an analytically rigid surface, which was constrained from moving laterally or rotationally, but was assigned a prescribed displacement appropriate to the experiment being simulated.

Contact surfaces were defined between the support rollers and specimen, and between the predefined crack faces. The contact interaction was modelled using the "Hard Contact" option for displacements normal to the surface, with a friction coefficient of 0.25 for tangential displacements.

Due to asymmetry imposed by the initial flaw, early simulations developed a numerical instability where the specimen would displace horizontally. This instability was corrected by connecting a corner of the specimen to ground, using a horizontal

spring of stiffness 200 N/m. This relatively small stiffness prevented instability in the horizontal degree of freedom, without affecting the vertical deflection of the specimen.

C.1.4 Overcoming instabilities in Cohesive Zone Models

The bi-linear traction separation constitutive model for cohesive zone modelling is known to be unstable [198]. The ABAQUS / Standard implicit solver struggles to converge due to these instabilities. In order to improve convergence, several solution control parameters for the solver need to be modified and viscous regularisation is also applied. The modified solution control parameters are detailed in Table C.3 and are based on parameters used in example problems in the ABAQUS manual [198] and cohesive element simulations presented by Turon [114]. A viscous regularisation parameter of 10^{-4} was used, which lies in the range recommended in the ABAQUS manual [198].

Table C.3: Modified solution control parameters for cohesive element problems in ABAQUS/Standard

Description	Abaqus Parameter	Default Value	Adjusted Value
Convergence criterion for the ratio of the largest residual to the corresponding average flux norm for convergence	R_n^α	5×10^{-3}	5×10^{-2}
Convergence criterion for the ratio of the largest solution correction to the largest corresponding incremental solution value	C_n^α	10^{-2}	1
Number of equilibrium iterations (without severe discontinuities) after which the check is made whether the residuals are increasing in two consecutive iterations	I_o	8	1500
Number of consecutive equilibrium iterations (without severe discontinutities) at which logarithmic rate of convergence check begins	I_R	10	1500
Upper limit on the number of consecutive equilibrium iterations (without severe discontinuities), based on prediction of the logarithmic rate of convergence	I_C	16	1500
Number of consecutive equilibrium iterations (without severe discontinuities) above which the size of the next increment will be reduced	I_L	10	1500
Maximum number of line search iterations	N^{ls}	0	4
Maximum scale correction factor	s_{max}^{ls}	1.0	4
Minimum scale correction factor	s_{min}^{ls}	10^{-4}	0.25
Ratio of new to old correction scale factors below which line searching terminates	η^{ls}	0.1	0.15

C.2 Virtual Crack Closure Technique Models for Fracture Mode Ratio Estimation

The fracture mode ratio of the FML debonding specimens was estimated by applying the Virtual Crack Closure Technique (VCCT) to FE simulation of the relevant experiments. These simulations were based on similar models to those described in §C.1, with the following important differences:

The initial crack tip was modelled as a seam, with the uncracked regions fully tied together. The mesh in the region of the crack tip was highly refined, as shown in Figure C.1. In order to capture the singularity at the crack tip, the elements immediately adjacent to the crack tip were modified according to the procedure described in the ABAQUS manual [198].

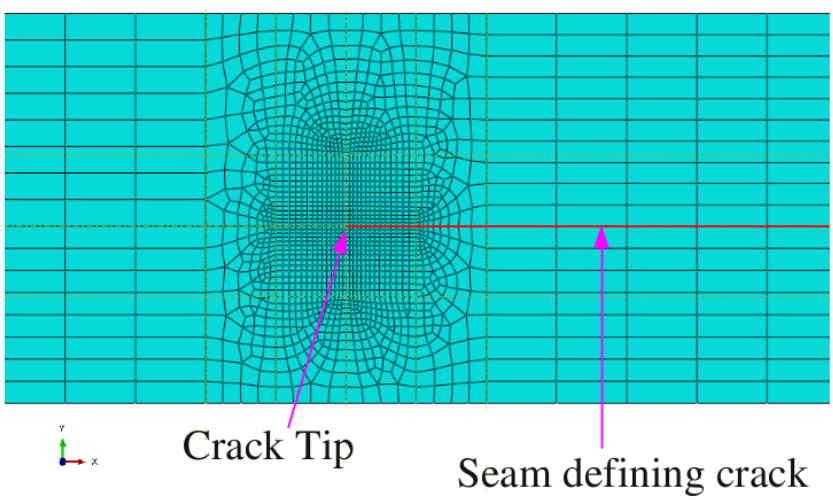

Figure C.1: Image of refined mesh at crack tip from simulation of End Notch Flexure experiment

Appendix D

Miscellaneous Scripts

D.1 Processing of Reflective Object Sensor

The voltage signals of the R.O.S. were post-processed to displacement-time using an algorithm suggested by Dr. M. Theobald, who was a Post-Doctoral Fellow at BISRU, and implemented in a script written by the author. The time domain of the signal was divided into intervals shorter than half the shortest expected wavelength. On each interval in turn, a quadratic polynomial was fitted to the voltage data. A quadratic was chosen as it has a single maxima or minima. If the time corresponding to the maxima or minima of the quadratic lay within the search interval, the time and whether the voltage was at a local maxima or minima was recorded. The time from a local maxima to the next local minima (or vice versa) of an individual sensor output corresponds to a displacement increment of half the pitch. The displacments corresponding to the initial peaks of the two sensors were offset by the measured sensor offset of 0.48 mm. The discrete displacement-time arrays of both sensors were concatenated and sorted according to time to give a single displacement history for the guide rod.

```
 % load data file for test
load 'Twtx_HPB_Bend_201102224_3.mat';

Channel1=data(:,1);
N=length(Channel1);
N2=nextpow2(N);
M=2^N2;
```

```
ROS_1=data(:,2);
ROS_2=data(:,3);

% shift strain gauge signal to bar tip
Time=dt.*[0:1:(M-1)]';

ImpBegin=input('Input time of impact (Seconds)?    ')
ImpEnd=ImpBegin+2.4e-3
Time_Imp=[ImpBegin:dt:ImpEnd]';

ROS_1_Imp=interp1(time,ROS_1,Time_Imp);
ROS_2_Imp=interp1(time,ROS_2,Time_Imp);

% Process ROS data
PksTrghs_ROS1=LocalMaxMin_2(Time(1:N),ROS_1,SearchSpan,PeakTol);
PksTrghs_ROS2=LocalMaxMin_2(Time(1:N),ROS_2,SearchSpan,PeakTol);

Disp_ROS_1=zeros(length(PksTrghs_ROS1),1);
Disp_ROS_2=zeros(length(PksTrghs_ROS2),1);


if PksTrghs_ROS1(1,1) < PksTrghs_ROS2(1,1)
    Disp_ROS_1(1)=0;
    Disp_ROS_2(1)=ROS_OffSet; %off set of sensors
else
   Disp_ROS_1(1)=ROS_OffSet;
    Disp_ROS_2(1)=0; %off set of sensors
end



for    p=2:length(PksTrghs_ROS1);
    Disp_ROS_1(p)=Disp_ROS_1(p-1)+ROS_Pitch/2;
end
clear p;

for    p=2:length(PksTrghs_ROS2);
```

```
    Disp_ROS_2(p)=Disp_ROS_2(p-1)+ROS_Pitch/2;
end
clear p;

Time_Disp_uns=vertcat([PksTrghs_ROS1(:,1) Disp_ROS_1], ...
  [PksTrghs_ROS2(:,1) Disp_ROS_2]);

Time_Disp=sortrows(Time_Disp_uns);

Time_Imp_2=Time_Disp(:,1).*(Time_Disp(:,1)>=ImpBegin) ...
  .*(Time_Disp(:,1)<=(ImpBegin+2.4e-3));
Disp_Imp_2=Time_Disp(:,2).*(Time_Disp(:,1)>=ImpBegin) ...
  .*(Time_Disp(:,1)<=(ImpBegin+2.4e-3));

Time_Imp_3=Time_Imp_2(Time_Imp_2>0);
Disp_Imp_3=Disp_Imp_2(Time_Imp_2>0);


function y=LocalMaxMin_2(X,Y,N,Tol)

i=1;
j=1;
P(1,1)=0;
P(1,2)=0;

while i+N <= length(X);
   Y_s=smooth(Y(i:i+N),32,'moving');
   QuadCoeff=polyfit(X(i:i+N),Y_s,2);
   X_LocalMaxMin=-QuadCoeff(2)/(2*QuadCoeff(1));
   i;
   j;

   if (j==1)
       disp('Finding first peak or trough')
       if (X_LocalMaxMin > X(i)) && (X_LocalMaxMin < X(i+N));
            P(j,1)=X_LocalMaxMin;
            P(j,2)=polyval(QuadCoeff,X_LocalMaxMin);
```

```
            j=j+1;
            i=i+N-128; % 20 is to overlap search intervals;
        else
            i=i+64;
        end

    elseif (abs(X_LocalMaxMin-P(j-1,1)) <= Tol)
        i=i+fix(N)/4
    elseif (X_LocalMaxMin > X(i)) && (X_LocalMaxMin < X(i+N));
        P(j,1)=X_LocalMaxMin;
        P(j,2)=polyval(QuadCoeff,X_LocalMaxMin);
        j=j+1;
        i=i+N-128; % 20 is to overlap search intervals

    else
        i=i+128; % short step forward in interval

    end

end

y=P;
```

D.2 Script for Measuring Crack Position

The script for extracting crack tip (or any other selected position) from digital photographs is presented here.

```
 % convert points in pixel image to x- y in mm
clc;
clear all;

ImgNum=824
N=42;
TimeNum=zeros(N,1);

[CalibFile,pathname,filterindex]=uigetfile( ...
  {'*.jpg;*.tif;*.png;*.gif','All Image Files';...
          '*.*','All Files' });
CalibImage=imread(CalibFile,'JPEG');
figure;
   image(CalibImage);
   pause;
   format short
disp('First corner...')
[x_a1 y_a1]=ginput(1)
disp('Second corner...')
[x_a2 y_a2]=ginput(1)
disp('Third corner ...')
[x_a3 y_a3]=ginput(1)
disp('First point on upper surface of specimen...')
[x_s1 y_s1]=ginput(1)
disp('Second point on upper surface of specimen...')
[x_s2 y_s2]=ginput(1)

a=0.5*(x_a1+x_a2)

b=-0.5*(y_s1+y_s2)

Orig=[a b]
```

```
% point 1 in x,y mm
x1=-10
y1=7

% pont 2 in x,y mm
x2=10
y2=7

%point 3
x3=10
y3=34

%point 1 in pixels
p1=x_a1
q1=-y_a1

% point 2 in pixels
p2=x_a2
q2=-y_a2

%point 3
p3=x_a3
q3=-y_a3

i1=p1-a
j1=q1-b

i2=p2-a
j2=q2-b

i3=p3-a
j3=q3-b

a_12=(x2-x1*i2/i1)/(j2-j1*i2/i1);

a_11=(x1-a_12*j1)/i1;
```

```
a_22=(y2-y1*i2/i1)/(j2-i2*j1/i1);

a_21=(y1-a_22*j1)/i1;


a_13=(x3-x1*i3/i1)/(j3-j1*i3/i1);

a_11_3=(x1-a_13*j1)/i1;

a_33=(y3-y1*i3/i1)/(j3-i3*j1/i1);

a_31=(y1-a_33*j1)/i1;


A12=[a_11 a_12;a_21 a_22]

A13=[a_11_3 a_13;a_31 a_33]

A=0.5.*(A12+A13)

Crack_Pix_Click=zeros(N,2);

for i=1:N
   FileName=['dscf0',num2str(ImgNum+i-1),'.jpg'];
   B=imread(FileName,'JPEG');
   figure;
   image(B);
   pause;
   [x_C y_C]=ginput(1)
   100*i/N
   Crack_Pix_Click(i,1)=x_C;
   Crack_Pix_Click(i,2)=-y_C;

end
clear i
```

```
Crack_Pix_Cent=Crack_Pix_Click-repmat(Orig,length(Crack_Pix_Click),1);

Crack_xy=Crack_Pix_Cent*A'

for i=1:N
   FileName=['dscf0',num2str(ImgNum+i-1),'.jpg'];
   %B=imread(FileName,'JPEG');
   ImgInfo=imfinfo(FileName,'JPEG');
   DateTime=ImgInfo.FileModDate;
   TimeNum(i)=datenum(DateTime);
end
clear i

ImgTime=24*60*60.*( TimeNum-TimeNum(1).*ones(size(TimeNum)));

CrackTime=ImgTime;
CrackPos=Crack_xy;
CrackLen=40*ones(length(Crack_xy),1)-Crack_xy(:,1);

figure;
    hold on;
    grid on;
    box on;
    set(gca,'FontName','FreeSerif','Fontsize',30);
    set(gca,'LineWidth',2,'GridLineStyle','--');
    plot(CrackTime,CrackLen,'+b')
    xlabel('Time(s)');
    ylabel('Crack length (mm)');

[filename,pathname] = uiputfile('*.mat','Save your Captured Data ');
save(filename,'CrackTime','CrackPos','CrackLen')
```

Appendix E

HPB Impact Bend Apparatus Drawings

E.1 Iteration of impacter design

The initial design for the impacter had a non-adjustable span of 50 mm, and a guide length of 150 mm. The specimen was held on 10mm diameter steel cylinders, using elastic bands looped over the cylinder ends, which is shown in Figure 5.9. The elastic bands provided restraint such that the specimen did not move during the acceleration phase, but did not constrain the specimen during the impact phase. The guide rod of the impacter was fitted with a key along its entire length. The key fitted in a keyway in the supporting brass bush, which prevented rotational motion. After initial tests, several negative aspects of this design were noted:

- The throat of the impacter only allowed a maximum specimen deflection of 13 mm. This was considered sufficient during the initial design process as the interesting features of the quasi-static tests, be it plasticity, fracture or delamination, had occurred before a deflection of 10 mm. However, during the impact tests, the impacter and specimen will continue moving until all the kinetic energy has been dissipated. This resulted in secondary impacts between the specimen and the cross member, which caused undesired damage to the specimen.

- The impacter has to be accelerated to the desired velocity, separated from the pusher bar and deflect the specimen the desired amount in less than the total guide length. The original length of 150 mm was insufficient to reach the desired velocity range of 5 to 10 m/s.

- The axial motion of the impacter was restricted at certain points in the stroke, indicating binding surfaces. This was traced to the key.

The specimen supports were increased in height, permitting specimen deflections of 24 mm. To permit higher impact velocities, the axial guide rod length was increased to 300 mm. During assembly of the revised design, the impacter sagged noticeably when at its extreme range of motion. This was due to the increased mass of the adjustable cross member, and the single support bush providing insufficient constraint. The support was modified to use two bushes, separated axially by 50 mm, which rectified the sag. The single long key was dispensed with, and rotational constraint was provided by screws with ends profiled to match the keyway in the guide. This alleviated the prior problems of binding, without sacrificing any rotational constraint.

E.2 Engineering Drawings

The engineering drawings for manufacture of the HPB Impact Bend apparatus are included hereafter.

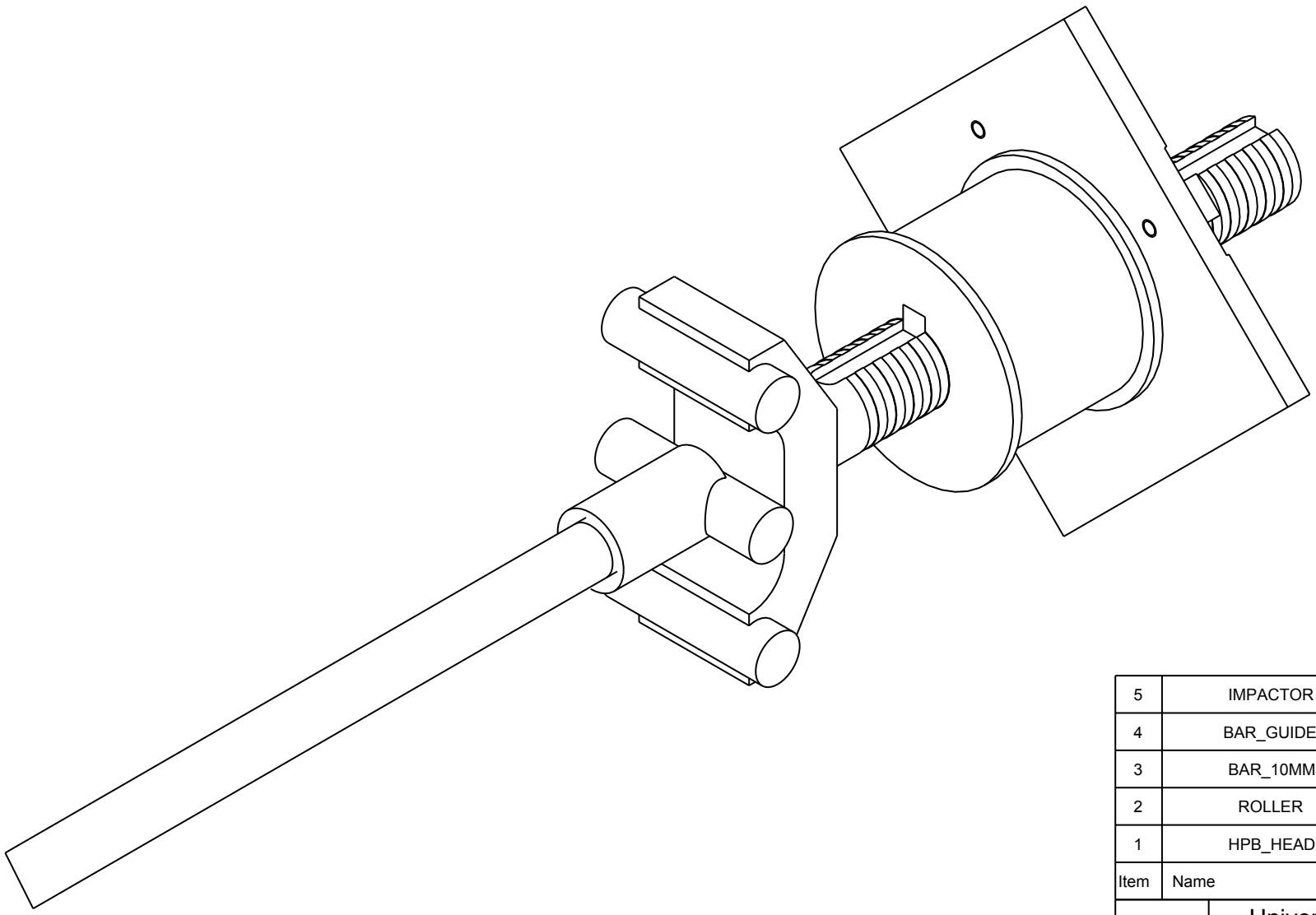

Item	Name	Qty	Material
5	IMPACTOR	1	
4	BAR_GUIDE	4	
3	BAR_10MM	1	STEEL_LC
2	ROLLER	1	SILVER_STEEL
1	HPB_HEAD	1	ALUM_6061

University of Cape Town
Department of Mechanical Engineering

Title
Double Impactor for HPB

Dimensions in mm Tolerance U.O.S.	Scale	Date	Sheet	of
0.1	0,010	15-Aug-05	xx	xx
	Drawn By: Reuben Govender		Drawing Number: xx	

SCALE 1,000

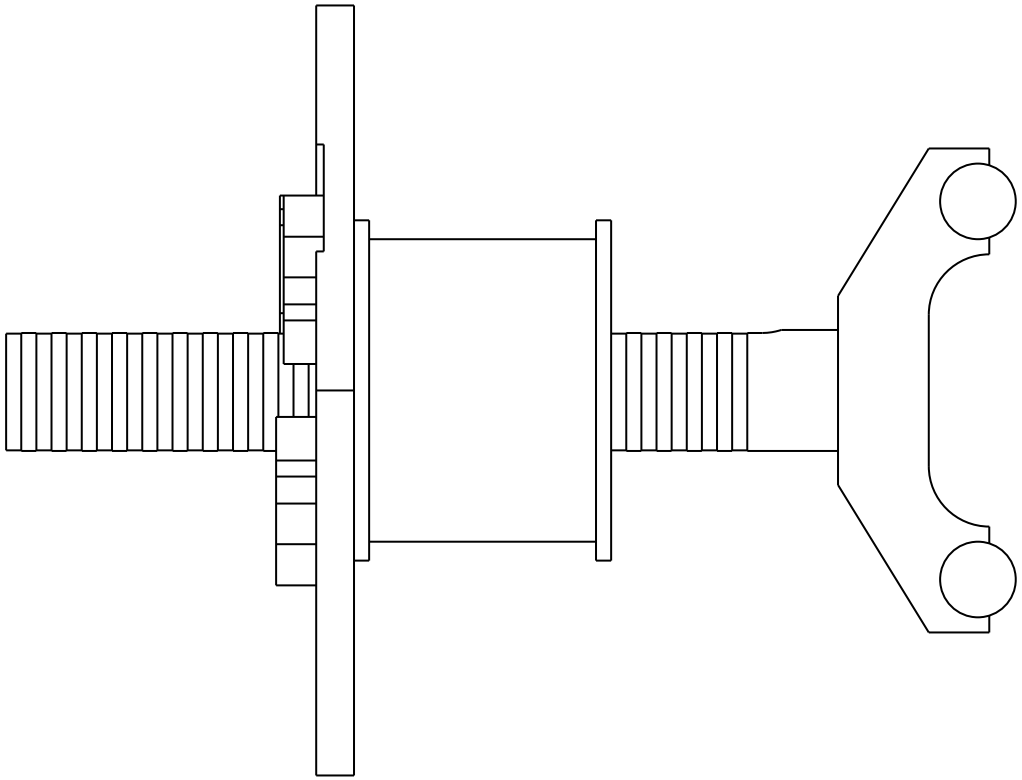

SCALE 1,000

Item	Name	Qty	Material
5	IMPACTOR	1	
4	BAR_GUIDE	4	
3	BAR_10MM	1	STEEL_LC
2	ROLLER	1	SILVER_STEEL
1	HPB_HEAD	1	ALUM_6061

University of Cape Town
Department of Mechanical Engineering

Title
Impactor and guide

Dimensions in mm Tolerance U.O.S.	Scale	Date	Sheet	of
	0,010	01-Apr-10	xx	xx
	Drawn By		Drawing Number	
0.1	Reuben Govender		xx	

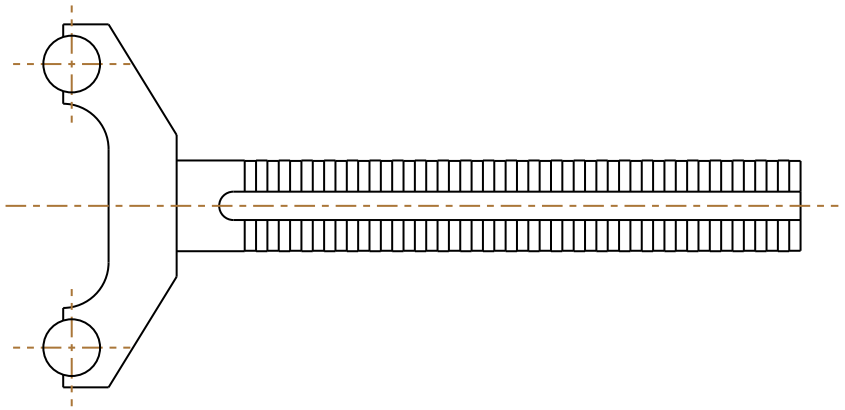

SCALE 0,750

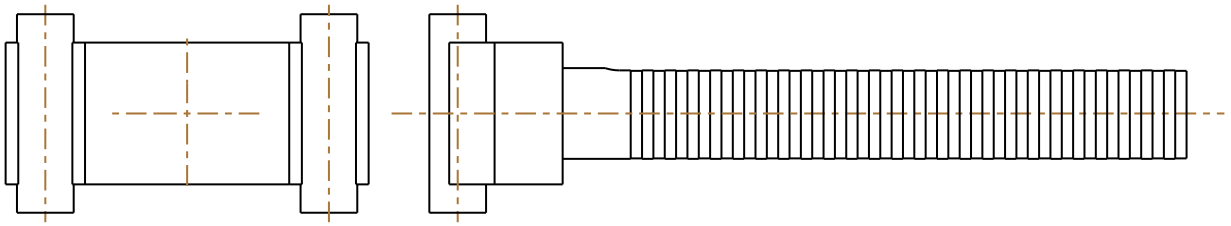

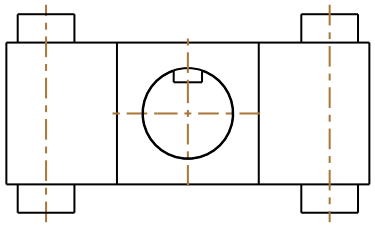

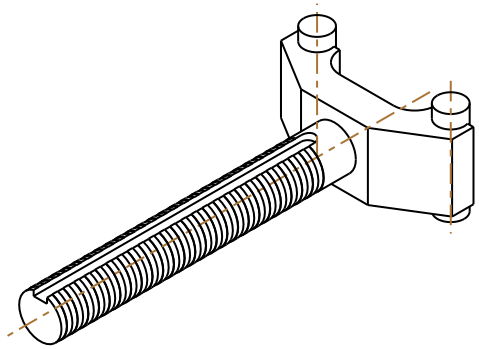

Item	Name	Qty	Material
6	SENSOR_ASSEM	1	
5	KEY	1	STEEL_LC
4	IMPACTOR_HEAD	1	STEEL_LC
3	IMPACTOR_GUIDE_ROD	1	STEEL_LC
2	ROLLER	2	SILVER_STEEL
1	IMPACTOR_GUIDE_BUSH	1	BRASS

University of Cape Town
Department of Mechanical Engineering

Title
IMPACTOR

Dimensions in mm Tolerance U.O.S.	Scale	Date	Sheet	of
	0,333	07-Apr-10	xx	xx
	Drawn By		Drawing Number	
0.1	Reuben Govender		xx	

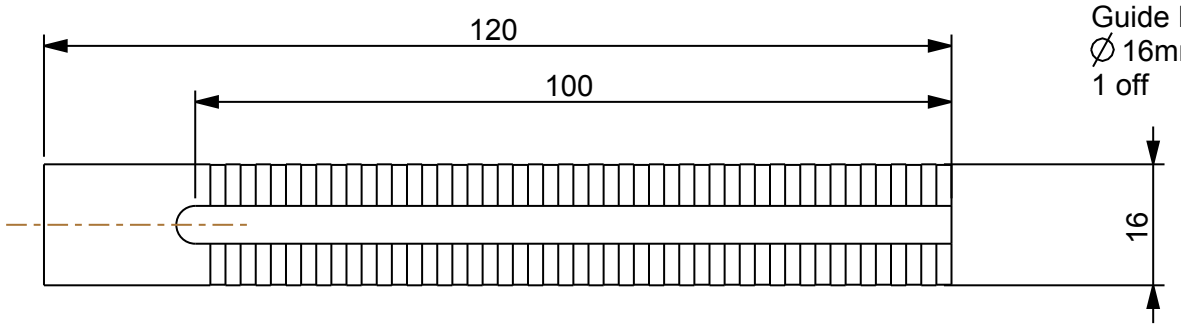

Guide Rod
∅ 16mm centerless ground silver steel
1 off

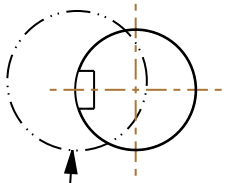

SEE DETAIL A

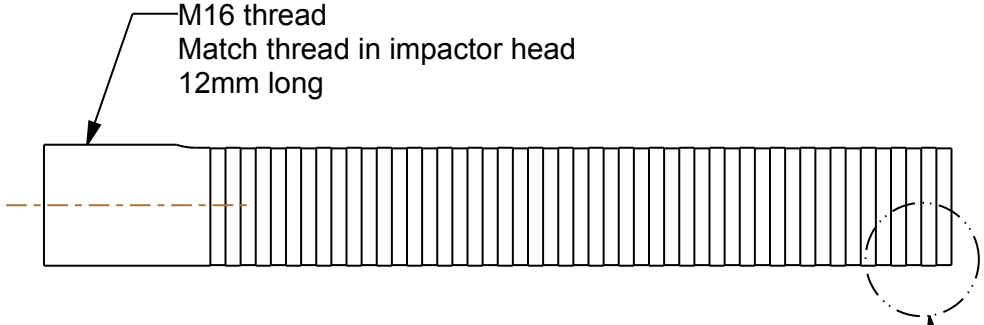

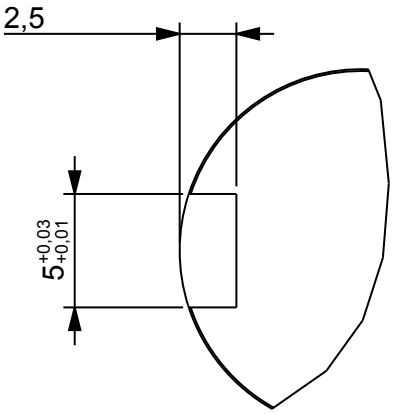

DETAIL A
SCALE 3,000

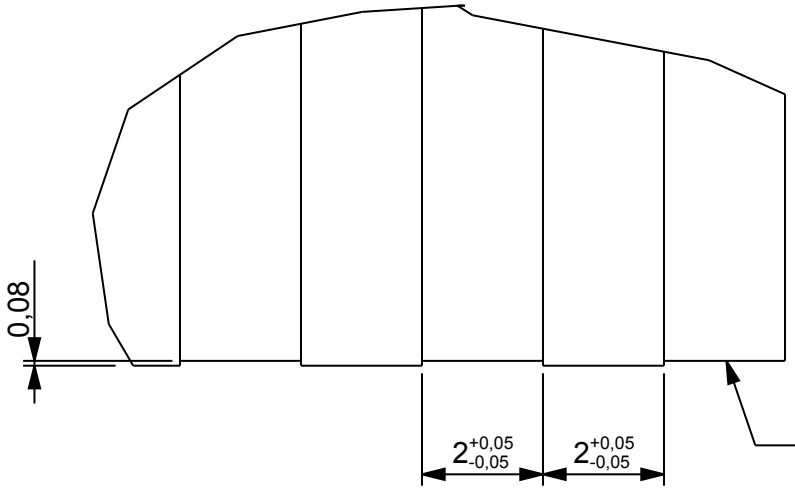

DETAIL B
SCALE 8,000

Cut 2mm wide groove
Approx. 0.08~0.10mm deep
Pitch distance 4mm

Item	Name	Qty	Material
3	IMPACTOR_HEAD	1	STEEL_LC
2	IMPACTOR_GUIDE_ROD	1	STEEL_LC
1	ROLLER	2	SILVER_STEEL

University of Cape Town
Department of Mechanical Engineering

Title: Guide Rod

Dimensions in mm Tolerance U.O.S.	Scale	Date	Sheet	of
0.1	0,500	07-Apr-10	xx	xx
	Drawn By: Reuben Govender		Drawing Number: xx	

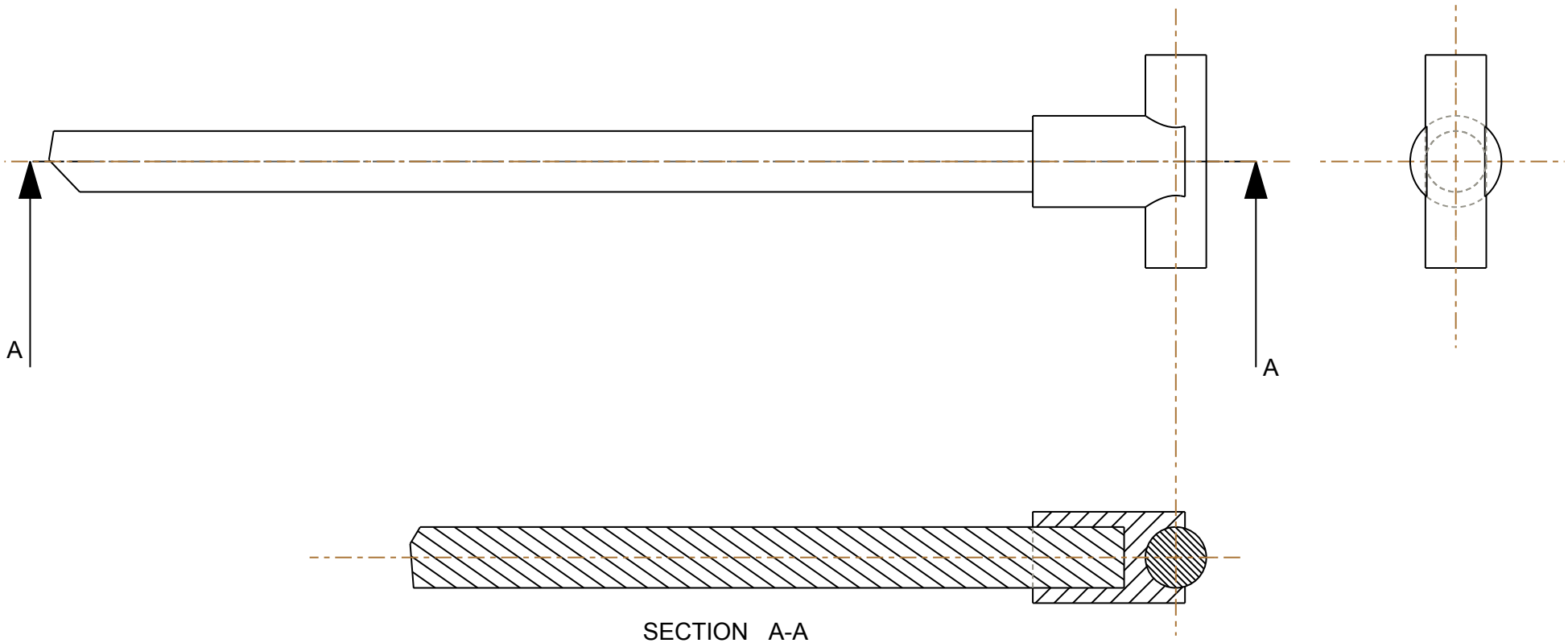

SECTION A-A

SCALE 1,000

HPB With Head

Item	Name	Qty	Material
	University of Cape Town Department of Mechanical Engineering		
	Title HPB with roller head		
Dimensions in mm Tolerance U.O.S. 0.1	Scale 1,000	Date 13-Apr-10	Sheet xx of xx
	Drawn By Reuben Govender		Drawing Number xx

SCALE 1,000

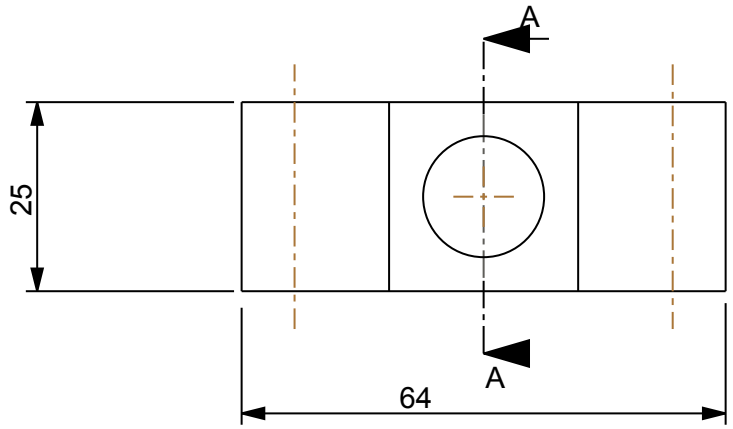

Internal M16 thread
Match thread to guide rod

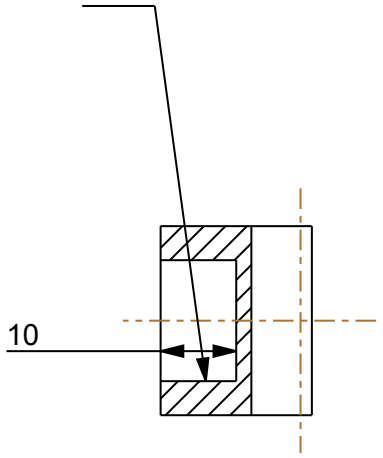

SECTION A-A

Press fit with
∅ 10mm silver steel roller

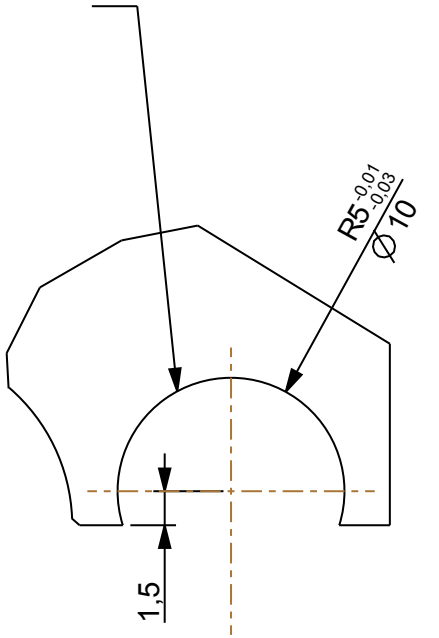

DETAIL C
SCALE 3,000

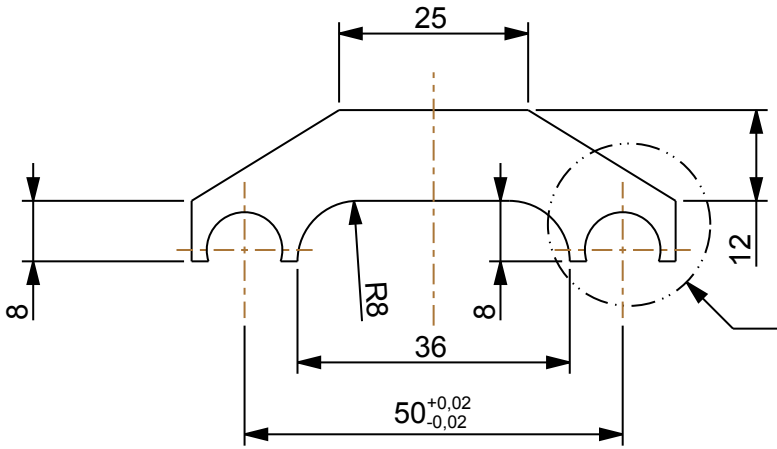

SEE DETAIL C

Impactor Head
Mild Steel
1 off

Item	Name	Qty	Material

University of Cape Town
Department of Mechanical Engineering

Title: Impactor Head

Dimensions in mm Tolerance U.O.S.	Scale	Date	Sheet	of
0.1	1,000	07-Apr-10	xx	xx
	Drawn By: Reuben Govender		Drawing Number: xx	

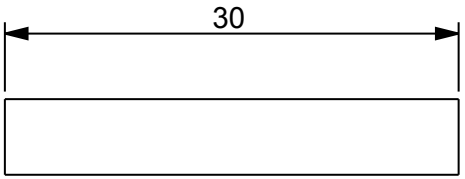

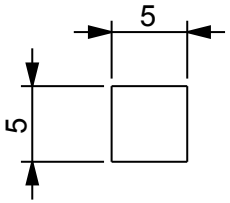

Key

5mm Key steel

2 off

SCALE 2,000

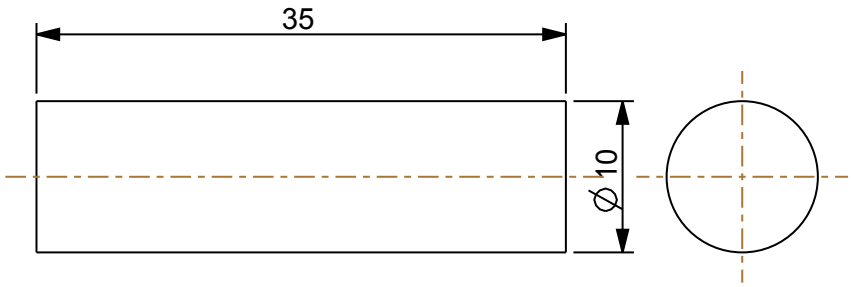

Roller

∅ 10mm centerless ground silver steel

4 off

SCALE 2,000

Item	Name	Qty	Material
	University of Cape Town Department of Mechanical Engineering		
	Title: Miscellaneous		
Dimensions in mm Tolerance U.O.S. 0.1	Scale: 1,000	Date: 08-Apr-10	Sheet: xx of xx
	Drawn By: Reuben Govender		Drawing Number: xx

HPB HEAD

Alum 6061 or 6082

2 Off

SCALE 2,000

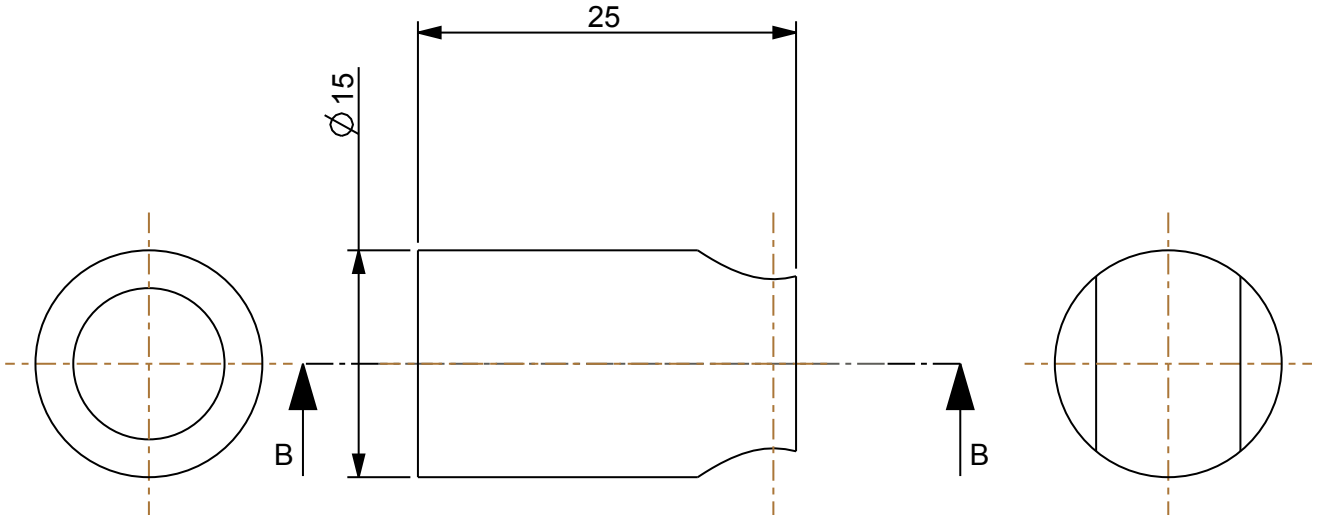

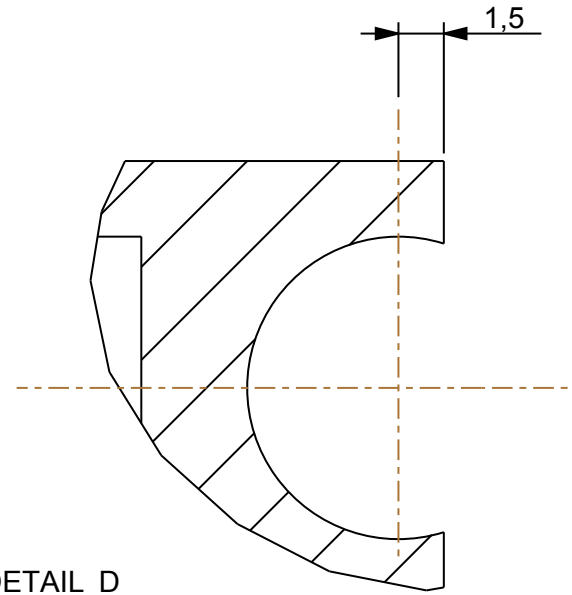

DETAIL D
SCALE 4,000

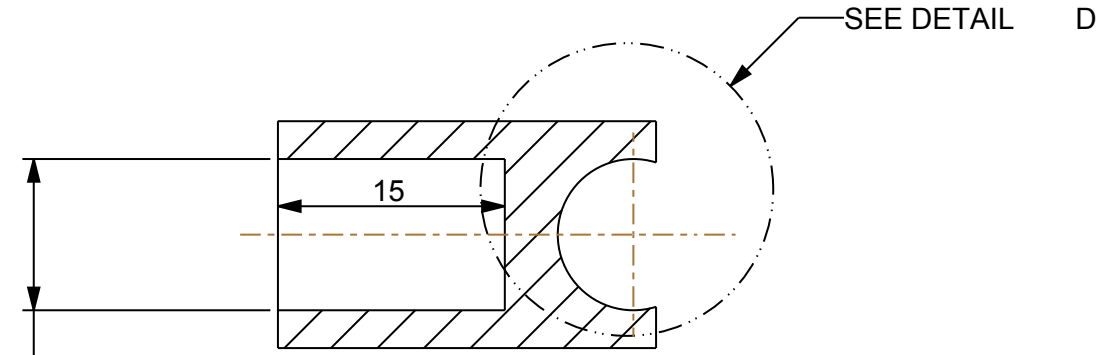

SECTION B-B

Item	Name	Qty	Material

University of Cape Town
Department of Mechanical Engineering

Title: HPB Head

Dimensions in mm Tolerance U.O.S.	Scale	Date	Sheet	of
0.1	1,000	08-Apr-10	xx	xx

Drawn By	Drawing Number
Reuben Govender	xx

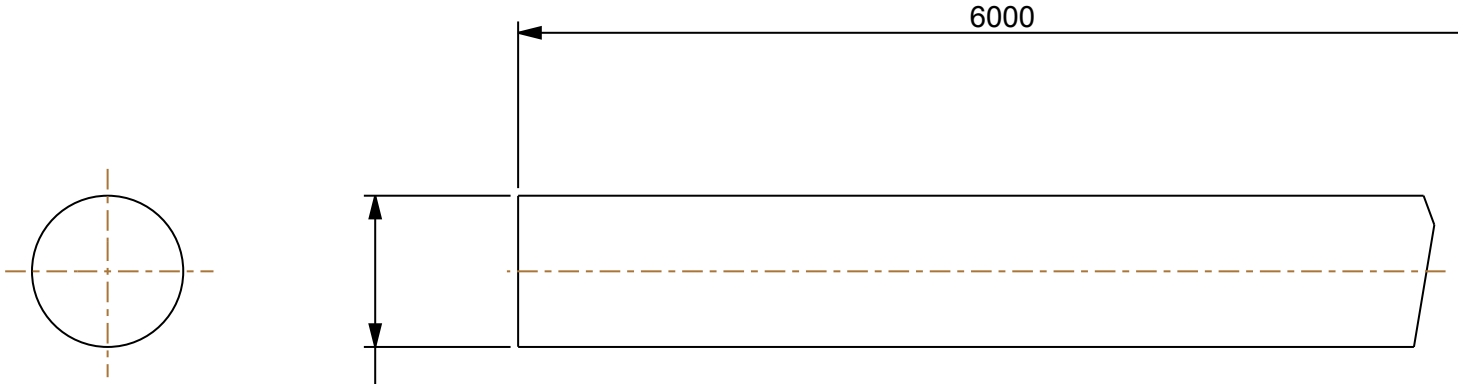

SCALE 2,000

M10Ext. thread
At least 15mm long
Match to threaded hole
on HPB Head

Hopkinson Bar
∅ 10mm x 6000mm length
Alum 6061 or 6082
1 off
Pls face off non-threaded end

Item	Name	Qty	Material

University of Cape Town
Department of Mechanical Engineering

Title: Hopkinson Bar

Dimensions in mm Tolerance U.O.S.	Scale	Date	Sheet	of
0.1	1,000	08-Apr-10	xx	xx
	Drawn By: Reuben Govender		Drawing Number: xx	

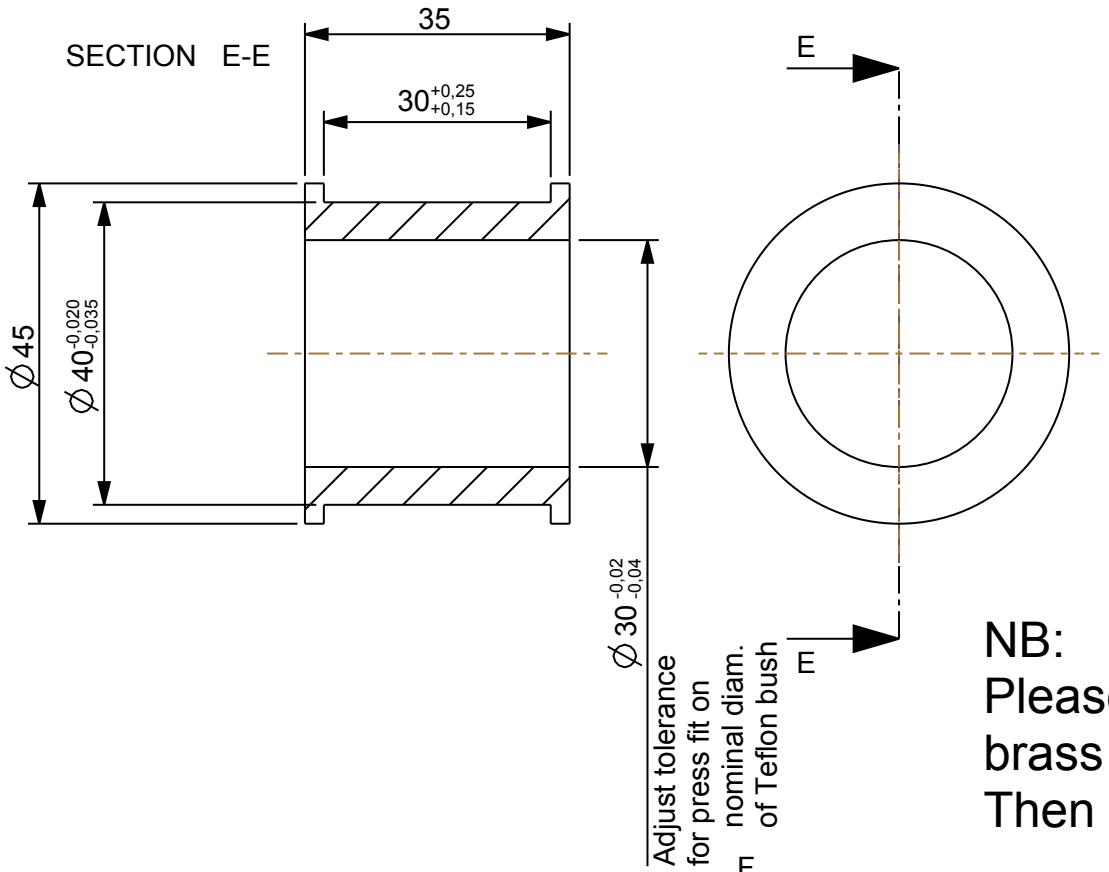

Bar Guide
Brass or similar
5 off

NB:
Please press Teflon sleeve into brass guide first.
Then bore ∅ 10mm hole

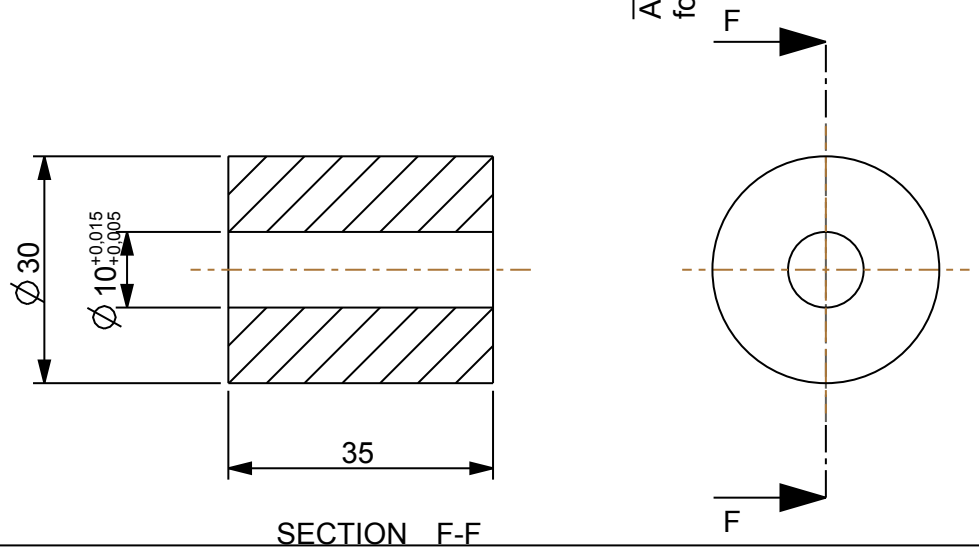

Sleeve
Teflon
5 off

Item	Name	Qty	Material

University of Cape Town
Department of Mechanical Engineering

Title: Bar Guides

Dimensions in mm Tolerance U.O.S.	Scale	Date	Sheet	of
	0,014	08-Apr-10	xx	xx
	Drawn By		Drawing Number	
0.1	Reuben Govender		xx	

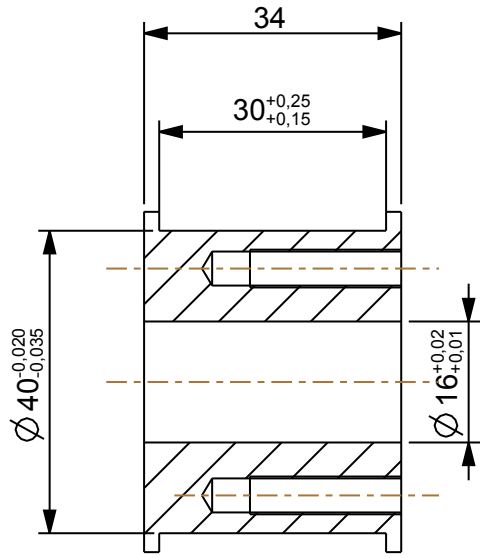

SECTION G-G

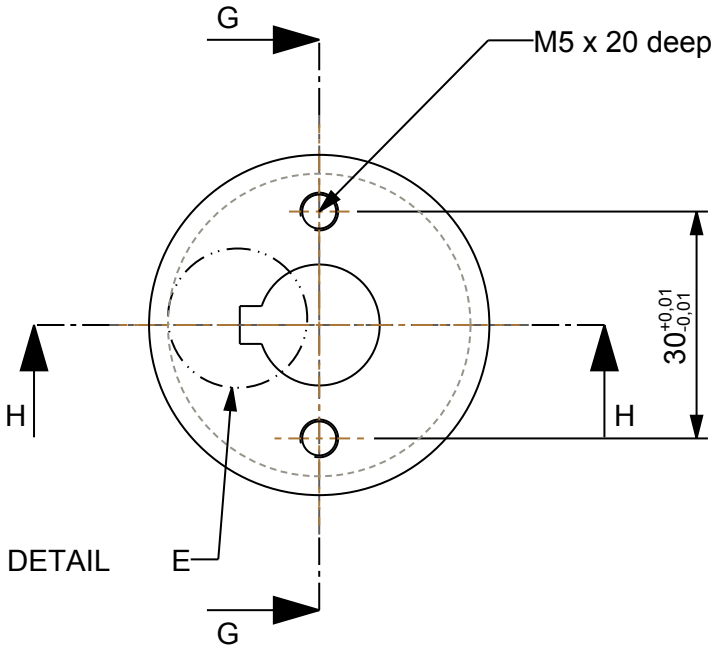

SEE DETAIL E

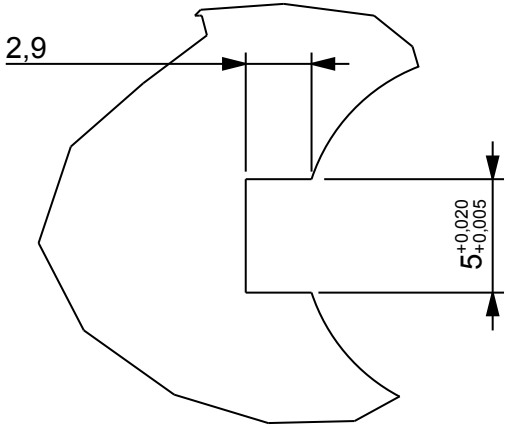

DETAIL E
SCALE 3,000

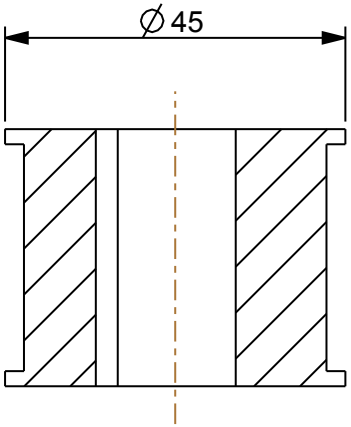

SECTION H-H

Impact Guide Bush

Brass or similar

1 off

Item	Name	Qty	Material

University of Cape Town
Department of Mechanical Engineering

Title: Impact Guide Bush

Dimensions in mm Tolerance U.O.S.	Scale	Date	Sheet	of
	1,000	08-Apr-10	xx	xx
	Drawn By		Drawing Number	
0.1	Reuben Govender		xx	

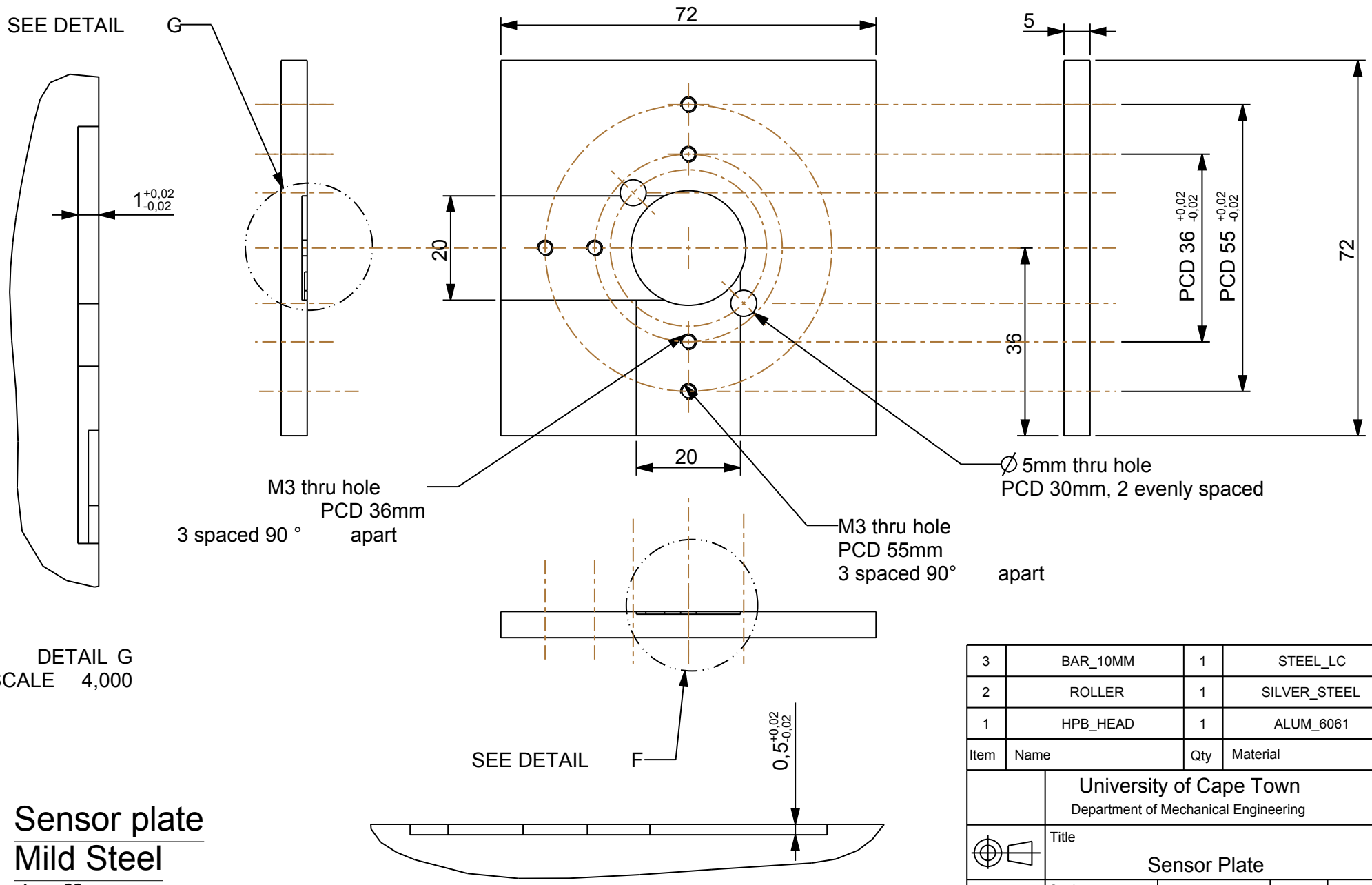

DETAIL G
SCALE 4,000

DETAIL F
SCALE 4,000

Sensor plate
Mild Steel
1 off

Item	Name	Qty	Material
3	BAR_10MM	1	STEEL_LC
2	ROLLER	1	SILVER_STEEL
1	HPB_HEAD	1	ALUM_6061

University of Cape Town
Department of Mechanical Engineering

Title: Sensor Plate

Dimensions in mm Tolerance U.O.S.	Scale	Date	Sheet	of
0.1	0,011	13-Apr-10	xx	xx

Drawn By	Drawing Number
Reuben Govender	xx

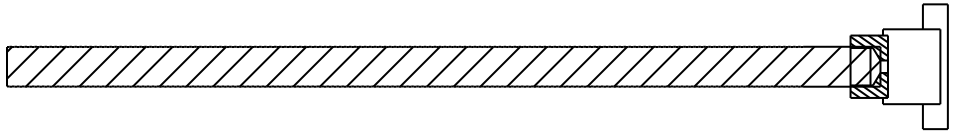

SECTION A-A

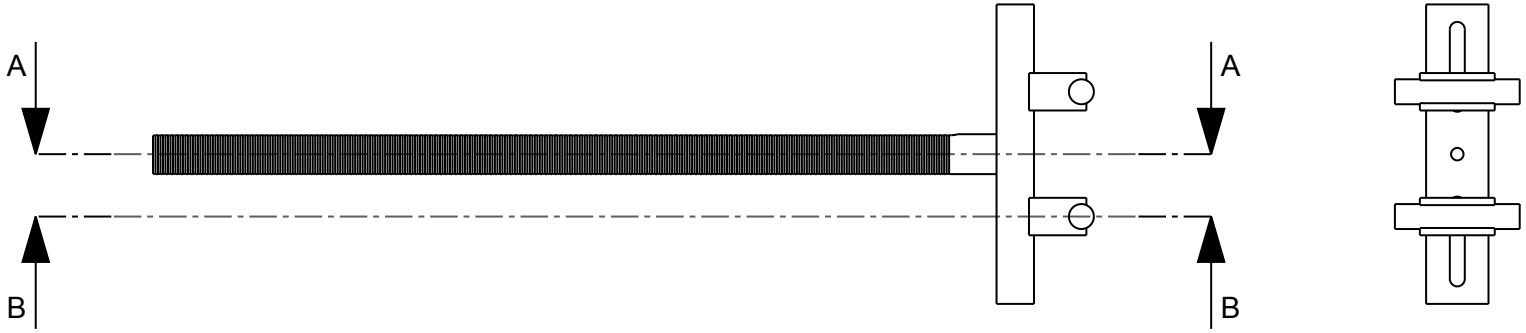

SCALE 0,330

SECTION B-B

Item	Name	Qty	Material
4	SLOTTED_CROSSHEAD	1	STEEL_LC
3	ROLLER_HOLDER	2	STEEL_LC
2	ROLLER_D10_L50	2	STEEL_LC
1	IMPACTOR_GUIDE_ROD_200	1	STEEL_LC

University of Cape Town
Department of Mechanical Engineering

Title
Adjustable impactor

Dimensions in mm Tolerance U.O.S.	Scale	Date	Sheet	of
	0,143	21-Jun-10	xx	xx
	Drawn By		Drawing Number	
0.1	Reuben Govender		xx	

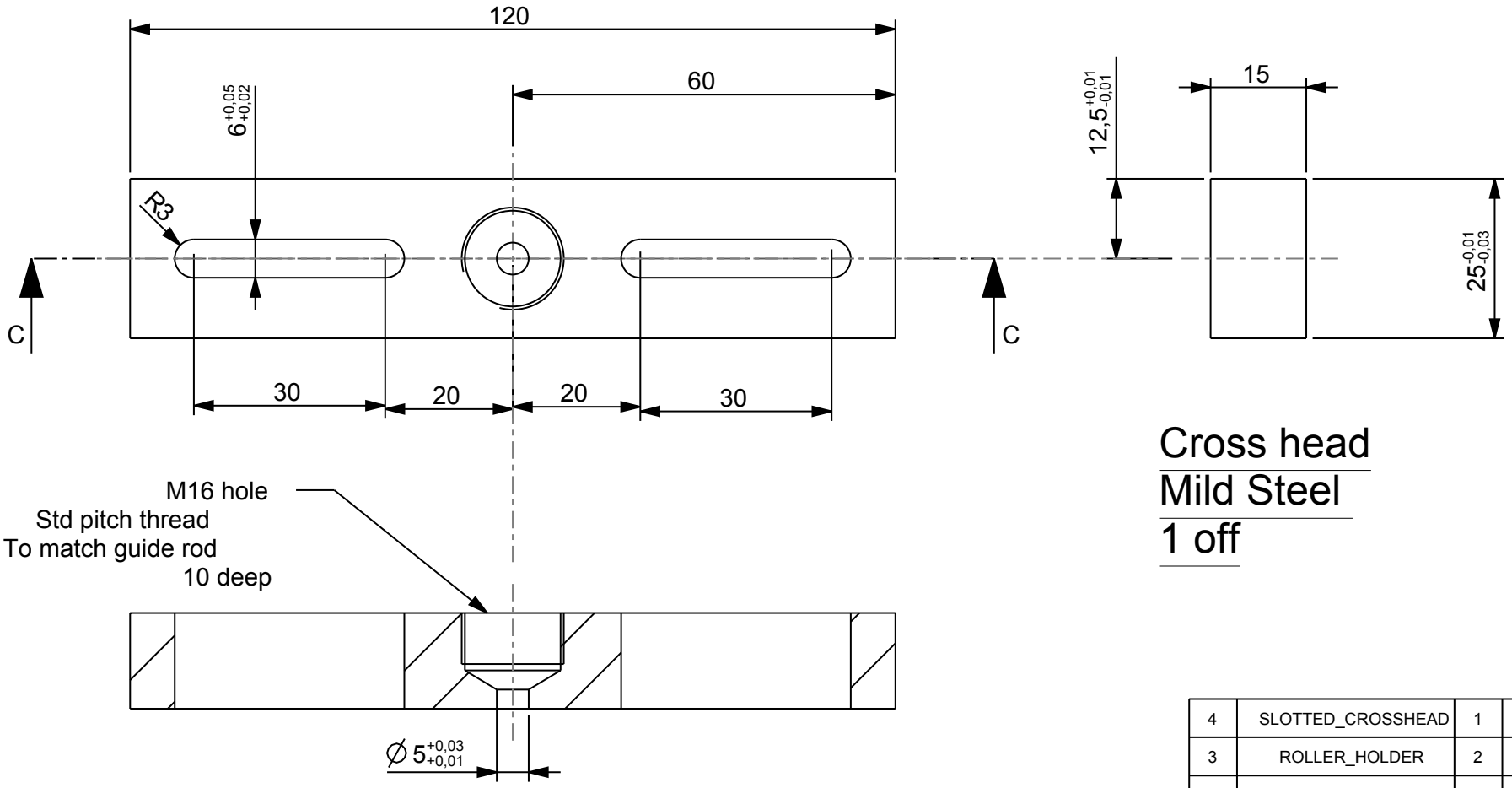

Cross head
Mild Steel
1 off

SCALE 1,000

SECTION C-C

Item	Name	Qty	Material
4	SLOTTED_CROSSHEAD	1	STEEL_LC
3	ROLLER_HOLDER	2	STEEL_LC
2	ROLLER_D10_L50	2	STEEL_LC
1	IMPACTOR_GUIDE_ROD_200	1	STEEL_LC

University of Cape Town
Department of Mechanical Engineering

Title: Cross head

Dimensions in mm Tolerance U.O.S.	Scale	Date	Sheet	of
0.1	0,143	21-Jun-10	xx	xx
	Drawn By: Reuben Govender		Drawing Number: xx	

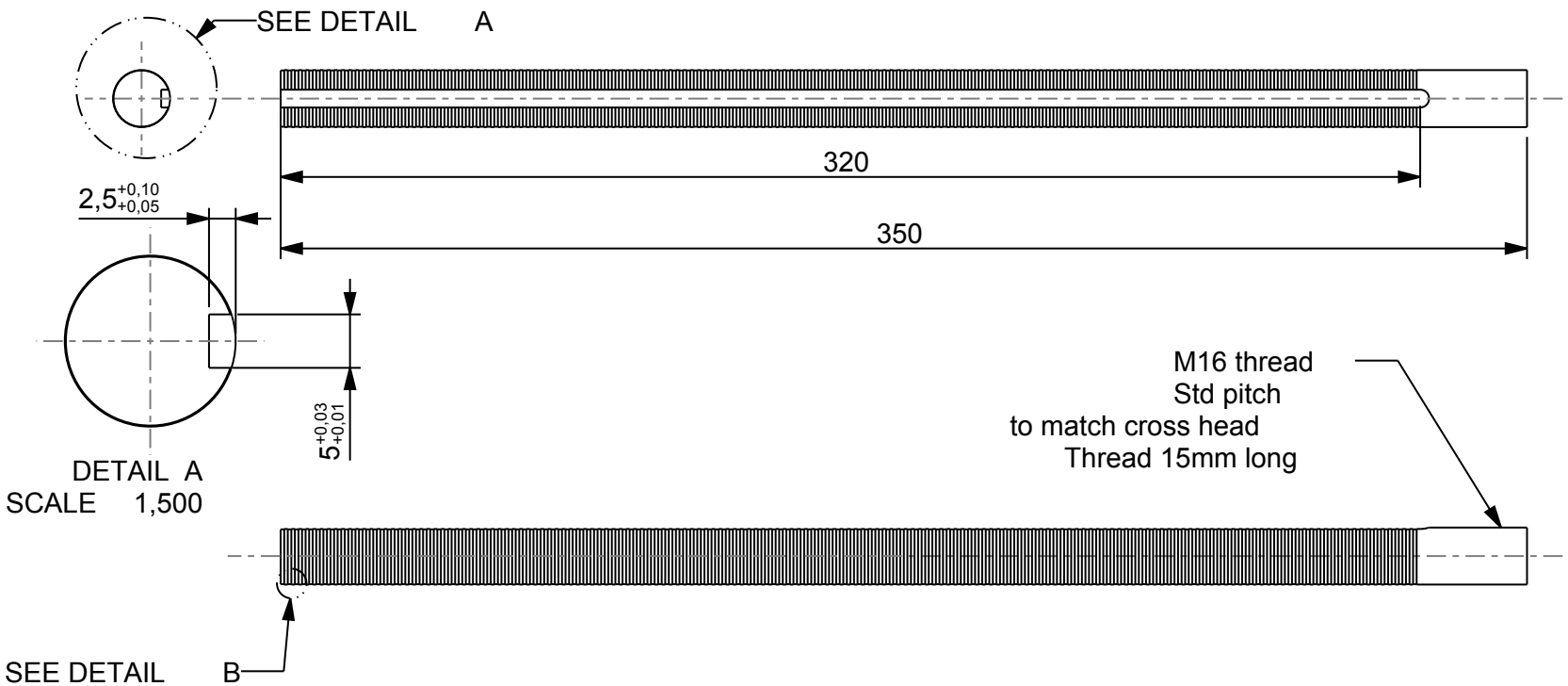

DETAIL A
SCALE 1,500

SCALE 0,500

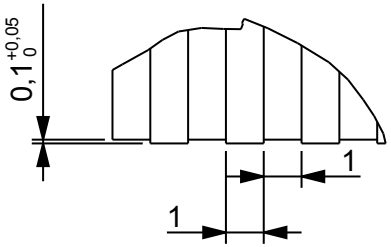

DETAIL B
SCALE 5,000

Guide Rod

Cut from 16mm centerless ground silver steel

1 off

Item	Name	Qty	Material

University of Cape Town
Department of Mechanical Engineering

Title: Guide Rod

Dimensions in mm Tolerance U.O.S.	Scale	Date	Sheet	of
0.1	0,500	21-Jun-10	xx	xx
	Drawn By: Reuben Govender		Drawing Number: xx	

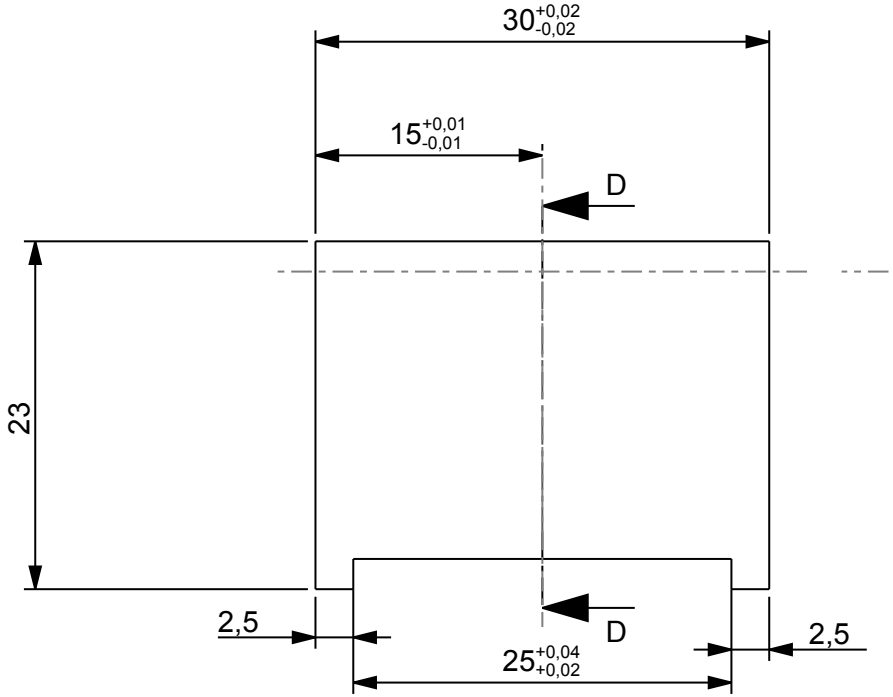

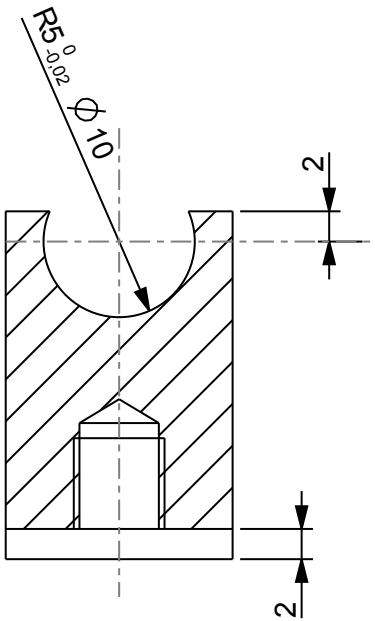

SECTION D-D

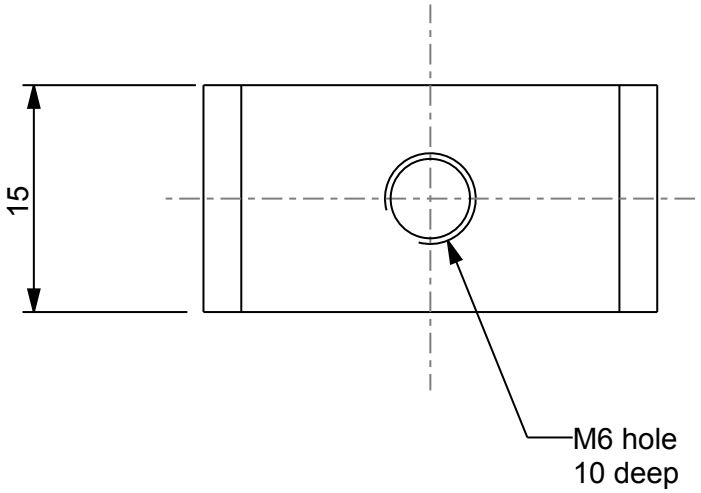

SCALE 2,000

Roller holder
Mild Steel
2 Off

Item	Name	Qty	Material

University of Cape Town
Department of Mechanical Engineering

Title: Roller holder

Dimensions in mm Tolerance U.O.S.	Scale	Date	Sheet	of
0.1	0,200	21-Jun-10	xx	xx
	Drawn By: Reuben Govender		Drawing Number: xx	

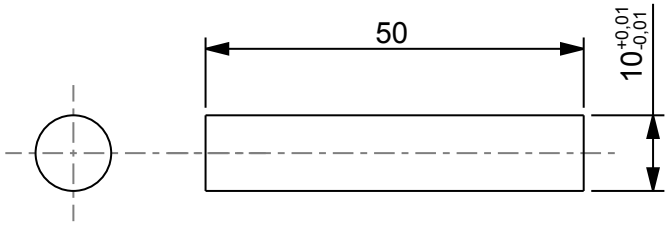

Roller
10mm Centerless ground silver steel
2 off

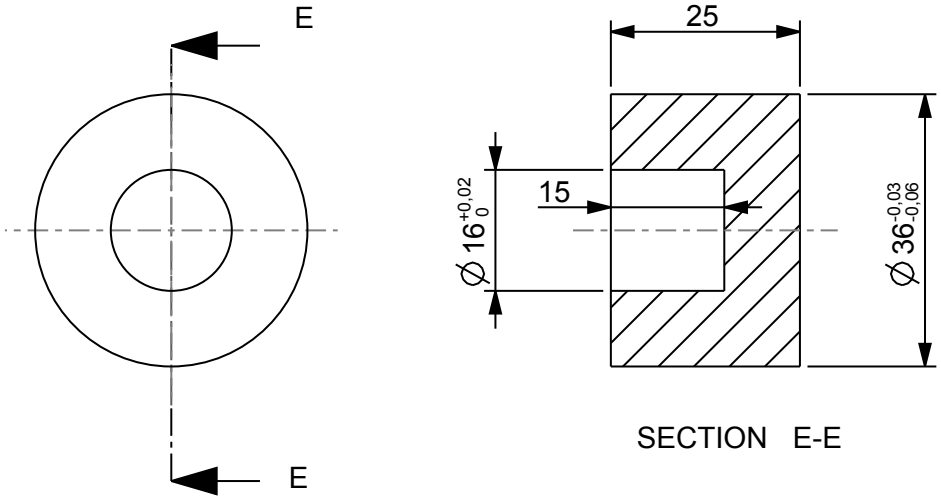

SECTION E-E

Back centering ring
Teflon
1 off

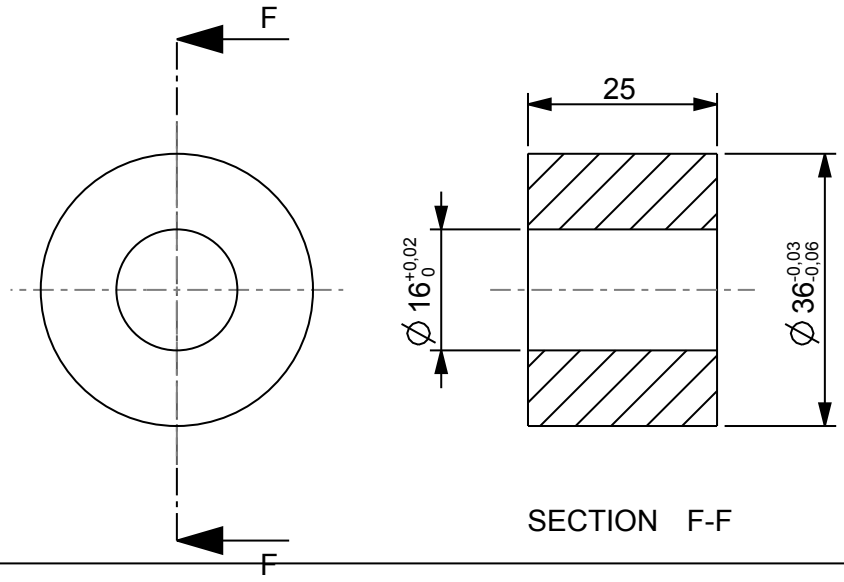

SECTION F-F

Mid Centering Ring
Teflon
2 off

Item	Name	Qty	Material

University of Cape Town
Department of Mechanical Engineering

Title: Rollers and rings

Dimensions in mm Tolerance U.O.S.	Scale	Date	Sheet	of
	1,000	21-Jun-10	xx	xx
	Drawn By		Drawing Number	
0.1	Reuben Govender		xx	

SCALE 1,500

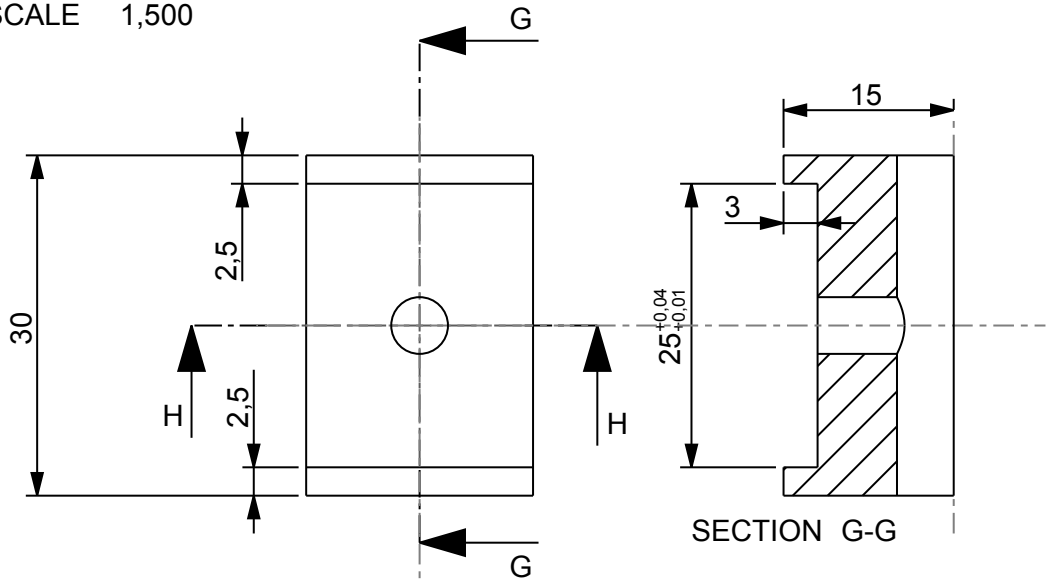

SECTION G-G

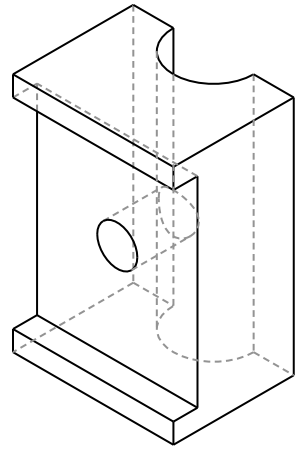

SCALE 1,500

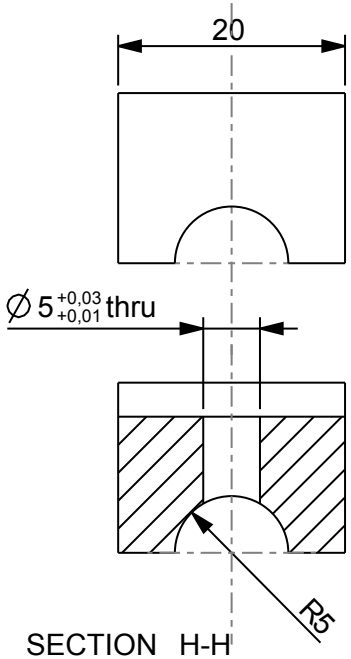

SECTION H-H

Centering Jig
Mild Steel
1 off

Item	Name	Qty	Material

University of Cape Town
Department of Mechanical Engineering

Title: Centering jig

Dimensions in mm Tolerance U.O.S.	Scale	Date	Sheet	of
0.1	1,000	21-Jun-10	xx	xx
	Drawn By: Reuben Govender		Drawing Number: xx	

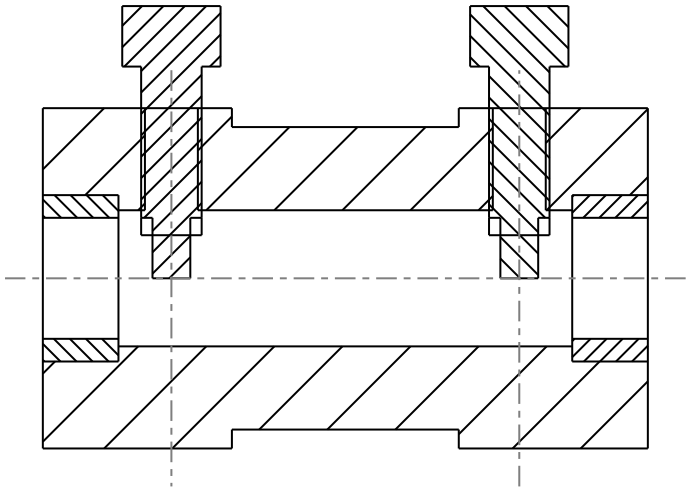

SECTION A-A

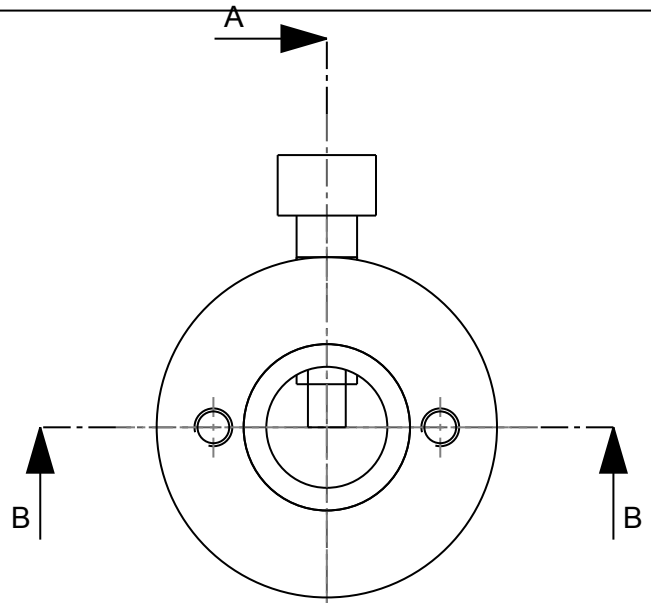

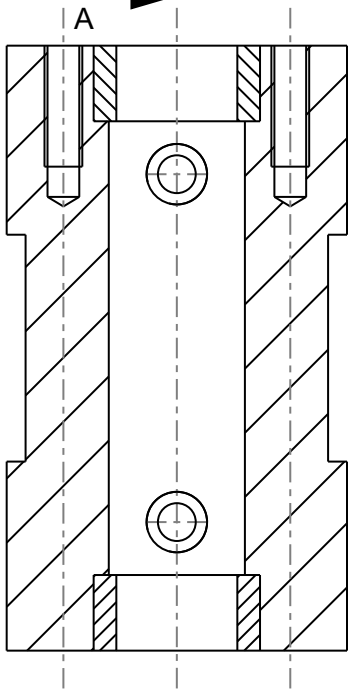

SECTION B-B

3	LONG_GUIDE	1	STEEL_LC
2	KEY_BOLT	2	STEEL_LC
1	BRONZE_SLEEVE	2	BRONZE
Item	Name	Qty	Material

University of Cape Town
Department of Mechanical Engineering

Title
IMPACTOR GUIDE

Dimensions in mm Tolerance U.O.S.	Scale	Date	Sheet	of
	1,000	8 DEC 2010	xx	xx
	Drawn By		Drawing Number	
0.1	R GOVENDER		xx	

SECTION C-C

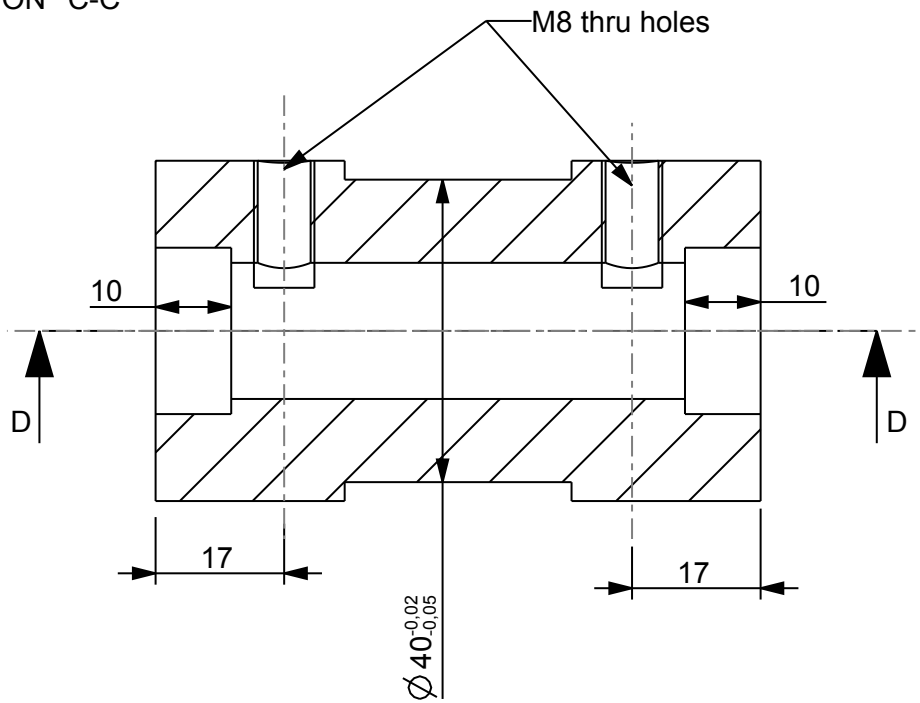

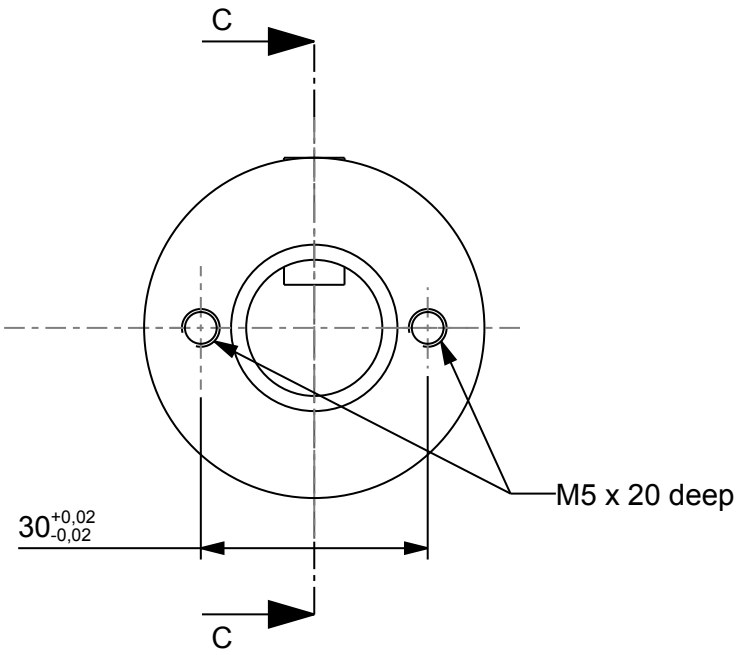

GUIDE HOUSING
MILD STEEL
1 OFF

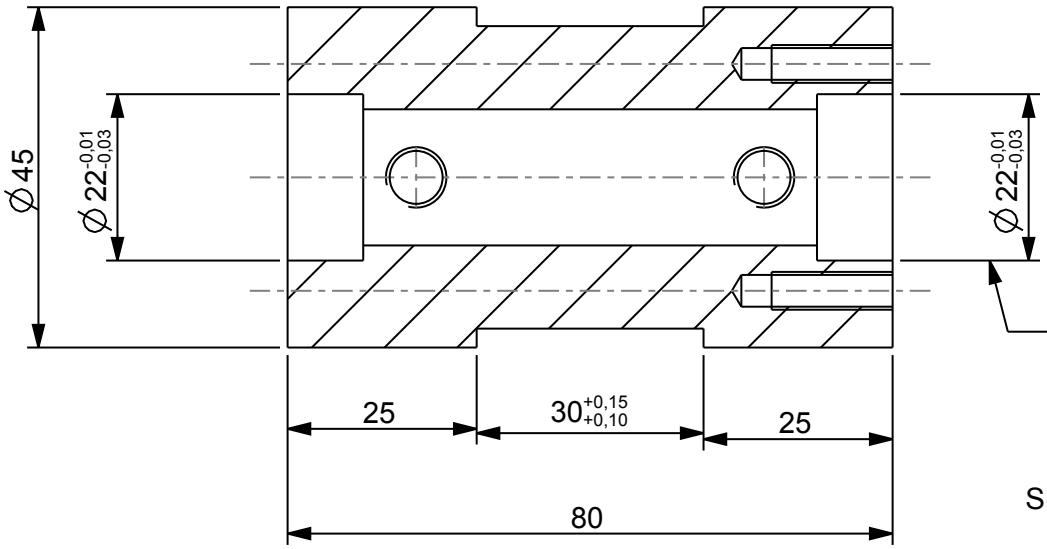

SECTION D-D

Item	Name	Qty	Material
3	LONG_GUIDE	1	STEEL_LC
2	KEY_BOLT	2	STEEL_LC
1	BRONZE_SLEEVE	2	BRONZE

University of Cape Town
Department of Mechanical Engineering

Title: GUIDE HOUSING

Dimensions in mm Tolerance U.O.S.	Scale	Date	Sheet	of
	1,000	08-Dec-10	xx	xx
0.1	Drawn By: REUBEN GOVENDER		Drawing Number: xx	

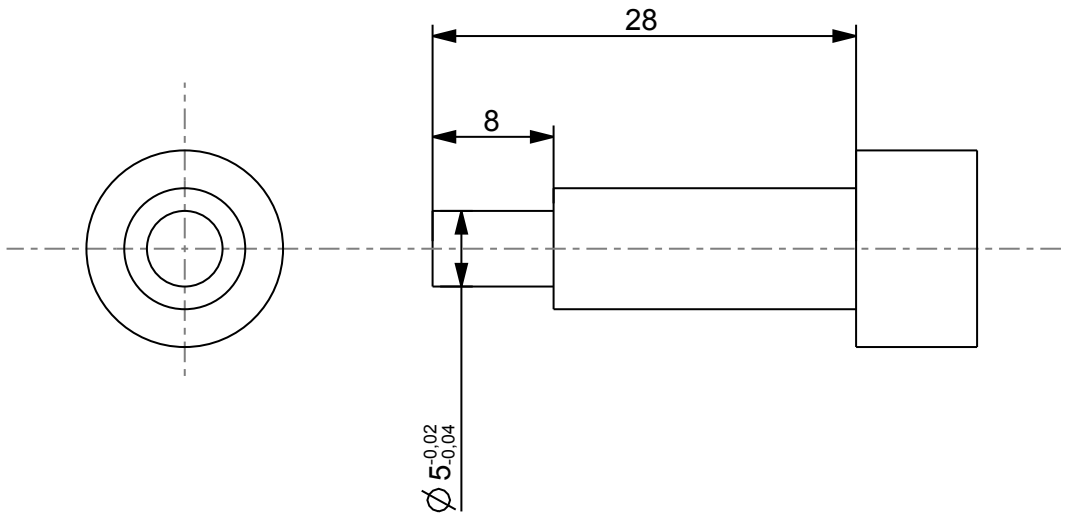

Modified M 8 cap screw
2 off

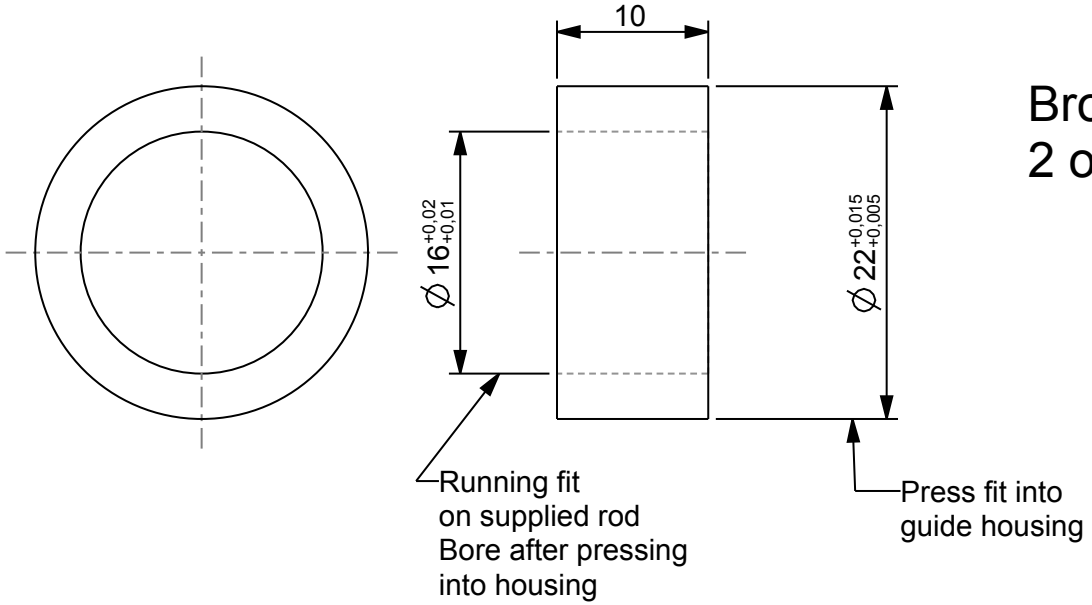

Bronze sleeve
2 off

SCALE 2,000

Item	Name	Qty	Material
	University of Cape Town Department of Mechanical Engineering		
	Title Screws and sleeves		
Dimensions in mm Tolerance U.O.S.	Scale 1,000	Date 08-Dec-10	Sheet xx of xx
0.1	Drawn By REUBEN GOVENDER		Drawing Number xx

SCALE 0,100

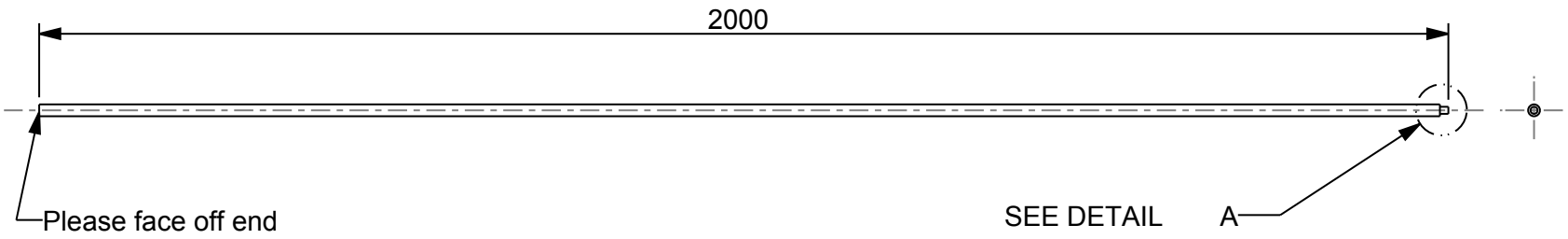

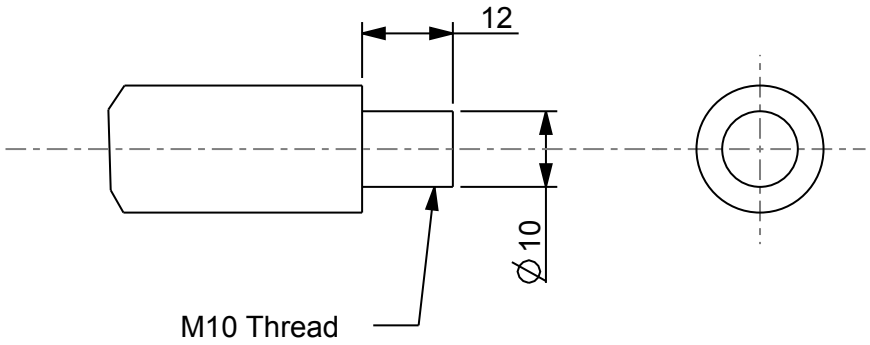

DETAIL A
SCALE 1,000

HPB
Polycarbonate
1 off

Item	Name	Qty	Material

University of Cape Town
Department of Mechanical Engineering

Title: Polycarbonate HPB

Dimensions in mm Tolerance U.O.S.	Scale	Date	Sheet	of
0.1	0,032	13 July 2010	xx	xx
	Drawn By: xx		Drawing Number: xx	

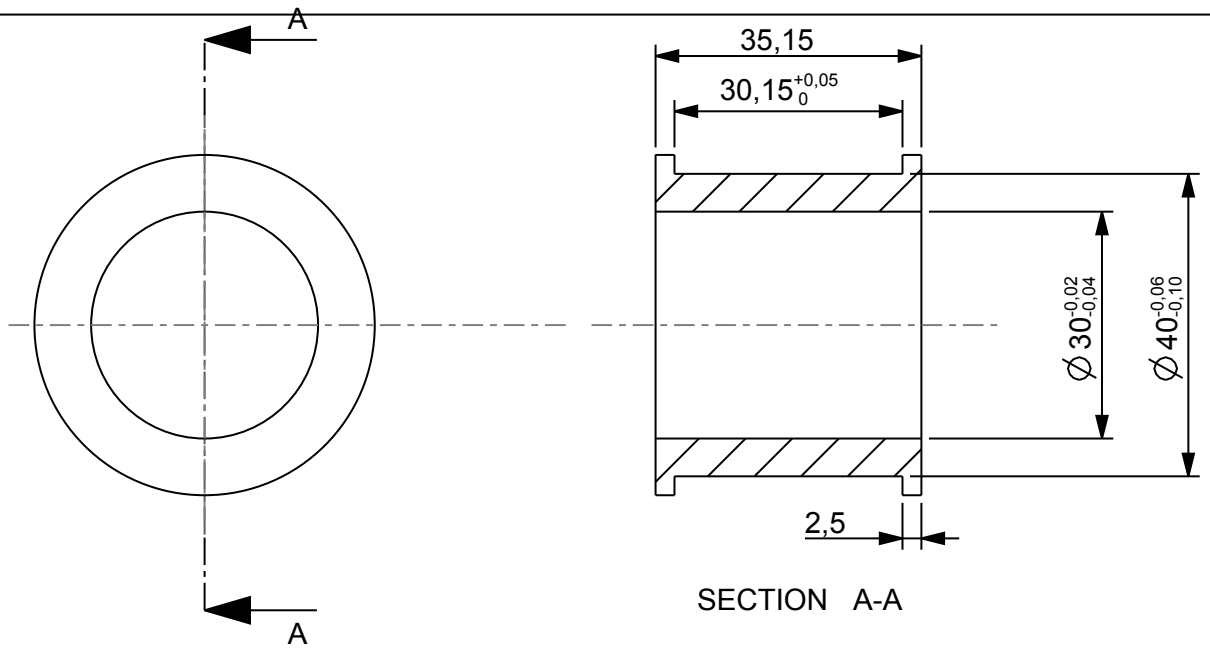

SECTION A-A

Bush
Mild steel
4 off
∅30 bore is for press fit
of Teflon sleeve

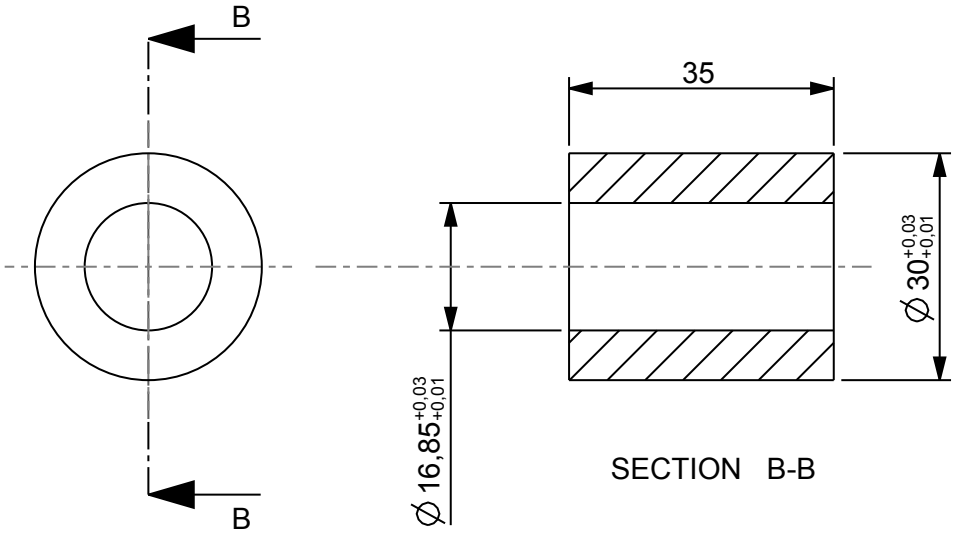

SECTION B-B

Sleeve
Teflon
4 off
Press into steel outer,
then bore inner hole

Item	Name	Qty	Material
	University of Cape Town Department of Mechanical Engineering		
	Title Bushes and sleeves		
Dimensions in mm Tolerance U.O.S. 0.1	Scale 0,032	Date 14-Jul-10	Sheet xx of xx
	Drawn By Reuben Govender		Drawing Number xx